Three Dimensional Hydrodynamic Modelling of Lake Erie: Kelvin Wave Propagation and Potential Effects of Climate Change on Thermal Structure and Dissolved Oxygen

by

Wentao Liu

A thesis
presented to the University of Waterloo
in fulfillment of the
thesis requirement for the degree of
Doctor of Philosophy
in
Applied Mathematics

Waterloo, Ontario, Canada, 2013

I hereby declare that I am the sole author of this thesis. This is a true copy of the thesis, including any required final revisions, as accepted by my examiners.

I understand that my thesis may be made electronically available to the public.

Abstract

This thesis investigates physical processes in Lake Erie, a large, shallow mid-latitude lake, from two perspectives: climate change impacts on the thermal structure and dissolved oxygen concentration and small-scale eddy dynamics generated by internal Kelvin wave propagation. A three-dimensional hydrodynamic and aquatic ecological coupled model ELCOM-CAEDYM, validated by the field data collected in 2008, is first used to investigate the responses of the thermal structure and dissolved oxygen concentration in Lake Erie to potential changes in air temperature and wind speed. A new method is presented to define spatially and temporally varying regions for the epilimnion, thermocline, and hypolimnion. Four metrics are selected to quantify the characteristics of the thermal structure: mean epilimnion temperature, mean hypolimnion temperature, onset and breakdown of stratification, and thermocline depth. Exploiting the power of the three dimensional model to provide a more authentic characterization of thermal structure in such large lakes, it is shown that patterns inferred from simple isotherm dynamics, as typically done with one dimensional models, are not always accurate. In the dissolved oxygen studies similar analyses are presented. Three factors related to lake hydrodynamics have strong influences on hypolimnetic hypoxia: water temperature, stratification duration, and hypolimnion thickness. In a warm and quiescent year the hypolimnetic hypoxia will likely become more severe if considering the effects of meteorological forcing changes only. The present results show the potential for complicated and interactive effects of climate forcing on important biogeochemical processes in Lake Erie as well as other large mid-latitude lakes. Taking advantage of high performance computing, the generation of eddies when a baroclinic Kelvin wave propagates past a peninsula is studied using the MITgcm. The grid resolution can be refined from 2 km to 200 m in the parallel computing environment. With the finer resolution small-scale processes which cannot be resolved in the coarse resolution applied previously are able to be explored. The eddy dynamics are studied in detail in both an idealized lake and in Lake Erie. This work presents a first attempt at simulating small-scale hydrodynamic processes in large lakes and contributes to our understanding of how energy is moved from large scales (the scale of the basins in Lake Erie) to smaller scales (the scale of the peninsula or Point Pelee).

Acknowledgements

First and foremost, I would like to thank my supervisor Dr. Kevin Lamb. Counting my Master's it has been more than six years, and Kevin has greatly influenced my development as a researcher and as a person. I am extremely grateful for his inspiration, guidance, encouragement, financial support, and not to mention the extra efforts of editing my mediocre English writing. More than just a supervisor, Kevin has been a good friend as well as a strong competitor in soccer and cycling.

I would like to thank my committee members Dr. Jinyu Sheng, Dr. Ralph Smith, Dr. Marek Stastna, and Dr. Francis Poulin for taking the time to review my thesis and provide valuable guidance. I thank Marek for numerous helpful discussions on my projects and his leadership in short-table ping pong, basketball, soccer, field trip, beer, BBQ, and "success at success". The CAEDYM setup and tuning were conducted by Dr. Serghei Bocaniov, Dr. Ralph Smith, Dr. Luis Leon, and their colleagues in the Department of Biology. Thanks also go to Dr. Leon Boegman and Dr. Ram Yerubandi for their guidance during collaboration. Ship time in the field was courtesy of Environment Canada (NWRI) and Ontario Ministry of Natural Resources (Wheatley). Part of this work was made possible by the high performance computing facilities SciNet and SHARCNET.

I would like to thank everyone in the fluids group for creating such an enjoyable work environment: Dr. Waite, Nancy, Kris, Michael, Chris, Tim, Anton, Derek, Jason, Sina, Subasha, Jared, Robbie, Aaron, Yangxin, Georges, and Vladimir. Thanks also go to my good friends from the department in the teaching team, soccer buddies, and immigration group: Rahul, Venkata, Andree, Ruibin, Alex, and Wilten. I would also like to express my appreciation to the department staff Stephanie and Helen and Robyn from MFCF. Thank 72 wonderful Management Engineering class of 2017 students that I had a delightful first ever teaching semester. I would like thank my high school math teacher Mr. Tianyun Liu for proving me a solid foundation in mathematics and his great inspiration.

Most importantly, I would like to thank my family. I thank my little cousin Dan at WLU for all the joys she brings in the past four years. I am grateful to my parents who always believe in me and encourage me. To let me acquire top-notch education is always their higher priority, even it means that we can only have several weeks of family time every year. There is no word to express my appreciation and gratefulness, and I love you both! Finally I would like to thank my fiancée and my love Yang. Time does fly when one is in love. From Harbin to Vancouver, to Waterloo, St. Catharines, and Calgary, it has been eleven years since we first met. I am so lucky to have you by my side. Without your support I could not have achieved my goals. You are my deepest love and I will always love you!

Dedication

To My Parents and Fiancée

Table of Contents

List of Tables

List of Figures

Chapter 1

Introduction

The Laurentian Great Lakes are a collection of freshwater lakes in eastern North America which form the largest group of their kind on Earth by total surface area. The Great Lakes have strong impacts on local weather and climate due to their large scales (Obolkin and Potemkin 2006). Conversely, climate change through changes in air temperature, wind, precipitation, and evaporation can in turn significantly affect lakes' thermal structure and biochemical processes (Lam and Schertzer 1999; Lehman 2002). Past work on lakes has focused on large spatial (several kilometres in grid size) and temporal (seasonal) scales. In light of the recent realization that high frequency internal waves can play important roles in biogeochemical processes in lakes and that many ecosystem processes occur at small spatial scales, small-scale hydrodynamic processes have recently received growing attention (Wuest and Lorke 2003; Lamb 2004). This thesis investigates physical processes in Lake Erie, which is a large, shallow mid-latitude lake, from two different perspectives: climate change impacts on the thermal structure and dissolved oxygen concentration and small-scale eddy dynamics generated by internal Kelvin wave propagation.

1.1 Climate impacts

The mean global surface air temperature has increased by about 0.5 to 0.9°C during the 20th century, and it is predicted to rise a further 1.1 to 2.9°C for low greenhouse gas emission scenarios and 2.4 to 6.4°C for high emission scenarios during the 21st century (Intergovernmental Panel on Climate Change 2007). Climate warming is anticipated to have great impacts on the Laurentian Great Lakes ecosystem (Lam and Schertzer 1999), including hydrology (Mortsch et al. 2000), plankton (Lehman 2002) and fisheries (Lynch et al. 2010). Recently Trolle et al. (2011) applied a one-dimensional ecosystem model to three morphologically different lakes, and suggested that a warmer climate can produce effects similar to increased nutrient loading. By contrast Rucinski et al. (2010) used a coupled one-dimensional temperature-dissolved oxygen model to argue that changes in the production of organic matter, rather than climate variability, is the dominant factor in dissolved oxygen changes in the central basin of Lake Erie. With the complexities inherent in modelling and predicting ecological impacts, it is important to start with an accurate account of the most direct impacts of climate variations, notably changes in thermal structure.

The thermal structure includes two fundamental components, water temperature and seasonal thermocline depth. Temperature determines the solubility of many substances, influences organism distributions based on thermal habitat preferences (Lynch et al. 2010), and affects the rate of chemical reactions and biological processes such as photosynthesis and respiration (Falkowski and Raven 2007). The epilimnion depth influences sedimentation losses (Diehl et al. 2002), phytoplankton biomass concentration (Kunz and Diehl 2003), and availability of light and nutrients in the surface mixed layer (Kunz and Diehl 2003) while also playing an important role in hypolimnetic hypoxia (Lam and Schertzer 1987). The epilimnion depth also affects the production to respiration balance of plankton communities (Bocaniov and Smith 2009) and thus the potential for export of organic matter to support other trophic levels or hypolimnetic consumption. Hydrodynamic processes and upwelling events can also significantly influence plankton production and respiration (Bocaniov et al. 2012).

Mortsch and Quinn (1996) developed a series of climate change scenarios for the Great Lakes Basin using general circulation models (GCMs), and stated that the direct impacts of climate change would occur through higher air and water temperatures. Rodgers (1987) examined how the onset of summer stratification in Lake Ontario responded to changes in air and water temperatures using records from 1965 to 1985. Robertson and Ragotzkie (1990) applied both a one-dimensional hydrodynamics model DYnamical REservoir Simulation Model (DYRESM) and a statistical regression approach to investigate the response of the thermal structure to changes in air temperature in Lake Mendota [Wisconsin, USA]. More recently Austin and Allen (2011) studied the sensitivity of the summer thermal structure in the western end of Lake Superior to meteorological forcing using the Regional Ocean Modeling System (ROMS) model run in a one-dimensional mode. Previous work leaves room for uncertainty about how the physical effects of climate change will be manifested in large lakes, and what they will mean for the ecology. From Austin and Allen (2011) it is expected that higher air temperatures will make the epilimnion shallower and increase its temperature, while higher winds will tend to have the opposite effect. However, three dimensional processes such as upwelling, inter-basin advection and nearshore-offshore exchange may be expected to influence the predicted sensitivity of the thermal structure to environmental forcing. Lake or basin depths will also affect the situation by changing the rate of equilibration between lake and atmosphere (Austin and Allen 2011).

Of great concern in recent years is hypoxia in the deep water of the central basin of Lake Erie, which is generally defined as oxygen concentration less than 2 mg L^{-1}. Seasonal hypoxia has significant effects on fish habitat in the lake (Arend et al. 2011). Billions of dollars have been spent on control of nutrient loading to Lake Erie in Canada and the United States. There has been success in meeting a variety of water quality targets, notably chlorophyll and phosphorus, in offshore lake waters. However, the hypoxia phenomenon may have worsened (Charlton and Milne 2004). The management of hypolimnetic hypoxia requires an understanding of physical, biological, and chemical coupling processes, which fortunately can be represented by computational models. The hypoxia issue in Lake Erie has been studied using various tools and numerical models (Rao et al. 2008; Leon et al. 2011). The 2011 record-setting algal bloom in Lake Erie is believed to have a tight connec-

tion with the unusual meteorological conditions (Michalak et al. 2013). However, like the thermal structure, there have been no sensitivity studies of the effects of climate change on dissolved oxygen conducted using fully three dimensional models. Not only is the Lake Erie hypoxia issue important in its own, it presents an excellent opportunity to advance the incorporation of hydrodynamics into ecological modelling in a system.

1.2 Small-scale dynamics

Due to limitations of current computational resources, most hydrodynamic models of large lakes focus on large spatial (several kilometres in grid size) and temporal (seasonal) scales. However, small-scale dynamics such as high frequency internal waves, boundary layer effects, turbulent mixing etc, also play important roles in the lake hydrodynamic and biochemical processes (Wuest and Lorke 2003). Bouffard et al. (2012) investigated Poincaré waves in Lake Erie, and found that wave induced mixing can significantly modify the energy flux paths. Leon et al. (2012) performed a nested (100 m grid nested in a 2 km grid) modelling of Lake Ontario. Their nearshore model captured the complexity of stratification, mixing, upwelling, and circulation that cannot be simulated on the lake-wide scale.

In coastal oceans leeward eddies have often been observed behind headlands and capes (Pattiaratchi et al. 1987; McCabe et al. 2006; Magaldi et al. 2008). These eddies affect coastal physical dynamics and play important roles in biological, chemical, and ecological processes. The eddy generation is related to flow separation and can be explained by the adverse pressure gradients and boundary layer theory (Schlichting and Gersten 2004). Due to their large horizontal scales the Great Lakes are dynamically similar to coastal oceans in some aspects, and certainly on the scale of headlands and capes. In Lake Superior McKinney et al. (2012) observed 45 eddies during the spring and summer using fine resolution Synthetic Aperture Radar (SAR) imagery, from satellite. Many eddies occurred along the southern and eastern shores as well as areas where the boundary current interacts with topographic features including islands and promontories (McKinney et al. 2012). To my

knowledge there are no studies focusing on the eddy generation due to Kelvin wave propagation in lakes. A higher resolution than the current lake-scale numerical simulations is utilized to investigate such dynamics. By taking advantage of parallel computing capability in the MITgcm, the resolution can be refined by a factor of 10 from 2 km to 200 m. At the finer resolution it is expected to be able to explore more small-scale processes that cannot be resolved when the resolution is on the order of kilometres, including eddies with diameters of a few kilometres.

1.3 Thesis organization

Chapter 2 briefly describes some necessary theoretical background and introduces the numerical models which are applied in this thesis. In Chapter 3 a coupled numerical model ELCOM-CAEDYM is applied to conduct hydrodynamic and biochemical modelling in Lake Erie. The numerical model is validated using 2008 field data, via water temperature, currents, and dissolved oxygen. An attempt to explain the 2012 Lake Erie fish kill from a hydrodynamic point of view is presented in the end. Chapter 4 studies climate change impacts on the lake at the basin scale. By combining three dimensional modelling with an original method for defining the extent of thermal stratification, a more complete portrayal of how thermal structure and dissolved oxygen responds to a changing climate is presented. To my knowledge, no previous study of the sensitivity of the thermal structure and dissolved oxygen to climate change scenarios has been conducted using a three-dimensional numerical model. In Chapter 5 an aspect of smaller scale dynamics in lakes, i.e. eddies, is studied. Internal Kelvin wave propagation around both a Gaussian peninsula in a rectangular lake and Point Pelee in Lake Erie are investigated in detail. A brief conclusion of this thesis and a list of future work are summarized in Chapter 6.

Chapter 2

Background

This chapter briefly presents some necessary background material about the numerical models used in this thesis and physical processes in lakes. Two numerical models that are applied in this thesis: ELCOM-CAEDYM and the MITgcm are introduced in Section 2.1. In Section 2.2 the heat budget and thermodynamics are discussed through their implementation in ELCOM. A short introduction to physical processes in large temperate lakes is given in Section 2.3.

2.1 Numerical models

Hydrodynamic modelling development for the Laurentian Great Lakes has been ongoing since the 1960s using many different numerical tools. The first three-dimensional hydrodynamic model for the Great Lakes used a finite difference method and was based on the hydrostatic and Boussinesq approximations (Simons 1974). Schwab and Bedford (1994) developed an experimental Great Lakes forecasting system using POM (Princeton Ocean Model). POM was developed in the late 1970's and is a sigma coordinate, free surface, three-dimensional, primitive equation ocean model, which includes a turbulence sub-model (Blumberg and Mellor 1987). The MITgcm (Massachusetts Institute of Technology's General Circulation Model) is a numerical model for studying the ocean and atmosphere. It is

capable of simulating these fluids at a wide range of scales and can resolve many different processes (Marshall et al. 1997a; Marshall et al. 1997b). Bennington et al. (2010) investigated the general circulation of Lake Superior using the MITgcm. Sheng and Rao (2006) applied a nested system based on the three-dimensional, primitive-equation z-level ocean model CANDIE (CANadian version of DIEcast, where DIEcast stands for the Dietrich Center for Air Sea Technology model) to simulate Lake Huron dynamics in 1974–75. An unstructured grid, finite-volume, sigma-coordinate terrain following ocean model known as the FVCOM (Finite Volume Coastal Ocean Model) was applied to Lake Ontario by Shore (2009). ELCOM (Estuary and Lake Computer Model) has been successfully applied to many large lakes including Lake Erie (Leon et al. 2005) and Lake Ontario (Huang et al. 2010a). ELCOM and the MITgcm are the two numerical models applied in this thesis, so both models will be discussed in the following sections in detail.

2.1.1 ELCOM-CAEDYM

ELCOM was developed at the Centre for Water Research at the University of Western Australia, implemented in FORTRAN 90 with F95 extensions. ELCOM is a numerical modelling tool that applies hydrodynamic and thermodynamic models to simulate the temporal behaviour of stratified water bodies with environmental forcing (ELCOM User Manual 2006). It is a nonlinear, three-dimensional, hydrostatic, free surface, z-level model. The hydrodynamic algorithms are based on the TRIM approach of Casulli and Cheng (1992) with modifications for accuracy, scalar conservation, numerical diffusion, and implementation of a mixed-layer turbulence closure. An eddy viscosity parametrization is used to represent horizontal subgrid-scale turbulent mixing. In the vertical ELCOM uses either a vertical eddy viscosity parametrization or a mixed-layer model which is discussed in detail in Hodges et al. (2000). The mean governing equations solved in ELCOM (ELCOM

Science Manual 2006) are

$$\textit{Momentum:}\quad \frac{\partial U_\alpha}{\partial t} + U_j\frac{\partial U_\alpha}{\partial x_j} = -g\Big(\frac{\partial \eta}{\partial x_\alpha} + \frac{1}{\rho_0}\frac{\partial}{\partial x_\alpha}\int_{x_3}^{\eta}\rho' dz\Big) + \frac{\partial}{\partial x_1}\Big(\nu_1\frac{\partial U_\alpha}{\partial x_1}\Big) + \frac{\partial}{\partial x_2}\Big(\nu_2\frac{\partial U_\alpha}{\partial x_2}\Big) + \frac{\partial}{\partial x_3}\Big(\nu_3\frac{\partial U_\alpha}{\partial x_3}\Big) - \delta_{\alpha\beta} f U_\beta, \tag{2.1}$$

$$\textit{Continuity:}\quad \frac{\partial U_j}{\partial x_j} = 0, \tag{2.2}$$

$$\textit{Transport of scalars:}\quad \frac{\partial C}{\partial t} + \frac{\partial}{\partial x_j}(CU_j) = \frac{\partial}{\partial x_1}\Big(\kappa_1\frac{\partial C}{\partial x_1}\Big) + \frac{\partial}{\partial x_2}\Big(\kappa_2\frac{\partial C}{\partial x_2}\Big) + \frac{\partial}{\partial x_3}\Big(\kappa_3\frac{\partial C}{\partial x_3}\Big) + S_C. \tag{2.3}$$

The equations are written in the Einstein summation convention, that is, whenever an index j occurs twice in a term, a summation over the repeated index is implied. (x_1, x_2, x_3) are the coordinates where x_3 denotes the vertical component. (U_1, U_2, U_3) are the velocities. α and β are running indices (i.e. they take the values 1, 2, 3) for the components of velocity. η is the free surface height. ρ_0 and ρ' is the reference density and density perturbation. (ν_1, ν_2, ν_3) are the kinematic viscosity in each direction. f is the Coriolis parameter. $\delta_{\alpha\beta}$ is the Kronecker delta. C is the scalar property being transported. $(\kappa_1, \kappa_2, \kappa_3)$ are the diffusivity of the scalar in each direction and S_C is the source term of the scalar.

Through coupling with a water quality module CAEDYM (Computational Aquatic Ecosystem DYnamics Model), ELCOM can be used to simulate three-dimensional transport and interactions of flow physics, biology and chemistry. CAEDYM consists of a system of mathematical equations representing the major biogeochemical processes influencing water quality. At its most basic, CAEDYM is a set of library subroutines that contain process descriptions for primary production, secondary production, nutrient and metal cycling, and oxygen dynamics and the movement of sediment (CAEDYM User Manual 2006). The coupling between ELCOM and CAEDYM is dynamic: ELCOM provides CAEDYM the hydrodynamic driver, and the thermal structure of the water body is dependent on the water quality concentrations by feeding back through water clarity which is simulated by CAEDYM (Fig. 2.1 and CAEDYM Science Manual 2006).

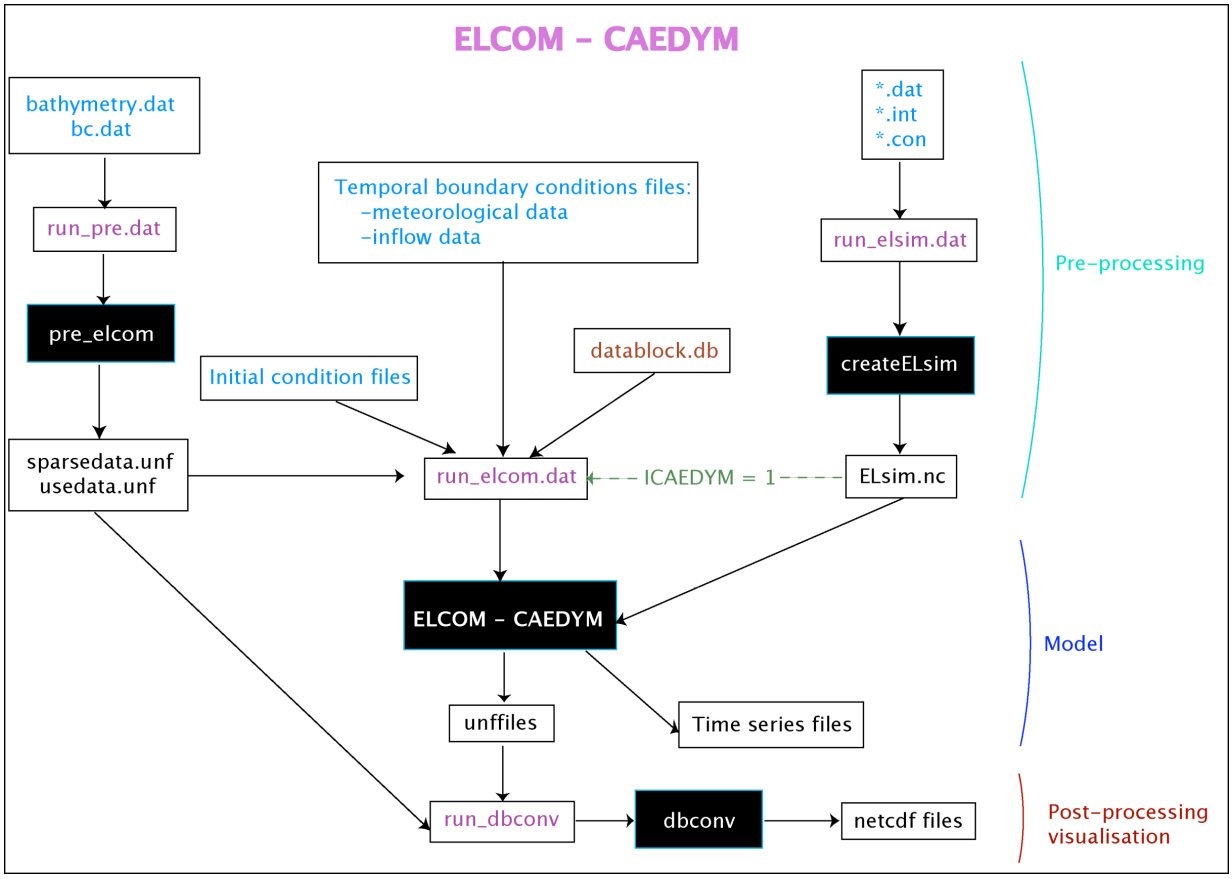

Figure 2.1: ELCOM-CAEDYM organization (from CAEDYM User Manual 2006).

2.1.2 The MITgcm

The MITgcm is a numerical model designed for the study of the atmosphere, ocean, and climate, which has a number of novel aspects (Marshall et al. 1997a; Marshall et al. 1997b; MITgcm Manual 2013). It can be used to study both atmospheric and oceanic phenomena using a single dynamical kernel. It has non-hydrostatic capability and can be used to study both small-scale and large-scale processes. Finite volume techniques are employed yielding an intuitive discretization and some support for the treatment of irregular geometries. Also the model is developed to perform efficiently on a wide variety of computational platforms.

In the ocean environment the MITgcm solves the incompressible, non-hydrostatic, Navier-Stokes equations under the Boussinesq approximation on the f-plane (MITgcm Manual 2013).

$$\frac{D\overrightarrow{V_h}}{Dt} + f\hat{k} \times \overrightarrow{V_h} + \frac{1}{\rho_0}\overrightarrow{\nabla_h} p = \overrightarrow{F_h}, \tag{2.4}$$

$$\epsilon_{nh}\frac{DW}{Dt} + \frac{\rho' g}{\rho_0} + \frac{1}{\rho_0}\frac{\partial p}{\partial z} = \epsilon_{nh} F_W, \tag{2.5}$$

$$\overrightarrow{\nabla_h} \cdot \overrightarrow{V_h} + \frac{\partial W}{\partial z} = 0, \tag{2.6}$$

$$\rho' = \rho(T, S), \tag{2.7}$$

$$\frac{DT}{Dt} = Q_T, \tag{2.8}$$

$$\frac{DS}{Dt} = Q_S, \tag{2.9}$$

where $\overrightarrow{V} = (\overrightarrow{V_h}, W)$ is the velocity, $\frac{D}{Dt} = \frac{\partial}{\partial t} + \overrightarrow{V} \cdot \overrightarrow{\nabla}$ is the total derivative, f is the Coriolis parameter, $\overrightarrow{\nabla_h}$ is the horizontal gradient, $\hat{k}$ is a unit vector in the vertical, $\overrightarrow{F} = (\overrightarrow{F_h}, F_W)$ is a vector combining the effects of forcing and dissipation, ρ_0 is the reference density, ρ' is the density perturbation, ϵ_{nh} is a switch that turns non-hydrostatic effects on and off, T is the temperature, Q_T is the temperature forcing, S is the salinity, and Q_S is the salinity forcing. When nonhydrostatic effects are turned on, $\epsilon_{nh} = 1$, and when $\epsilon_{nh} = 0$, the vertical momentum equation reduces to a statement of hydrostatic balance.

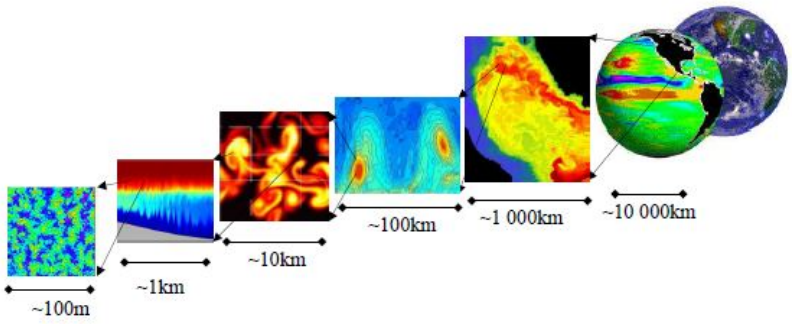

Figure 2.2: The MITgcm can be applied to a wide range of phenomenon, from convection on the left to the global circulation on the right (from MITgcm Manual 2013).

2.2 Heat budget and thermodynamics in lakes

Solar radiation is fundamentally important to the lake ecosystem. The solar radiation spectrum is generally divided into three groups by the wavelength (Wetzel 2001): ultraviolet (10 to 400 nm), visible (380 to 780 nm), and infrared (700 to 10^6 nm). Shortwave radiation contains visible, near-ultraviolet, and near-infrared, and the wavelength is normally in the range between 280 and 2800 nm. Longwave radiation is the radiant energy with wavelength greater than 2800 nm (Hodges 1998). Shortwave radiation is usually measured directly, while the longwave radiation emitted from clouds and water vapour can be measured or calculated. Trenberth et al. (2009) presented the global annual mean Earth's energy budget from March 2000 to May 2004 (Fig. 2.3). In this figure the incoming arrows show shortwave radiation from the sun reflected to space and absorbed in the atmosphere and at the surface, and the outgoing arrows show longwave radiation.

Heat transfer at a free surface is generally classified into radiation, convection, conduction, and evaporation. For numerical modelling it is convenient to classify it by its ability to penetrate the water surface. Evaporation, conduction, and longwave radiation occur only at the surface and hence are part of the surface heat transfer. Shortwave radiation, on the other hand, can penetrate through the water column. In the following each flux component is briefly introduced and presented through its implication in ELCOM. Most

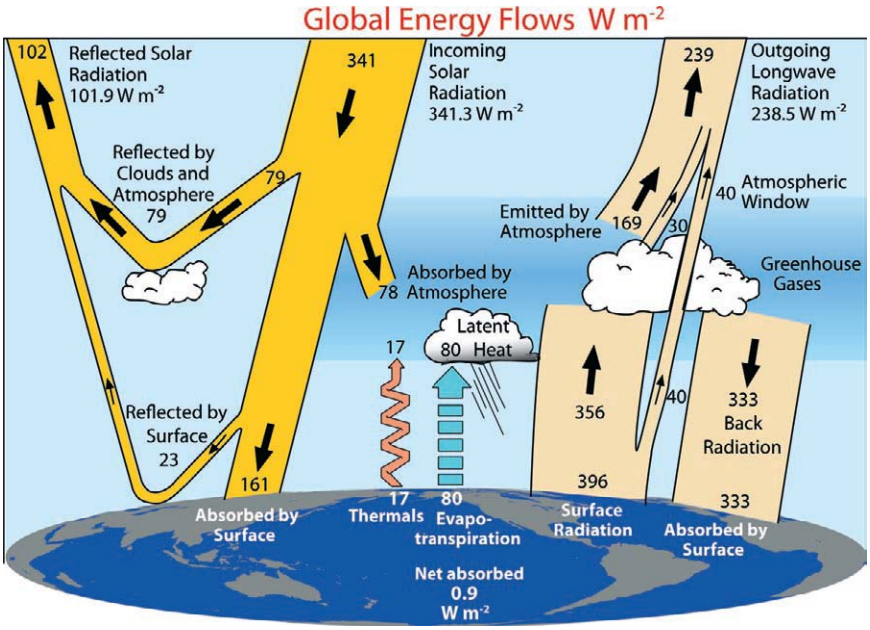

Figure 2.3: The global annual mean Earth's energy budget from March 2000 to May 2004 (from Trenberth et al. 2009).

materials in this section are based on ELCOM Science Manual (2006) and Hodges (1998).

Shortwave radiation can be divided into four components, and ELCOM 2.2 assumes the following percentages for each component: Photosynthetically Active Radiation (PAR) 45%, Near Infrared (NIR) 41%, Ultra Violet A (UVA) 3.5%, and Ultra Violet B (UVB) 0.5%. The distance of the radiation penetrating into the water column depends on the extinction coefficient for each bandwidth, which is a function of water colour, turbidity, plankton concentration, etc. ELCOM allows users to set the extinction coefficient for each band. If water quality is simulated in the coupled model then the PAR extinction coefficient is calculated by CAEDYM. The net solar radiation penetrating the water is given by

$$Q_{\mathrm{sw}} = Q_{\mathrm{sw(total)}}\left(1 - r_a^{(\mathrm{sw})}\right), \tag{2.10}$$

where Q_{sw} and $Q_{\mathrm{sw(total)}}$ are net shortwave radiation penetrating the water surface and total shortwave radiation reaching the water surface, and $r_a^{(\mathrm{sw})}$ is the shortwave albedo of the

water surface depending on the latitude and day of year. Shortwave radiation penetrates the water column according to the Beer-Lambert law,

$$Q(z) = Q_{\mathrm{sw}} e^{-\eta_\alpha z}, \tag{2.11}$$

where z is the depth and η_α is the attenuation coefficient for each band.

Longwave radiation is calculated in ELCOM by one of three methods depending on the input data. (i) If given measurements of the incident long wave radiation, then the net longwave radiation is calculated by the difference of the parts penetrating the surface and emitted from the water,

$$Q_{\mathrm{lw}} = \left(1 - r_a^{(\mathrm{lw})}\right) Q_{\mathrm{lw(incident)}} - \epsilon_{\mathrm{w}} \sigma T_{\mathrm{w}}^4, \tag{2.12}$$

where $Q_{\mathrm{lw(incident)}}$ is the total incident longwave radiation, $r_a^{(\mathrm{lw})} = 0.03$ is the albedo, $\epsilon_{\mathrm{w}} = 0.96$ is the emissivity of the water surface, σ is the Stefan-Boltzmann constant, and T_{w} is the water temperature in degree Kelvin. (ii) If the net longwave radiation measurement is given,

$$Q_{\mathrm{lw}} = \left(1 - r_a^{(\mathrm{lw})}\right) Q_{\mathrm{lw(net)}}. \tag{2.13}$$

(iii) Long wave radiation can also be estimated from atmospheric conditions, using cloud cover fraction ($0 \leq C \leq 1$). The net longwave radiation is calculated the same way as in Equation (2.12), and $Q_{\mathrm{lw(incident)}}$ is obtained through the atmospheric conditions,

$$Q_{\mathrm{lw(incident)}} = (1 + 0.17C^2)\epsilon_{\mathrm{a}}(T_{\mathrm{a}})\sigma T_{\mathrm{a}}^4, \tag{2.14}$$

where the subscript refers to properties of the air.

Sensible heat is heat exchanged due to a change of temperature. In ELCOM it is formulated as

$$Q_{\mathrm{sh}} = C_s \rho_{\mathrm{a}} C_P U_{\mathrm{a}} (T_{\mathrm{a}} - T_{\mathrm{w}}), \tag{2.15}$$

where C_S is the sensible heat transfer coefficient for wind speed at 10 m reference height, ρ_{a} is the air density in kg m^{-3}, C_P the specific heat of air at constant pressure, and U_{a} is

the wind speed at 10 m reference height.

Latent heat is the heat released or absorbed during a constant temperature process, typically a change of state. In lake thermodynamics the latent heat flux typically results from evaporation. In ELCOM the latent heat flux is given by

$$Q_{\text{lh}} = \min\Big(0, \frac{0.622}{P} C_L \rho_{\text{a}} L_E U_{\text{a}} \big(e_{\text{a}} - e_s(T_S)\big)\Big), \tag{2.16}$$

where P is the atmospheric pressure, C_L is the latent heat transfer coefficient for wind at 10 m height, L_E the latent heat of evaporation of water, e_{a} the air vapour pressure, and e_s the saturation vapour pressure at the water surface temperature T_S. The condition of $Q_{\text{lh}} \leq 0$ is because no condensation effects are considered.

The total non-penetrative heat flux is given by the sum of longwave radiation, sensible heat, and latent heat

$$Q_{\text{non-pen}} = Q_{\text{lw}} + Q_{\text{sh}} + Q_{\text{lh}}. \tag{2.17}$$

2.3 Physical processes in temperate lakes

Most fresh water lakes in temperate regions undergo a seasonal change, alternating between a two-layer stratification and a complete mixed state. The greatest source of heat is solar radiation, and most of the solar radiation is absorbed in the upper few meters with an exponential decay with depth. As the surface water is warmed and becomes less dense, the relative thermal resistance to mixing increases, which is defined as a measure of a body's ability to prevent heat from flowing through it. A difference of only a few degrees in the vertical is sufficient to prevent complete mixing of the water column (Wetzel 2001). Because of wind-induced mixing, the surface layer is well mixed with an almost vertically uniform temperature. The water temperature at the bottom remains relatively cold due to the thermal resistance of the middle stratified layer. From that time onward, the water column is thermally divided into three regions: the epilimnion, metalimnion, and hypolimnion. In Wetzel (2001), the epilimnion is defined as *"the upper stratum of less dense,*

more or less uniformly warm, circulating, and fairly turbulent water", the hypolimnion is *"the lower stratum of more dense, cooler, and relatively quiescent water lying below the epilimnion"*, the metalimnion is *"the transitional stratum of marked thermal change between epilimnion and hypolimnion"*, and finally the thermocline is *"the plane or surface of maximum rate of decreases of temperature in the metalimnion"*. Figure 2.4 shows a typical thermal stratification of a temperate lake, and the dotted lines indicate the approximated boundaries of three regions.

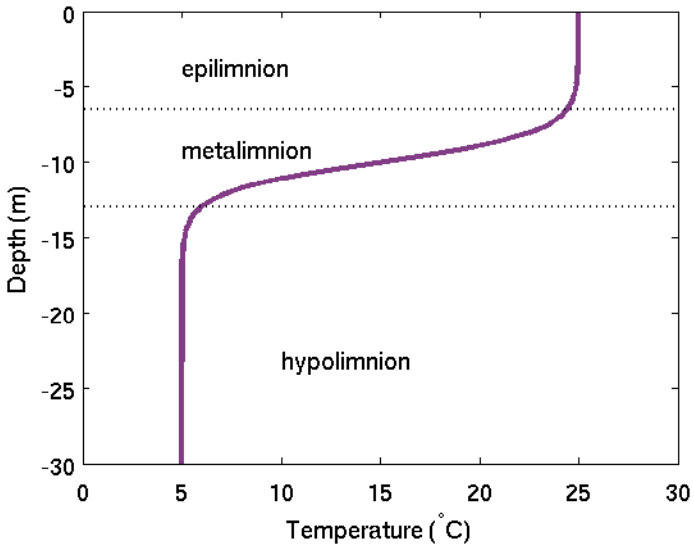

Figure 2.4: Typical thermal stratification of a temperate lake.

The metalimnion is a barrier to the mixing of surface and bottom water. Kinetic energy is required for mixing, which is primarily provided by wind in the absence of inflows and outflows during the stably stratified period. Convection, which converts potential energy to kinetic energy, is another source of kinetic energy. During the summer stratified period convection driven by surface cooling often occurs at night during the stratified summer period or during episodic cold events. Convectively driven overturning is associated with warming in the early spring and cooling in the fall. As wind blows over the surface for a period of time, wind drift causes water to pile up at the lee end of the lake. The accumulated water is then forced down by gravity and when it hits the more dense water

of the metalimnion, it flows back in a direction opposite to the wind (Fig. 2.5, Mortimer 1974). The metalimnion is tilted in the process. When the wind stops blowing, the tilted metalimnion is released and adjusts through the generation of basin-scale internal waves. In general the response of the metalimnion to an imposed wind stress is a complex function of geometry, stratification, and the temporal dynamics of the wind forcing (Monismith 1986). For simply shaped and small-to-medium sized lakes, modal-type responses are usually observed (Rao 1966).

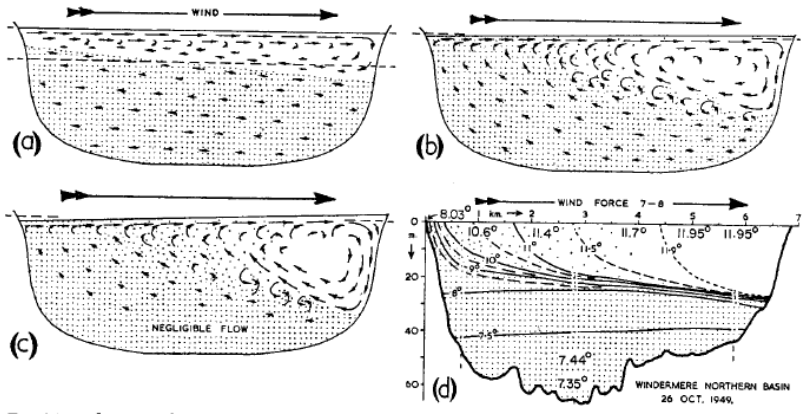

Figure 2.5: Two-dimensional representation of the effects of wind on a stratified lake: (a) to (c) stages in the development of the epilimnetic wedge and of shear instability at the downwind end of the thermocline; (d) isotherm distribution in Windermere, northern basin, after about 12 hours of relatively steady wind (from Mortimer 1974).

The Rossby number is a dimensionless number used to characterize the importance of Coriolis effects generated by the Earth rotation (Kundu and Cohen 2004). It is a ratio of inertia to Coriolis terms

$$Ro = \frac{U^2/L}{fU} = \frac{U}{fL}, \tag{2.18}$$

where f is the Coriolis parameter, and U and L are characteristic velocity and length of the flow. A length scale named the Rossby radius of deformation is defined to indicate at

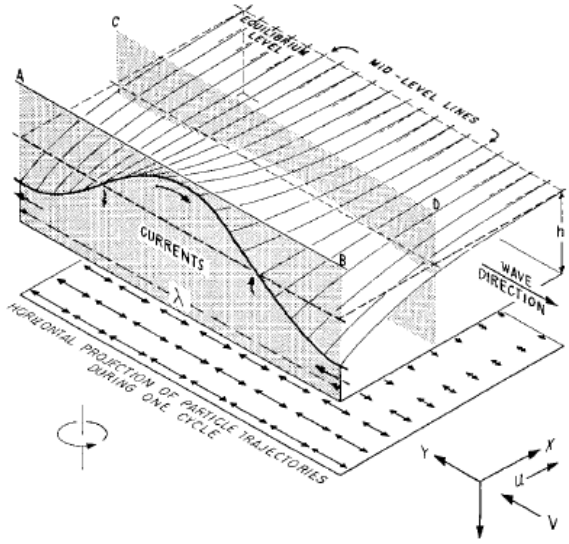

Figure 2.6: A long Kelvin wave in a uniform depth model (from Mortimer 1974).

which length Coriolis effects become important,

$$R = \frac{c}{f}, \tag{2.19}$$

where c is the non-rotating phase speed. R is classified as the external or internal Rossby radius of deformation for barotropic and baroclinic motions respectively. For small lakes the effect of Earth's rotation is negligible. The baroclinic motions are then mostly standing waves. The internal waves can be characterized by numbers (modes) indicating the number of the wave nodes in the horizontal and the vertical. When the lake dimension is larger than the internal Rossby radius, the Coriolis effects cannot be neglected. The effect of rotation changes the characteristics of basin-scale internal waves. The wave crests begin to propagate around the boundaries of the lake. The modified long gravity waves usually appear in two different forms: Kelvin waves and Poincaré waves (Wetzel 2001). Kelvin waves develop when seiching is deflected by the Coriolis force to the right boundary in the northern hemisphere (left in the southern hemisphere), and they are boundary-trapped waves. The wave amplitude decreases exponentially away from the boundary (Fig. 2.6), and

the waves travel along the shore of basins in a counterclockwise direction in the northern hemisphere (clockwise in the southern hemisphere). In large lakes long gravity waves can travel in open water without the interference of shore boundaries. Influenced by rotation, these long waves, named Poincaré waves, form a wave pattern of alternating hills and valleys with corresponding cellular patterns of currents (Fig, 2.7, Wetzel 2001). In the northern hemisphere, they have clockwise rotating structures with maximum velocities in the centre. Both types of waves have been observed and studied in many large lakes including Lake Biwa (Saggio and Imberger 1998), Lake Kinneret (Hodges et al. 2000), and Lake Erie (Bouffard et al. 2012).

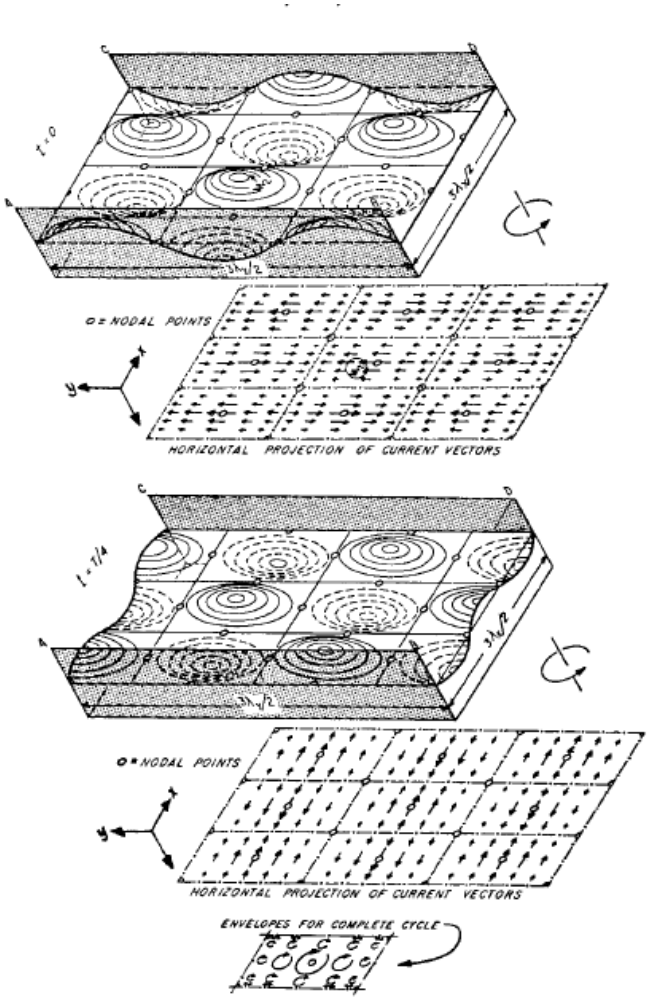

Figure 2.7: A standing Poincaré wave in a wide, rotating channel of uniform depth (from Mortimer 1974).

Chapter 3

Hydrodynamic and Biochemical Modelling in Lake Erie

In this chapter the coupled ELCOM-CAEDYM is utilized to conduct hydrodynamic and biochemical modelling in Lake Erie. In Section 3.1 the meteorological forcing data are compared and analyzed, and the numerical model is set up in detail in Section 3.2. In Section 3.3 the numerical model is validated using field data collected in 2008, via water temperature, currents, and dissolved oxygen. Section 3.4 demonstrates another application of the ELCOM modelling, where an attempt to explain the 2012 Lake Erie fish kill from a hydrodynamic point of view is proposed.

3.1 Meteorological data process

Lake Erie has three major physiographic divisions: the western, central, and eastern basins. The western basin is the shallowest, with average and maximum depths of 7.4 and 18.9 m. The central basin has average and maximum depths of 18.5 and 25.6 m. It is separated from the western basin by a chain of islands and Point Pelee, and from the eastern basin by a relatively shallow sand and gravel bar between Erie and Long Point.

The eastern basin is the deepest with a mean depth of 24.4 m and a 64.0 m maximum (Bolsenga and Herdendorf 1993). Water levels vary by about 0.5 m on seasonal time scales. The Detroit river provides about 95% of the inflow to Lake Erie at the western end of the western basin. This water then passes through the flat central basin, the bowl-shaped eastern basin, and is finally drained through the Niagara River. The residence time of Lake Erie is about 2.6 years (O'Sullivan and Reynolds 2004).

In 2008 an intensive field investigation was carried out to gather new information about the meteorology, water temperature, currents, dissolved oxygen, and nutrients in Lake Erie. This field program was part of a project funded by a Strategic Project Grant awarded by the Natural Sciences and Engineering Research Council (NSERC). Ship time was courtesy of Environment Canada (National Water Research Institute) and Ontario Ministry of Natural Resources (Wheatley). We thank Ram Yerubandi from NWRI and the crews of these vessels for support in the field. Some of the data used in this study were obtained from Environment Canada, the Great Lake Environmental Research Laboratory, and the National Data Buoy Center.

This section compares available observational meteorological data and prepares the environmental forcing input for ELCOM-CAEDYM, namely, solar and longwave radiation, air temperature, wind, and relative humidity.

3.1.1 Available dataset

There are two sets of observational data available. The first is available from the National Water Research Institute (NWRI) of Environment Canada (EC) and the second from the United State National Data Buoy Center (NDBC) of the National Oceanic and Atmospheric Administration (NOAA). The locations of all available stations are marked in Fig. 3.1. The deployment details at NWRI meteorological stations in 2008 are listed in Table 3.1, and the details at NDBC stations can be found on www.ndbc.noaa.gov. In addition to these measurements the North American Regional Reanalysis (NARR) dataset is occasionally used to estimate data when observational data are not available. NARR is a long-term, consistent, high-resolution, combined model and assimilated climate dataset

over the North American region (Mesinger et al. 2006). It covers 1979 to near present and is provided 8-times daily on a Northern Hemisphere Lambert Conformal Conic grid (32 km in the horizontal and 45 vertical layers).

Most of the NDBC stations are on the coast, but NWRI buoys were deployed off shore. Schwab and Morton (1984) found that the wind speeds from over-land stations need adjustments in order to accurately approximate the over-lake wind speeds. Moreover, the NWRI buoys also recorded the solar and longwave radiation data which were not measured by NDBC stations. Therefore the NWRI buoy data are chosen over NDBC data if available in the desired locations.

Table 3.1: Deployment details at meteorological stations by NWRI in 2008

Station	latitude (N), longitude (W)	Deployment time (GMT)	Sampling interval	Air temperature sensor height	Wind sensor height	Components
341	41-47-40, 82-17-35	May 1 - Oct 15	10 min	3.5 m	3.5 m	wind, air temperature, solar and longwave radiation, and relative humidity
Stanley	42-28-00, 81-13-00	Mar 18 - Dec 4	1 hour	5.0 m	5.0 m	wind and air temperature
Colborne	42-44-12, 79-17-24	Mar 14 - Dec 4	1 hour	5.0 m	5.0 m	wind and air temperature
452	42-34-55, 79-55-23	N.A. in 2008, has 2009 data	10 min	3.5 m	3.5 m	wind, air temperature, solar and longwave radiation, and relative humidity

3.1.2 Data comparison

In this sub-section the available observational data are compared and analyzed. The methods to generate input files required by ELCOM-CAEDYM are described, to be specific, solar and longwave radiation, relative humidity, air temperature, and wind.

Solar radiation

In 2008 the observational solar radiation is only available at EC341 (Environment Canada station 341, Fig. 3.1), so it has to be used to force the whole lake. Both EC341

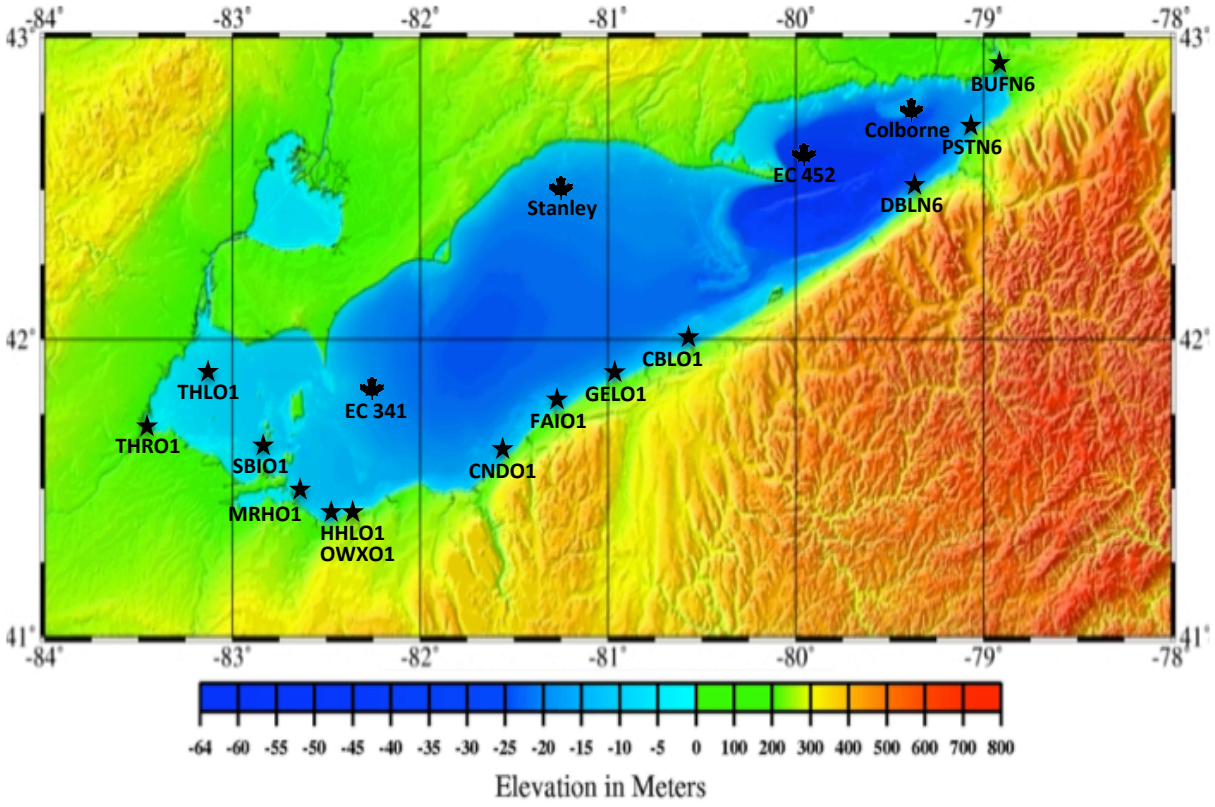

Figure 3.1: Available meteorological stations in Lake Erie from both NWRI (maple leaf) and NDBC (star). The elevation and bathymetry map is from the NOAA Great Lakes Environmental Research Laboratory (GLERL).

and EC452, which are more than 200 km apart, have solar radiation recorded in 2009. Therefore we can compare the measurements at two stations along with the NARR simulated data to investigate how accurate the approximation will be. Notice that EC data are cumulative for 10 mins with the unit KJ m^{-2}, so it needs to be converted to SI units W m^{-2}, using 1 (KJ m^{-2})/600 s = 1000/600 W m^{-2}. Figure 3.2 compares three sets of data from day 185 to 200. Solar radiation has a clear on and off pattern due to the sunrise and sunset every day. In Fig. 3.2(A) EC452 and EC341 data are very similar, indicating that the solar radiation is nearly uniform across the lake. Hence it is reasonable to use one set of data for the whole lake. Figure 3.2(B) compares EC452 and NARR data generated at the same location, and the agreement is satisfactory. Therefore NARR solar radiation will be used to "fill in" when the field observational data are not available.

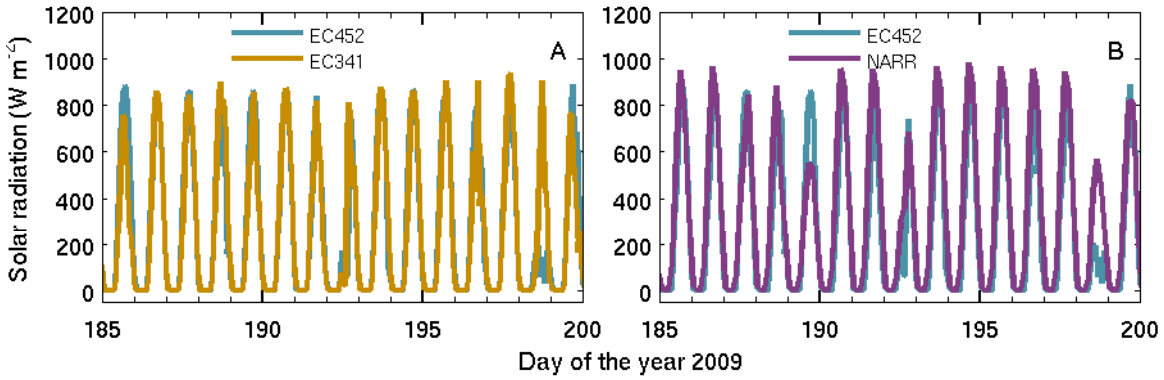

Figure 3.2: Solar radiation comparison in 2009 at: (A) EC452 and EC341, and (B) EC452 and NARR.

Longwave radiation

The measurements of downward longwave radiation are in the same situation as those for the solar radiation, namely that the measurements are only available at EC341 in 2008. Figure 3.3 compares the three sets of data again. The agreement is not as good as in the case of solar radiation, but they do follow a similar trend and have comparable magnitudes. The RMSE between 3-hour EC452 data and 3-hour EC341 data is about

27 W m^{-2}. The longwave radiation is in the range between 250 and 450 W m^{-2}, so it is reasonable to assume that data from EC341 can be used to represent the whole lake. The NARR prediction at EC452 agrees well with the observations (Fig. 3.3(B,D)), and the RMSE is only 25 W m^{-2}. Therefore the NARR data for longwave radiation should also be trustworthy when the field data are not available.

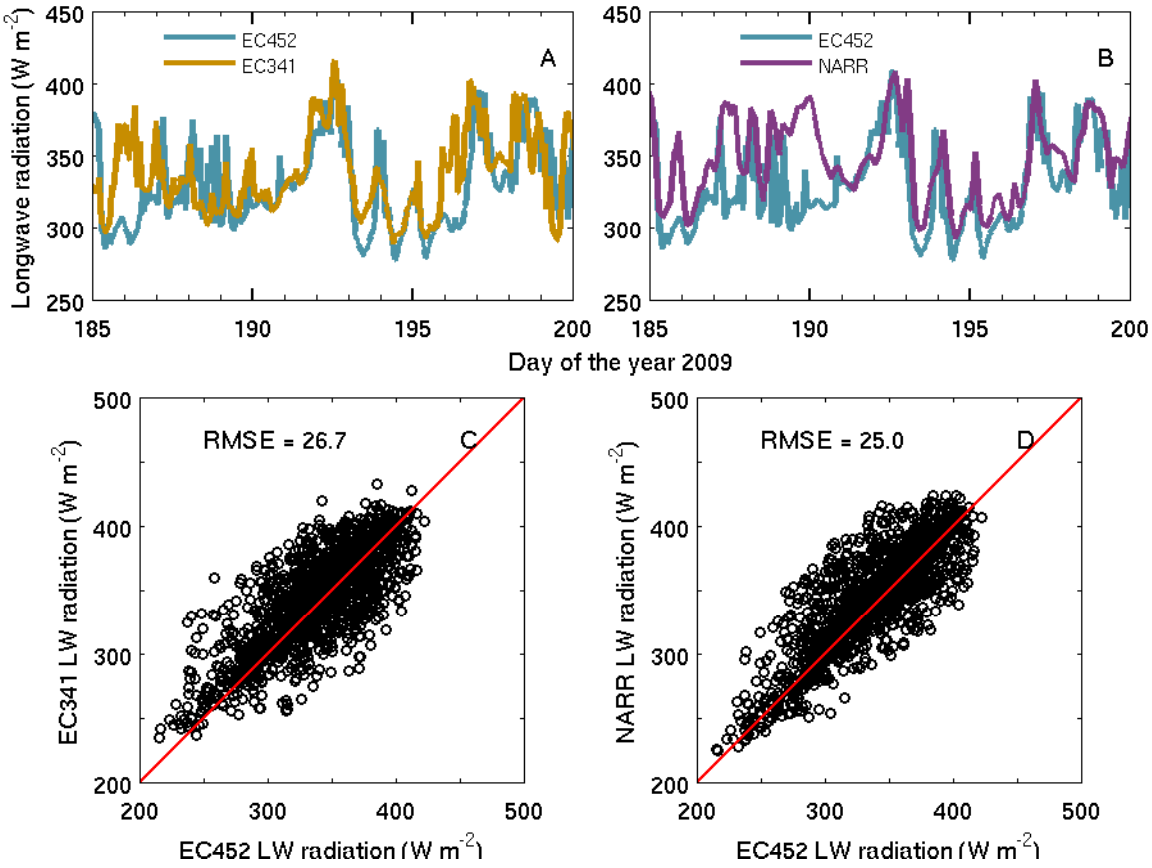

Figure 3.3: Downward longwave radiation comparison in 2009 at: (A,C) EC452 and EC341, and (B,D) EC452 and NARR.

Relative humidity

The relative humidity data were again only measured at EC341 in 2008. Unlike solar and longwave radiation, the relative humidity depends more on local air temperature and pressure, so data from EC452 and EC341 are not expected to be in good agreement, which is shown in Fig. 3.4(A). The NARR prediction is fairly close to the field data at EC452 between day 185 and 200 in Fig. 3.4(B); however, NARR has a warmer bias in air temperature (discussed in the following sub-section). The relative humidity strongly depends on the air temperature, so NARR data should not be used unless there are no field data at all. Hence the dataset from EC341 (the only one available) is chosen for the whole lake in the model setup.

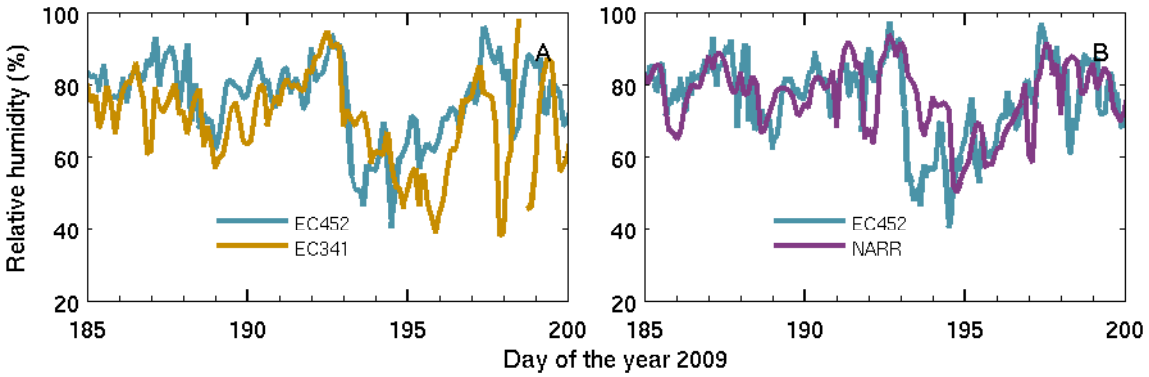

Figure 3.4: Relative humidity comparison in 2009 at: (A) EC452 and EC341, and (B) EC452 and NARR.

Air temperature

Air temperature observations are available from all stations but measured at different heights. Unlike winds, air temperature does not vary much in a few metres above the ground. Therefore, all the air temperature data can be treated at a standard height, say 3.5 m which is the sensor height at EC341.

Figure 3.5 plots the air temperature at EC341 and EC Colborne in 2008 and the NARR generated data at the same locations. The NARR data are clearly warmer at both stations through the whole season. In Fig. 3.5(C,D) the data distribution has a strong bias towards the NARR side and the RMSE is about 2.2°C at EC341 and 2.5°C at EC Colborne, which are not negligible in both cases. This warmer air temperature bias has been previously mentioned in the literature (e.g. Bennington et al. 2010).

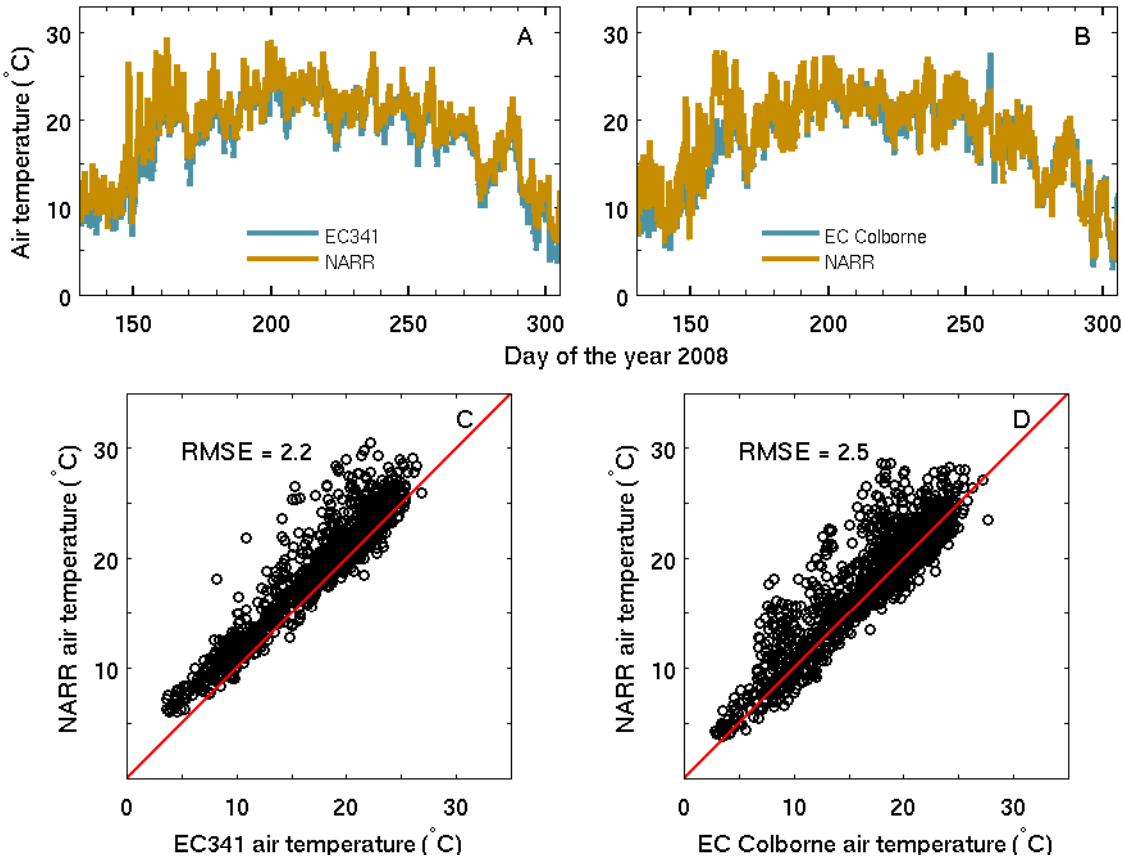

Figure 3.5: Air temperature comparison in 2008 at: (A,C) EC341 and NARR, and (B,D) EC Colborne and NARR.

Wind

Wind speeds and directions were recorded at all available stations. Similar to the air temperature situation, different stations have various anemometer heights, ranging from 5 to 26 m above the ground (or water). The different measurement heights will significantly affect wind speeds, so we need to convert the wind data to a standard height of 10 m. The conversion method follows Verburg and Antenucci (2010). There is no such method to adjust the wind directions, so they are assumed to remain unchanged in the conversion process.

Table 3.2 lists all the variables and constants that will be used in the conversion process. First estimate U_{10} by

$$u_{10\text{guess}} = U_z(10/z)^{1/7}. \tag{3.1}$$

Then the friction velocity is initialized by

$$u_{*\text{guess}} = u_{10\text{guess}}\Big(0.0015\big[1+\exp(\frac{-u_{10\text{guess}}+12.5}{1.56})\big]^{-1}+0.00104\Big)^{1/2}. \tag{3.2}$$

The roughness length for momentum is given by

$$z_0 = \alpha u_*^2/g + 0.11\nu/u_*, \tag{3.3}$$

where ν is the kinematic viscosity defined as

$$\nu = \mu/\rho_a. \tag{3.4}$$

The dynamic viscosity of air is

$$\mu = 4.94\times10^{-8}T_a + 1.7184\times10^{-5}. \tag{3.5}$$

There is not enough information to calculate the air density exactly, so it is estimated by the empirical relation between density and temperature. From z_0 the friction velocity is

obtained

$$u_* = (C_D U_z^2)^{1/2} = \kappa U_z[\ln(z/z_0)]. \tag{3.6}$$

Next loop over (3.3) and (3.6) until z_0 is within 0.001% of the previous value of z_0. After obtaining z_0 the wind speeds at 10 m height can be calculated by

$$U_{10} = U_z \ln(10/z_0)/[\ln(z/z_0)]. \tag{3.7}$$

Station SBIO1 (South Bass Island, Ohio, Fig. 3.1) from NDBC had wind speeds measured from 21 m above the ground and EC Colborne had data from 5 m above. Figure 3.6 compares the original data in both stations with the converted 10 m data. In general wind is stronger when measured further away from the ground. Smaller wind speed values are not affected much by the measurement height, but when the wind speed is larger than 10 m s^{-1}, the difference becomes noticeable.

Table 3.2: A list of variables used in converting wind speeds to 10 m height

Variable	Variable name	Unit
U_{10}	wind measured from 10 m above	m s^{-1}
U_z	wind measured from z m above	m s^{-1}
u_*	friction velocity	m s^{-1}
z	measurement height	m
z_0	roughness length for momentum	m
T_a	air temperature	°C
ν	kinematic viscosity of air	m^2 s^{-1}
μ	dynamic viscosity of air	kg m^{-1} s^{-1}
ρ_a	air density	kg m^{-3}
g	gravity of Earth	m s^{-2}
C_D	drag coefficient	dimensionless
κ	von Karman constant	dimensionless
α	Charnock constant	dimensionless

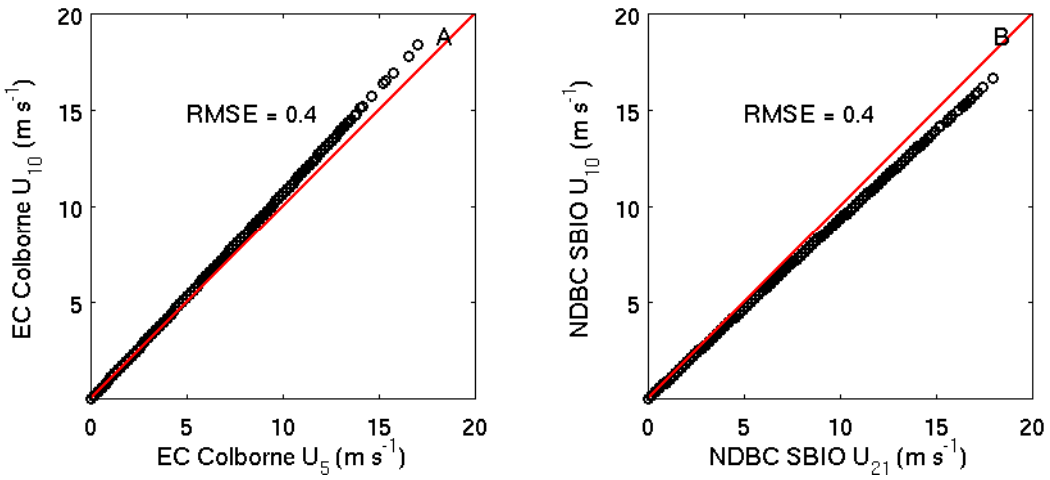

Figure 3.6: (A) EC Colborne wind speeds comparison at 5 m and 10 m above, and (B) NDBC SBIO1 wind speeds comparison at 21 m and 10 m above.

3.1.3 Summary

In this section the meteorological forcing data from the field observations are compared and analyzed. (i) Solar radiation is almost uniform at two measurement stations 200 km apart in 2009, which indicates very little variation in the horizontal. Hence it is reasonable to use one set of data for the whole lake. The NARR data is compared with EC452 and the agreement is quite good as well. Therefore the NARR outputs can be used to "fill in" solar radiation forcing if the observational data are not available. (ii) The situation for downward longwave radiation is similar. Two sets of field data from Environment Canada in 2009 show reasonable agreement, and the NARR prediction is considered acceptable as well. Hence one set of data for can be used for the whole lake and NARR data are adequate to estimate if needed. (iii) Unlike solar and longwave radiation, the relative humidity strongly depends on local air temperature and pressure, and the comparison of two sets of field data in 2009 confirms it. Unfortunately there is only one dataset containing the relative humidity measurement in 2008. Although NARR does provide the desired data, the warmer bias in the air temperature makes the NARR data problematic. In the model setup the EC341 relative humidity data are chosen to force the whole lake instead of using NARR data. (iv) It was assumed that temperature variations between 2 and 10 m above the surface are insignificant. The comparison between field data and NARR data at the same location shows an obvious warmer bias in NARR. The RMSE is as large as 2.5°C through the ice-free season. We should always keep this in mind when dealing with the air temperature in NARR. (v) Finally using the method in Verburg and Antenucci (2010) the wind speeds from various measurement heights are converted to the standard 10 m. The difference in the measurement heights has a larger effect on stronger winds (larger than 10 m s^{-1}).

3.2 Model setup

Numerical simulations were conducted using ELCOM-CAEDYM (EL-CD). In order to address the spatial variability of meteorological conditions across the lake, the computational domain was divided into four sections: the eastern, east-central, west-central, and western (Fig 3.7). In each section the environmental forcing was set to be uniform and equal to the observational data at the nearby station, i.e., Port Colborne in the eastern section, Port Stanley in the east-central, and station 341 in the west-central. Due to insufficient field data in the western basin from NWRI, data from station SBIO1 at NDBC were used instead. Only the buoy at station 341 recorded solar and longwave radiation and relative humidity, so these values are used over the whole lake. Data from station 341 were only available from May 2 to October 15 so data from NDBC and reanalysis NARR were used for the time periods from April 21 to May 2 and Oct 16 to 30. The time series of 3-hour averaged meteorological data at station 341 is plotted in Fig. 3.8.

Inflow from eleven major tributaries to Lake Erie (Detroit, Raisin, Maumee, Sandusky, Vermilion, Rocky, Cuyahoga, Grand [Ohio, USA], Cattaraugus, Buffalo and Grand [Ontario, Canada]) was included in the study. The Detroit River, which is the largest inflow, and ten other inflows together account for 99.7% of all lake inflows. The remaining tributaries have negligible impact on the lake's physical dynamics or heat budget. Lake water is drained through the Niagara River to Lake Ontario. The data on flow rates and water temperatures for the modelled tributaries were obtained by Dr. Serghei Bocaniov from several datasets that included the US Geological Service, the US EPA database on water quality monitoring data (STORET), Water Survey of Canada from Environment Canada and Grand River Conservation Authorities (GRCA, Ontario).

Processing the river data and the CAEDYM setup were performed by Dr. Serghei Bocaniov, formerly in the Department of Biology at the University of Waterloo, along with Professor Ralph Smith and their colleagues. CAEDYM simulates the C, N, P, DO, and Si cycles, along with inorganic suspended solids and phytoplankton. Twelve state variables are required to model the algal biomass. Five dissolved inorganic nutrients (PO_4, NO_3, NH_4, DIC, and RSi), three dissolved organic (DOC, DON, and DOP) and three particulate

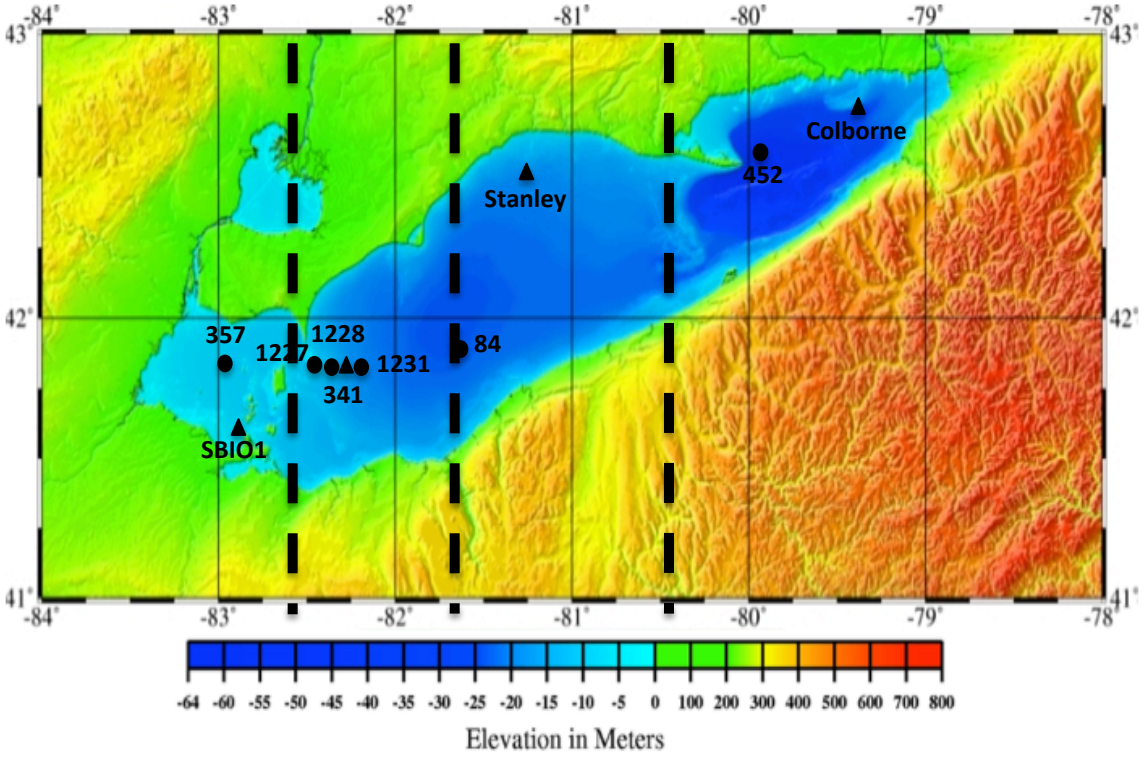

Figure 3.7: Lake Erie bathymetry (from GLERL) with four forcing sections (divided by dash lines) and the locations of meteorological buoys (▲) and thermistor chains (●).

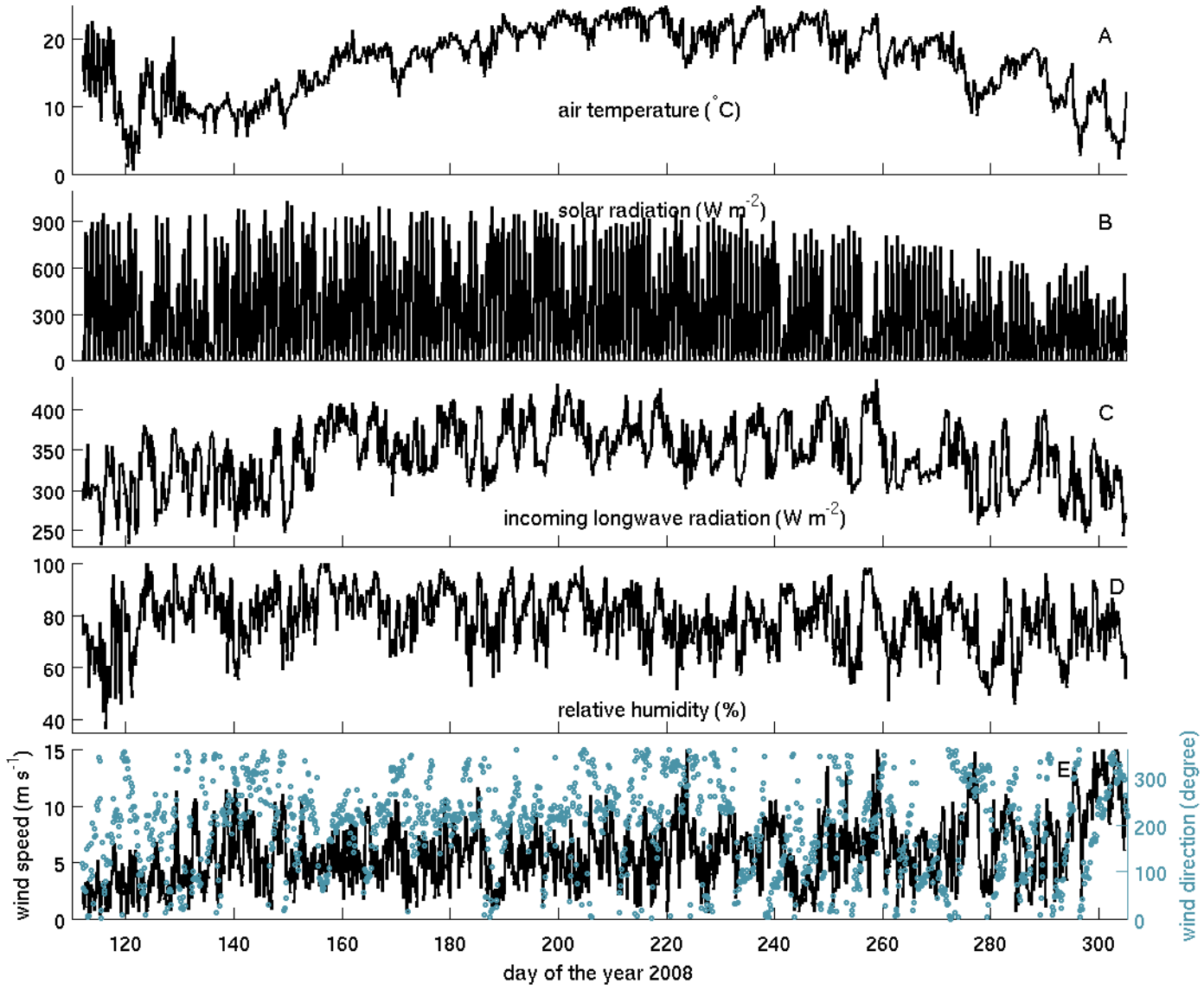

Figure 3.8: Time series of 3-hour averaged meteorological data at station 341: (A) air temperature, (B) solar radiation, (C) downward longwave radiation, (D) relative humidity, and (E) wind speed (lines) and wind direction (dots, measured clockwise from north in direction wind is coming from).

detrital organic matter groups (POC, PON, and POP), two inorganic suspended solids size classes (SS_1 and SS_2), and dissolved oxygen (DO) were simulated.

The Lake Erie bathymetry was obtained from the Great Lake Environmental Research Laboratory (GLERL). The computational grid used a 2 km horizontal resolution and 45 unevenly spaced vertical layers with thicknesses varying between 0.5 to 5 m. The simulations started with the lake at rest with the water temperature initialized with observational data from mooring stations, which is then horizontally interpolated using the inverse distance weighting method (ELCOM User Manual 2006). The typical spin up time of the lake circulation is relatively short, largely because of the shallow depth of the lake and the strong wind-driven character of the lake hydrodynamics (Beletsky and Schwab 2001). Therefore, the effect of initial conditions on the seasonal scale is negligible after a few weeks. A mixed-layer turbulence scheme and a drag parametrization along the bottom and side boundaries was applied. The model runs for a period of 193 days, from April 21 to October 30 with a 5-minute time step, which is used to achieve both numerical stability and a reasonable completion time. A seasonal ELCOM simulation takes about 13 physical hours to finish using one 3.0 GHz Intel Xeon processor, and a coupled EL-CD run takes approximately seven times longer.

3.3 Model validation

In the 2008 field investigation seven temperature logger chains with a 10-minute sampling interval were deployed at stations 357, 1227, 1228, 1231, 341, 84, and 452 (Fig. 3.7). Three high frequency data sets with a 10-second sampling time interval were recorded at stations 1227, 1228, and 1231 as well. One Acoustic Doppler Current Profiler (ADCP) was set at station 341. The deployment details are listed in Table 3.3. In addition, the lake surface temperature averaged over the Great Lakes derived from satellite remote sensing is available for model validation from GLERL.

EL-CD has been shown capable of simulating the hydrodynamic and biochemical dynamics in medium to large size lakes (Laval et al. 2003; Huang et al. 2010a; Leon et al.

2005; Leon et al. 2011). In this section another model validation in a different year is provided to confirm its modelling ability to capture the lake dynamics. The ability of the model to simulate quantities of interest is quantified by calculating the root mean square error (RMSE) and average percentage difference (APD):

$$\text{RMSE} = \Big(\frac{1}{M}\sum_{i=1}^{M}(f_i^m - f_i^o)^2\Big)^{1/2}, \tag{3.8}$$

$$\text{APD} = \frac{1}{M}\sum_{i=1}^{M}\Big(\frac{f_i^m - f_i^o}{f_i^o} \times 100\%\Big), \tag{3.9}$$

where f_i^m and f_i^o are modelled and observed quantities for sample case i out of M cases (Huang et al. 2010a).

Table 3.3: Deployment details at mooring stations by NWRI in 2008

Station	latitude (N), longitude (W)	Depth (m)	Type	Deployment time (GMT)	Sampling interval (min)	Depth of measurement (m)
357	41-49-59, 82-57-03	10.1	Temperature	May 1 - Oct 14	10	[1 3 5 7 9]
1227	41-48-36, 82-30-09	11.5	Temperature	Jun 3 - Oct 15	10	[1 2 3 4 6 7 8 8.7 9.2 11]
1228	41-47-40, 82-21-13	14.5	Temperature	Jun 4 - Oct 15	10	[1 2 3 5 6 7 8 11.5 12 12.5 13 13.5]
1231	41-47-30, 82-11-38	19.8	Temperature	Jun 3 - Oct 15	10	[1 2 3 4 5 6 7 8 10 11.5 12.5 13 14 15 15.5 16 16.5]
341	41-47-40, 82-17-35	17.6	Temperature	May 2 - Oct 14	15	[1 2 3.5 4.5 5.5 6.5 7.5 8.5 9.5 12.75 13.5 14.5 15 15.5 15.9 16.5 17]
341	41-47-40, 82-17-35	15.3	ADCP	Apr 28 - Nov 8	15	[1 2 3 4 5 6 7 8 9 10 11 12 13 14 15]
84	41-55-07, 81-38-46	23.6	Temperature	Apr 29 - Oct 16	10	[1 3 5 7 9 11 13 15 16 17 18 19 20 21 22 23]
452	42-34-55, 79-55-23	53.5	Temperature	Apr 29 - Oct 16	10	[1 3 5 7 9 11 13 15 16 17 18 19 20 23 26 30 35 40 45 50]

3.3.1 Water temperature

Temperature determines the solubility of many substances, influences organism distributions based on thermal habitat preferences (e.g. Lynch et al. 2010), and affects the rate of chemical reactions and biological processes such photosynthesis and respiration (Falkowski and Raven 2007).

Figures 3.9 and 3.10 compare the observed and modelled temperature time series at several different locations. (i) At station 357 the numerical model successfully predicts the heating of the lake in the spring and summer and cooling in the fall (Fig. 3.9(A,D,J)). Station 357 is located in the shallowest western basin where the stratification is very weak, so the excellent agreement is not surprising. (ii) Moving eastwards to station 1227 in the central basin, the lake becomes slightly deeper (11.5 m) and is only weakly stratified near the bottom in the summer. The model correctly captures the stratification but with slightly warmer predictions (Fig. 3.9(B,E,H,K)). (iii) At station 341 (Fig. 3.9(C,F,I,L)) and 1231 (Fig. 3.10(A,D,G,J)) the stratification becomes stronger and lasts longer. The model captures the seasonal evolution; however, the water temperature is overestimated in the summer, and the predicted metalimnion is deeper and thicker. The modelled metalimnion is thicker than observed due to numerical diffusion and this is a known problem of all current hydrodynamic models (Huang et al. 2010b). Moreover it also may be caused by the weaknesses of the mixing parametrization in ELCOM. Around day 210 (July 28) a strong storm was believed to emerge near station 1231, which is indicated in the observational data by the colder 10°C water that appears at depths between 6 to 10 m. This cooling event was not simulated by the model, probably because the strong storm was not recorded by the meteorological buoy at station 341, from which the data are used to force the central-west section. (iv) Station 84 (Fig. 3.10(B,E,H,K)) is located in the deeper eastern side of the central basin. The onset and breakdown of the stratification is correctly modelled in our results. The position of the metalimnion and the stratification strength outcomes are acceptable although the modelled thermocline oscillates in summer comparing with the observational data. (v) Finally at station 452 (Fig. 3.10(C,F,I,L)) in the eastern basin, the numerical model does a great job in reproducing the thermal structure. The stratification duration, thermocline position, and temperature in different depths are all well simulated, but again metalimnion is too thick as in the central basin. Figure 3.9(G) compares the modelled and observed (from GLERL) lake averaged surface temperature, and the agreement is exceptionally good with an almost negligible 0.6°C RMSE.

To better quantify the model results, the RMSE and APD from all available mooring stations at all depths are calculated and plotted in Fig. 3.11. At station 357 the RMSE is

about 0.9°C at all depths, which confirms the excellent agreement in the previous contour comparison plot. In the central basin (station 1227, 1228, 1231, 341, and 84) the RMSE is around 2°C in the top 5 m below the lake surface. At greater depths the RMSE values increase with maximum values between 3 and 5°C. These larger values are indicative of errors in simulating the depth of the thermocline and the thickness of the metalimnion. Near the bottom of the lake the RMSE decreases to about 2°C. Results for the eastern basin are similar. The model generally does a good job simulating the water temperature in the surface mixed layer where the RMSE is only around 2°C. The maximum RMSE values are smaller than some results reported in literature of the Great Lakes (for instance the largest error is about 7°C in Lake Ontario in Huang et al. (2010a)). Similar outcomes can be drawn as well in the APD plots from Fig. 3.11.

Given the current modelling restrictions, i.e., the low horizontal resolution and availability of only four meteorological data sets to force the whole lake, the simulated outcomes are generally satisfactory. Although the simulated metalimnion is too thick, the presence or absence of stratification as well as surface and bottom temperatures are well described so the model appears to have potential for describing some of the changes to be expected under altered climate scenarios. The three basins are shown to have very distinct thermal structures and EL-CD is expected to provide innovative and trustworthy results for the sensitivity studies in the next chapter.

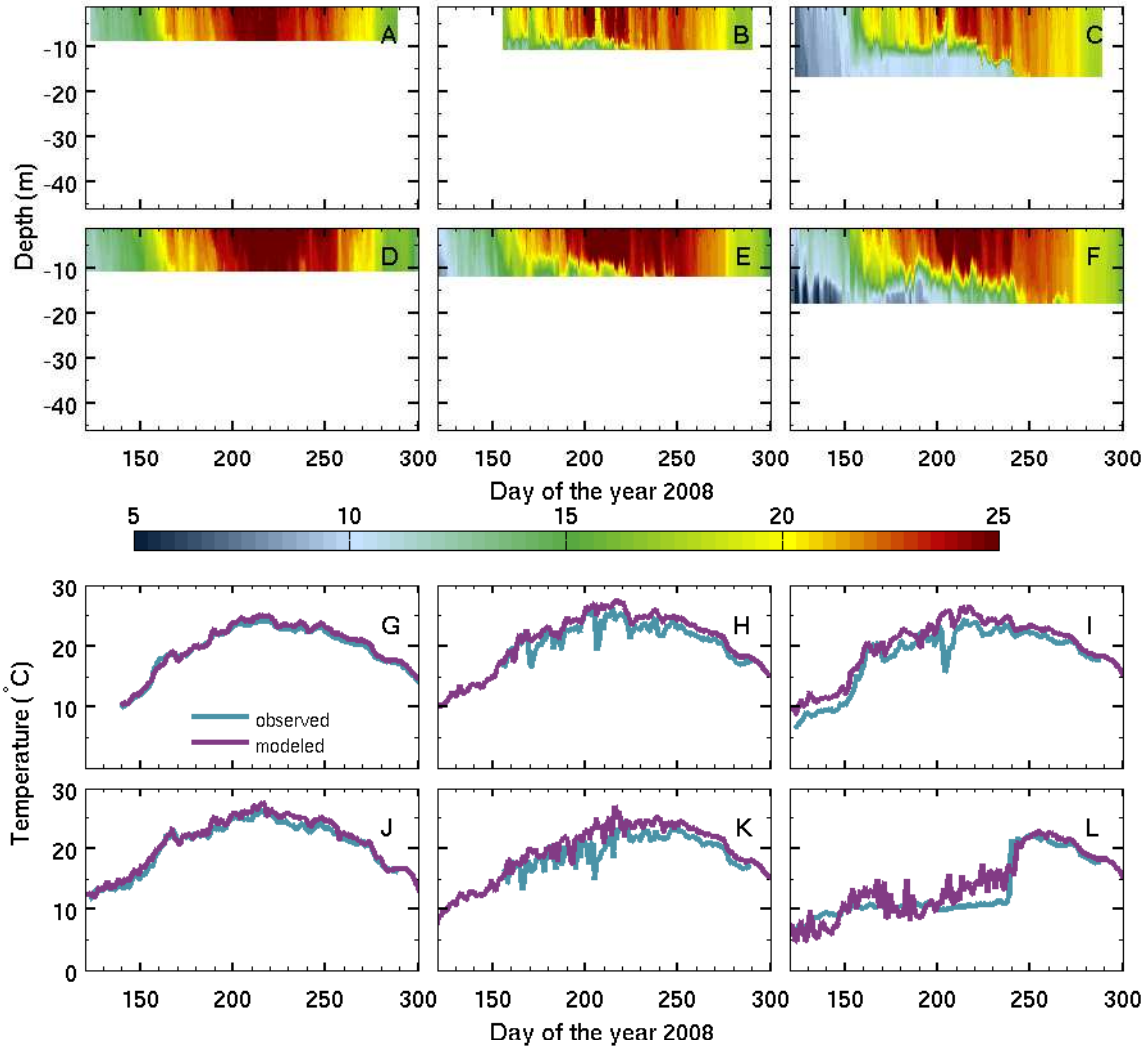

Figure 3.9: Contour plots: the observed (A-C) and EL-CD modelled (D-F) temperature comparison at (A,D) station 357, (B,E) 1227, and (C,F) 341. Line plots: (G) mean surface temperature; (J) station 357 at -1 m; station 1227 at (H) -1 m and (K) -8 m; and station 341 at (I) -6 m and (L) -15 m.

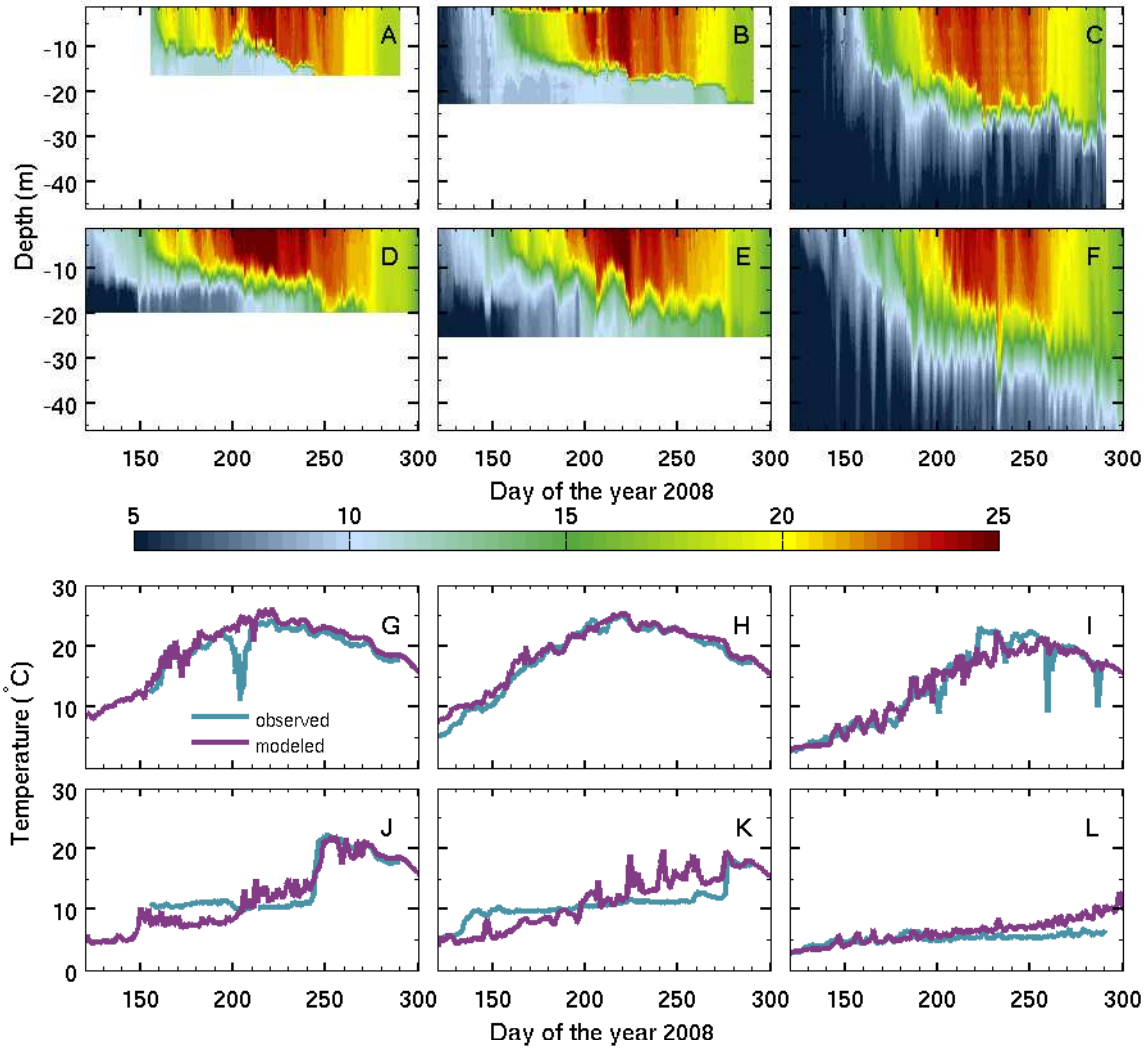

Figure 3.10: Contour plots: the observed (A-C) and EL-CD modelled (D-F) temperature comparison at (A,D) station 1231, (B,E) 84, and (C,F) 452. Line plots: station 1231 at (G) −7 m and (J) −16 m; station 84 at (H) −5 m and (K) −20 m; and station 452 at (I) −20 m and (L) −40 m.

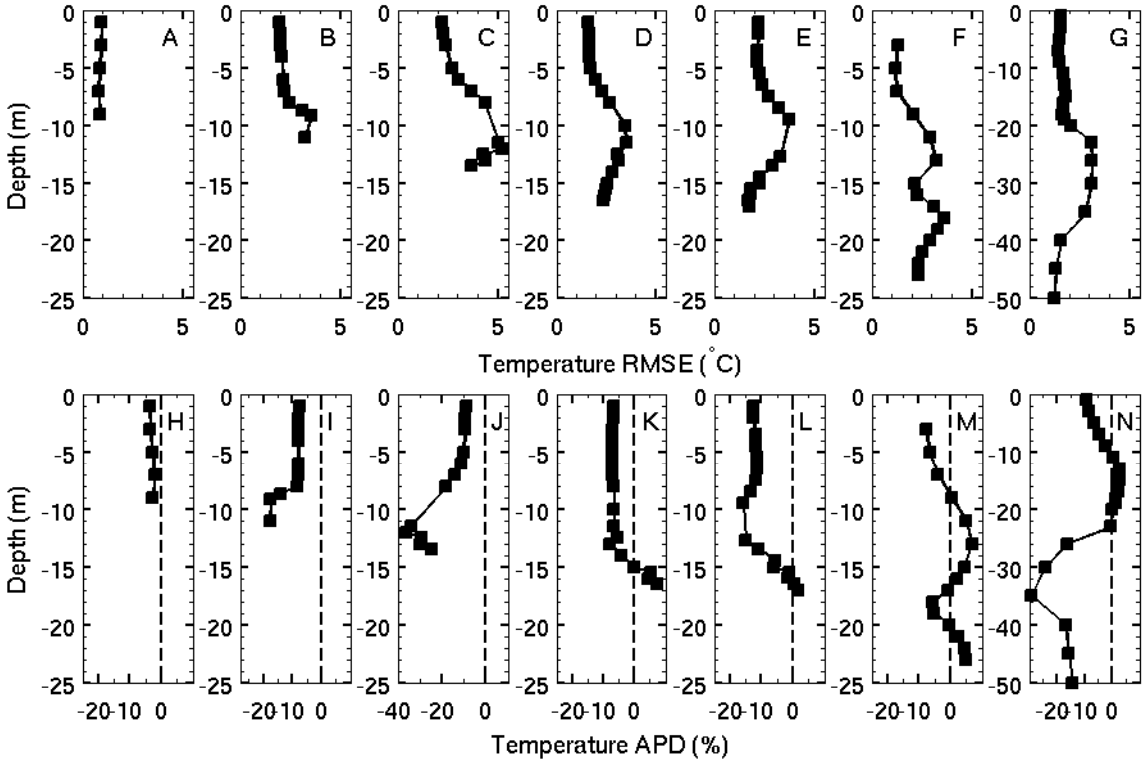

Figure 3.11: The vertical profiles of the root mean square error (RMSE, top panels) and the average percentage difference (APD, bottom panels) between the modelled and observed temperature at stations: (A,H) 357, (B,I) 1227, (C,J) 1228, (D,K) 1231, (E,L) 341, (F,M) 84, and (G,N) 452.

3.3.2 Water currents

The modelled velocities are validated against observed ADCP data at station 341 in this section. Figure 3.12 plots the velocities contours against depth and time from day 195 to 205. The numerical model does a relatively good job in predicting the velocities except near the surface. However, the observed ADCP data in this region usually have large errors due to the acoustic backscattering reflection from the surface, so the simulated results are considered acceptable.

Another metric to quantify the simulated velocities is to calculate the vertical distribution of normalized Fourier norms between the observed and modelled currents (Beletsky et al. 2006),

$$F_n = \frac{\left(\frac{1}{M}\sum_{t=\Delta t}^{M\Delta t}|\overrightarrow{V_m} - \overrightarrow{V_o}|^2\right)^{\frac{1}{2}}}{\left(\frac{1}{M}\sum_{t=\Delta t}^{M\Delta t}|\overrightarrow{V_o}|^2\right)^{\frac{1}{2}}}, \tag{3.10}$$

where $\overrightarrow{V_m}$ and $\overrightarrow{V_o}$ are modelled and observed currents. The mean F_n value is around 1.3 in our simulated results (Fig. 3.13) which almost doubles the values (0.4–0.9) in Huang et al. (2010a). Since F_n compares both speeds and directions, out of phase simulated velocities, which happens in our simulated results, can result in very large F_n number as well.

Both observed and modelled velocities (east-west U and north-south V) exhibit a periodic change in direction. Figure 3.14 plots the power spectral density of the velocities at the 7 m depth (MATLAB codes courtesy of Leon Boegman and Reza Valipour). Seventeen 20-day segments are chosen spanning the whole season, the overlap time in the consecutive segments is about 10 days, and a Hanning window is applied. The observed velocity spectral density has a peak of 15.6-hour period and the peak for the modelled one is about 19.6 hours.

The numerical model generally does a satisfactory job simulating the currents. The oscillation period is similar, but modelled amplitude of the fluctuations is often too large. However one thing should that be borne in mind is that there is only one set of ADCP

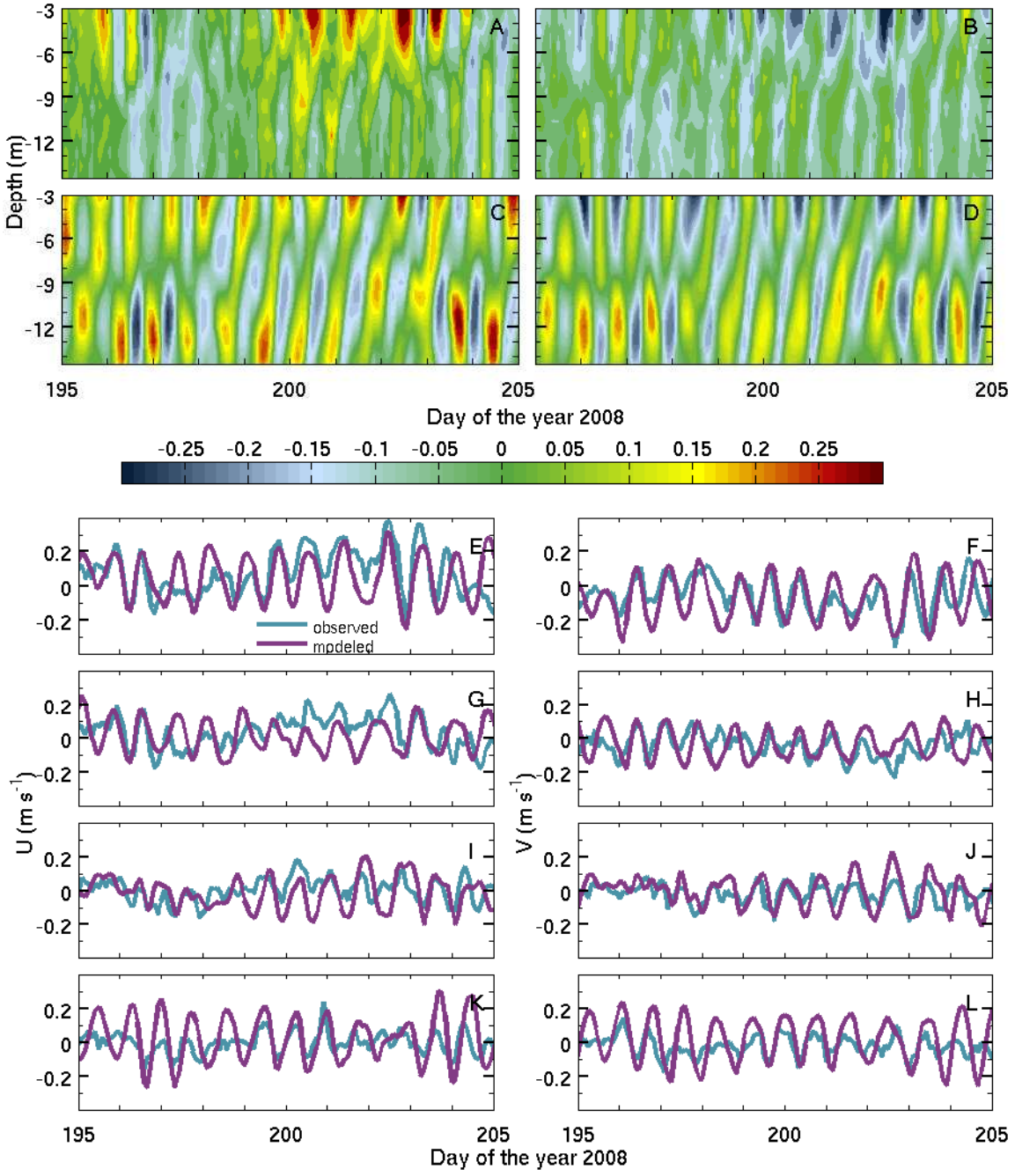

Figure 3.12: Contour plots: velocities (m s^{-1}) comparison at station 341: (A) observed and (C) modelled east-west U, (B) observed and (D) modelled north-south V. Line plots: U (left panels) and V (right panels) at station 341 at: (E,F) -3 m; (G,H) -6 m; (I,J) -9 m; and (K,L) -12 m.

data available. Unlike the temperature in the previous section, currents are more sensitive to locations and environmental forcing, hence accurate simulations of currents are not expected due to the low resolutions and limitations of the forcing data.

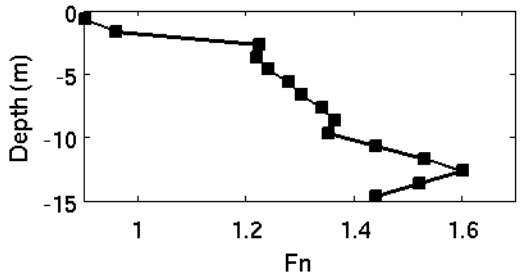

Figure 3.13: The vertical profile of normalized Fourier norms between observed and modelled currents at station 341.

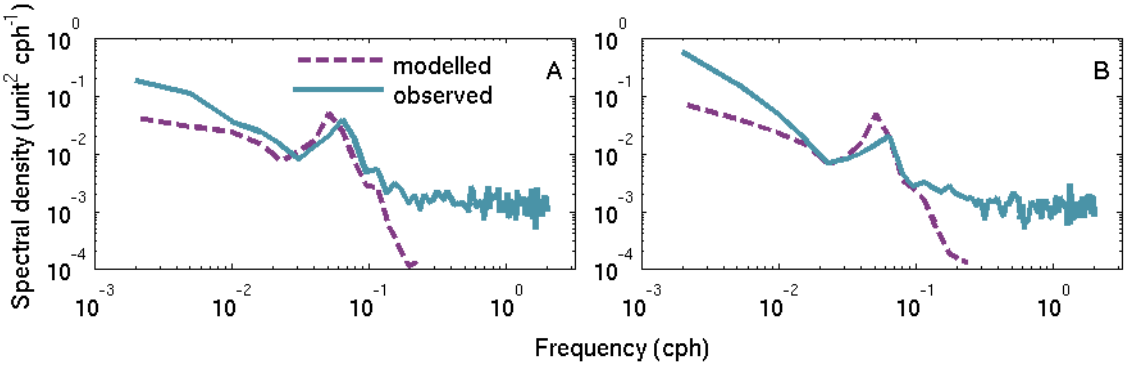

Figure 3.14: Observed and modelled power spectral density of velocities at 7 m deep at station 341: (A) U and (B) V.

3.3.3 Dissolved oxygen concentration

Figures 3.15 and 3.16 compare the simulated DO with the observational data at stations 1228, 341, and 1231. At station 1228 the observational data are available from 0.5 meters above the bottom (mab) to 3 mab, and the lake is 14.5 m deep at this location. The contour plots (Fig. 3.15(A,D)) show great agreement between observations and simulations. In the detailed line plots at 5 mab (Fig. 3.16(A)) DO does not vary a lot and maintains a high level of concentration of 6-12 mg L^{-1}. At deeper depths 3 mab (Fig. 3.16(D)) and 0.5 mab (Fig. 3.16(G)) DO starts decreasing from day 170 (Jun 18), reaches to a minimum of less than 2 mg L^{-1} near day 240 (Aug 27), and increases dramatically afterwards. Recall that hypoxia is defined as a concentration of DO less than 2 mg L^{-1}. Both observations and simulations confirm that the bottom water in the central basin was hypoxic in late August 2008. The numerical model correctly captured the dynamics and predicted the correct time of onset. In Fig. 3.15(G,J) the comparison of the corresponding temperature at the same locations is presented, and there is a strong correlation between DO and the thermal structure. In the region between 0.5 and 5 mab water lies in the hypolimnion from day 170 to 240. Less DO can penetrate to the hypolimnion from the epilimnion due to the barrier formed by the metalimnion. DO in the hypolimnion continues to decrease during the stratified period, due to oxygen consumption. In the Fall, around day 240, the stratification breaks down, which explains the sudden increase in DO at this time. The model successfully captured the stratification breakdown time, although the temperature is overestimated and the metalimnion is thicker as discussed in the previous section. Therefore the good agreement in DO is not surprising. At station 341 (Fig. 3.15(B,E,H,K)), the model correctly predicted the breakdown time around day 240, hence the DO dynamics are again represented reasonably well. Similar conclusions can be drawn at station 1231 (Fig. 3.15(C,F,I,L)) as well. The RMSE of observations and simulations at these three stations is calculated and plotted in Fig. 3.16(M,N,O), and the value is in the range of 1 to 4 mg L^{-1}. Although the error cannot be considered negligible, the model does a satisfactory job of simulating DO concentrations.

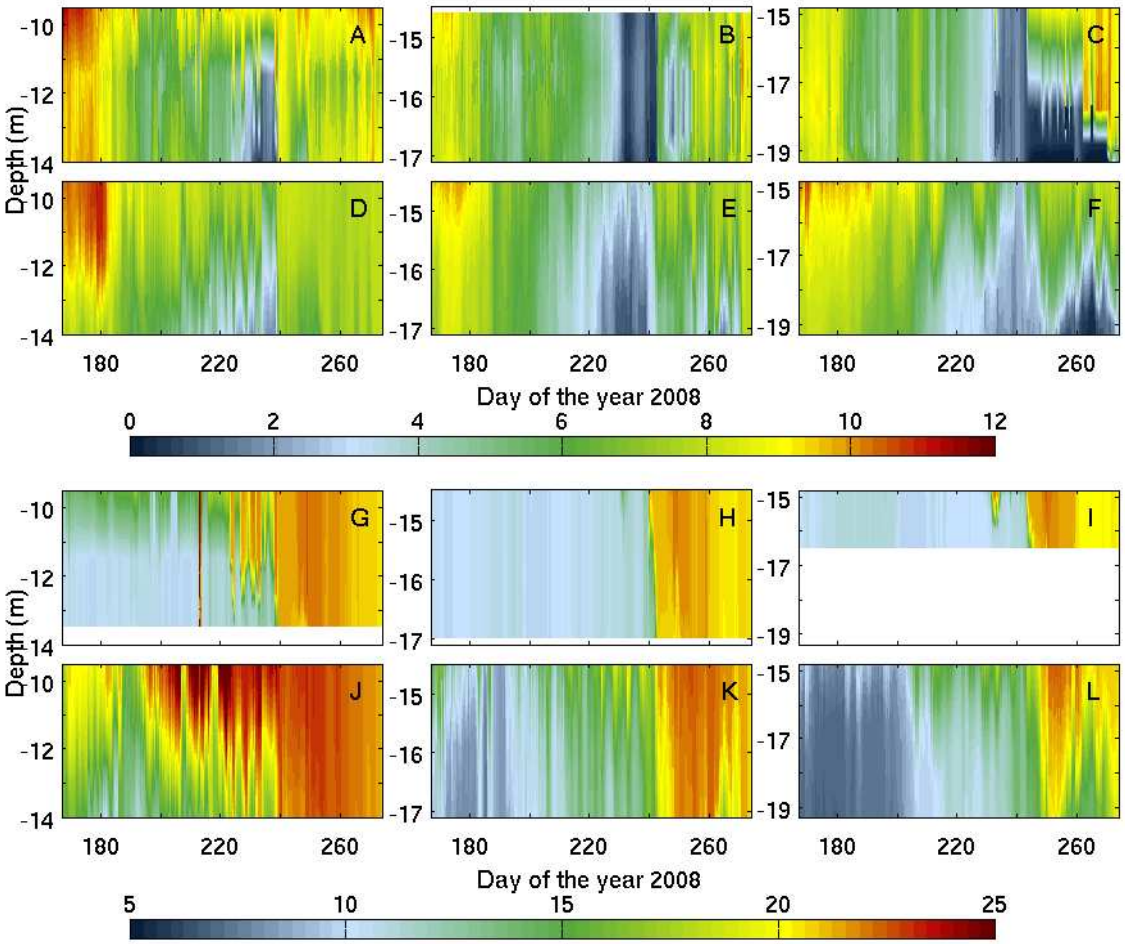

Figure 3.15: Upper half: observed (A-C) and EL-CD modelled (D-F) DO (mg L^{-1}) profile comparison at station 1228 (A,D), 341 (B,E), and 1231 (C,F). Lower half: observed (G-I) and EL-CD modelled (J-L) temperature (°C) profile comparison at station 1228 (G,J), 341 (H,K), and 1231 (I,L).

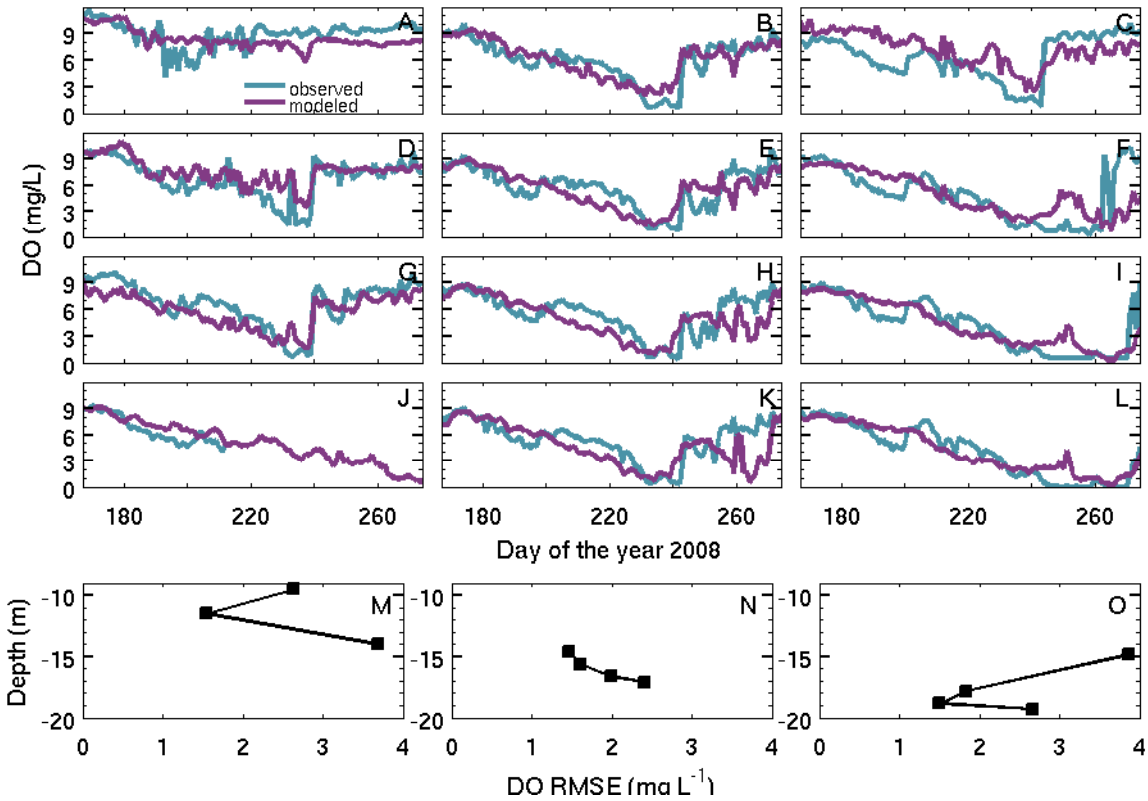

Figure 3.16: Top panels: station 1228 at (A) 5 mab, (D) 3 mab, (G) 0.5 mab; station 341 at (B) 3 mab, (E) 2 mab, (H) 1 mab, (K) 0.5 mab; station 1231 at (C) 5 mab, (F) 2 mab, (I) 1 mab, (L) 0.5 mab; (J) station 84 at 0.5 mab. Bottom panels: DO RMSE at stations: (M) 1231, (N) 341, and (O) 1231.

3.4 2012 Lake Erie fish kill analysis from a hydrodynamic point of view

During the 2012 Labour Day (September 3) weekend thousands of fish were killed and washed up on a 40-kilometre stretch of shoreline along Lake Erie from Rondeau to Port Stanley. According to the Ontario Ministry of the Environment, it is believed this incident was caused by natural phenomena. Some experts think it is because a temperature inversion brought an oxygen-depleted layer of water from the bottom of the lake close to the surface, while some suspect it was associated with the emergence and dissipation of a large gyre [1]. From the satellite dataset MODIS (http://ge.ssec.wisc.edu/modis-today), we can clearly see a large gyre near Rondeau on August 28 (Fig. 3.17). In this section a numerical simulation using ELCOM is set up to try to explain this unfortunate incident from the hydrodynamic point of view.

Figure 3.17: MODIS satellite image near Rondeau on Aug 28 (from NASA).

The meteorological data processes and the numerical model setup follows similar approaches in Sections 3.1 and 3.2. In 2012 the only data currently available from NWRI for the period of interest are wind measurements at Port Stanley from July 4 to October 1. Together with NDBC data, the computational domain is divided into three regions: the

[1] http://www.chathamdailynews.ca/2012/09/06/fish-kill-cause-could-have-huge-implications

western, central, and eastern section. In each section the environmental forcing is set to be uniform and equal to the observational data at nearby stations (Fig. 3.18).

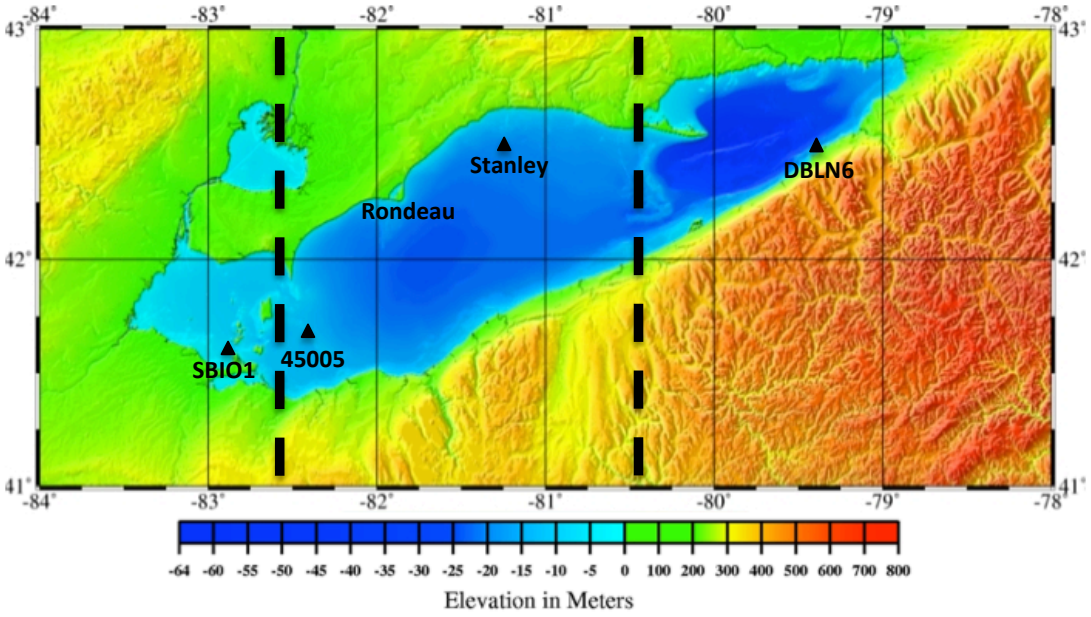

Figure 3.18: Meteorological stations used in 2012 simulations (bathymetry from GLERL). Three computational domains are divided by the dot lines.

NDBC data include only wind and air temperature measurements. Field data from station DBLN6 (Dunkirk, New York) were used in the eastern basin and station SBIO1 (South Bass Island, Ohio) was used in the western basin. In the central basin the data were from station 45005, except that the winds from July 4 to the end of the simulation were replaced by NWRI Port Stanley measurements. Stanley data are preferred here since it is off-shore data and the buoy is close to Rondeau. There was no observational data available for solar and longwave radiation and relative humidity at the time of our model set up. Hence the modelled reanalysis NARR data have to be used and these were set to be uniform across the lake. Based on the previous experience from the 2008 and 2009 field data comparison in Section 3.1, NARR produces accurate solar radiation and acceptable longwave radiation. Relative humidity depends more on local forcing, so it is not very reasonable to make it horizontally uniform. Accurate values of the relative humidity is

not critical because the thermal structure and the gyre appearance are expected to be determined by winds and air temperature with relative humidity playing a minor role.

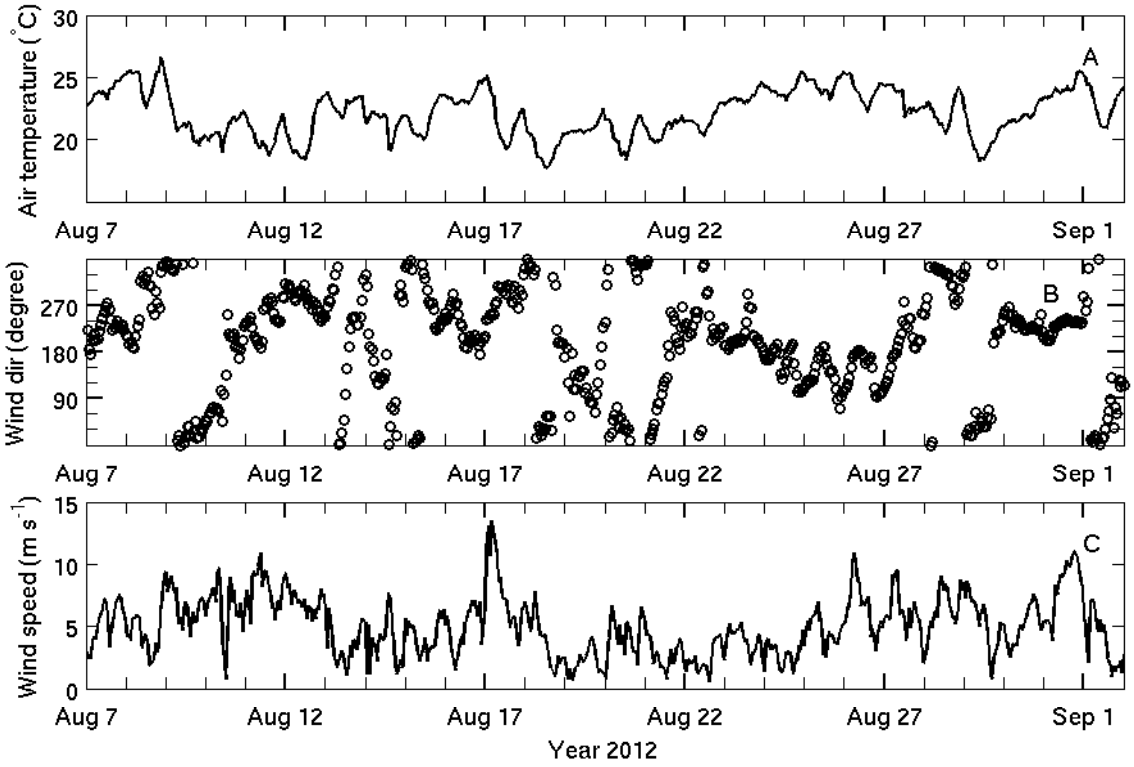

Figure 3.19: Meteorological forcing at Port Stanley: (A) air temperature, (B) wind direction, and (C) wind speed.

The simulation was run from April 20 to September 30. The lake was initially at rest and initialized with temperature observed at the mooring stations in 2008 due to the lack of measurements in 2012. Although the gyre and the fish kill appeared around the beginning of September, validation for 2008 suggests that starting a run from early April will give reasonable temperature fields in the late summer. This will give enough time for the model spin-up to minimize the effects of inaccurate initialization such as temperature (2008 mooring data) and velocities (zeros initially). River inflows and temperature were also set using the 2008 data. However Rondeau is far away from the largest inflow (the Detroit River), so river data should have no major impact on the gyre. In short although

the 2012 simulation set up is not ideal due to lack of measurements, it should produce trustworthy lake dynamics because the key forcing of winds and air temperature are all from field observations.

The ELCOM setup for year 2012 is the same as in 2008: 2-km horizontal grid, 45 uneven vertical layers, 5-minute time step, mixed layer turbulence scheme, and a drag parametrization along the bottom and side boundaries. The model ran for a period of 164 computational days, and took about 12 physical hours to finish using one 3.0 GHz Intel Xeon processor.

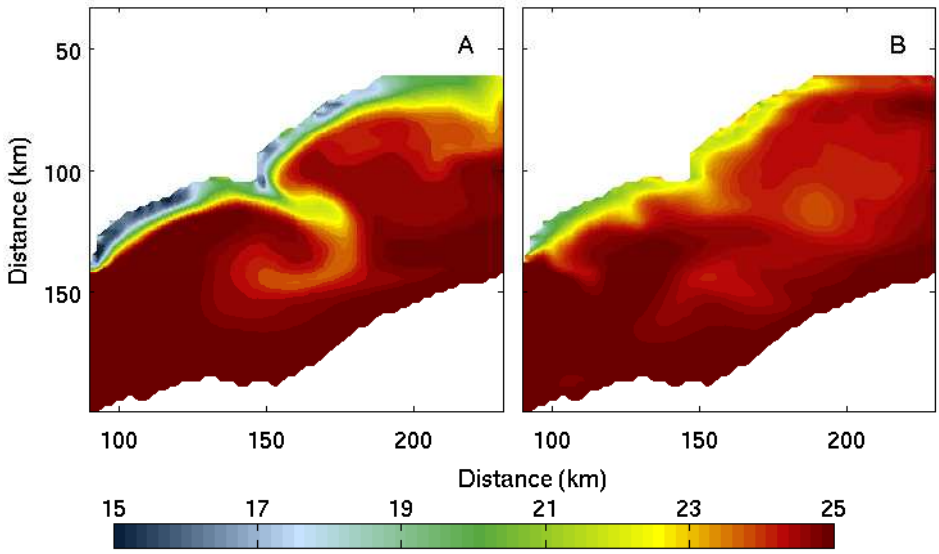

Figure 3.20: Surface temperature at (A) 12:00, 17 Aug 2012 and (B) 06:00, 01 Sep 2012.

Figure 3.19 plots the air temperature and wind at Port Stanley from Aug 7 to Sep 2. Near Aug 17 very strong south-west winds (peak nearly 14 m s^{-1}) were recorded. As a result a strong and wide upwelling was formed from Point Pelee to Port Stanley (Fig. 3.20(A)). The lowest temperature reached less than 15°C while the mean temperature in the lake at this time was about 25°C. A gyre-like blob of water was spotted near Rondeau. From Aug 27 to Sep 1 winds were relatively strong (peak around 10 m s^{-1}) and persistent. In particular, strong westward winds appeared around Aug 31 and Sep 1. A wide upwelling on the northern shore can again be seen, though the strength is weaker than the one on

Aug 17 (Fig. 3.20(B)). It is suspected that these two upwelling events could potentially cause the fish kill. That strong winds force lake upwelling is a known phenomena (Rao and Schwab 2007), but how could such events kill fish? Recall that the dissolved oxygen (DO) validation done in section 3.3.3 shows that DO levels in the deep water continuously decrease until the end of August (Fig. 3.16). The minimum of DO happened around Aug 27 in 2008 and it can drop below 2 mg L^{-1}, the threshold for hypoxia. This was confirmed by both observational and simulated results. Though the DO validation is from 2008, other years are expected to have a similar pattern (for instance 2004 and 2005 in Rao et al. 2008), i.e., low oxygen water in the hypolimnion in the western end of the central basin.

Fish habitat is strongly constrained by water temperature and DO (Fang et al. 2004). Sudden decreases in water temperature may lead to significant consequences for fishes, which is called "cold shock" (Donaldson et al. 2008). The cold shock results in a cascade of physiological and behavioural responses and, in some cases, death (Donaldson et al. 2008). In addition DO significantly affects the fish habitat (Kramer 1987; Fang et al. 2004; Arend et al. 2011). The two upwelling events described previously may have brought a large volume of oxygen depleted cold water from the hypolimnion to the shallower mixed layer or even near surface. This sudden drop in temperature and DO may have killed the fish residing in the shallower and warmer water that had formerly contained abundant oxygen. Of course this is still at the stage of speculations based on the lake's physical condition changes only. To better explain the fish kill, the connection between hydrodynamics and biology is vital. Suppose the upwelling event on Aug 17 brought a large portion of hypoxic bottom water to the surface. How does fish response to the oxygen depletion, for example can they swim away? How long after they are exposed to low oxygen water would the fish die and how long after they die would they wash up on shore? Perhaps this strong upwelling led to a chain reaction, for example, it caused a sediment resuspension, released anaerobic bacteria and their waste products, and changed the aquatic environment. If this is the case, then how long does it take the bacteria to degrade the water quality? One way to address some of these questions is to run the EL-CD to simulate DO and other related biological and chemical groups. Unfortunately there are no observational data yet to set up the model at this time, and hence this coupled simulation is left for future work.

Chapter 4

Three Dimensional Modelling of Meteorological Forcing Effects on Thermal Structure and Dissolved Oxygen Concentration

Global warming and resulting changes in meteorological forcing are anticipated to significantly affect the Laurentian Great Lakes ecosystem in many different ways. This chapter will investigate the responses of the thermal structure and dissolved oxygen concentration in Lake Erie to possible changes in air temperature and wind speed. In Section 4.1 a new method is proposed to define spatially and temporally varying regions for the thermocline, epilimnion, metalimnion, and hypolimnion. The detailed sensitivity analyses of the thermal structure and dissolved oxygen concentration are presented in Sections 4.2 and 4.3 respectively.

4.1 Quantitative definitions of thermocline, epilimnion, metalimnion, and hypolimnion

The thermocline, epilimnion, metalimnion, and hypolimnion in lakes are usually described only qualitatively in the literature. In Wetzel (2001), *"the epilimnion is defined as an upper stratum of more or less uniformly warm, circulating, and fairly turbulent water, the hypolimnion is a cold and relatively undisturbed bottom region, and the thermocline as the plane of maximum rate of decrease of temperature with respect to depth."* This chapter will study the response of the thermal structure to systematic changes in meteorological forcing, therefore it is necessary to start with an accurate quantitative definition to characterize these regions.

In the literature, especially when using one dimensional numerical models, a simple fixed-depth method is often applied. For instance Robertson and Ragotzkie (1990) defined the epilimnion to lie between depths of 0 and 7 m and the hypolimnion to lie between depths of 15 and 18 m in Lake Mendota, Wisconsin. This may be acceptable for one dimensional models applied to lakes with simple bathymetries, however in many large lakes, like Lake Erie, the bathymetry varies significantly with location. Recall from the previous chapter that the three basins in Lake Erie have quite distinct bathymetry and thermal structures, so this fixed-depth method is not appropriate. Moreover, the thermal structure often depends on time as well, for example the epilimnion in the central basin starts forming in the spring, becomes thicker in the summer, and shrinks in the fall. Therefore a more accurate definition of these regions is needed.

Following Wetzel (2001) the thermocline is defined as the surface of maximum vertical temperature gradient. This produces a very noisy thermocline when the stratification is very weak hence a threshold value T_{thres} is imposed: the thermocline is only defined when the difference between the surface water temperature T_{s} and the temperature T_{b} at the bottom of the lake satisfies

$$T_{\text{s}} - T_{\text{b}} > T_{\text{thres}}. \tag{4.1}$$

Based on the study in the previous chapter, $T_{\text{thres}} = 4°\text{C}$ is a suitable parameter to generate a reasonable thermocline in Lake Erie. Figure 4.1 plots the calculated thermocline at stations 1231 and 452, and they are reasonably positioned on the temperature contours.

After locating the depth of the thermocline Z_{therm}, the epilimnion, metalimnion, and hypolimnion can be specified. There are several possible ways to define these regions numerically: (i) The simplest method is to extend the thermocline by several vertical grid points (or some certain depth) up and down to form the metalimnion (the layer of large temperature gradients). However, the metalimnion thickness strongly depends on bathymetry and time. Hence this method will not be accurate for Lake Erie. (ii) The vertical gradient can also be used as the indicator. We can define the region boundary to be a certain percentage of the maximum vertical temperature gradient (dT/dz), say 80%. The problem with this method is that the dT/dz function is not smooth due to the limited number of vertical grid points (45) and coarse grid size near the bottom of the eastern basin (up to 5 m), so this method is not applicable here as well. (iii) Carignan et al. (2000) described the epilimnion as "*the warmer surface mixed layer where the vertical temperature gradient does not exceed* $1°C\ m^{-1}$", when dealing with observational data. Numerical diffusion results in a thicker metalimnion and correspondingly weaker temperature gradients than are often observed. Therefore, there are many time intervals during which the vertical temperature gradient is less than $1°\text{C m}^{-1}$ throughout the water column. As a result according to Carignan's definition there is no epilimnion present even though there is clearly stratification (blue lines in Fig. 4.1). Therefore Carignan et al. (2000)'s definition is not suitable in our studies.

In this thesis a different criterion is proposed based on the relative temperature difference between the surface (or bottom) water and the thermocline. The epilimnion is defined to lie between the surface and the first grid point where the temperature T_{epi} satisfies

$$T_{\text{epi}} \leq T_{\text{s}} - (T_{\text{s}} - T_{\text{therm}}) \times c_{\text{epi}}, \tag{4.2}$$

where T_{therm} is the thermocline temperature. The parameter c_{epi} determines the temperature difference between the surface and the epilimnion boundary. According to the mixing scheme in ELCOM (Hodges et al. 2000) the water temperature in each layer from surface

to bottom is a non-increasing function of depth because the water density solely depends on the temperature with the zero salinity setting in the model. Based on the stratification $c_{\text{epi}} = 25\%$ is chosen. For instance if $T_{\text{s}} = 30°\text{C}$ and $T_{\text{therm}} = 15°\text{C}$, then the epilimnion region is from 26.25 to 30°C. In a weaker stratification with $T_{\text{s}} = 15°\text{C}$ and $T_{\text{therm}} = 10°\text{C}$, the range is between 13.75 and 15°C. Similarly, the hypolimnion region is defined to lie between the bottom and the first grid where the temperature T_{hyp} satisfies

$$T_{\text{hyp}} \geq T_{\text{therm}} - (T_{\text{therm}} - T_{\text{b}}) \times c_{\text{hyp}}, \tag{4.3}$$

where c_{hyp} is the parameter to set the relative temperature difference between the bottom water and the hypolimnion boundary. The calculated epilimnion and hypolimnion boundaries using $c_{\text{epi}} = c_{\text{hyp}} = 25\%$ are plotted in white lines in Fig. 4.1. The metalimnion is the remaining intermediate layer of water. According to our definition the larger c_{epi} and c_{hyp} are, the thicker the resulting epilimnion and hypolimnion. In Fig. 4.2 three pairs of boundaries are plotted using $c_{\text{epi}} = c_{\text{hyp}} = 15\%$, 25%, and 35% respectively, and the results are as predicted. The value 25% is somewhat arbitrary; however, the trends associated with our climate change scenarios are not very sensitive to the precise value chosen. Note that T_{s}, T_{therm} and T_{b} are determined separately for each grid-column and hence they vary spatially, i.e., they depend on x and y. The corresponding MATLAB code is attached in Appendix A.1.

The mean temperature can be calculated after the regions are defined. Taking into account the uneven vertical grid spacing and the uniform horizontal grid size the mean temperature is calculated via

$$T_{\text{ave}} = \frac{\sum_{i=i_1}^{i_2} \sum_{j=j_1}^{j_2} \sum_{k=k_1}^{k_2} T_{ijk} \Delta z_{ijk}}{\sum_{i=i_1}^{i_2} \sum_{j=j_1}^{j_2} \sum_{k=k_1}^{k_2} \Delta z_{ijk}}, \tag{4.4}$$

where i, j and k are the grid indices in the x, y and z directions, the sums being over the cells in the appropriate region and basin. Three basins are defined by the forcing lines

in Fig. 3.7, where the central basin is the combination of east-central and west-central sections. In the western basin only the basin average is calculated since the stratification is very weak in this shallow basin.

During the onset and breakdown of the stratification, there may be times when the water in only a few grid-columns is stratified making the average epilimnion/hypolimnion temperature somewhat meaningless. Therefore at each time point t the average epilimnion and hypolimnion temperatures are calculated only if the total number of stratified grid-columns is larger than 10% of the total grid-columns in the basin. The MATLAB code on averaging is attached in Appendix A.2.

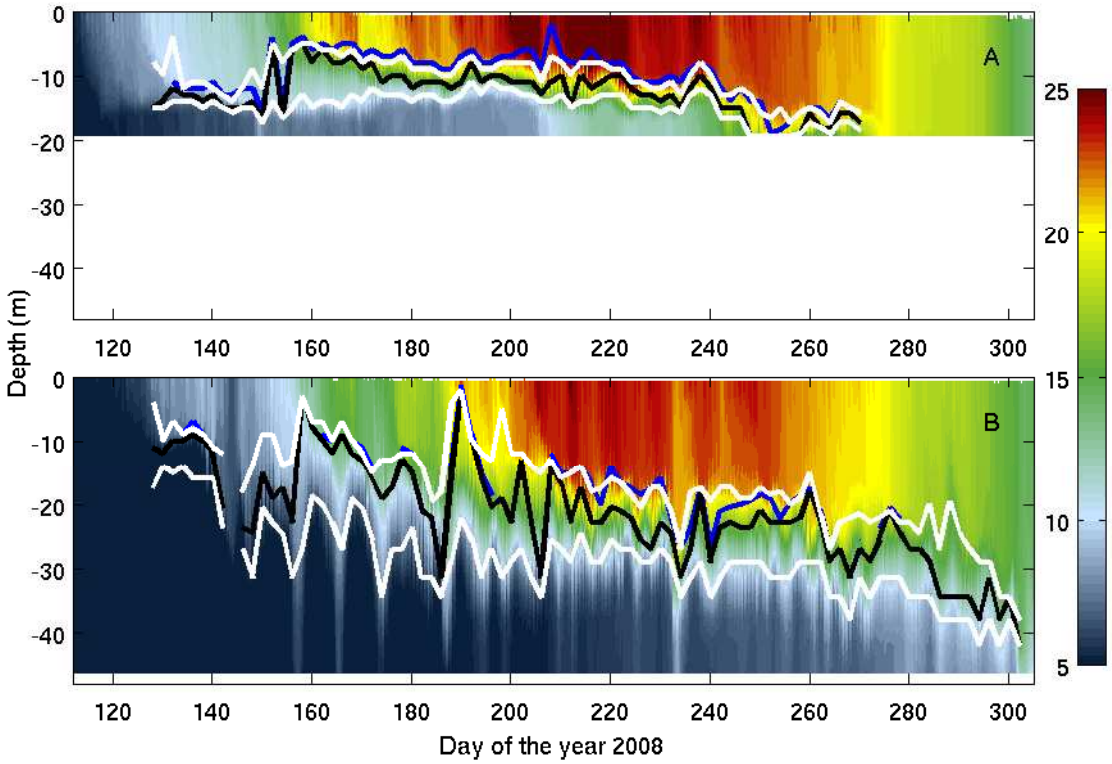

Figure 4.1: The modelled temperature profiles at station (A) 1231 and (B) 452. The black line is the calculated thermocline, two white lines are the epilimnion and hypolimnion boundaries with $c_{\text{epi}} = c_{\text{hyp}} = 25\%$, and the blue line is the epilimnion boundary using the definition in Carignan et al. (2000).

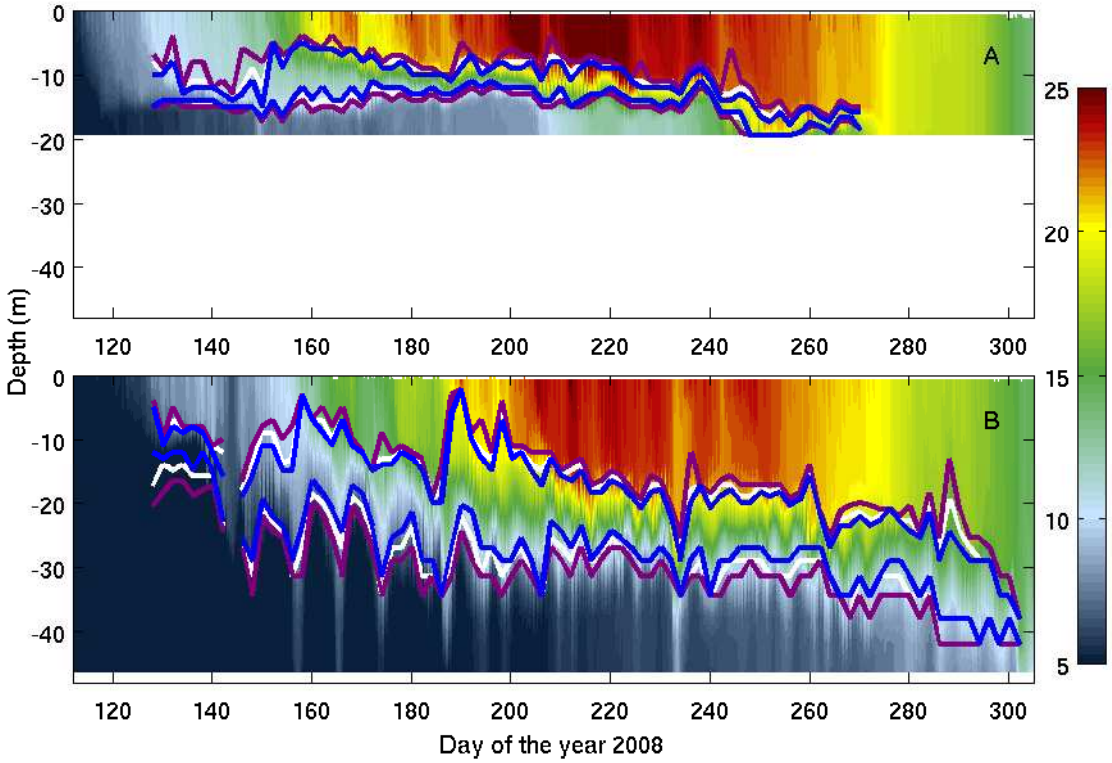

Figure 4.2: The modelled temperature profiles at station (A) 1231 and (B) 452. The lines are calculated epilimnion and hypolimnion boundaries with: $c_{\text{epi}} = c_{\text{hyp}} = 15\%$ (purple), 25% (white), and 35% (blue).

4.2 Three dimensional modelling of meteorological forcing effects on thermal structure

Dr. Luis Leon and Dr. Serghei Bocaniov, formerly in the Department of Biology at the University of Waterloo, along with Professor Ralph Smith and their colleagues maintain a 2 km resolution ELCOM-CAEDYM set up using a $87 \times 193 \times 45$ grid. All the EL-CD simulations in this thesis were conducted with this set up. The exact values of points in the three dimensions are not important for EL-CD, which can only run in serial at the moment. However, it becomes inconvenient or even impossible to apply the same grids in a parallel computing environment, for example using the Message Passing Interface (MPI) protocol in the MITgcm. In order to resolve this issue, I created a separate set of Lake Erie bathymetries. Based on the high resolution 100 m grid obtained from GLERL, I made several sets of different grid sizes, 500 m ($408 \times 800 \times 45$), 1 km ($204 \times 400 \times 45$), and 2 km ($100 \times 200 \times 45$). In this section all the simulations were done using my 2 km grid, corresponding to the ELCOM set up (Appendix B.1). The difference between the two sets is essentially negligible.

To study the sensitivity of the thermal structure to meteorological forcing, the 2008 simulation is taken as the base case. The $2\times CO_2$ experiments in Mortsch and Quinn (1996) suggest air temperature increases of 2.9-9.1°C. To incorporate extreme weather cases varying the air temperature by ± 1, ± 2, and ± 4°C should give insights into both the short term variability and the long term impact. Since the longwave radiation depends on the air temperature, the adjustments suggested by Austin and Allen (2011) are applied,

$$Q_{\mathrm{LW}_{adj}} = Q_{\mathrm{LW}} \left(\frac{T_{\mathrm{A}} + \Delta T_{\mathrm{A}}}{T_{\mathrm{A}}} \right)^4, \tag{4.5}$$

where $Q_{\mathrm{LW}_{\mathrm{adj}}}$ and Q_{LW} are the adjusted and the original longwave radiation, T_{A} and ΔT_{A} are the air temperature and the air temperature change (both measured in degree Kelvin). For $T_{\mathrm{A}} = 293$ K (20°C), a temperature increase $\Delta T_{\mathrm{A}} = 4$ leads to about a 5.6% increase in Q_{LW}. To better compare with the results in Robertson and Ragotzkie (1990), who did not adjust the longwave radiation, the simulations without this adjustment were conducted as

well. The relative humidity is also affected by air temperature changes. Unfortunately there are no similar approaches to adjust the relative humidity so it remains the same in all test cases.

The surface wind speeds over Lake Superior during the summer have increased about 5% per decade since 1985 (Desai et al. 2009). In order to investigate the effects of such wind speed changes, in a second set of simulations the wind speed is changed by ±5%, ±10%, and ±20% with the wind direction and other forcing remaining the same.

Several mechanisms responsible for heat transfer between the atmosphere and lakes strongly depend on air temperature and wind. To be specific, longwave radiation, sensible heat flux, and latent heat flux (indirectly through humidity) are related to air temperature, and sensible and latent heat flux are functions of wind speed. Therefore changing the air temperature and wind speed is expected to affect the lakes' thermal structure significantly. Four metrics from Robertson and Ragotzkie (1990) are adopted to quantify the sensitivity of the thermal structure, which are changes in: (i) mean epilimnion temperature; (ii) mean hypolimnion temperature; (iii) onset and breakdown of stratification; and (iv) thermocline depth.

4.2.1 Effects of air temperature changes

For this set of simulations the air temperature was changed by ±1, ±2, ±4°C, and the observed longwave radiation was used both with and without the adjustment from Equation (4.5). The four metrics from Robertson and Ragotzkie (1990) are used to quantify the response.

Mean epilimnion temperature

The mean epilimnion and hypolimnion temperatures are plotted in Fig. 4.3. The upper five panels show the mean temperatures as a function of time while the lower five show the temperature changes relative to the base case. The mean epilimnion temperature

(Fig. 4.3(A-C, F-H)) is strongly affected by the air temperature changes, and it increases/decreases by approximately 0.5-0.7°C for every 1°C increase/decrease in air temperature (further details are provided in Table 4.1). The response is slightly different in each basin, becoming stronger as the basin depth increases, to be specific about 0.5°C in the western basin, 0.6°C in the central, and 0.7°C in the eastern for a 1°C air temperature increase. The response in April and May is weaker than that in the summer and fall. First of all, this is because all simulations start with the same water temperatures and it takes time for the warmer or colder air temperature to change the lake temperature. Moreover the stratification is well established in mid-summer and once a thermocline has formed the bottom water is somewhat isolated from the surface. The extra heat in the atmosphere will preferentially heat the upper layer. In the cases of no longwave radiation adjustment, the response is 0.4-0.6°C for a 1°C increase in air temperature — about 0.1°C weaker than in the adjusted cases. This is unsurprising because the adjusted longwave radiation is increased/decreased accordingly from Equation (4.5), which will in turn enhance/weaken the warming process.

Mean hypolimnion temperature

The response of the mean hypolimnion temperature to the air temperature change is significantly weaker (Fig. 4.3(D,E,I,J) and Table 4.2). In the eastern basin the change is less than 0.1°C for every 1°C change in the air temperature, which is essentially negligible. The response in the central basin is in the range of 0.1-0.2°C. It is slightly larger than in the eastern basin due to the fact that the hypolimnion in the central basin is thin and the thermocline is not as deep. In the cases of no longwave radiation adjustment the response is again weaker than adjusted experiments as in the epilimnion.

Duration of stratification

The time of onset and breakdown of the stratification is strongly affected by air temperature changes. In general increasing the air temperature leads to an earlier onset and a later breakdown. Taking advantage of the three dimensional output, the total number of

stratified grid-columns was counted at each time in the central and eastern basins (recall that water column is deemed to be stratified only if the difference between the surface and bottom water is greater than 4°C). The result is plotted in Fig. 4.4(A,B) where it can be clearly seen that the higher the air temperature the longer the stratified period. We consider a basin to be stratified when at least 25% of the grid-columns in the basin are stratified, that is, in our 2 km resolution setup $3880 \times 25\% = 970$ grid columns (3880 km^2) in the central basin, and $1520 \times 25\% = 380$ (1520 km^2) in the eastern basin. The 25% criterion is somewhat arbitrary and its efficacy depends to some extent on the fraction of the basin shallower than the depth of the thermocline which in general is a function of time. Thus, simply deepening the thermocline can potentially reduce the percentage of stratified grid-columns in the basin below the selected cutoff. This argues for using a relatively small percentage for the cutoff criterion. The differences between each experiment and the base case are our primary interest, however, and these are insensitive to the particular threshold value chosen unless it is too large. The detailed comparison is listed in Table 4.3. When the air temperature increases, the breakdown time is delayed significantly. On average it is about 1-2 days in the central basin and 4-8 days in the eastern basin per 1°C air temperature increase. On the other hand, when the air temperature decreases, the breakdown time is shortened by 1-4 days in the central basin and 2-3 days in the eastern basin per 1°C air temperature decrease. Again the results in Table 4.3 depend on the choice of the threshold value (25% here), however, the trend remains consistent when other values are used.

Compared with the breakdown time, the onset time is rather complicated as seen from Fig. 4.4(A,B). Several factors cause this complexity. First of all the dynamics of the stratification onset itself is complicated, as it is determined by the combination of air temperature, wind, radiation, and humidity, etc. The stratification is quite weak during the spring and as a consequence grid-columns can switch from being stratified to unstratified quite often during the period of weak stratification. The second factor comes from the limitation in our model setup. The simulation starts on day 112 (April 21) with the lake at rest and the initial temperatures are vertically uniform as observed. The model requires several weeks of spin-up time (Beletsky and Schwab 2001). Unfortunately the lake

stratifies during the spin-up period hence we cannot quantify the changes in onset times. Nonetheless near day 150 (May 29) after the spin-up, we do see a clear pattern that warmer air temperature leads to a greater portion of the basin being stratified.

In addition to considering the total number of stratified grid-columns to determine the onset and breakdown of stratification, we also used the presence of a particular temperature contour, as has been used in many one-dimensional modelling analyses (Robertson and Ragotzkie 1990; McCormick 1990). Based on the seasonal temperature evolution at the observational stations (Fig. 3.9 and 3.10), the 18°C contours at the basin centres (Fig. 4.4(C,D)) were chosen to quantify the stratification response. The 18°C contour lasted from around day 173 to 281 in the centre of the central basin and from day 186 to 281 in the centre of the eastern basin. The results are summarized in Table 4.4. Both methods of quantifying the length of the stratified period give similar predictions of the response to air temperature changes. Different values of temperature contours at different locations could be used as well, and obviously result in different responses on the stratification duration. This raises the concern of the choice of one dimensional criterion, i.e., how can we select the optimal location and contour value to better represent the stratification conditions for the whole basin? This will be discussed in the following section.

The locations and depths of the thermocline, averaged over the month of October, are shown in Fig. 4.5(A-F). As the air temperature increases the area of the thermocline grows, a clear indication that increasing air temperature delays the breakdown of the stratification.

Mean thermocline depth

The changes in the thermocline depth in response to air temperature changes are small but gradually increase at the end of the season. Figures 4.4(E,F) show the evolution of the mean depth of the thermocline in the central and eastern basins. Higher/lower air temperature raises/deepens the thermocline. When the air temperature is increased by 4°C the thermocline is raised by up to 3 m in the eastern basin and 1 m in the shallower central basin.

Table 4.1: Responses in the mean epilimnion temperature (A.T. = air temperature, unit: °C, the difference per 1°C or 1% wind is calculated by subtracting the base case value from the varying case and then normalizing.)

	Difference per 1°C or 1% wind in Western basin	Difference per 1°C or 1% wind in Central basin	Difference per 1°C or 1% wind in Eastern basin
A.T. +4°C adjusted	+0.54	+0.66	+0.74
A.T. +2°C adjusted	+0.55	+0.66	+0.73
A.T. +1°C adjusted	+0.55	+0.65	+0.72
A.T. −1°C adjusted	−0.56	−0.63	−0.73
A.T. −2°C adjusted	−0.56	−0.63	−0.73
A.T. −4°C adjusted	−0.56	−0.67	−0.78
A.T. +4°C	+0.44	+0.53	+0.58
A.T. +2°C	+0.44	+0.53	+0.58
A.T. +1°C	+0.45	+0.52	+0.58
A.T. −1°C	−0.45	−0.51	−0.60
A.T. −2°C	−0.45	−0.51	−0.58
A.T. −4°C	−0.45	−0.51	−0.59
Wind speed +20%	−0.02	−0.03	−0.04
Wind speed +10%	−0.02	−0.03	−0.04
Wind speed +5%	−0.02	−0.03	−0.04
Wind speed −5%	+0.02	+0.03	+0.04
Wind speed −10%	+0.02	+0.03	+0.04
Wind speed −20%	+0.02	+0.04	+0.05

Table 4.2: Responses in the mean hypolimnion temperature (unit: °C)

	Difference per 1°C or 1% wind in Central basin	Difference per 1°C or 1% wind in Eastern basin
A.T. +4°C adjusted	+0.12	+0.06
A.T. +2°C adjusted	+0.15	+0.06
A.T. +1°C adjusted	+0.17	+0.05
A.T. −1°C adjusted	−0.19	−0.06
A.T. −2°C adjusted	−0.17	−0.06
A.T. −4°C adjusted	−0.20	−0.10
A.T. +4°C	+0.11	+0.05
A.T. +2°C	+0.14	+0.05
A.T. +1°C	+0.17	+0.05
A.T. −1°C	−0.17	−0.04
A.T. −2°C	−0.10	−0.04
A.T. −4°C	−0.13	−0.07
Wind speed +20%	+0.08	+0.09
Wind speed +10%	+0.09	+0.09
Wind speed +5%	+0.09	+0.09
Wind speed −5%	−0.09	−0.08
Wind speed −10%	−0.09	−0.08
Wind speed −20%	−0.10	−0.07

Table 4.3: Responses of the stratification breakdown time based on the number of stratified grid-columns (unit: days)

	Central basin		Eastern basin	
	Difference	Difference per 1°C or 1% wind	Difference	Difference per 1°C or 1% wind
A.T. +4°C adjusted	+8	+2	+16	+4
A.T. +2°C adjusted	+2	+1	+11	+6
A.T. +1°C adjusted	+1	+1	+8	+8
A.T. −1°C adjusted	−1	−1	−3	−3
A.T. −2°C adjusted	−8	−4	−5	−3
A.T. −4°C adjusted	−16	−4	−7	−2
A.T. +4°C	+5	+1	+15	+4
A.T. +2°C	+2	+1	+11	+6
A.T. +1°C	+1	+1	+8	+8
A.T. −1°C	−1	−1	−1	−1
A.T. −2°C	−8	−4	−4	−2
A.T. −4°C	−16	−4	−7	−2
Wind speed +20%	−35	−2	−24	−1
Wind speed +10%	−16	−2	−7	−1
Wind speed +5%	−9	−2	−5	−1
Wind speed −5%	+2	+0	+11	+2
Wind speed −10%	+9	+1	+16	+2
Wind speed −20%	+23	+1	+20	+1

Table 4.4: Responses of the stratification duration based on the 18°C contours (unit: days)

	Central basin			Eastern basin		
	Onset diff.	Breakdown diff.	Total duration	Onset diff.	Breakdown diff.	Total duration
base	-	-	108	-	-	95
A.T. +4°C adjusted	−15	+20	143	−19	+21	135
A.T. +2°C adjusted	−12	+15	135	−10	+12	117
A.T. +1°C adjusted	−9	+5	122	−7	+4	106
A.T. −1°C adjusted	+4	−3	101	+2	−1	92
A.T. −2°C adjusted	+7	−4	97	+3	−4	88
A.T. −4°C adjusted	+18	−18	72	+12	−18	65
A.T. +4°C	−13	+18	139	−14	+18	127
A.T. +2°C	−10	+15	133	−7	+12	114
A.T. +1°C	−1	+3	112	−7	+3	105
A.T. −1°C	+3	−3	102	+2	−1	92
A.T. −2°C	+5	−4	99	+3	−3	89
A.T. −4°C	+16	−5	87	+7	−14	74
Wind speed +20%	+5	+2	105	+2	+1	94
Wind speed +10%	+3	0	105	+2	0	93
Wind speed +5%	+2	−1	105	−1	0	96
Wind speed −5%	0	−1	107	+1	0	94
Wind speed −10%	−1	−1	108	−2	+1	98
Wind speed −20%	−12	+1	119	−9	+2	106

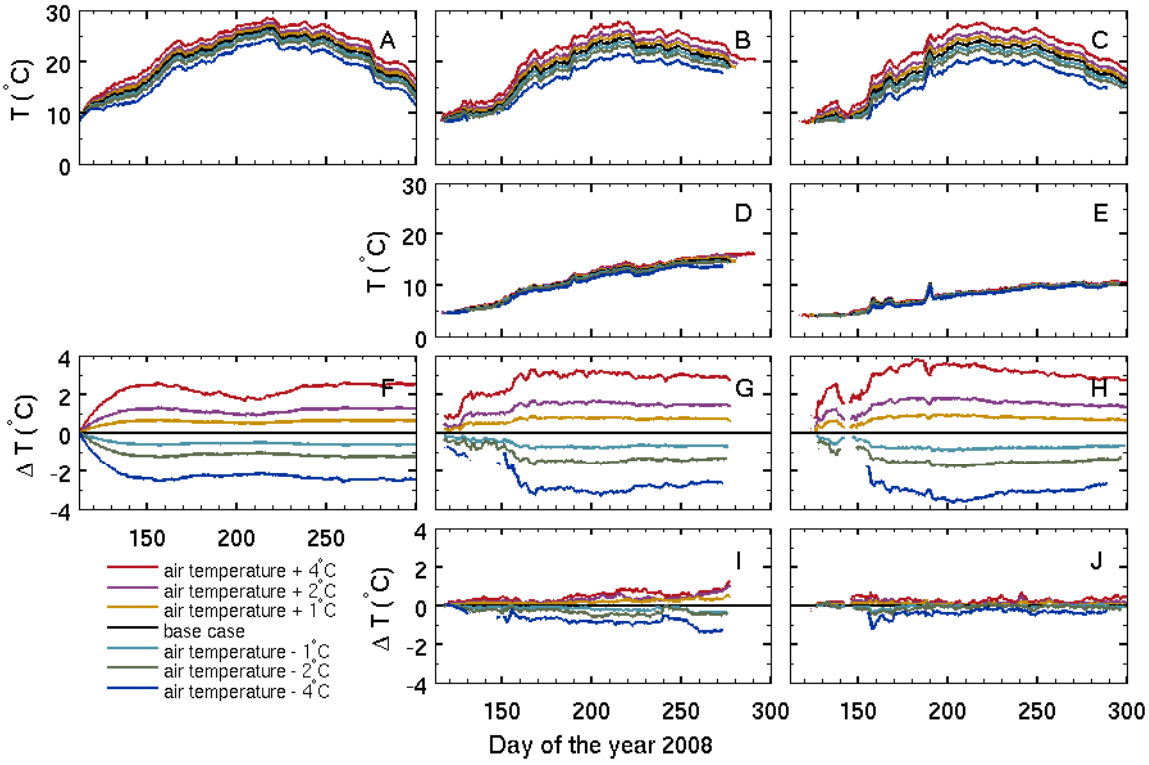

Figure 4.3: Mean temperature response to the air temperature changes in: (A,F) western basin, (B,G) central basin epilimnion, (C,H) eastern basin epilimnion, (D,I) central basin hypolimnion, and (E,J) eastern basin hypolimnion. The upper five are the mean temperature and the lower five are the difference from the base case.

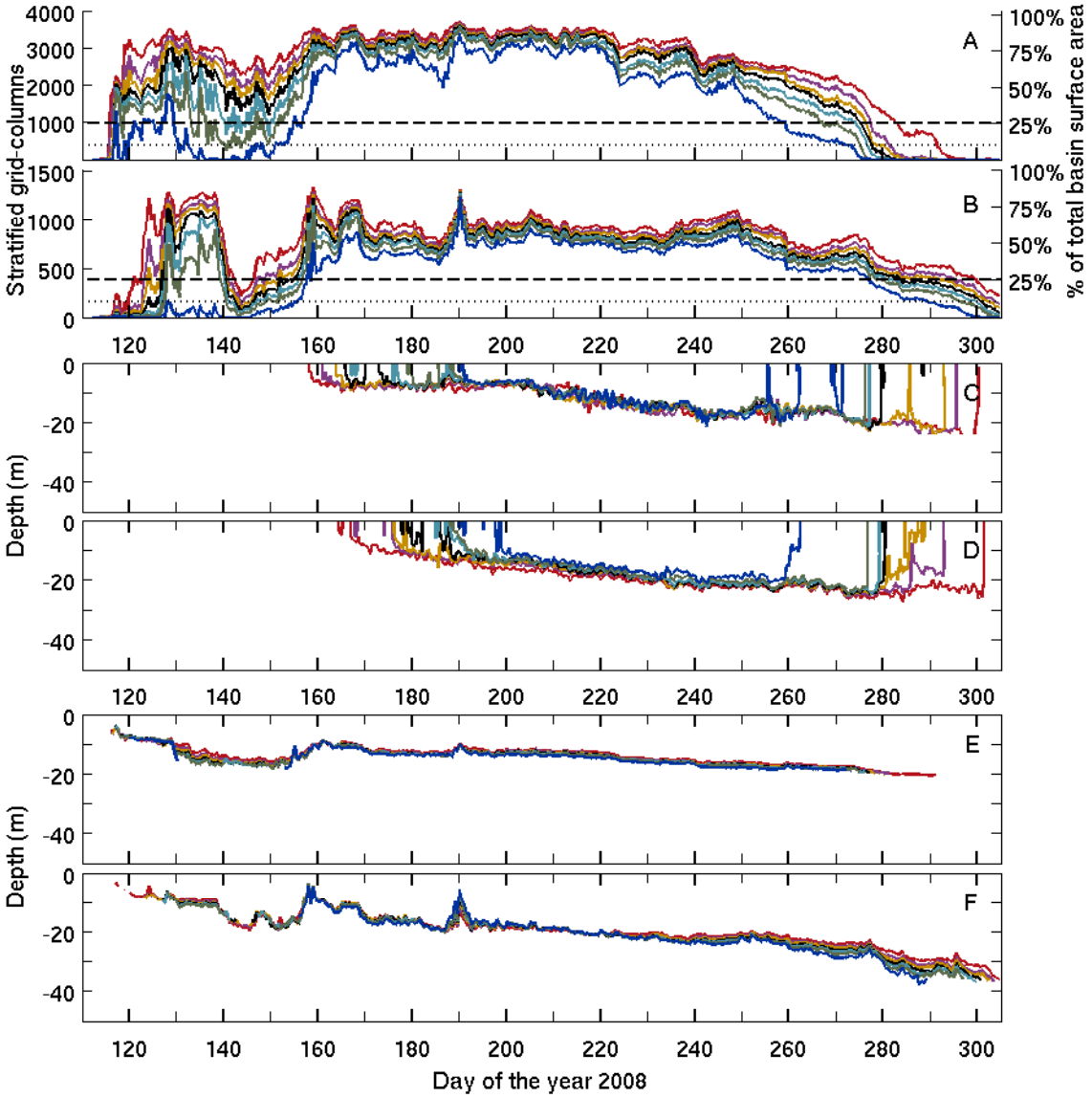

Figure 4.4: Total number of stratified grid-columns in response to air temperature change in (A) central basin and (B) eastern basin, where the dash line is 25% of the total number of water grid-columns and the dot line is 10%. The right label shows the percentage of the total basin surface area. The 18°C contours in (C) central basin and (D) eastern basin. Mean thermocline depth in (E) central basin and (F) eastern basin. Please refer to Fig. 4.3 for the colour legend.

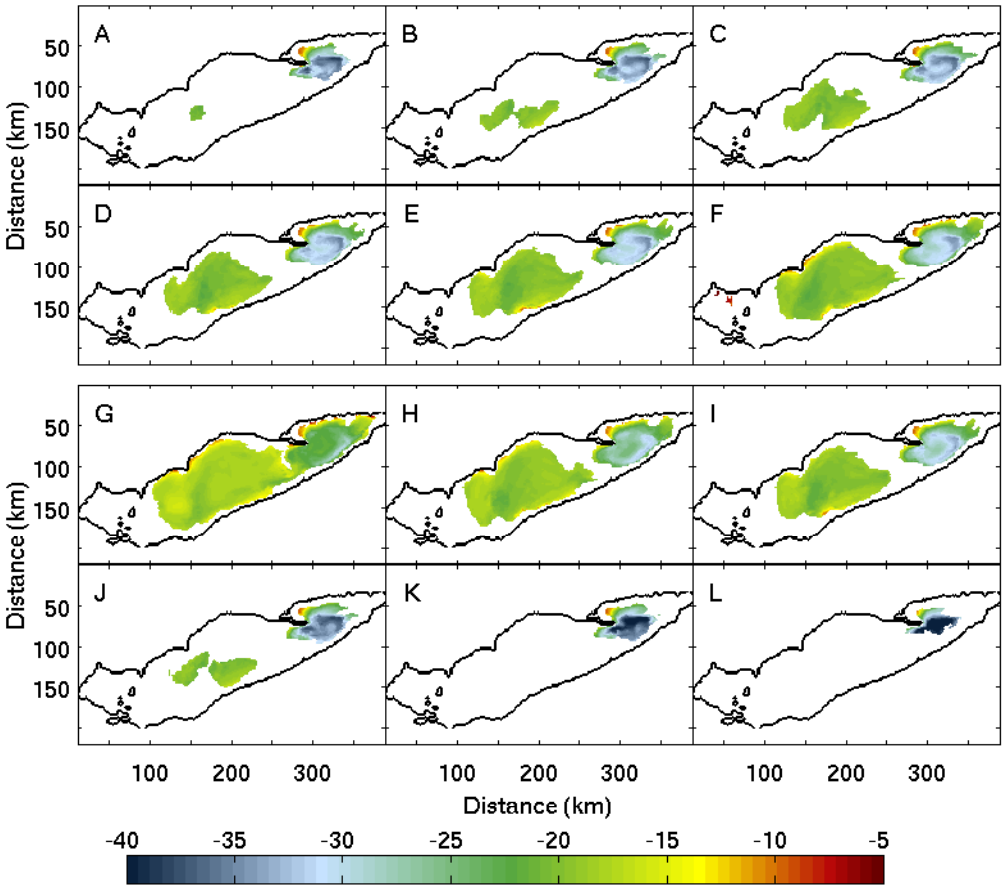

Figure 4.5: Mean thermocline depth in October when the air temperature is changed by: (A) −4°C, (B) −2°C, (C) −1°C, (D) +1°C, (E) +2°C, (F) +4°C, and when the wind speed is changed by: (G) −20%, (H) −10%, (I) −5%, (J) +5%, (K) +10%, (L) +20%.

4.2.2 Effects of wind speed changes

To investigate the sensitivity of the thermal structure to changes in wind forcing the wind speed is changed by ±5%, ±10%, and ±20% with wind direction and the other forcings unchanged.

Mean epilimnion temperature

Stronger winds cool the epilimnion water, and weaker winds have the opposite effect (Fig. 4.6(A-C, F-H) and Table 4.1). The epilimnion temperature can be cooled/warmed by nearly 2°C when the wind speed is increased/decreased by 20%, but on average the temperature change is in the range of 0.02-0.04°C per percent change in wind speed ($\%^{-1}$). Similar to the air temperature change experiments, the responses in the epilimnion temperature vary between basins. The wind speed changes have larger effects on the deeper eastern basin with 0.04°C $\%^{-1}$, and 0.03°C $\%^{-1}$ in the central, and 0.02°C $\%^{-1}$ in the western basin.

Mean hypolimnion temperature

Changes in wind speed have the opposite effect in the hypolimnion, where stronger/weaker winds warm up/cool down the deep water (Fig. 4.6(D,E,I,J) and Table 4.2). The temperature changes are larger than in the epilimnion and continue to grow until near the end of the simulation. This difference is a consequence of stronger winds leading to the formation of a deeper thermocline (discussed in (iv) below) and stronger vertical mixing. The change in the hypolimnion temperature increases as a function of time, and on average it is about 0.1°C $\%^{-1}$. The gradually increasing response is the result of the continuous deepening (or raising) of the thermocline.

Duration of stratification

Changes in wind speed have a strong effect on the onset and breakdown of the stratification as well. Figures 4.7(A,B) show the total number of stratified grid-columns in

the central and eastern basins respectively. The stratification breaks down earlier/later by approximately 1-2 days per 1% increase/decrease in wind speed. The 18°C contour (Fig. 4.7(C,D) and Table 4.3) in the centre of the basin, on the other hand, shows very little difference in the breakdown time. This raises the question of the efficacy of one-dimensional versus three-dimensional approaches for determining the presence of stratification in the basin, which will be discussed in the following section. As in the air temperature experiments, the curves showing basin averaged temperature (Fig. 4.6(B-E)) and thermocline depth (Fig. 4.7(E,F)) illustrate the strong impact of wind speed on the duration of the stratification, as well as on the mean area of thermocline in October (Fig. 4.5(G-L)).

Mean thermocline depth

Figures 4.7(E,F) plot the mean thermocline depth in the central and eastern basins. Increasing the wind speeds deepens the thermocline by as much as 4 m in the central basin and 10 m in the eastern basin in the +20% case. The response increases with time. On average, by the end of the season the thermocline is deepened (or raised) by about 0.2 $\mathrm{m}\,\%^{-1}$ eastern basin. A similar conclusion can be drawn from the central basin but with a smaller changes 0.1 $\mathrm{m}\,\%^{-1}$ due to the shallower basin depth.

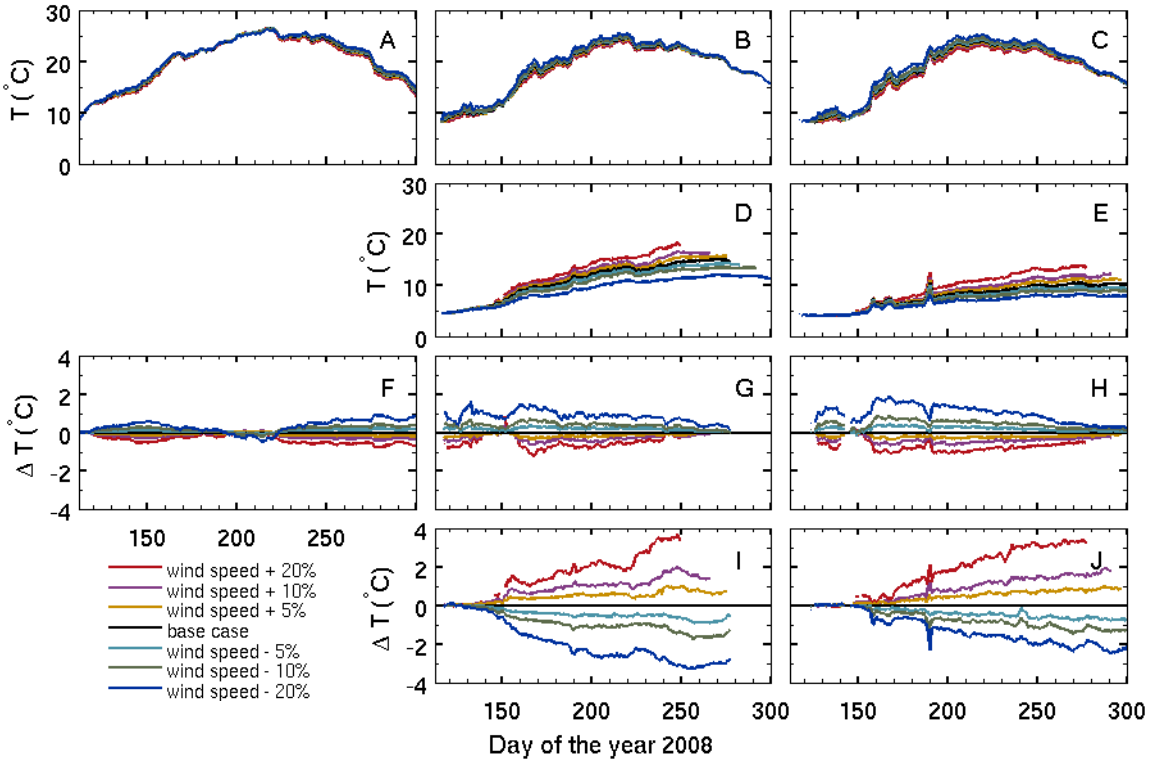

Figure 4.6: Mean temperature response to the wind speed changes in: (A,F) western basin, (B,G) central basin epilimnion, (C,H) eastern basin epilimnion, (D,I) central basin hypolimnion, and (E,J) eastern basin hypolimnion. The upper five are the mean temperature and the lower five are the difference from the base case.

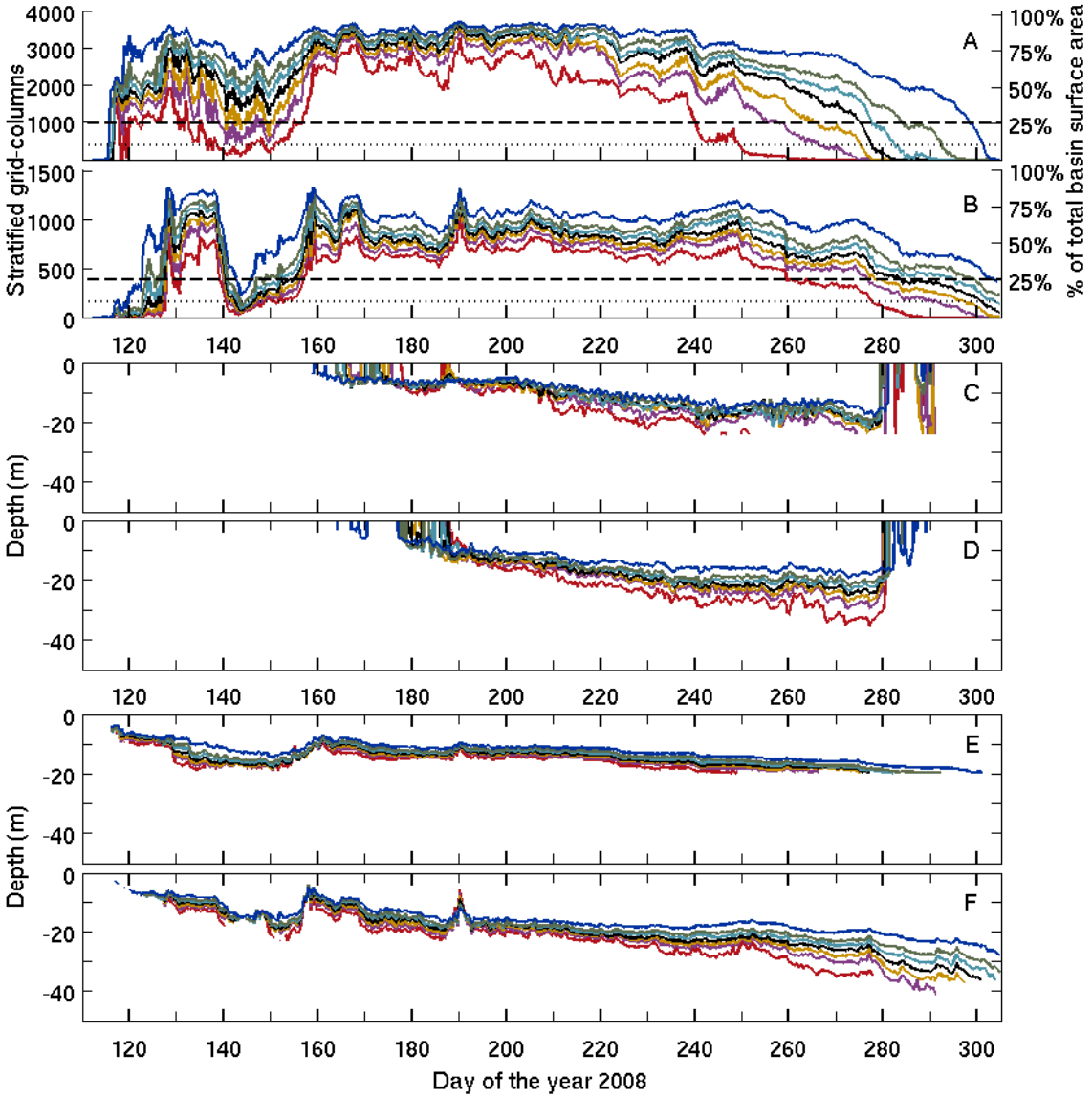

Figure 4.7: Total number of stratified grid-columns in response to wind speed change in (A) central basin and (B) eastern basin, where the dash line is 25% of the total number pf water grid-columns and the dot line is 10%. The right label shows the percentage of the total basin surface area. The 18°C contours in (C) central basin and (D) eastern basin. Mean thermocline depth in (E) central basin and (F) eastern basin. Please refer to Fig. 4.6 for the colour legend.

4.2.3 Discussion

Our sensitivity tests for Lake Erie suggest thermal structure responses similar to previous results for the Great Lakes and other lakes, for instance Lake Erie (Blumberg and Ditoro 1990), Lake Michigan (McCormick 1990), Lake Superior (Austin and Allen 2011) and Lake Mendota (Robertson and Ragotzkie 1990). The analysis is summarized in Table 4.5. Though both air temperature and wind are important parameters affecting the lake thermal structure with equal importance for the duration of stratification, our findings indicate that the thermocline depth and the hypolimnetic temperature are more sensitive to wind, while the epilimnetic temperature is more sensitive to changes in air temperature.

Table 4.5: Impacts due to air temperature and wind speed changes on the thermal structure in three basins (H: high, M: medium, L: low, and n.a.: not applicable)

	Due to air temperature			Due to winds		
	Western	Central	Eastern	Western	Central	Eastern
Epilimnetic temperature	H	H	H	L	L	L
Hypolimnetic temperature	n.a.	L	L	n.a.	H	H
Stratification duration	n.a.	H	H	n.a.	H	H
Thermocline depth	n.a.	L	M	n.a.	H	H

Air temperature changes can significantly affect the mean epilimnion temperature. The response is about 0.5-0.7°C with, and 0.4-0.6°C without, the longwave radiation adjustment per 1°C air temperature change. This is similar to the estimates of Robertson and Ragotzkie (1990) for Lake Mendota, who suggested an increase of 0.5 to 1.0°C per 1°C increase in air temperature from a statistical approach, and 0.4 to 0.85°C from the DYRESM modelling. In Lake Superior Austin and Allen (2011) approximated a value of 0.8°C for the surface water temperature. The hypolimnion temperature is insensitive to air temperature changes. In the eastern basin the response is less than 0.1°C per 1°C change while the thin hypolimnion in the central basin undergoes a slightly larger response of 0.1-0.2°C. The weaker response of the hypolimnion is expected because higher air temperature leads to a warmer epilimnion, enhancing the stratification and the stability of the metalimnion. This results in less downward heat flux to warm the hypolimnion. Robertson and Ragotzkie (1990) also found that changes in air temperature had a negligible affect on the hypolimnion temperature during the stratified period. Changes in air temperature strongly

affected the time of onset and breakdown of stratification. In general warmer/cooler air temperature prolongs/shortens the stratification duration in qualitatively agreement with previous results. Robertson and Ragotzkie (1990) suggested that the onset and breakdown of the stratification were three days earlier and two days later for every 1°C increase in air temperature. McCormick (1990) presented comparable results in Lake Michigan. Finally, increasing air temperature raises the thermocline depth modestly and the response increases with time. Using DYRESM Robertson and Ragotzkie (1990) found very little change in the thermocline depth.

Wind changes have opposite effects on the epilimnion and hypolimnion temperature. Stronger winds cool down the epilimnion slightly, but warm up the hypolimnion with much larger temperature changes in the latter. Stronger winds induce stronger mixing with larger downward heat fluxes that penetrate into the hypolimnion. In addition, due to the deepening of the thermocline, the epilimnion becomes thicker and hypolimnion becomes thinner, which will help cool down the epilimnion and warm up the hypolimnion respectively. The response to the wind speed change is not as consistent as the results in the air temperature cases possibly due to the nonlinear relative changes in the experiment setup. On average the mean epilimnion temperature is changed by approximately 0.02-0.04°C $\%^{-1}$ and the response is much larger in the hypolimnion with 0.1°C $\%^{-1}$. There were no similar studies for comparison, but Austin and Allen (2011) presented a larger 0.1°C $\%^{-1}$ surface temperature response. This is reasonable since winds will affect the surface water more than the epilimnion. The change in wind speed has strong effects on the duration of the stratification and on the thermocline depth. In the +20% case the thermocline is up to 10 m deeper in the eastern basin which is quite significant.

Figures 4.8–4.11 plot the water temperature evolution contours at stations 1231 and 452 in all experimental scenarios. When air temperature is changed, plots from stations 1231 (Fig. 4.8) and 452 (Fig. 4.9) clearly show that as the air temperature increases, the epilimnion temperature increases significantly, the hypolimnion temperature increases slightly, and the stratification is extended. The change in thermocline depth is difficult to tell from the contour plots, which agrees with our previous conclusion that the thermocline is slightly raised. When the wind speed is increased (Fig. 4.10 and 4.10), the mean epilimnion tem-

perature decreases, hypolimnion temperature increases, stratification is shortened, and the thermocline is deepened.

A three dimensional model obviously brings more insights to our sensitivity analysis relative to a one dimensional one. The three basins in Lake Erie have quite distinct bathymetry and thermal structures. The stratification in the western basin is very weak for the entire season. In the central and eastern basins a three-layer stratification forms and the responses to changes in air temperature and wind speeds in the two basins are different, largely because of differences in the hypolimnion thickness which is thin in the central basin. Air temperature and wind have a stronger affect on the mean epilimnion temperature in the deeper eastern basin. The mean hypolimnion temperature and thermocline depth have different characteristics in two basins due to their different depths.

In this thesis two methods are proposed to determine the onset and breakdown of the stratification, one based on the number of stratified grid-columns and one using the 18°C contour at a location near the centre of the basin. In our air temperature experiments both methods indicated that increasing/decreasing the air temperature increased/decreased the length of the stratified period. In the wind forcing experiments, however, they gave contradictory results. Consideration of the total number of stratified grid-columns (Fig. 4.7(A,B)), changes in basin averaged temperatures (Fig. 4.6(B-E)), thermocline depth (Fig. 4.7(E,F)) and the mean thermocline contours in October (Fig. 4.5(G-L)) all clearly show that wind speed has a significant effect on the duration of the stratification. On the other hand the 18°C contours imply that the duration is not very sensitive to the wind speed. Due to the three dimensional complexity in both basin depth and thermal structure, the one dimensional approach has its limitations. Measurements at various locations will certainly lead to different results. Even at the same location, different values of temperature contours may give inconsistent conclusions. For instance, in the wind speed changing scenarios, both 16°C and 18°C contours show little difference in breakdown time in the eastern basin, however, 20°C contours suggest that stronger winds cause an earlier breakdown of the stratification (not shown). This offers a useful lesson in the perils of using one grid location and an arbitrary isotherm to infer stratification patterns: the stratification at one grid cell may inaccurately reflect the basin averaged stratification.

The hypolimnetic hypoxia in the central basin in Lake Erie is an ongoing object of concern. Recent modelling has concluded that climate-related physical forcing of thermocline depths and mixing are not important to the seasonal oxygen depletion (Rucinski et al. 2010). This result may seem surprising, given that temperature is a strong influence on volumetric oxygen consumption rates (Patterson et al. 1985), and might suggest the climate effects on temperatures and mixing depths shown here are not important. However, Rucinski et al. (2010) were intending to isolate the "truly" physical effects so their model used values of volumetric oxygen depletion that had been calibrated against actual observations in each year of study. Such values will include the effects of altered hypolimnetic temperatures (due to effects on microbial metabolism) and hypolimnetic volumes (due to effects on concentration of organic matter exported from the epilimnion as well as relative importance of sediment surface interactions). Much of the indirect physical forcing effect would therefore not appear, being counted in the inter-annual variations of the calibrated, empirical, consumption rates. For purposes of forecasting, a more fundamental approach would be needed, one that allows for projection of future volumetric consumption rates from consideration of the concentration of organic material entering the hypolimnion and its decomposition rates. In such a framework, the present results raise the potential for multiple influences of climate-related physical forcing on the oxygen regime in Lake Erie. Working out the cumulative effects of altered physical conditions will require coupling of models with process-based models for oxygen dynamics, which will be investigated in detail in the following section.

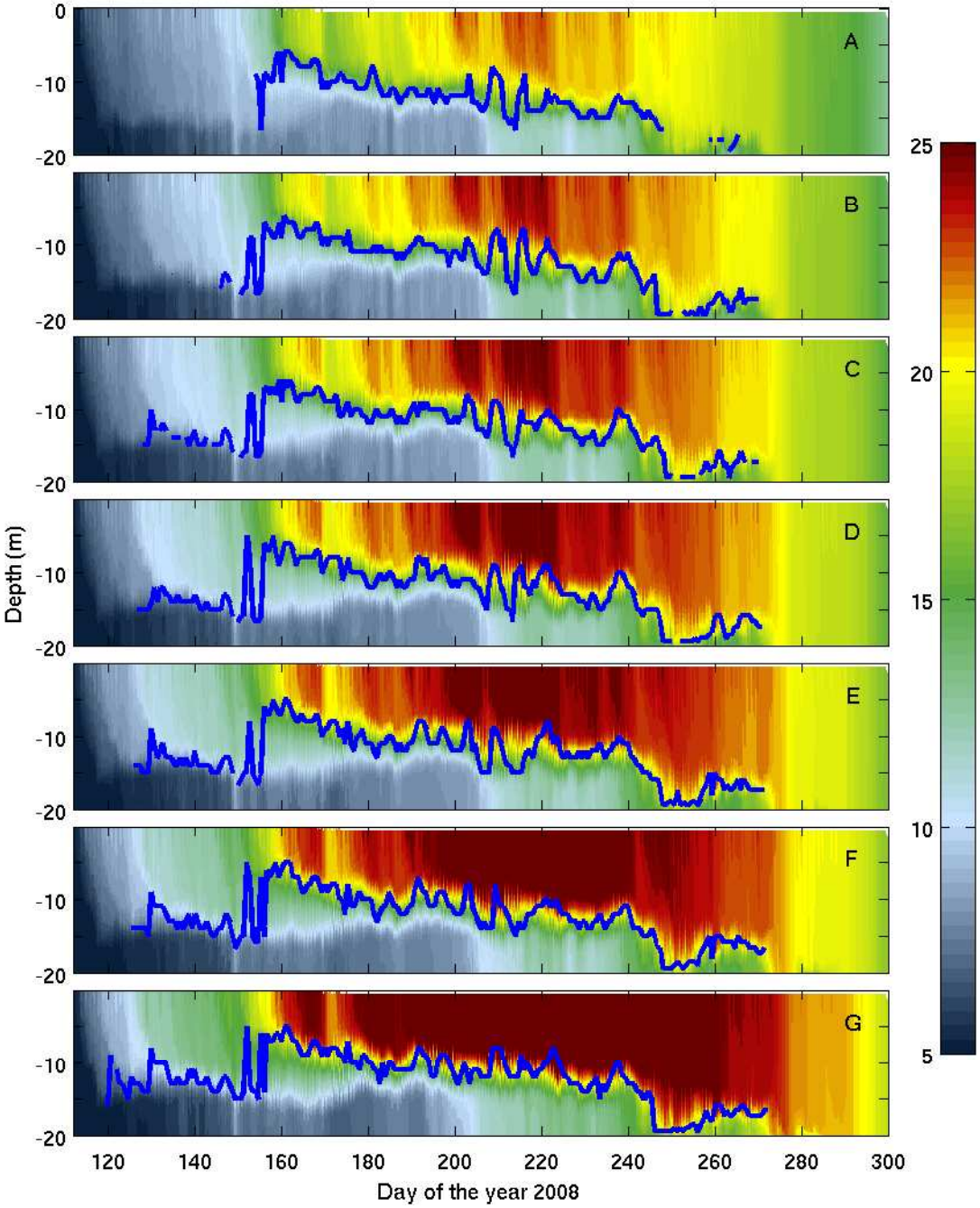

Figure 4.8: Temperature (°C) contours at station 1231 (western central basin) with the air temperature changed by: (A) −4°C, (B) −2°C, (C) −1°C, (D) 0 (base case), (E) +1°C, (F) +2°C, and (G) +4°C. The blue lines are calculated thermoclines.

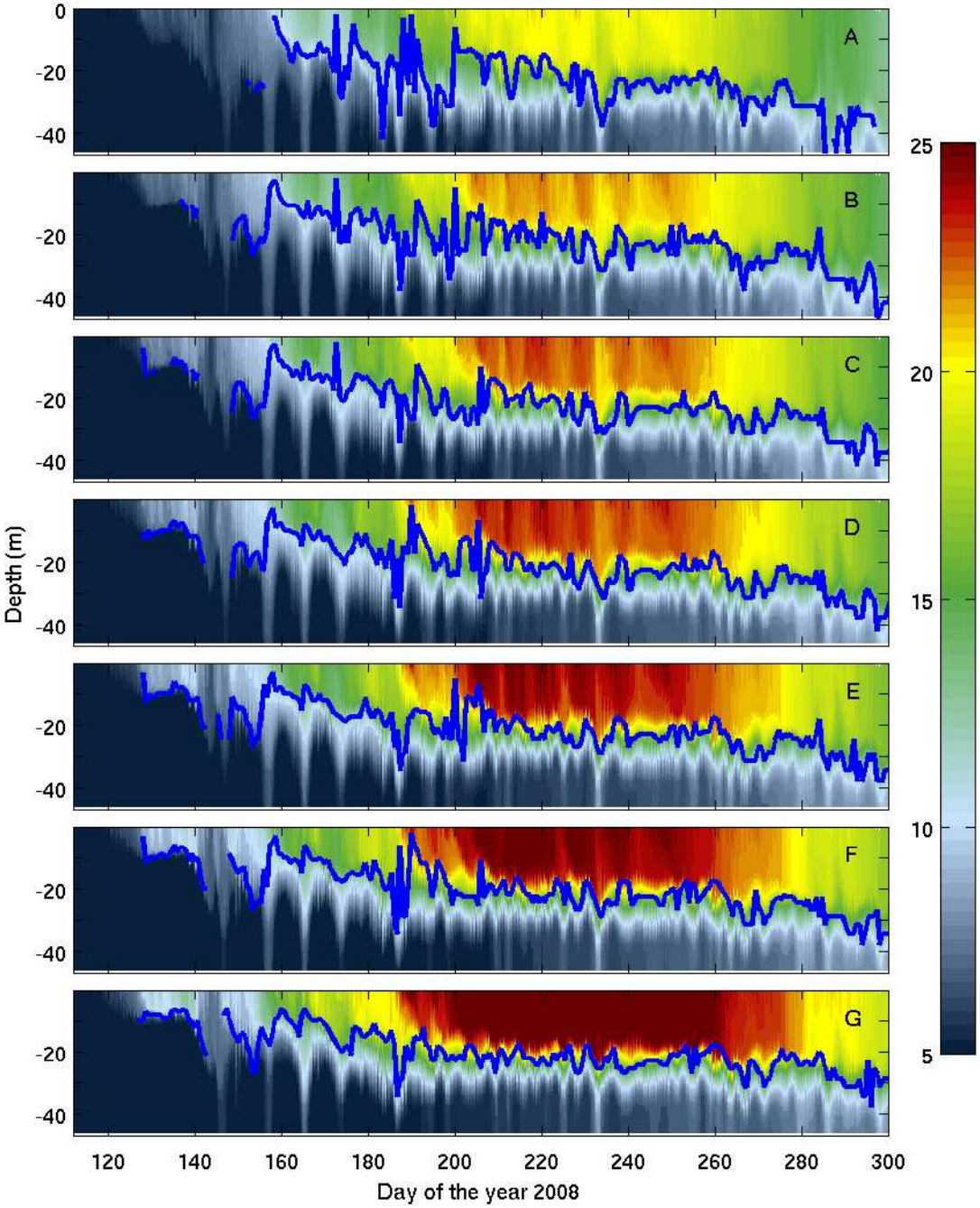

Figure 4.9: Temperature (°C) contours at station 452 (eastern basin) with the air temperature changed by: (A) −4°C, (B) −2°C, (C) −1°C, (D) 0 (base case), (E) +1°C, (F) +2°C, and (G) +4°C. The blue lines are calculated thermoclines.

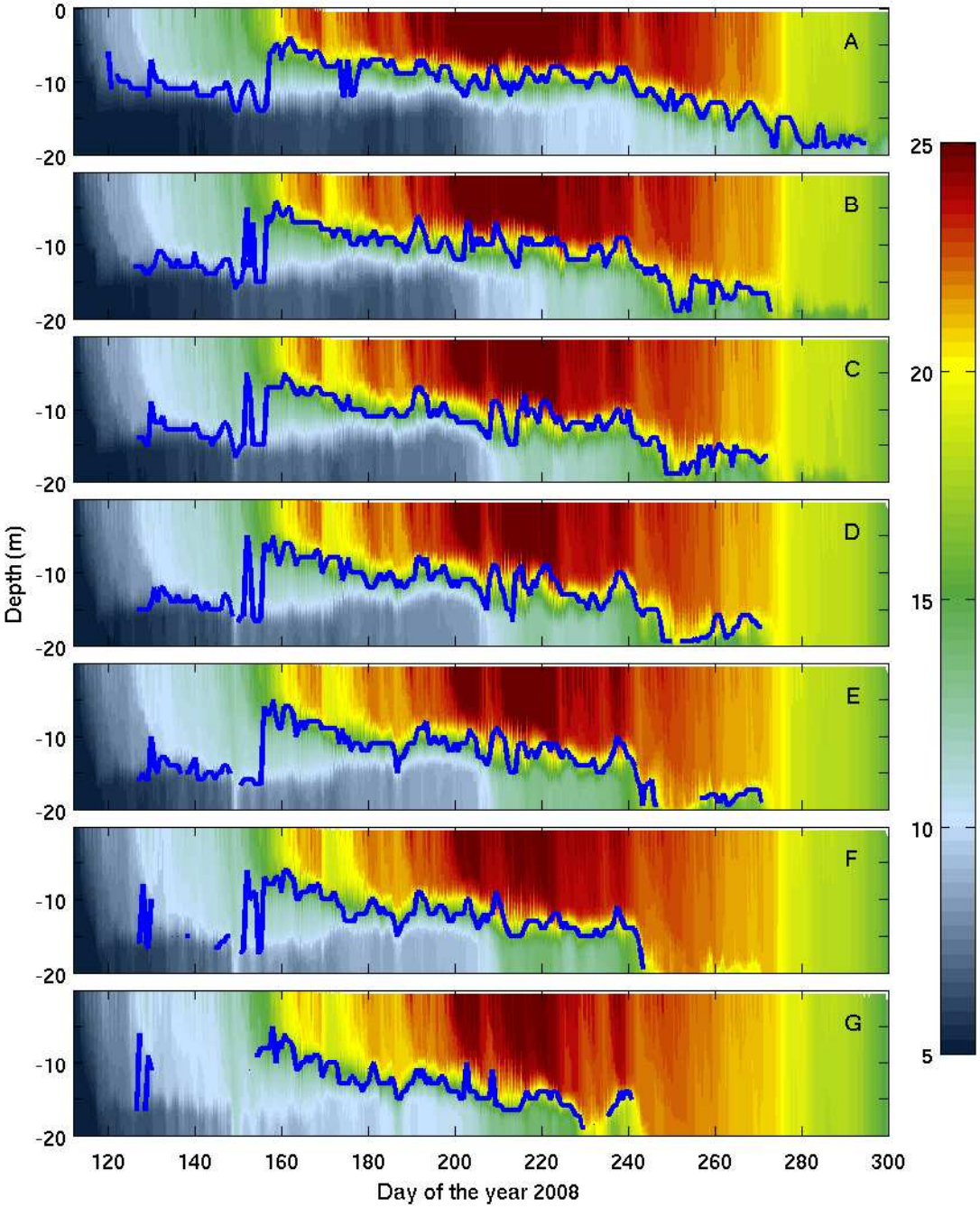

Figure 4.10: Temperature (°C) contours at station 1231 (western central basin) with the wind speed changed by: (A) −20%, (B) −10%, (C) −5%, (D) 0 (base case), (E) +5%, (F) +10%, and (G) +20%. The blue lines are calculated thermoclines.

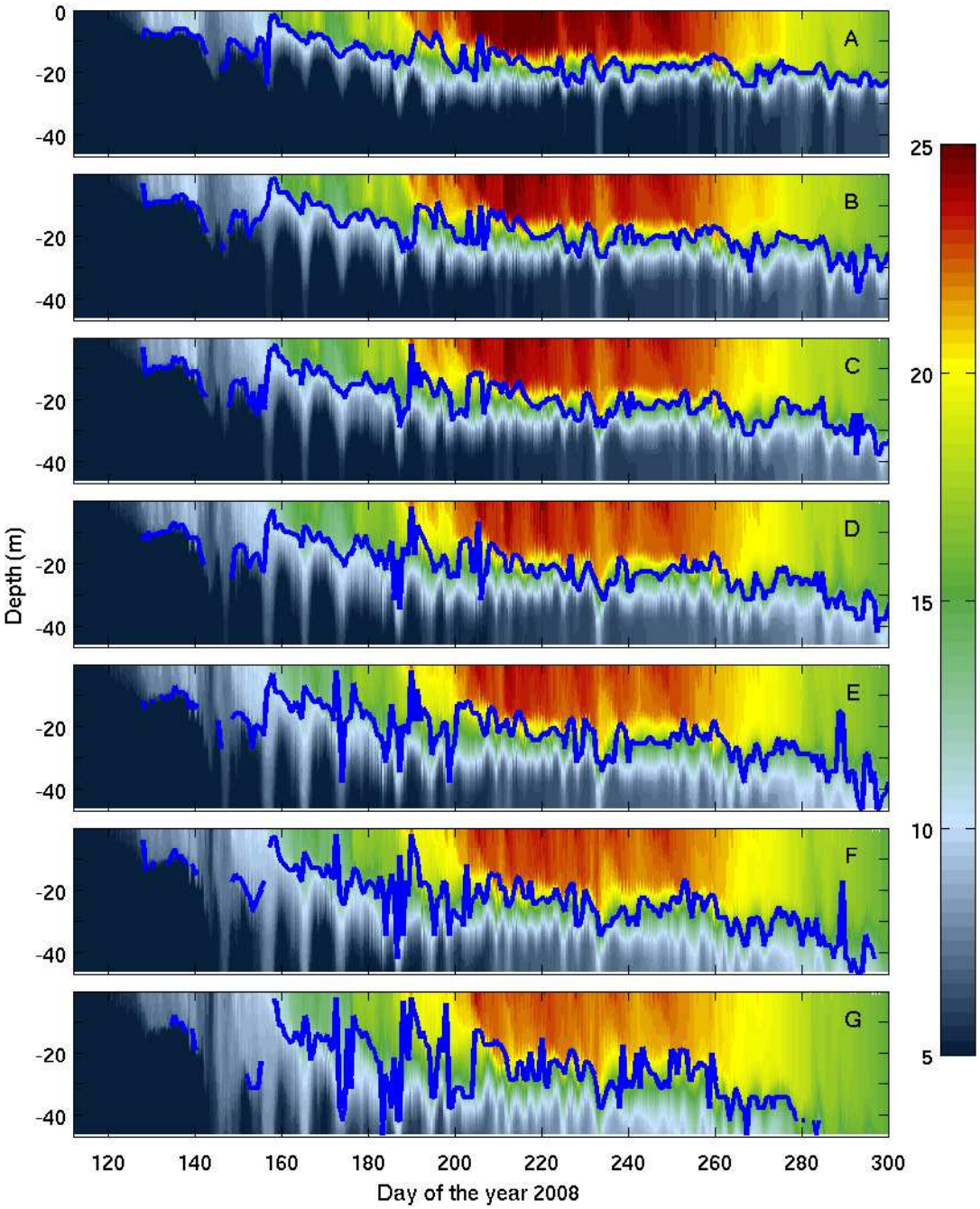

Figure 4.11: Temperature (°C) contours at station 452 (eastern basin) with the wind speed changed by: (A) −20%, (B) −10%, (C) −5%, (D) 0 (base case), (E) +5%, (F) +10%, and (G) +20%. The blue lines are calculated thermoclines.

4.3 Three dimensional modelling of meteorological forcing effects on dissolved oxygen concentration

In this section the coupled hydrodynamic and aquatic ecological model ELCOM-CAEDYM is utilized to study the sensitivity of the dissolved oxygen (DO) concentration to changes in air temperature and wind speed. The same experiments are set up as in the thermal structure studies, i.e., air temperature was changed by ±1, ±2, ±4°C both with and without the longwave radiation adjustment, and wind speed was varied by ±5%, ±10%, and ±20%. Three metrics are used to analyze the meteorological forcing effects: mean epilimnion DO, mean hypolimnion DO, and central basin hypolimnetic hypoxia.

4.3.1 Effects of air temperature changes

Mean epilimnion DO

Water temperature has significant influences on volumetric oxygen consumption rates and equilibrium solubility (Patterson et al. 1985), so it is expected to have a strong correlation between water temperature and DO. Recall in Section 4.2.1 that air temperature changes can significantly affect the mean epilimnion temperature. Higher air temperature warms up the epilimnion by about 0.5-0.7°C with, and 0.4-0.6°C without, the longwave radiation adjustment per 1°C air temperature change. Warmer temperature increases the oxygen consumption rate, reduces the DO equilibrium solubility, and as a result DO decreases in the higher air temperature scenario. The mean epilimnion and hypolimnion DO is plotted in Fig. 4.12. The upper five panels show the mean DO as a function of time while the lower five show the DO changes relative to the base case. The mean epilimnion DO (Fig. 4.12(A-C, F-H) and Table 4.6) is strongly affected by the air temperature changes, and it decreases/increases on average 0.13-0.15 mg L^{-1} for every 1°C increase/decrease in air temperature. The response of both the temperature and DO is stronger in the deeper eastern basin. The DO change is approximately 0.13 mg L^{-1} in the western basin, 0.14 mg L^{-1} in the central, and 0.15 mg L^{-1} in the eastern. In the cases of no longwave radiation

adjustment, the water temperature response is approximately 0.1°C weaker than in the adjusted cases. As a results the DO changes are weaker when no longwave adjustment was applied, with values in the range of 0.10-0.12 mg L^{-1}.

Mean hypolimnion DO

Air temperature changes have very little effect on hypolimnion temperature, so the response of the mean hypolimnion DO to air temperature changes is relatively weaker as well (Fig. 4.12(D,E,I,J) and Table 4.7). Higher/lower air temperature decreases/increases the mean hypolimnion DO. Unlike the epilimnion DO, the hypolimnion DO responses vary among different cases between basins, nonetheless less than 0.1 mg L^{-1}.

Central basin hypolimnetic hypoxia

Recall that hypoxia is generally defined as dissolved oxygen below 2 mg L^{-1}. Figure 4.13 plots the total number of bottom cells which contain less than 2 mg L^{-1} of DO. In the thermal structure sensitivity studies, we learned that increasing air temperature can extend the stratification duration (Fig. 4.13(A)). As a result the number of bottom hypoxic cells increases significantly (Fig. 4.13(B)). The number of bottom hypoxic cells in the central basin, which can be easily converted to the area of bottom hypoxia, starts growing at the beginning of August, continuously increasing through September, and falls down in October when overturning commences. Figure 4.14 plots the bottom DO on September 1 for all experiment cases. In Fig. 4.14(A-F) when air temperature is increased, the bottom DO in the central basin decreases, and the area of bottom hypoxia clearly grows.

Table 4.6: Responses in the mean epilimnion DO (A.T. = air temperature, unit: mg L^{-1}, the difference per 1°C or 1% wind is calculated by subtracting the base case value from the varying case and then normalizing.)

	Difference per 1°C or 1% wind in Western basin	Difference per 1°C or 1% wind in Central basin	Difference per 1°C or 1% wind in Eastern basin
A.T. +4°C adjusted	−0.12	−0.13	−0.15
A.T. +2°C adjusted	−0.13	−0.13	−0.14
A.T. +1°C adjusted	−0.13	−0.13	−0.15
A.T. −1°C adjusted	+0.13	+0.14	+0.15
A.T. −2°C adjusted	+0.13	+0.14	+0.15
A.T. −4°C adjusted	+0.14	+0.15	+0.16
A.T. +4°C	−0.10	−0.10	−0.11
A.T. +2°C	−0.10	−0.11	−0.12
A.T. +1°C	−0.10	−0.11	−0.12
A.T. −1°C	+0.10	+0.11	+0.11
A.T. −2°C	+0.11	+0.11	+0.12
A.T. −4°C	+0.11	+0.11	+0.13
Wind speed +20%	+0.006	−0.004	0
Wind speed +10%	+0.007	−0.005	0
Wind speed +5%	+0.007	−0.005	+0.001
Wind speed −5%	−0.008	+0.005	−0.003
Wind speed −10%	−0.007	+0.005	−0.002
Wind speed −20%	−0.007	+0.006	−0.002

Table 4.7: Responses in the mean hypolimnion DO (unit: mg L^{-1})

	Difference per 1°C or 1% wind in Central basin	Difference per 1°C or 1% wind in Eastern basin
A.T. +4°C adjusted	−0.03	−0.06
A.T. +2°C adjusted	−0.04	−0.05
A.T. +1°C adjusted	−0.03	−0.06
A.T. −1°C adjusted	+0.08	+0.08
A.T. −2°C adjusted	+0.06	+0.08
A.T. −4°C adjusted	+0.07	+0.09
A.T. +4°C	−0.03	−0.05
A.T. +2°C	−0.02	−0.05
A.T. +1°C	−0.03	−0.03
A.T. −1°C	+0.06	+0.06
A.T. −2°C	+0.05	+0.06
A.T. −4°C	+0.05	+0.06
Wind speed +20%	−0.02	−0.02
Wind speed +10%	−0.02	−0.02
Wind speed +5%	−0.03	−0.02
Wind speed −5%	+0.04	+0.03
Wind speed −10%	+0.04	+0.02
Wind speed −20%	+0.04	+0.02

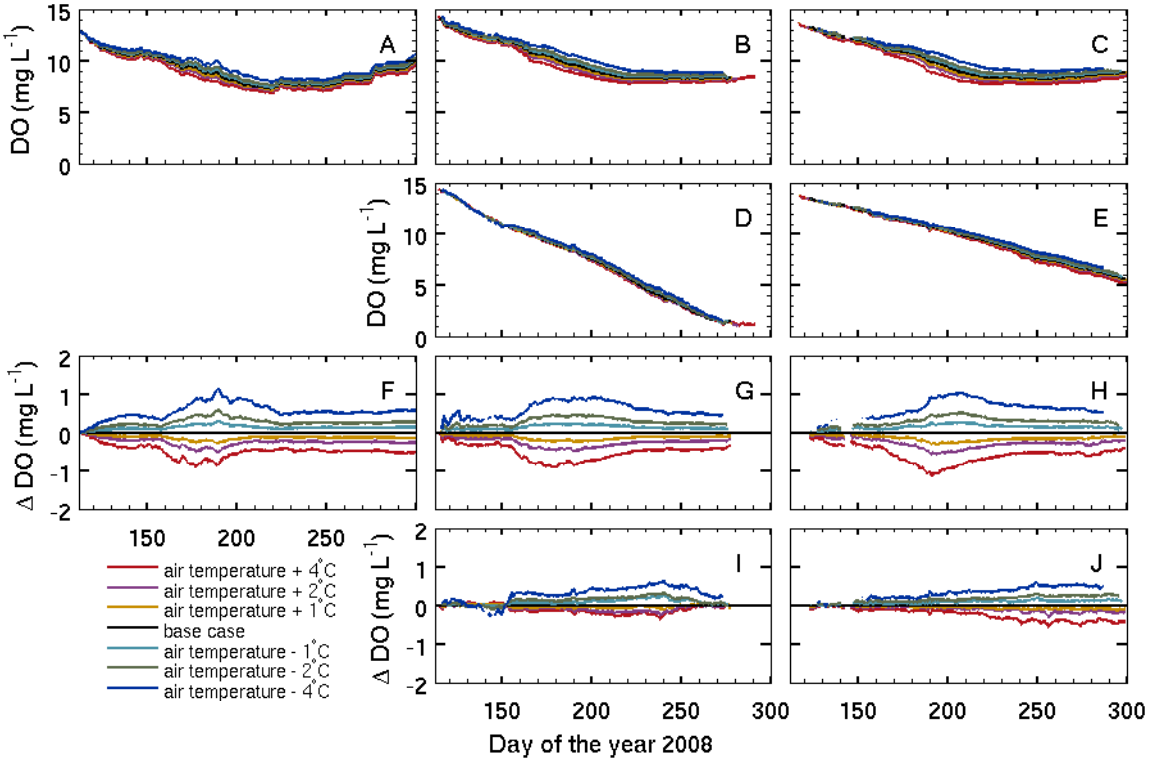

Figure 4.12: The mean DO response to air temperature changes in: (A,F) western basin, (B,G) central basin epilimnion, (C,H) eastern basin epilimnion, (D,I) central basin hypolimnion, and (E,J) eastern basin hypolimnion. The upper five are the mean DO and the lower five are the difference from the base case.

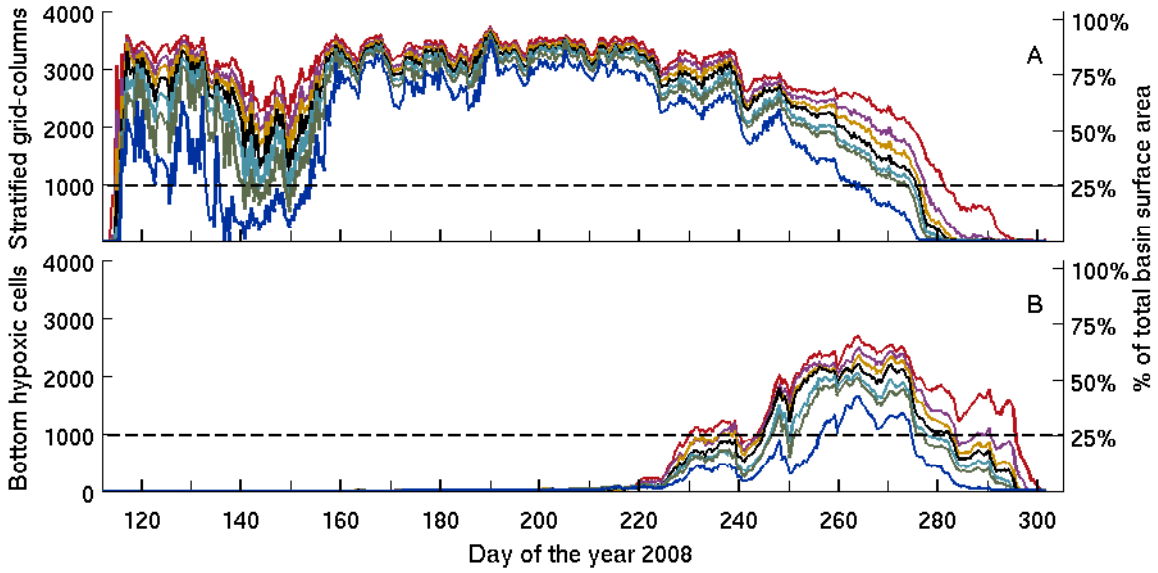

Figure 4.13: (A) Total number of stratified grid-columns and (B) total number of bottom hypoxic cells in the central basin in response to air temperature change. The dash line is 25% of the total number of water grid-columns. The right label shows the percentage of the total basin surface area. Please refer to Fig. 4.12 for the colour legend.

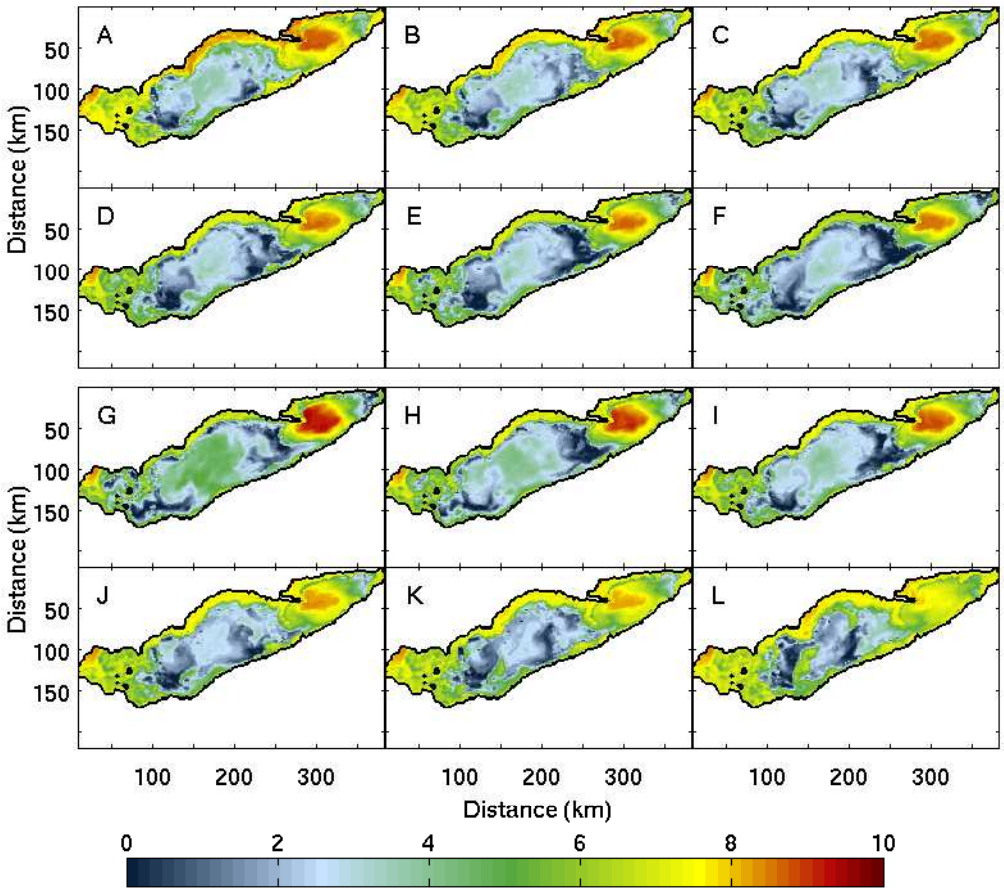

Figure 4.14: Bottom DO (mg L^{-1}) on September 1 when the air temperature is changed by: (A) −4°C, (B) −2°C, (C) −1°C, (D) +1°C, (E) +2°C, (F) +4°C, and when the wind speed is changed by: (G) −20%, (H) −10%, (I) −5%, (J) +5%, (K) +10%, (L) +20%.

4.3.2 Effects of wind speed changes

Mean epilimnion DO

Winds have very little effect on the epilimnion temperature, and as a result the mean DO response in this layer is small as well (Fig. 4.15(A-C, F-H) and Table 4.6). Unlike the pattern found in water temperature, the DO changes in the epilimnion vary with time and with basin, but nonetheless are only in the range of 0 to 0.007 mg $L^{-1}\%^{-1}$. The maximum change when the wind speed is increased/decreased by 20% is less than 0.8 mg L^{-1}.

Mean hypolimnion DO

The response of mean hypolimnion DO is noticeably stronger than in the epilimnion (Fig. 4.15(D,E,I,J) and Table 4.7). Stronger/weaker winds decrease/increase DO, and on average the response is about 0.02-0.04 mg $L^{-1}\%^{-1}$. Stronger winds warm up the hypolimnion significantly, so DO is expected to decrease accordingly. On the other hand stronger winds enhance the vertical mixing, which supplies DO to the hypolimnion. These two processes have the opposite effects on DO. From the mean hypolimnion response, which shows stronger winds decreasing DO, we may suspect that the effect of increasing the temperature dominates the gain of DO from the stronger vertical mixing. Does this really tell us all? We will discuss this more in the following Section 4.3.3.

Central basin hypolimnetic hypoxia

The total number of stratified grid-columns and bottom hypoxic cells in the central basin are plotted in Fig. 4.16 for various wind forcing cases. Recall that stronger winds shorten the stratification duration from the thermal structure sensitivity study. Hence with the earlier disappearance of the metalimnion barrier, the bottom hypoxic area decreases significantly. Figures 4.14(G-L) plot the bottom DO on September 1 for the difference wind forcing cases. As wind speeds are increased, the area of bottom hypoxia clearly shrinks.

Notice that the response of bottom hypoxic cells is more complex than the stratified grid-columns. For instance compared with the base case, the -20% case has fewer bottom hypoxic cells before day 270 and more afterwards (Fig. 4.16). Two possible factors may explain this. During the stratified season decreasing winds leads to colder hypolimnion temperature and an increase of DO, which will in turn result in fewer bottom hypoxic cells. Around day 270 approximately 25% of the grid-columns are still stratified in the base case (Fig. 4.16(A)), whereas more than 75% are stratified in the -20% wind speeds case. The breakdown of stratification in most parts of the basin in the base case causes a sudden increase in DO, so the number of bottom hypoxic cells decreases. In the -20% experiment on the other hand the stratification still persists, and the number of bottom hypoxic cells increases for a longer period of time. The second reason is due to the difference in basin bathymetry and forcing, and resulting thermal and DO profiles. Even within the central basin different parts of the lake may behave differently in terms of stratification strength and duration. Therefore the basin average may be affected.

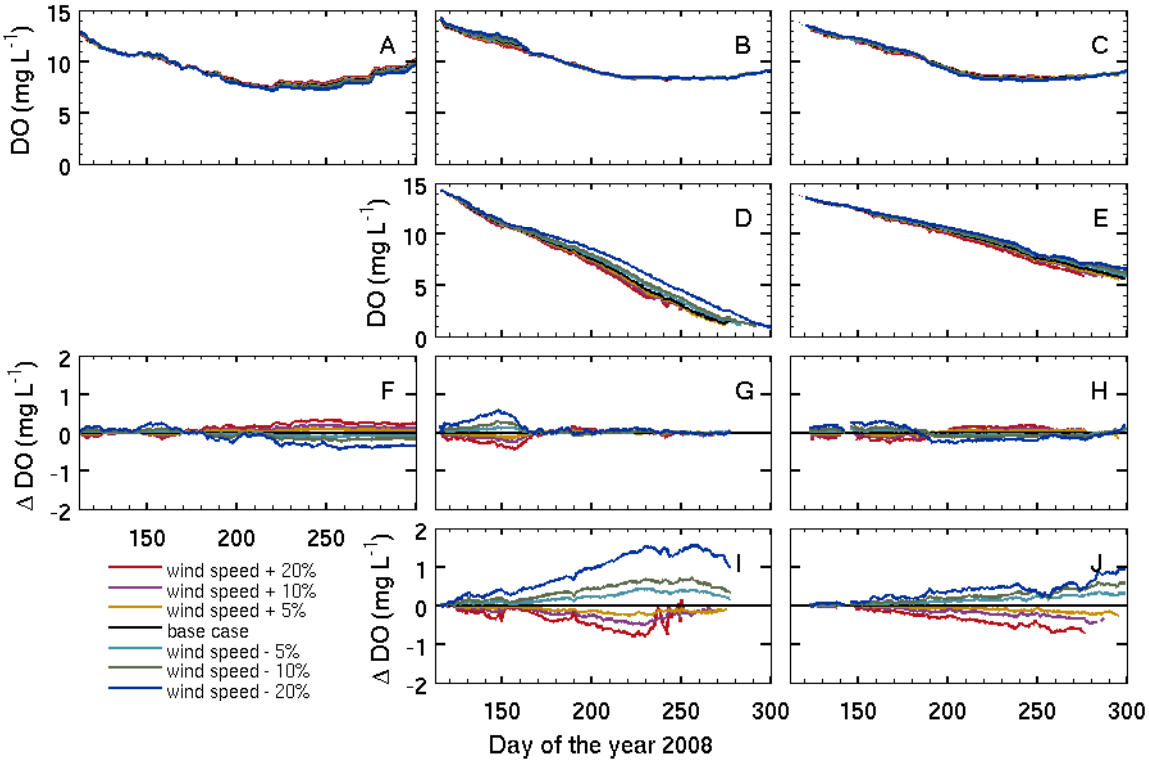

Figure 4.15: The mean DO response to wind speed changes in: (A,F) western basin, (B,G) central basin epilimnion, (C,H) eastern basin epilimnion, (D,I) central basin hypolimnion, and (E,J) eastern basin hypolimnion. The upper five are the mean DO and the lower five are the difference from the base case.

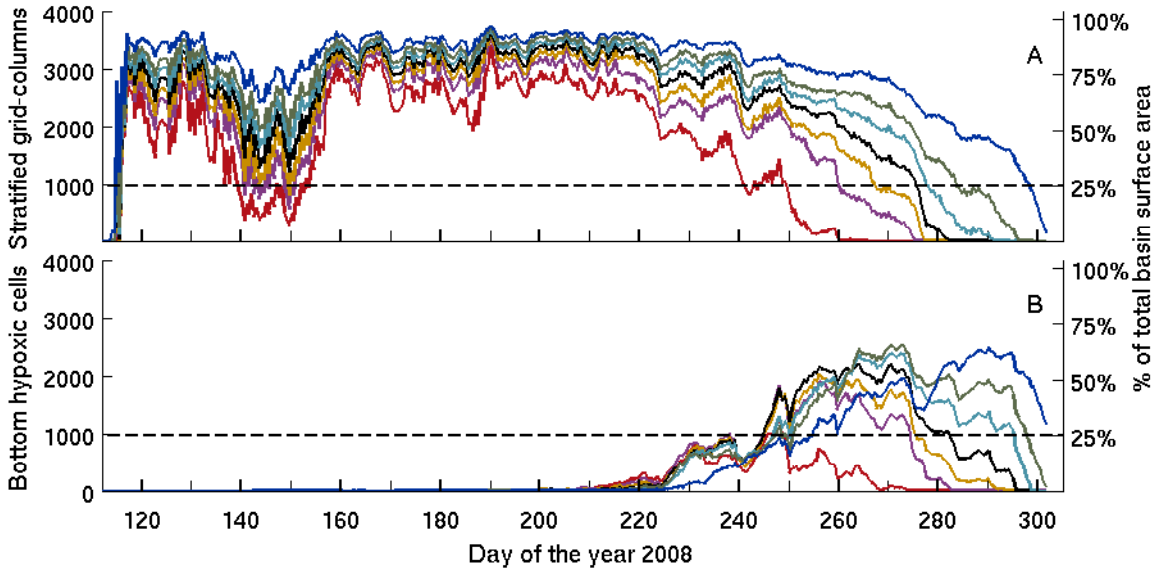

Figure 4.16: (A) Total number of stratified grid-columns and (B) total number of bottom hypoxic cells in the central basin in response to wind speed change. The dash line is 25% of the total number of water grid-columns. The right label shows the percentage of the total basin surface area. Please refer to Fig. 4.15 for the colour legend.

4.3.3 Discussion

Higher/lower air temperature decreases/increases DO in both the epilimnion and hypolimnion, but with a larger response in the former. Figure 4.17(A) shows the mean bottom DO in the central basin which can be compared to the mean DO in the layer as a whole shown in Fig. 4.12. We also plot the DO contours at stations 1231 (western central basin, Fig. 4.18) and 452 (eastern basin, Fig. 4.19). Here the white lines are the calculated hypolimnion boundaries. Recall that the thermal structures at both stations were presented in Fig. 4.8 and 4.9, so we will analyze the DO dynamics along with the thermal structure plots. At station 1231 as the air temperature increases, we can clearly see the decrease of DO in the epilimnion. From the DO validation in Section 3.3.3 we know both observational and simulated hypolimnion DO in the central basin decrease and are below 2 mg L^{-1} in the fall. When the air temperature increases, the stratification period is extended. As a consequence of the continuous oxygen consumption, the DO in the hypolimnion drops even lower. In the +4°C experiment (Fig. 4.18(G)), bottom hypoxia becomes more severe and lasts longer. Therefore bottom hypoxia strongly depends on the duration of stratification. However, this is not the only decisive factor. At station 452 in eastern basin, the similar plots are demonstrated in Fig. 4.19. Though the stratification is extended due to warmer air temperature, the hypolimnion still maintains a high level of DO, with no part of the basin suffering hypoxia. The reason why hypolimnion DO at station 452 differs from station 1231 is that the hypolimnion in the eastern basin is much thicker (10-20 m compared with several meters), so DO decreases at a much slower rate.

Wind speeds have little effect on epilimnetic DO, but change hypolimnion DO noticeably. From the mean DO response (Fig. 4.15), stronger winds decrease hypolimnion DO due to the increase in temperature. On the other hand stronger winds enhance vertical mixing, which helps more DO penetrate into the hypolimnion. Moreover Fig. 4.17(B) plots the mean bottom layer DO in the central basin. In this figure winds do not have significant effects before day 220, and after that stronger winds lead to higher DO. Figure 4.15(D,I) and 4.17(B) seem to give contradictory conclusions. However, both figures are believed to be correct, but they demonstrate different aspects of DO dynamics. Similar to the air

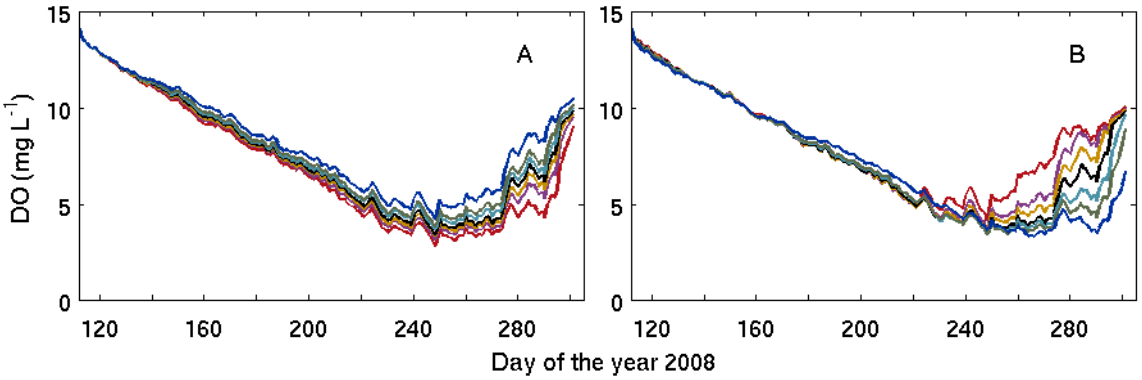

Figure 4.17: Average bottom layer DO in the central basin when air temperature (A) and wind speed (B) are changed. Please refer Fig. 4.12 and 4.15 for colour legends.

temperature change experiments, DO evolution contours at stations 1231 (Fig. 4.20) and 452 (Fig. 4.21) are plotted when wind speeds vary. Recall from the thermal structure in Fig. 4.10 and 4.11, stronger winds increase the mean hypolimnion temperature. Prior to day 230 the hypolimnion DO is clearly decreasing as the winds increase due to warmer hypolimnion water. This explains why stronger winds decrease the mean hypolimnion DO in Fig. 4.15(D,I). Stronger winds deepen the thermocline and shorten the duration of stratification. Although in the base case the water at station 1231 remains stratified, the earlier disappearance of stratification in stronger wind cases explains the shorter line in Fig. 4.15(D,I). During this time most bottom cells lie in the hypolimnion, and we expect winds will have weaker effects on the bottom layer than the hypolimnion. Therefore, the weak response in the bottom layer DO in Fig. 4.17 makes sense. After day 230 the stratification is broken down early in the stronger winds experiments. Coincident with the disappearance of the metalimnion barrier, the DO near the lake bottom increases dramatically. On the other hand if we look at the weaker winds cases (Fig. 4.20(A-C)), the stratification still persists. The hypolimnion DO continues to decrease because the strong stratification blocks the flux of DO from the epilimnion and the existing DO is continuously consumed. This explains why stronger winds increase bottom DO significantly at the end of simulation. In fact we are comparing different layers during this time, epilimnion DO in the stronger winds cases and hypolimnion DO in the weaker cases, though they are all

bottom cells. Again the hypolimnion at station 452 is not hypoxic due to the much thicker hypolimnion.

From the two sets of experiments above, it is found that three factors related to lake hydrodynamics have strong influences on the hypolimnetic hypoxia: water temperature, stratification duration, and hypolimnion thickness. To be specific, warmer water temperature increases the DO consumption rate and reduces the maximum possible DO levels, longer stratification extends the consumption duration, and a thin hypolimnion leads to a faster approach to hypoxia. In a future climatic scenario of a warm and quiescent year, if we consider the effects of meteorological forcing changes only and ignore the biochemical impacts, the hypolimnetic hypoxia in the central basin will likely become more severe. Warmer air temperature and weaker wind both extend the stratification significantly. For instance at station 1231 in the western side of the central basin (Fig. 4.20), weaker winds leads to a severe hypolimnetic hypoxia in the fall due to the extension of the stratification period. Adding the effects of warmer air temperature (Fig. 4.18), which extend the stratification duration and warm up the hypolimnion, the hypolimnetic hypoxia situation is expected to become worse and last longer.

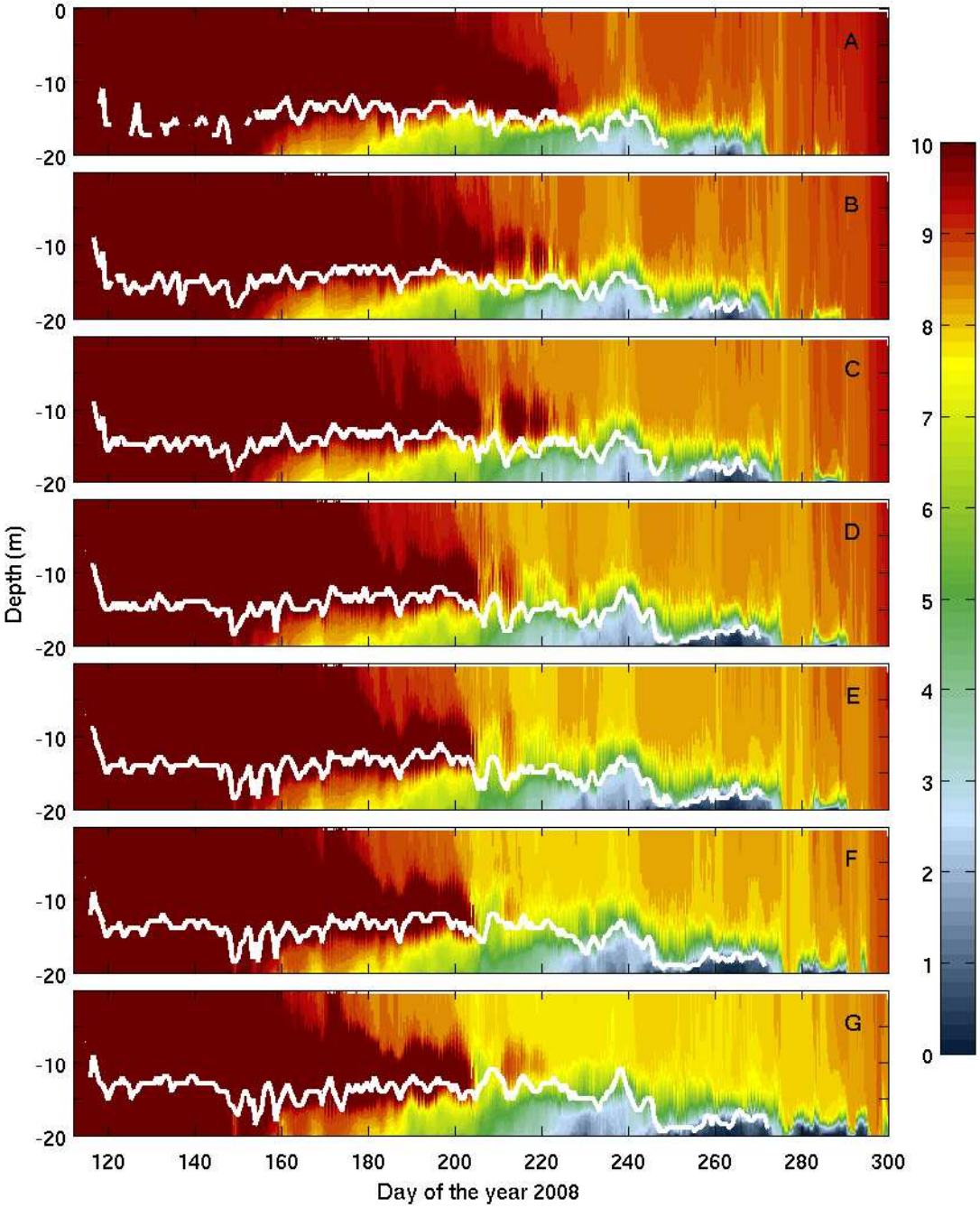

Figure 4.18: DO (mg L^{-1}) contours at station 1231 (western central basin) with the air temperature changed by: (A) -4°C, (B) -2°C, (C) -1°C, (D) 0 (base case), (E) $+1$°C, (F) $+2$°C, and (G) $+4$°C. The white lines are calculated hypolimnion boundaries.

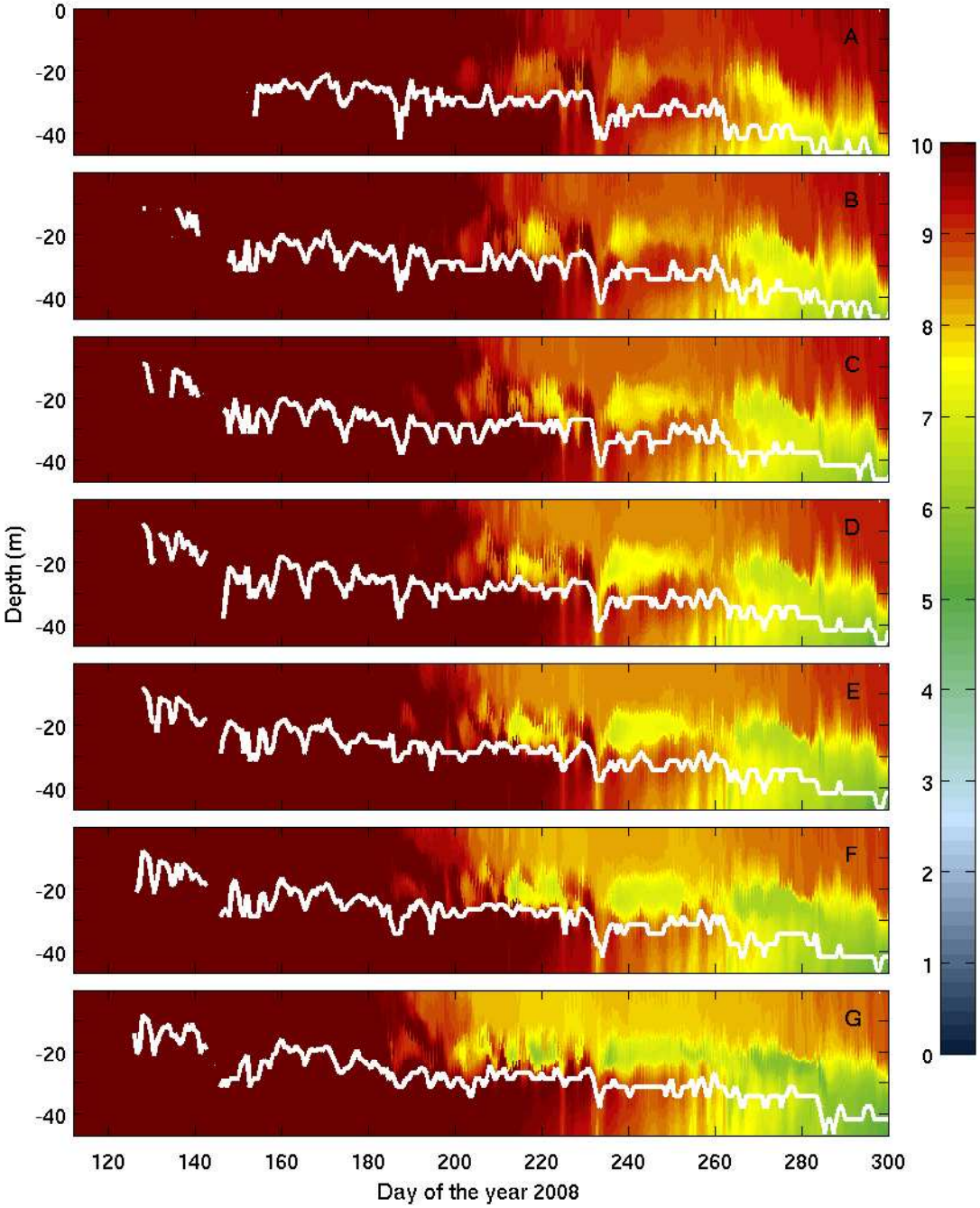

Figure 4.19: DO (mg L^{-1}) contours at station 452 (eastern basin) with the air temperature changed by: (A) -4°C, (B) -2°C, (C) -1°C, (D) 0 (base case), (E) $+1$°C, (F) $+2$°C, and (G) $+4$°C. The white lines are calculated hypolimnion boundaries.

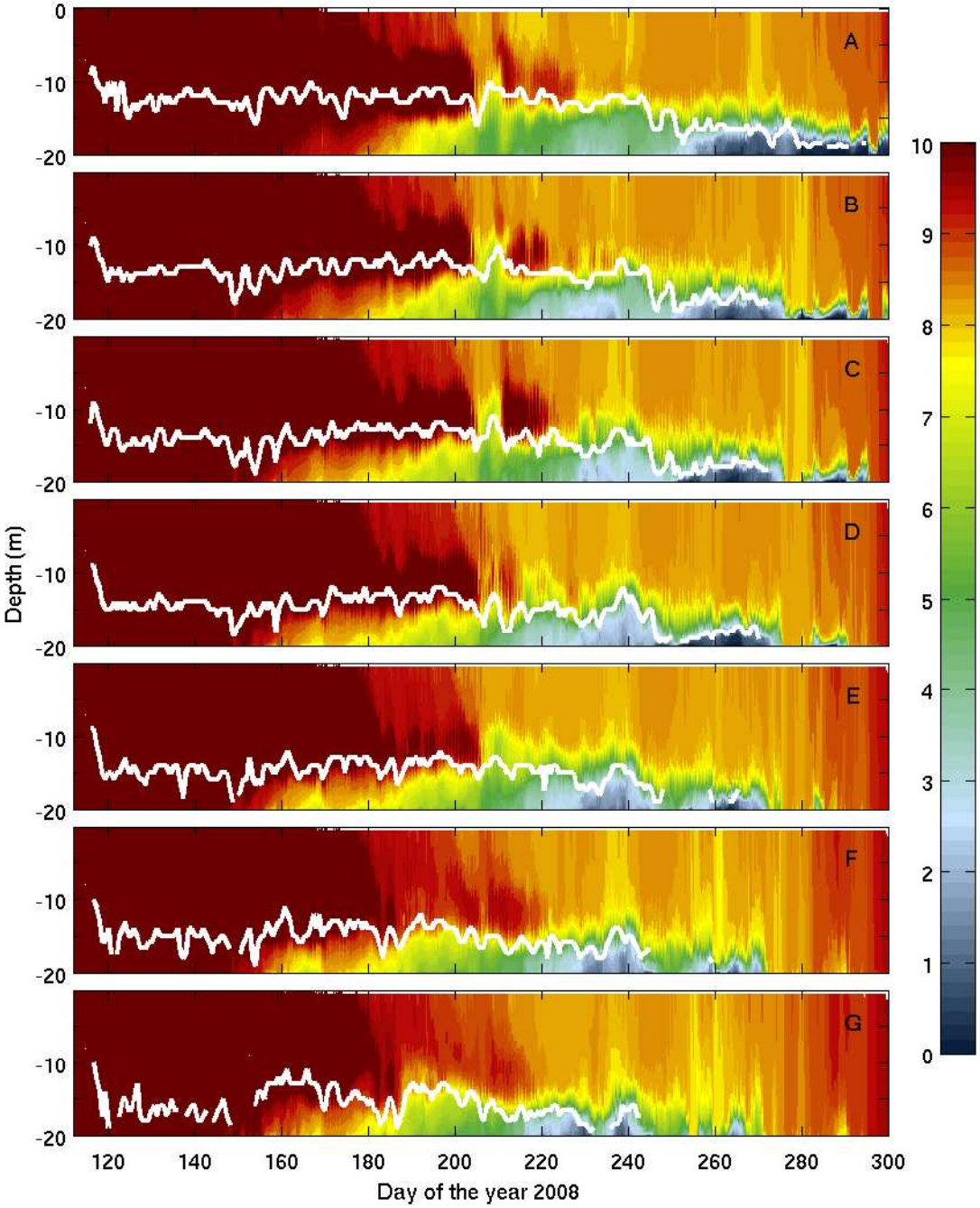

Figure 4.20: DO (mg L^{-1}) contours at station 1231 (western central basin) with the wind speed changed by: (A) −20%, (B) −10%, (C) −5%, (D) 0 (base case), (E) +5%, (F) +10%, and (G) +20%. The white lines are calculated hypolimnion boundaries.

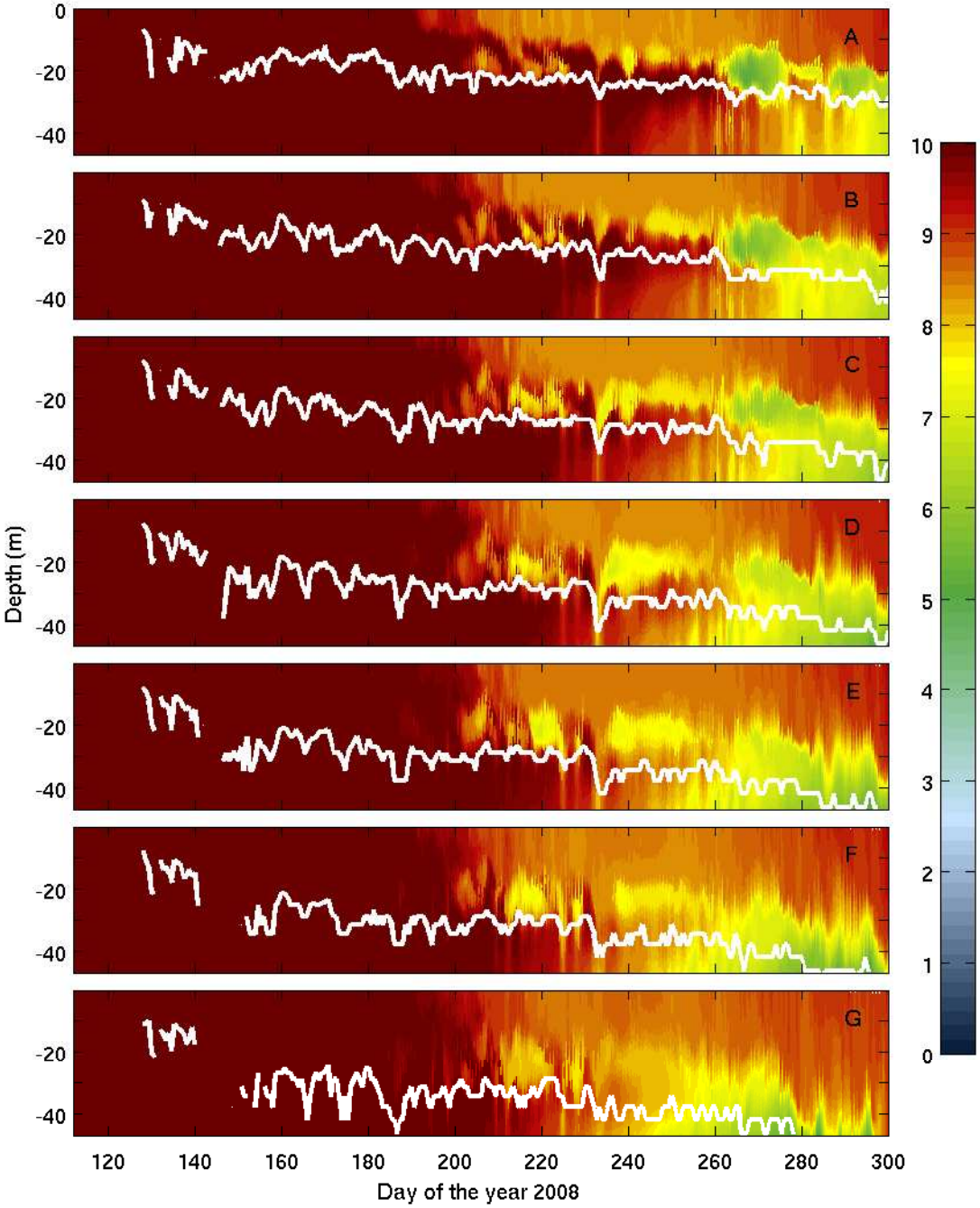

Figure 4.21: DO (mg L^{-1}) contours at station 452 (eastern basin) with the wind speed changed by: (A) −20%, (B) −10%, (C) −5%, (D) 0 (base case), (E) +5%, (F) +10%, and (G) +20%. The white lines are calculated hypolimnion boundaries.

Chapter 5

Internal Kelvin Wave Propagation Around a Peninsula

In this chapter high resolution numerical simulations are utilized to investigate an aspect of small-scale lake dynamics, namely eddies. By taking advantage of the parallel computing capability of the MITgcm, the grid resolution can be easily increased by a factor of 10 from 2 km to 200 m, and as high as 50 m in idealized experiments with only a reasonable increase in computational effort. With the finer resolution more small-scale processes that cannot be resolved in the coarse resolution used in the previous chapters can be explored, for instance eddies with diameters of a few kilometres. We begin in Section 5.1 by revisiting the classical problem of incompressible viscous flow past a circular cylinder by undertaking a set of numerical simulations using the MITgcm. Through comparisons with results in the literature it is shown that the MITgcm has the capability of simulating flow separation processes. The eddy dynamics generated by internal Kelvin wave propagation around a peninsula are then investigated in an idealized lake in Section 5.2 and in Lake Erie in Section 5.3.

5.1 Flow past a circular cylinder experiments using the MITgcm

The classical problem of incompressible viscous flow past a circular cylinder has been widely studied analytically (Goldstein and Rosenhead 1936; Collins and Dennis 1973), experimentally (Tritton 1959; Coutanceau and Defaye 1991), and numerically (Tuann and Olson 1978; Kalita and Ray 2009). In this section a series of flow past a circular cylinder experiments are conducted using the MITgcm to test the model's ability to accurately simulate flow separation and the corresponding eddy dynamics. We undertake numerical experiments similar to those in Kalita and Ray (2009) (KR afterwards) and test the model performance by comparing with their results.

Table 5.1: Flow past a circular cylinder using the MITgcm setup

Variables and parameters	Values
Physical dimensions	$L = 50$ m, $W = 15$ m, $H = 0.5$ m
Radius of the cylinder	$R = 1$ m
Far field velocity	$U_\infty = 1$ m s^{-1}
Vertical grid number	$nz = 1$
Horizontal grid size	$dx = dy = 0.05$ (when Re = 200) m or 0.025 m (when Re = 1000)
Horizontal resolution	$nx \times ny = 1000 \times 300$ (when Re = 200) or 2000×600 (when Re = 1000)
Time step	dt=0.01 s or 0.001 s
Vertical viscosity	$A_z = 1 \times 10^{-4}$ m^2 s^{-1}
Horizontal viscosity	$A_h = (U_\infty D)/\text{Re}$
Advection scheme	33 (3$^{\text{rd}}$ order direct space time with flux limiting)
ridgidLid	Yes

The computational domain has dimensions of 50 m $\times$ 15 m $\times$ 0.5 m, and the radius of the circular cylinder is 1 m. More details about the model set up are listed in Table 5.1. The "obcs" package (open boundary condition) in the MITgcm is used to implement the open flow. In "OBCS_OPTIONS.h" the east and west sides are set to be open boundaries.

```
C OBCS_OPTIONS.h
#undef ALLOW_OBCS_NORTH
#undef ALLOW_OBCS_SOUTH
#define ALLOW_OBCS_EAST
#define ALLOW_OBCS_WEST
```

"obcs_calc.F" is modified to specify the flow

```
INTEGER zu
zu = 1.0
#ifdef ALLOW_OBCS_EAST
            IF (I_obc.ne.0) THEN
              OBEu(J,K,bi,bj)=zu
              OBEv(J,K,bi,bj)=0.
...
#endif /* ALLOW_OBCS_EAST */
#ifdef ALLOW_OBCS_WEST
            IF (I_obc.ne.0) THEN
              OBWu(J,K,bi,bj)=zu
              OBWv(J,K,bi,bj)=0.
...
#endif /* ALLOW_OBCS_WEST */
```

When using a $1000 \times 300 \times 1$ resolution, the numerical model takes about 12 hours to finish 50,000 steps with 30 1.6 GHz Intel Itanium processors. The MITgcm generally does a satisfactory job simulating the vortex shedding. To avoid a cumbersome thesis, here only two cases are presented with the Reynolds number (Re) of 200 and 1000. The Reynolds number is a dimensionless number that gives a measure of the ratio of inertia forces to viscous forces,

$$\mathrm{Re} = \frac{UL}{\nu}, \tag{5.1}$$

where U is the characteristic velocity, L is the characteristic length, and ν is the kinematic viscosity of the fluid (Kundu and Cohen 2004).

From KR when Re = 200 it is expected that the flow becomes periodic and develops vortex shedding represented by the von Kármán vortex street. Figure 5.1 plots the streamlines at several times. In the initial stage (Fig. 5.1(A-C)) the vorticity starts growing behind the cylinder, but the flow is still stable. At $t = 229$ s (Fig. 5.1(D)) the flow

becomes unstable and begins to develop vortex shedding. At later times vortex shedding occurs continuously in a periodic nature (Fig. 5.1(E-H)). Figure 5.2 attaches the original figure in KR, and comparing the two sets of results it can be seen that the MITgcm does a relatively good job simulating vortex shedding. One of the noticeable differences is the time when the flow becomes unstable. In the MITgcm the vortex has been generated at $t = 229$ s (Fig. 5.1(D)); however, in KR the flow is still stable but about to generate vortices (Fig. 5.2(d)). In addition the size of the initial eddy is smaller comparing with KR's results. When Re = 200, the vortex shedding has a periodic nature. Figure 5.3 plots the vorticity contours at t_0, $t_0 + T/2$, $t_0 + T$, $t_0 + 2T$, $t_0 + 3T$, and $t_0 + 4T$, where $t_0 = 262$ s and $T = 4$ s, from which we can clearly see the periodicity in the vortex shedding. Figure 5.4 shows the similar contour plots from KR, and the results from the MITgcm agree well. The periodic nature of the flow can also be seen in the streamline plots in Fig. 5.5.

When Re = 1000 the flow eventually becomes three-dimensional and turbulent (KR). Figure 5.7 shows the vorticity in the early stages of the flow evolution, before three-dimensionalization would occur in a 3D simulation. Figure 5.8 shows results from KR. Comparing the two sets of results it can be seen that the MITgcm also does a good job simulating the flow in this range of Re. Another feature in this Re range is that the flow has the so called α phenomena (Bouard and Coutanceau 1980). In Fig. 5.6 the streamlines at $t = 3.5$ s are plotted. In addition to the primary vortex, there are two pairs of secondary vortices forming next to the separation points. The MITgcm results successfully capture that and agree well with KR in Fig. 5.6.

In summary, by reproducing the flow past a circular cylinder experiments from KR and comparing with their results, it has been demonstrated that the MITgcm has the ability to duplicate the general features of flow separation and eddy formation, well-enough to make the following Kelvin wave simulations credible. The MITgcm correctly simulates the vortex shedding and the secondary vortices features in higher Re cases. Therefore it is expected to provide innovative and trustworthy results for the Kelvin waves studies in the following sections.

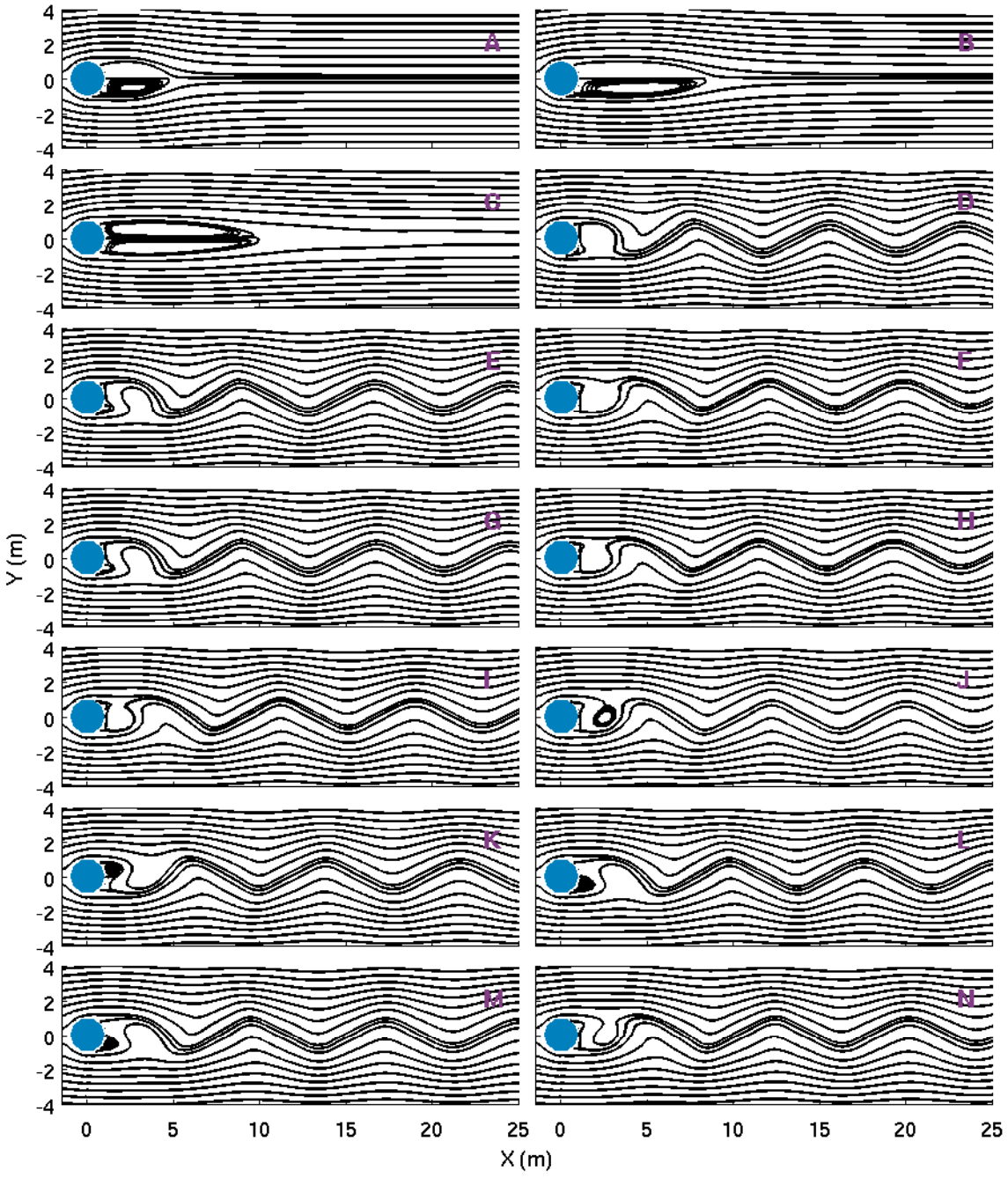

Figure 5.1: MITgcm simulations: streamlines when Re = 200 at (A) $t = 12$, (B) 34, (C) 100, (D) 229, (E) 280, (F) 300, (G) 305, (H) 316, (I) 324, (J) 350, (K) 360, (L) 364, (M) 372, and (N) 400 s.

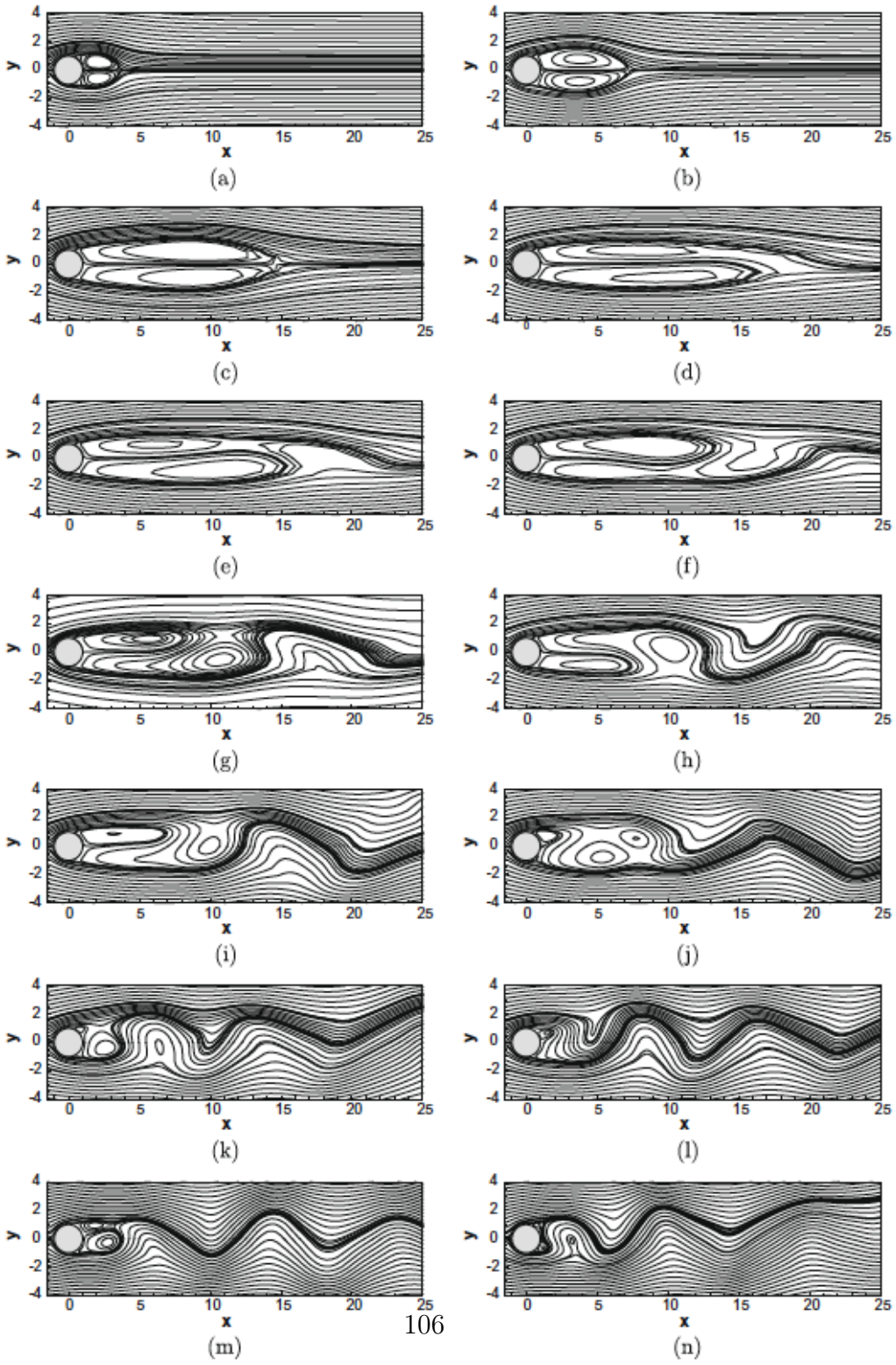

Fig. 12. Streamlines at $Re = 200$ for flow past a circular cylinder at: (a) $t = 12$, (b) 34, (c) 100, (d) 229, (e) 280 (f) 300, (g) 305, (h) 316, (i) 324, (j) 350, (k) 360, (l) 364, (m) 372 and (n) 400.

Figure 5.2: Streamlines when Re = 200 from KR.

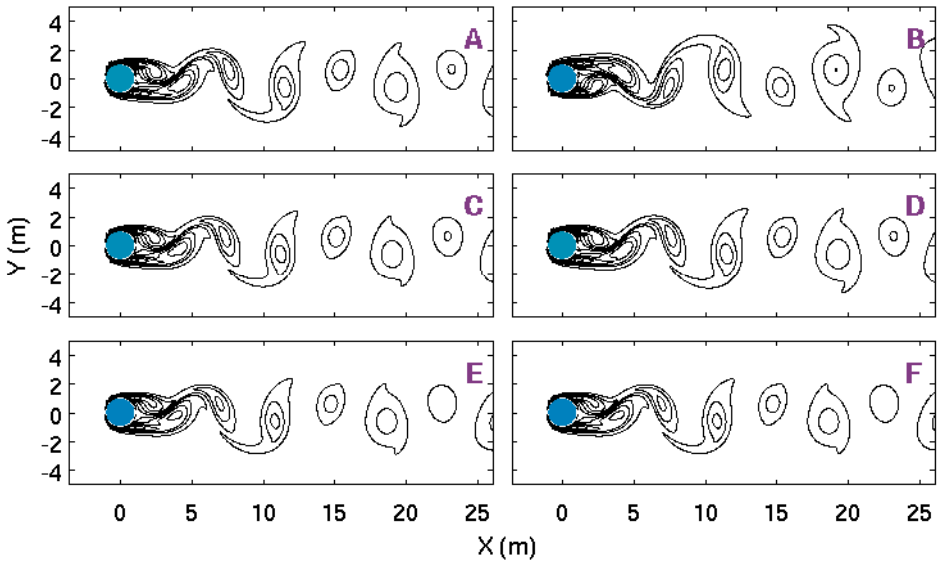

Figure 5.3: MITgcm simulations: vorticity contours when Re = 200 at (A) $t = t_0$, (B) $t_0 + T/2$, (C) $t_0 + T$, (D) $t_0 + 2T$, (E) $t_0 + 3T$, and (F) $t_0 + 4T$. $t_0 = 262$ s and $T = 4$ s.

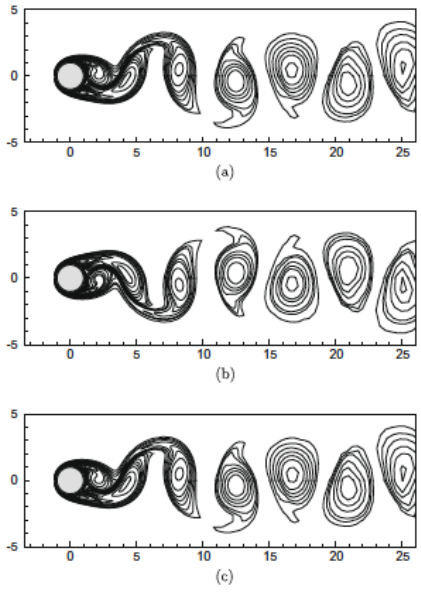

Fig. 14. The vorticity contours depicting the wake behind three successive instants of time over one vortex shedding period for $Re = 200$. (a) $t = t_0$, (b) $t = t_0 + \frac{T}{2}$ and (c) $t = t_0 + T$.

Figure 5.4: Vorticity contours when Re = 200 from KR.

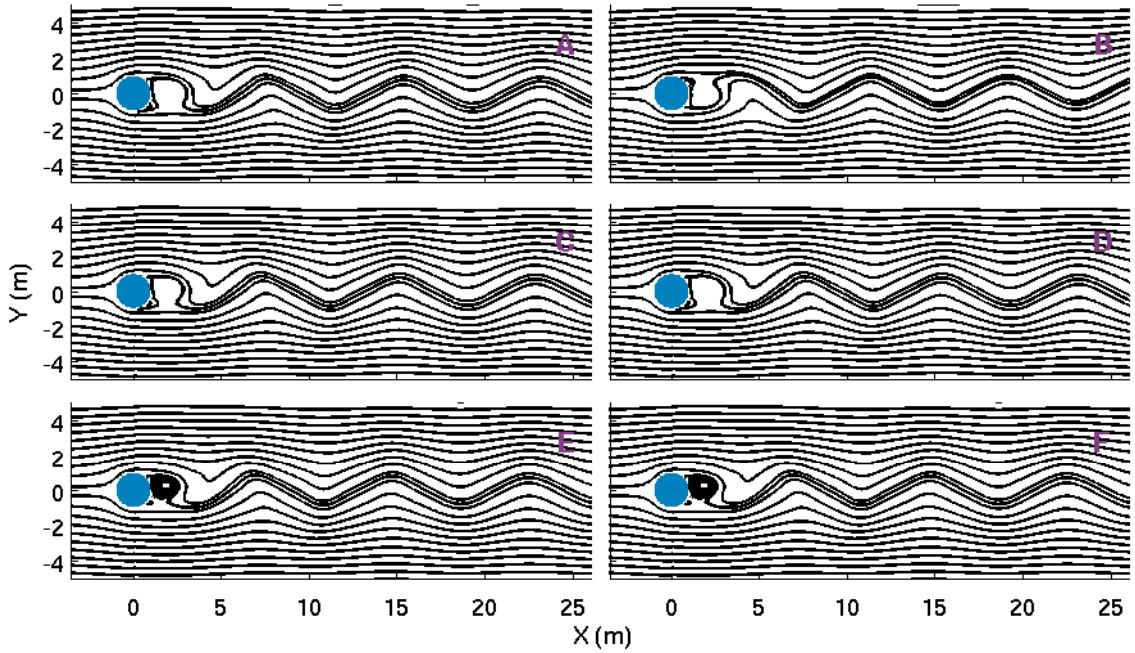

Figure 5.5: MITgcm simulations: streamlines when Re = 200 at (A) $t = t_0$, (B) $t_0 + T/2$, (C) $t_0 + T$, (D) $t_0 + 2T$, (E) $t_0 + 3T$, and (F) $t_0 + 4T$, where $t_0 = 262$ s and $T = 4$ s.

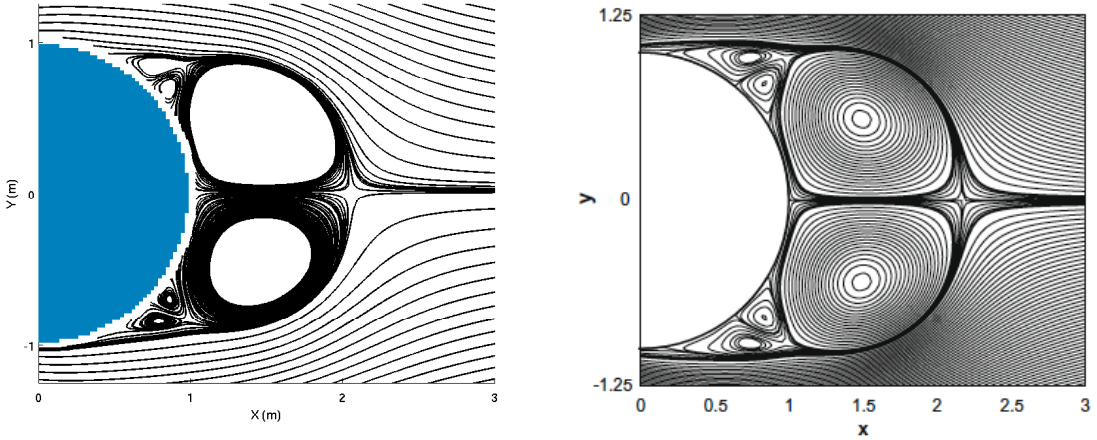

Figure 5.6: Streamlines when Re = 1000 at $t = 3.5$ s (left: the MITgcm, right: from KR).

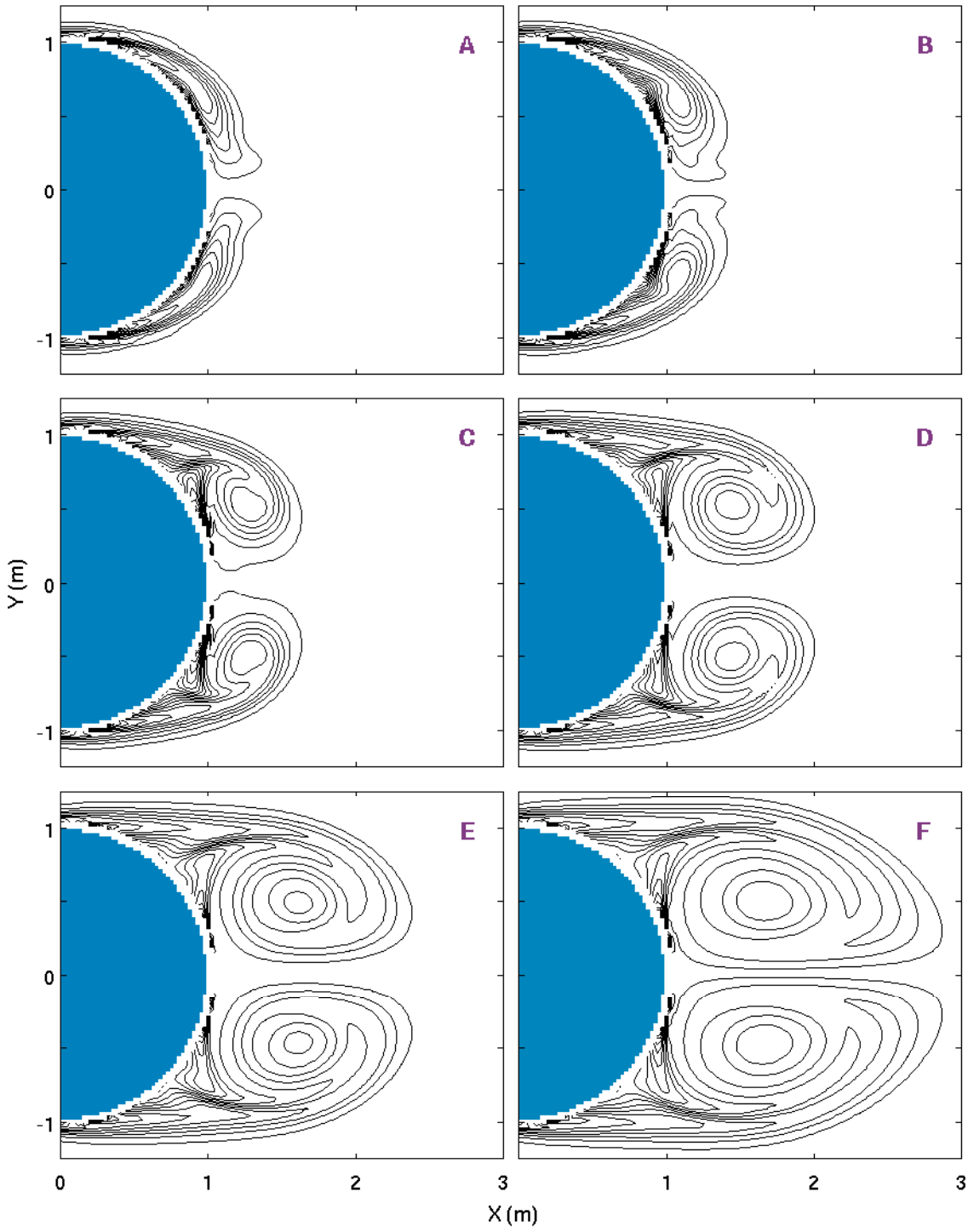

Figure 5.7: MITgcm simulations: vorticity contours when Re = 1000 at (A) $t = 1.25$, (B) 1.75, (C) 2.50, (D) 3.50, (E) 4.50, and (F) 6.00 s.

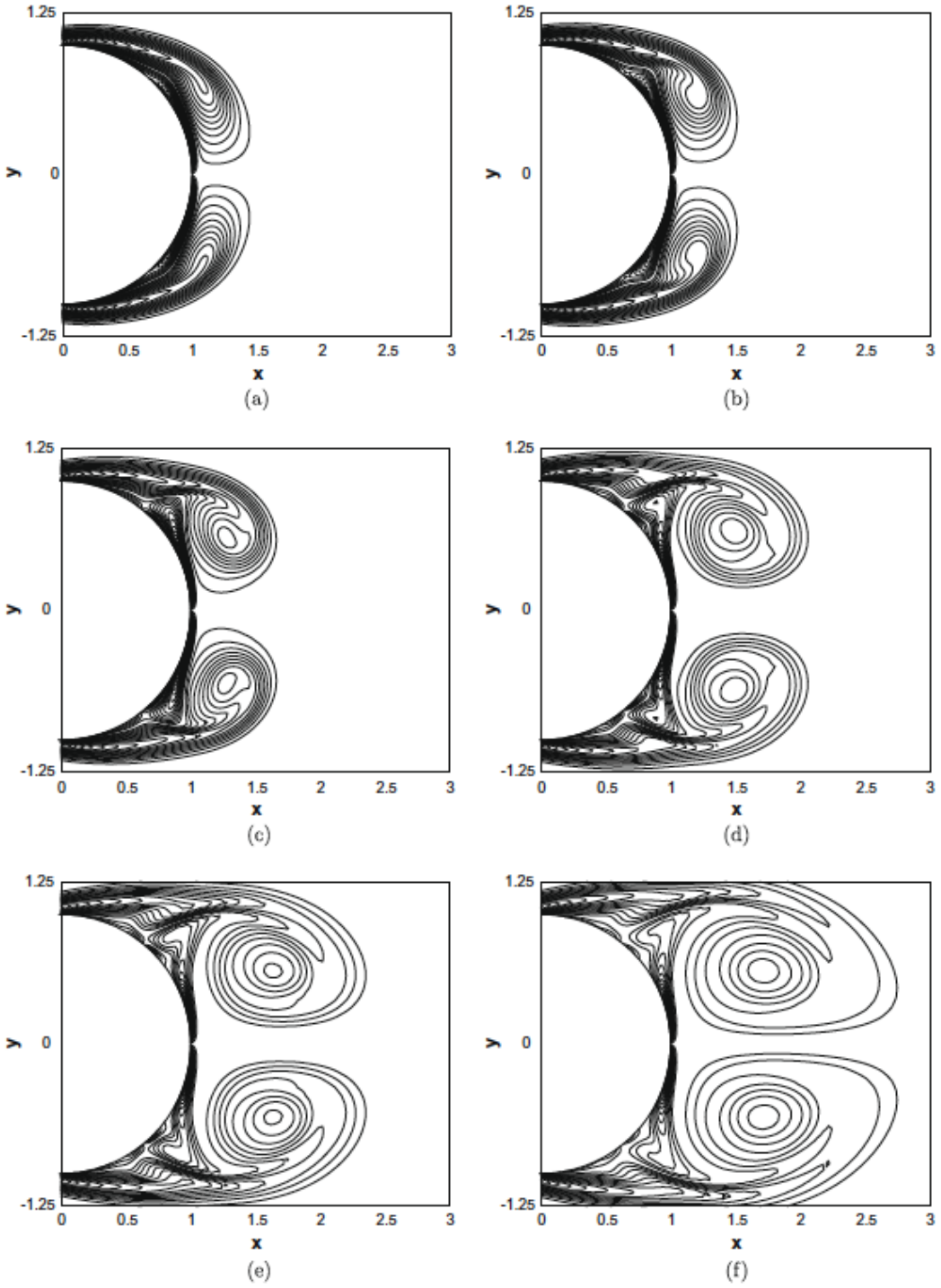

Fig. 24. Vorticity contours for $Re = 1000$ at (a) $t = 1.25$, (b) $t = 1.75$, (c) $t = 2.50$, (d) $t = 3.50$, (e) $t = 4.50$ and (f) $t = 6.00$.

Figure 5.8: Vorticity contours when Re = 1000 from KR.

5.2 Internal Kelvin wave propagation around a Gaussian peninsula in a rectangular lake

In the previous section it has been shown that the MITgcm is capable of correctly simulating the general features of vortex shedding associated with the flow past a circular cylinder. This section will investigate internal Kelvin wave propagation around a Gaussian peninsula in an idealized rectangular lake and the resulting eddy dynamics.

5.2.1 Numerical experiment design

The Gaussian peninsula

The propagation of an internal Kelvin wave generated by releasing a tilted thermocline is investigated in an idealized lake of length $L = 160$ km, width $W = 40$ km, and depth $H = 15$ m, around a narrow peninsula similar in size to Point Pelee is investigated first. The peninsula has the form of a Gaussian function:

$$G(x) = W - L_p e^{\frac{-(x-x_0)^2}{\sigma^2}}, \tag{5.2}$$

where $x_0 = 40$ km specifies the peninsula centre on the x axis. The length and width of the peninsula will be varied in later simulations to investigate the sensitivities of the eddy forming dynamics. The peninsula length is L_p, and the default value is 15 km, which is 3/8 of the lake width. Different L_p values will be used in later simulations as shown in Fig. 5.9(A). The width W_p is characterized by the full width at half maximum (FWHM) of the Gaussian function (Fig. 5.10)

$$W_p = 2\sqrt{\ln 2}\sigma, \tag{5.3}$$

then

$$\sigma = \frac{W_p}{2\sqrt{\ln 2}}. \tag{5.4}$$

The default value is $W_p = 4$ km, and later different values will be investigated (Fig. 5.9(B)).

The slopes of the peninsula at certain locations may be an important factor affecting eddy dynamics. Differentiating the Gaussian function in (5.2) gives

$$G'(x) = -L_p e^{\frac{-(x-x_0)^2}{\sigma^2}} \Big(- \frac{2(x-x_0)}{\sigma^2} \Big). \tag{5.5}$$

We choose to compare the slope at the right half width (x_2 in Fig. 5.10, and notice that the Gaussian point is reflected and shifted by the y-axis). We know $x_2 - x_0 = W_p/2$, then the slope at x_2 is

$$m = G'(x_2) = \frac{L_p W_p}{\sigma^2} e^{-\frac{W_p^2}{4\sigma^2}}. \tag{5.6}$$

In addition, the radius of curvature R_c of peninsula tip is calculated through

$$R_c|_{x=x_0} = \Big| \frac{[1+G'(x)]^{3/2}}{G''(x)} \Big|_{x=x_0} = \frac{W_p^2}{8 \ln 2 \; L_p}. \tag{5.7}$$

Initial temperature field

The temperature field is initialized with a partially tilted metalimnion,

$$T = T_b + \frac{T_s - T_b}{2} \Big(1 + \tanh \big(\frac{z - z_0 - \alpha y}{d} \big) \Big), \tag{5.8}$$

where $T_s = 25°$C is the surface temperature, $T_b = 10°$C is the lake bottom temperature, $d = 0.6$ m is the thickness of the metalimnion, and $z_0 = -12$ m and $\alpha = 2 \times 10^{-4}$ specify the tilting. The metalimnion is partially tilted in the northern part of the lake on the right side of the Gaussian peninsula. The horizontal temperature field at $z = -4.7$ m is plotted in Fig. 5.11 and the vertical temperature field at $x = 100$ km in Fig. 5.12.

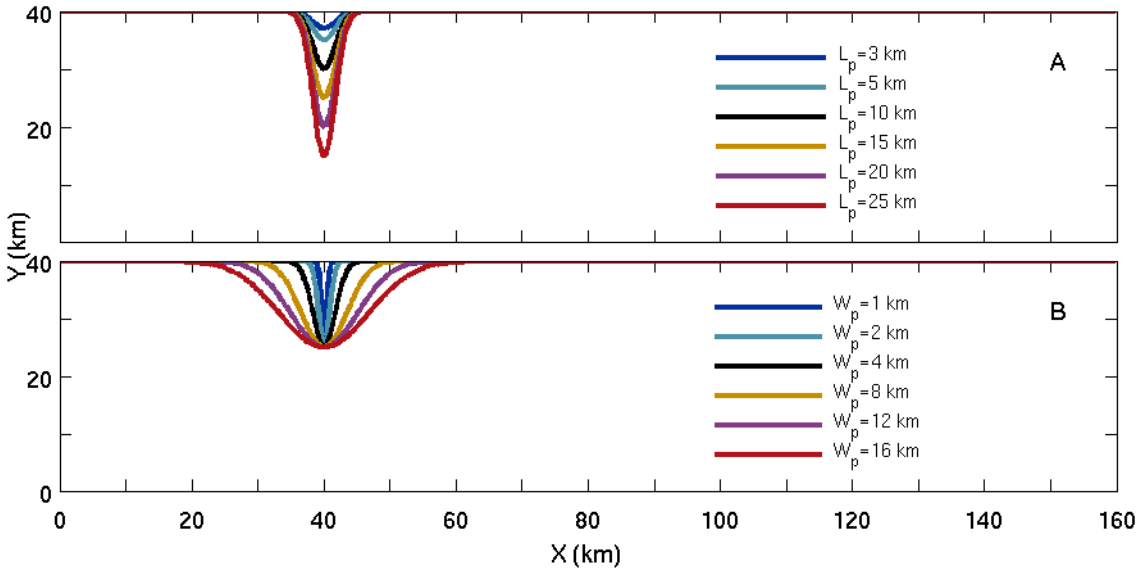

Figure 5.9: The Gaussian peninsula with: (A) $W_p = 4$ km and L_p varies and (B) $L_p = 15$ km and W_p varies.

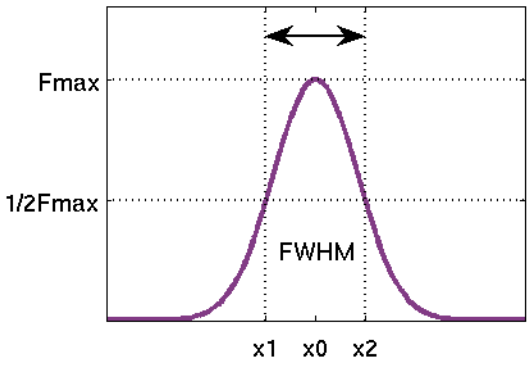

Figure 5.10: Full width at half maximum of a Gaussian function.

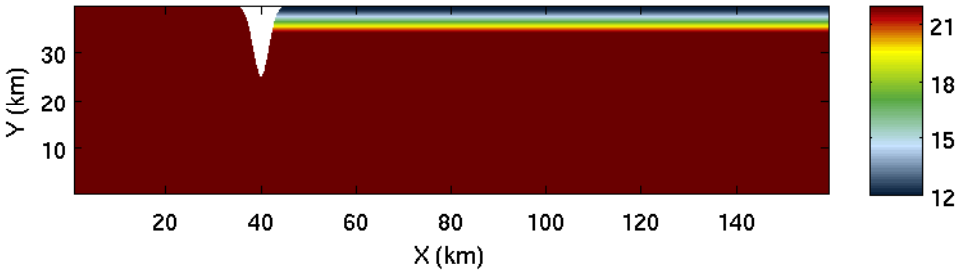

Figure 5.11: The horizontal initial temperature profile at $z = -4.7$ m

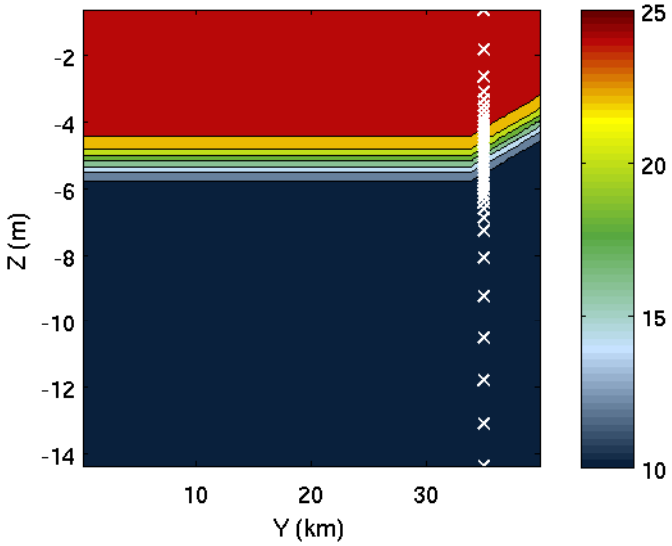

Figure 5.12: The vertical initial temperature profile on the tilted side, and the white x's denote the vertical grid spacing.

Numerical model set up

The numerical simulations are conducted using the MITgcm on the high performance computing facilities SciNet and SHARCNET (Shared Hierarchical Academic Research Computing Network). SciNet and SHARCNET are two of seven High Performance Computing (HPC) consortia in Canada that operates under the umbrella of Compute/Calcul Canada.

We set $L = 160$ km, $W = 40$ km, $nx = 800$, and $ny = 200$. In the x direction (east-west) uneven grid spacing is used, where small dx's are used near the point (MATLAB codes courtesy of Michael Dunphy, Fig. 5.13(A)). In the y direction (north-south) a constant $dy = 200$ m is set. For the peninsula lengths selected this provides adequate resolution to resolve the dynamics we are interested in this direction. In the vertical direction $H = 15$ m and $nz = 40$. Uneven grids are applied as well, with more grid points in the metalimnion (see Fig. 5.12 and 5.13(B)).

The proposed experiment has a resolution of $800 \times 200 \times 40$, and 64 processors on SciNet are used. In the default case with $dt = 120$ s, a 10-day run takes about 30 minutes to finish with the hydrostatic setting and 5-9 time longer when the non-hydrostatic setup is turned on.

Rossby radius of deformation

The internal Rossby radius of deformation is defined as,

$$R = \frac{\sqrt{g' H_1 H_2/(H1 + H2)}}{f_0}, \tag{5.9}$$

where g' is the reduced gravity, H_1, H_2 is the upper and lower layer depth, and f_0 is the Coriolis parameter (Gill 1982). g' is given by

$$g' = g\frac{\rho_2 - \rho_1}{\rho_0}, \tag{5.10}$$

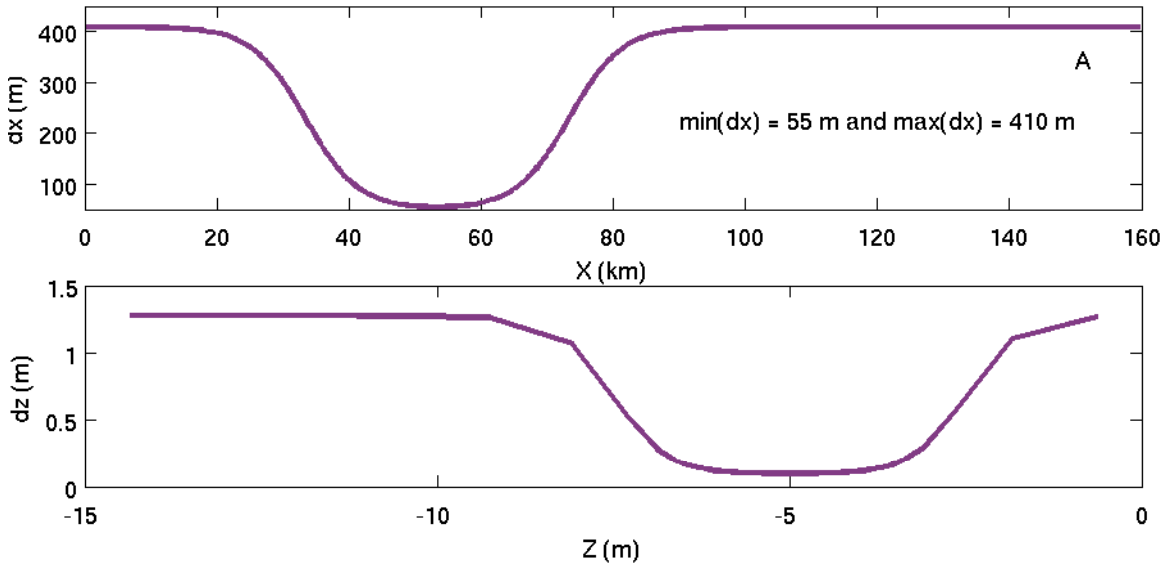

Figure 5.13: Uneven grid spacing in: (A) x direction and (B) z direction.

where ρ_1 and ρ_2 are the densities of the upper and lower layers, ρ_0 is the reference density, and g is the gravity of Earth. The simulation is initialized by water temperature instead of density, so an equation of state (EOS) is required to calculate R. A simple linear EOS is used

$$\rho = \rho_0\big(1 - \alpha_T(T - T_0)\big), \tag{5.11}$$

where ρ and T are the density and temperature, ρ_0 and T_0 are the reference density and temperature, and α_T is the thermal expansion coefficient. Hence

$$g' = g\alpha_T(T_1 - T_2), \tag{5.12}$$

and then

$$R = \frac{\sqrt{g\alpha_T(T_1 - T_2)H_1H_2/(H1 + H2)}}{f_0}. \tag{5.13}$$

The latitude of Lake Erie is about 42° N, so the Coriolis parameter is given by

$$f_0 = 2\Omega\sin(\phi) \approx 9.7587 \times 10^{-5} \approx 1 \times 10^{-4}\mathrm{s}^{-1}. \tag{5.14}$$

In addition, $g = 9.81$ m s^{-2}, $\alpha_T = 2 \times 10^{-4}$ (°C)$^{-1}$, $T_1 = 25$°C, $T_2 = 10$°C, $H_1 = 5$ m and $H_2 = 10$ m, and it gives $R = 3.1$ km.

5.2.2 Results and discussion

The numerical set up using the MITgcm is listed in Table 5.2 and in Appendix B.2. The "non-hydrostatic" switch is turned off for the 200 m resolution experiments. The smallest horizontal grid size is 50 m and the lake depth is 15 m. The ratio of lake depth to the horizontal grid size is 3/10, and this is still likely too small to accurately simulate non-hydrostatic effects.

Table 5.2: Idealized internal Kelvin wave simulations setup

Variables and parameters	Values
Physical dimensions	$L = 160$ km, $W = 40$ km, $H = 15$ m
Grid resolution	$nx \times ny \times nz = 800 \times 200 \times 40$
Time step	dt=120 s
Horizontal viscosity	$A_h = 0.25$ m^2 s^{-1}
Vertical viscosity	$A_z = 1 \times 10^{-4}$ m^2 s^{-1}
Coriolis parameter	$f_0 = 10^{-4}$ s^{-1}
Linear EOS thermal expansion coefficient	$T_\alpha = 2 \times 10^{-4}$ °C^{-1}
Advection scheme	33 (3$^{\text{rd}}$ order direct space time with flux limiting)
Bottom boundary condition	no-slip
Lateral boundary condition	no-slip
staggerTimeStep	Yes
ridgidLid	Yes
nonHydrostatic	No

Effects of the horizontal eddy viscosity A_h

First the effects of the horizontal eddy viscosity A_h will be studied. Different values are tested in Table 5.3. The goal is to choose the smallest A_h possible (the largest Re) that gives results with low noise levels. Figure 5.14 plots the vertical component of the vorticity at $z = -4.7$ m on day 5 with different A_h's. Notice that in the plots vorticity with magnitudes less than 10^{-6} s^{-1} have been filtered out. When $A_h = 0.01$ and 0.1 m^2 s^{-1} (Fig. 5.14(A,B)), the results are quite noisy, so we have to increase A_h. When $A_h = 0.25$, 0.5, and 1.0 m^2 s^{-1} (Fig. 5.14(C-E)), the results are much cleaner, and the eddy is resolved

in all experiments. Last when A_h is increased to 10.0 m^2 s^{-1} (Fig. 5.14(F)), the flow is so viscous that no eddy is generated. In Fig. 5.15 the corresponding temperature fields are plotted. We can see that the cold wave front is propagating counterclockwise along the boundary. A blob of cold water is trapped on the right side of peninsula due to the generation of the eddy for A_h between 0.01 and 1.0 m^2 s^{-1} (Fig. 5.15(A-E)). However, when A_h becomes larger at 10.0 m^2 s^{-1} the wave front can pass through the peninsula smoothly without flow separation and eddy formation occurring (Fig. 5.15(F) and later time not shown here). Moreover in the velocity field figure all cases except $A_h = 10$ m^2 s^{-1} clearly exhibit the eddy (Fig. 5.16). From the sensitivity test above, $A_h = 0.25$ m^2 s^{-1} seems to be the best choice to use for later investigations of the eddy dynamics.

Figures 5.17 and 5.18 present the vorticity and temperature evolution for the case with $A_h = 0.25$ m^2 s^{-1}. After the initial tilt is released, the cold wave front starts propagating counterclockwise along the boundary. After 10 hours (Fig. 5.17(A) and 5.18(A)) the wave front arrives at the right side of the peninsula. After 16 hours (Fig. 5.17(B) and 5.18(B)) it reaches the peninsula tip and a clockwise (cyclonic) eddy is being generated. After 2 days (Fig. 5.17(C) and 5.18(C)), the eddy still persists strongly. After 5 days (Fig. 5.17(D) and 5.18(D)) notice that the vorticity generated near the north-east corner arrives at the tip and is added to the existing eddy. As a result, the cyclonic eddy becomes larger and stronger. After 7 days (Fig. 5.17(E) and 5.18(E)), the main eddy is still developing, and a smaller anticyclonic eddy appears. Finally after 10 days (Fig. 5.17(F) and 5.18(F)) the main eddy detaches from the peninsula tip. In addition to the Kelvin waves, Poincaré waves have been generated as well, which are evident from the bands of vorticities south of the initial upwelling region extending into the middle of the lake (Fig. 5.17).

Table 5.3: Group 1: effects of the horizontal eddy viscosity A_h

Case number	A_h (m^2 s^{-1})	Re	Comments
G01C01	0.01	250	noisy
G01C02	0.1	25	noisy
G01C03	0.25	10	eddy appears (chosen to be the default value)
G01C04	0.5	5	eddy appears
G01C05	1.0	2.5	eddy appears
G01C06	10.0	0.25	no eddy

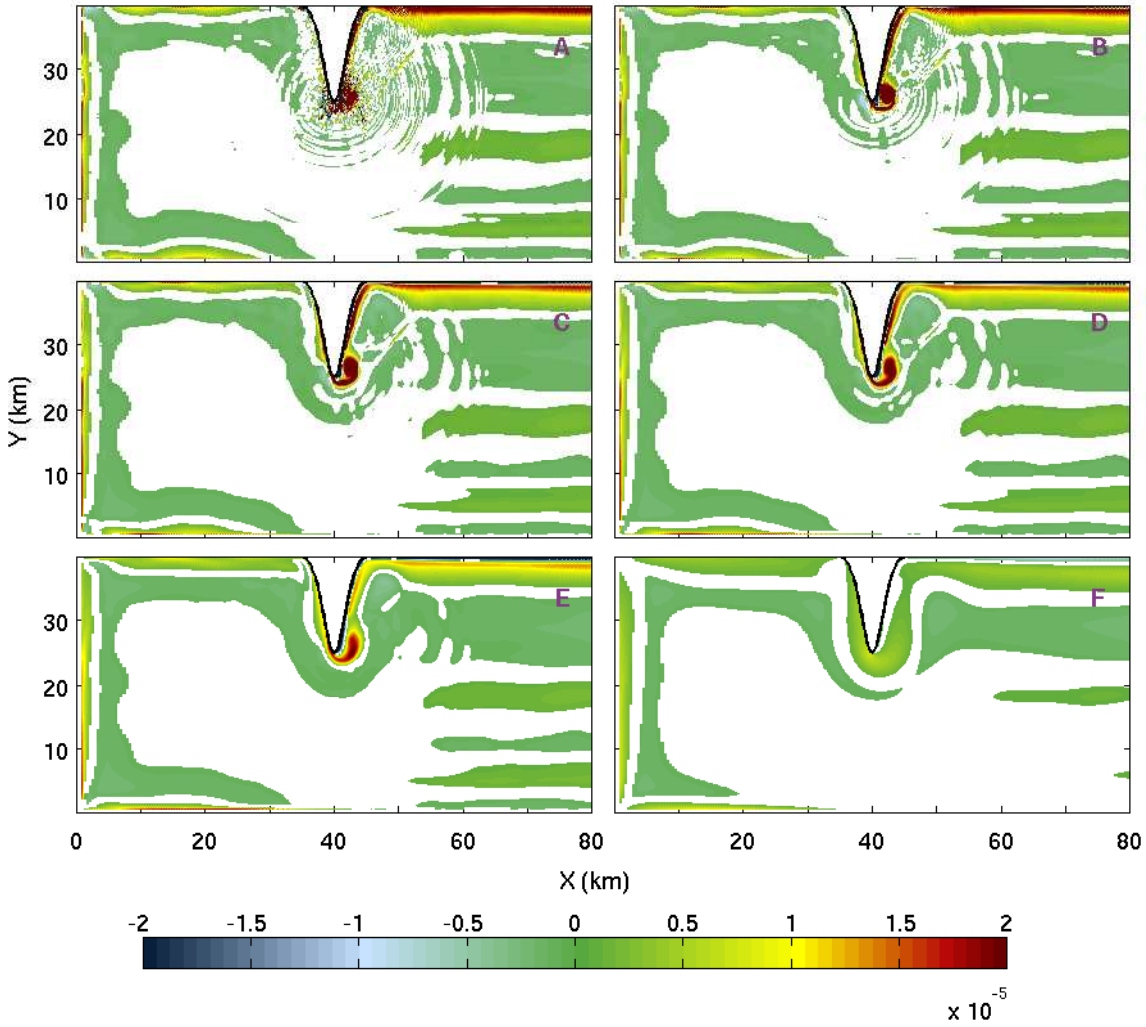

Figure 5.14: Vorticity at $z = -4.7$ m on day 5 with varying A_h's: (A) 0.01, (B) 0.1, (C) 0.25, (D) 0.5, (E) 1.0, and (F) 10.0 $\mathrm{m^2 s^{-1}}$.

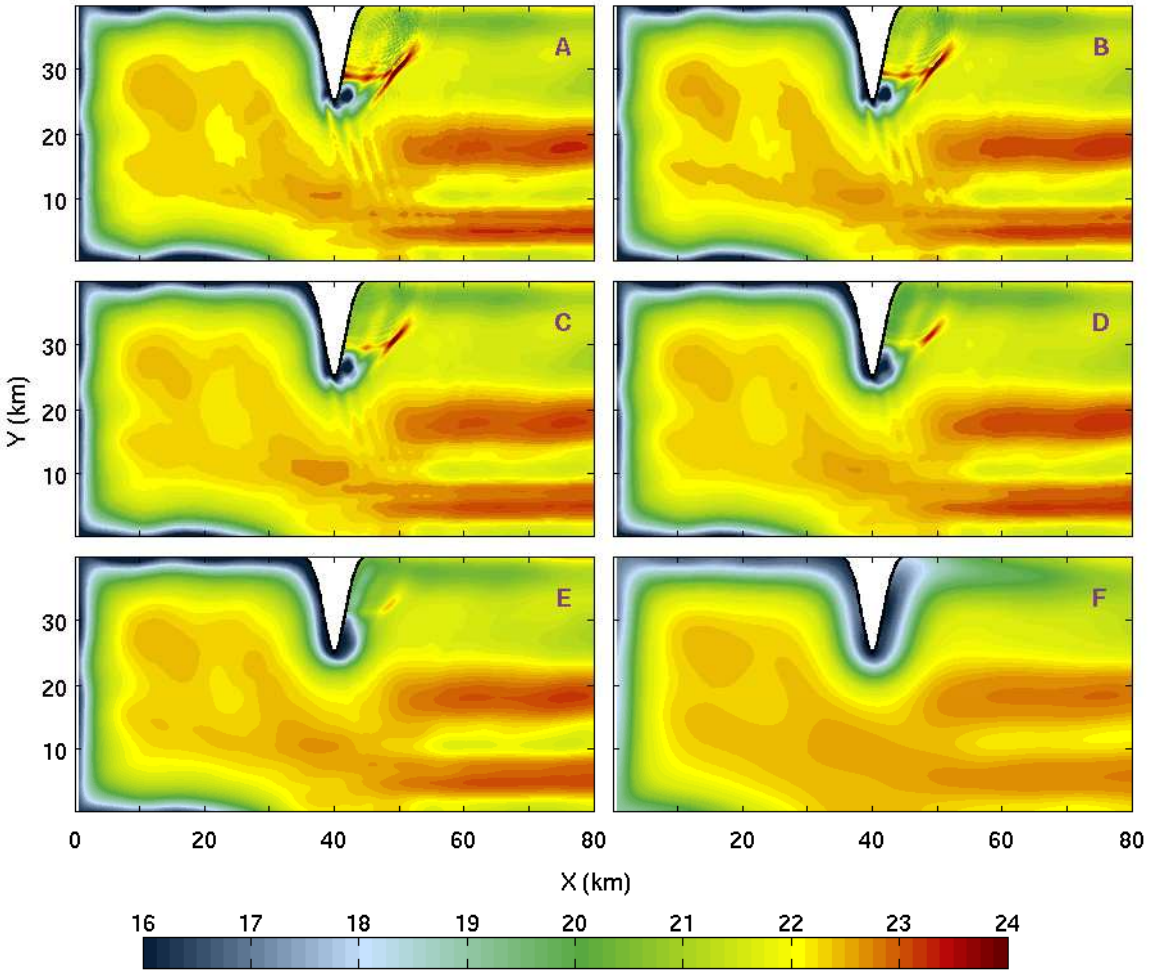

Figure 5.15: Temperature at $z = -4.7$ m on day 5 with varying A_h's: (A) 0.01, (B) 0.1, (C) 0.25, (D) 0.5, (E) 1.0, and (F) 10.0 $\mathrm{m^2 s^{-1}}$.

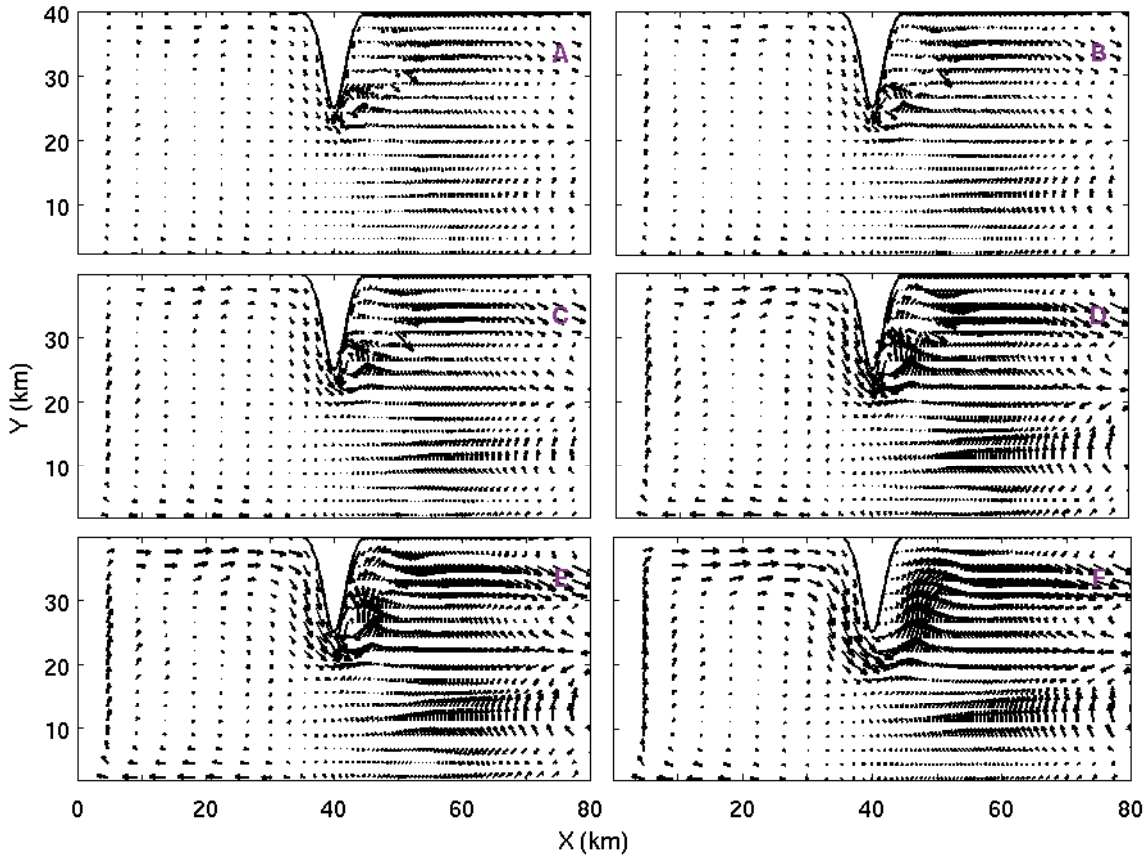

Figure 5.16: Velocity field at $z = -4.7$ m on day 5 with varying A_h's: (A) 0.01, (B) 0.1, (C) 0.25, (D) 0.5, (E) 1.0, and (F) 10.0 $\mathrm{m^2 s^{-1}}$.

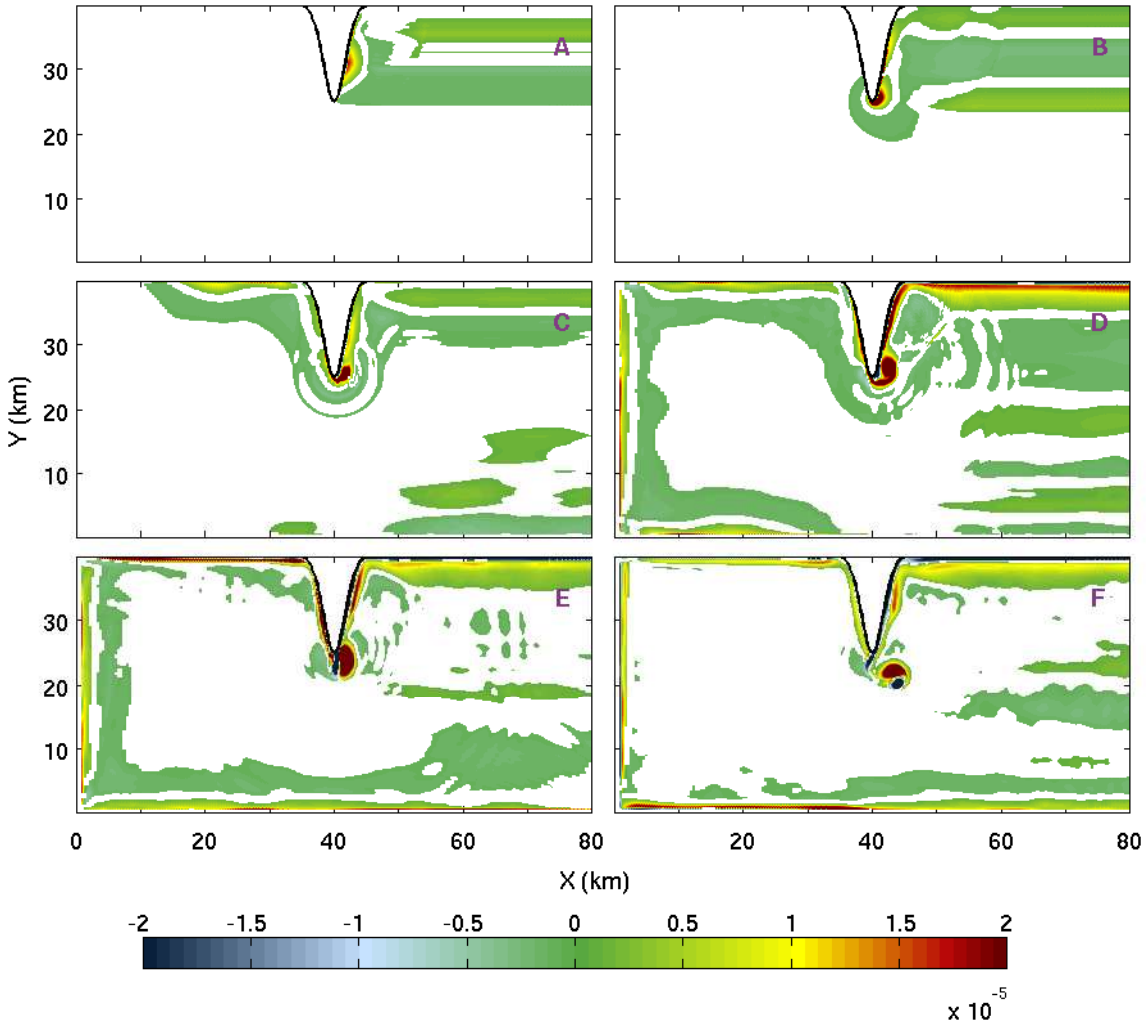

Figure 5.17: Vorticity evolution at $z = -4.7$ m with $A_h = 0.25$ m^{2}s^{-1} at (A) 10 hours, (B) 16 hours, (C) 2 days, (D) 5 days, (E) 7 days, and (F) 10 days.

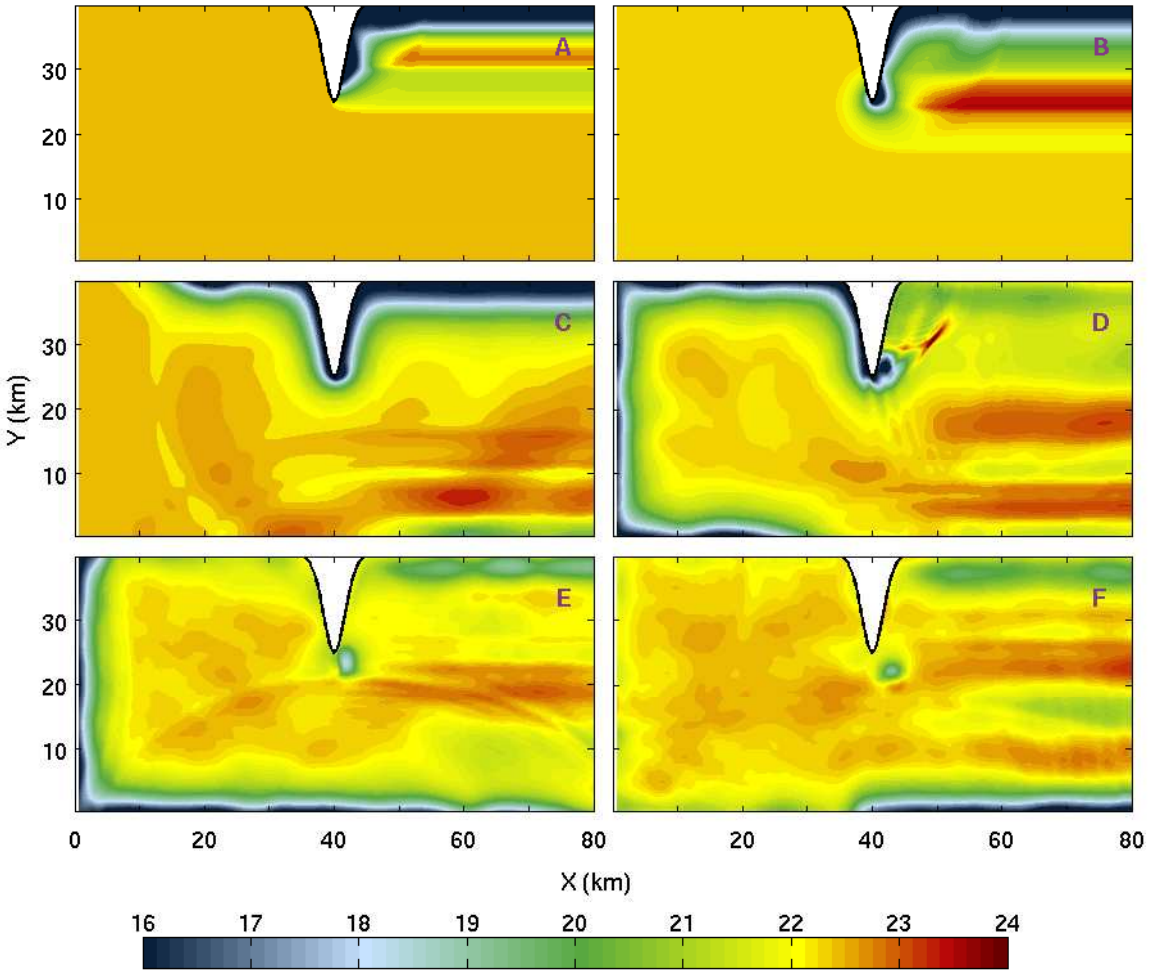

Figure 5.18: Temperature evolution at $z = -4.7$ m with $A_h = 0.25$ m^{2}s^{-1} at (A) 10 hours, (B) 16 hours, (C) 2 days, (D) 5 days, (E) 7 days, and (F) 10 days.

Effects of boundary conditions

Group 2 tests the effects of lateral boundary conditions. In the numerical experiments all the side walls are vertical, so the bottom boundary condition has very little effect on the eddy dynamics we are interested in and it will be set to be no-slip for all experiments.

In the MITgcm manual (MITgcm Manual 2013), the boundary condition is stated as following: If free-slip is specified, then $\frac{\partial U}{\partial Y} = 0$ along boundaries in Y and $\frac{\partial V}{\partial X} = 0$ along boundaries in X. If no-slip is specified, then $U = 0$ along boundaries in Y and $V = 0$ along boundaries in X.

The boundary conditions are implemented in subroutine MOM_FLUXFORM in the source codes. If no-slip is set to be TRUE, then set sideMaskFac = sideDragFactor. This sideDragFactor is a tuning parameter due to the underestimation of vorticity at no slip boundary and the default is 2. If free-slip is specified, sideMaskFac = 0.

```
C note: using standard stencil (no mask) results in under-estimating
C vorticity at a no-slip boundary by a factor of 2 = sideDragFactor
IF ( no_slip_sides ) THEN
  sideMaskFac = sideDragFactor
ELSE
  sideMaskFac = 0. _d 0
ENDIF
```

Next if no-slip is set, then the drag is calculated. If free-slip is set, then the strain of horizontal velocities and the vertical component of vorticity are set to be 0 on the boundary because sideMaskFac is 0.

```
IF ( hFacZ(i,j).EQ.0. ) THEN
  vort3(i,j)  = sideMaskFac*vort3(i,j)
  strain(i,j) = sideMaskFac*strain(i,j)
ENDIF
```

Figure 5.19 plots the vorticity at $Z = -4.7$ m on day 5 with two lateral boundary conditions, and the general features of eddy generation are similar. Figure 5.20 plots the velocities U and V along certain cross sections at $Z = -4.7$ m on day 5. Along $X = 63$ km when no-slip is specified, $U|_{Y=0 \text{ or } 40 \text{ km}} = 0$ as it is supposed to be. However, when free-slip is set, $\frac{\partial U}{\partial Y}|_{Y=40 \text{ km}} \neq 0$, which should be zero according to the implementation. The velocity U in the two cases are very similar except near the north boundary where U is noticeable larger in the free-slip case. Along $Y = 20$ km the velocity V are quite small and are almost identical in two cases. The no-slip and free-slip constrains on V are satisfied as well. Deremble et al. (2011) tested no-slip, free-slip, and drag setup based on the classical Law of the Wall theory applied to coarsely resolved ocean models. They found that no-slip is too viscous, and free-slip solutions tend to be weakly dissipative in western boundary layers. In Fig. 5.20(A,B) the free-slip case does generate a faster flow in the simulations. Therefore no-slip seems to be a better choice for the lateral boundary condition.

Table 5.4: Group 2: effects of the lateral boundary condition

Case number	lateral BC	bottom BC	Comments
G02C01	no-slip	no-slip	It does what is supposed to do.
G02C02	free-slip	no-slip	It generate faster flows and one of constrains on U fails on northern boundary.

Effects of peninsula sizes

Next the peninsula length L_p and width W_p are varied, and the setup details can be found in Tables 5.5, 5.6, and 5.7. First when W_p is fixed at 4 km, Fig. 5.21 and 5.22 plot the vorticity at $z = -4.7$ m on day 3 and 10 with varying L_p's. The eddy is formed on the right side of the peninsula in all cases because the flow is clockwise around the lake boundary at this depth. In the last case with $L_p = 3$ km the vorticity is very weak so this is denoted as "in transition". After the injection from the follow up vorticity generated from the north-east corner, all cases clearly generate eddies (Fig. 5.22). Next $L_p = 15$ km is fixed, while W_p is varied. On day 10 (Fig. 5.23) as the peninsula becomes wider, the size and strength of the eddies decrease accordingly, and in the last case when $W_p = 16$ km no eddy is generated. From Tables 5.5 and 5.6 it seems that the eddy generation could

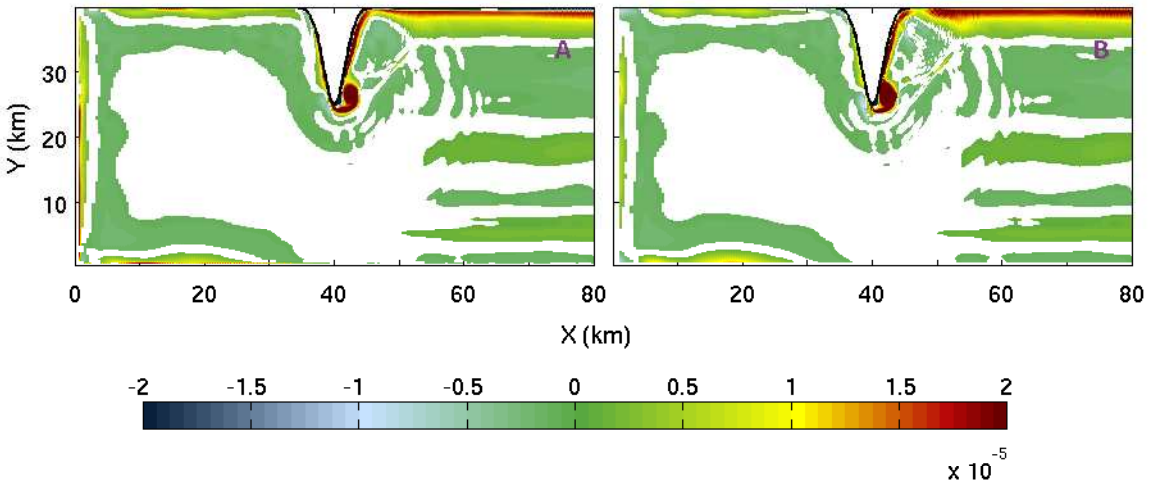

Figure 5.19: Vorticity at $Z = -4.7$ m on day 5 with varying lateral boundary conditions: (A) no-slip and (B) free-slip.

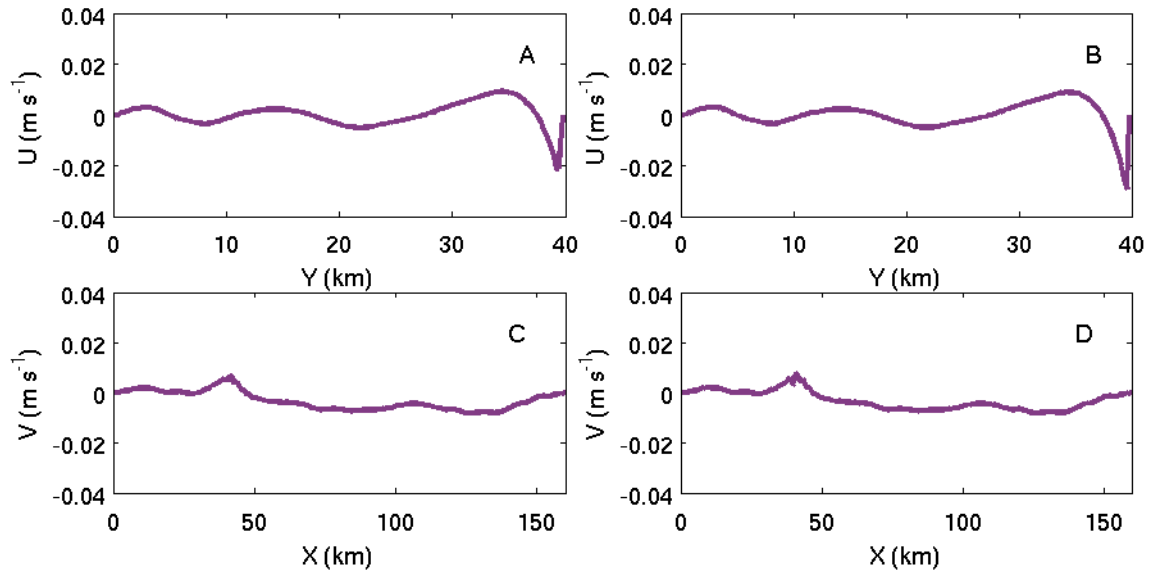

Figure 5.20: East-West velocity U at $X = 63$ km $Z = -4.7$ m on day 5 with (A) no-slip and (B) free-slip lateral boundary conditions. North-South velocity V at $Y = 20$ km $Z = -4.7$ m on day 5 with (C) no-slip and (D) free-slip lateral boundary conditions.

depend on the radius of curvature R_c (or the ratio with the Rossy radius R_c/R) and the slope at half maximum m. To explore more on the "in transition" range, another set of experiment is conducted with a fixed $L_p = 5$ km and varied W_p (Table 5.7 and Fig. 5.24).

From all three groups of simulations, for the Gaussian shape peninsulas eddy generation has a strong dependence on the size and shape. When the ratio $R_c/R < 0.25$, there are cyclonic near surface eddies are generated initially. None are generated when $R_c/R > 0.75$. When the ratio is larger than 1, i.e. the the radius of curvature R_c of peninsula tip is larger than the internal Rossby radius, there is no eddy formed in all stages, and the Kelvin wave propagates around the peninsula smoothly. A similar criterion can be derived using the slope m. Notice that the current findings are highly idealized, and depend on the functional form of the peninsulas. Even the two criteria are not consolidated due to their definitions. For example, both G04C05 and G05C05 cases have a similar R_c/R, but have different m values. Moreover, both measurements are difficult to apply in a real lake due to the complexity of the coast line. Therefore the above results are only a preliminary first attempt for future work. More metrics are needed to better represent and generalize the Kelvin wave passing a peninsula problems.

Magaldi et al. (2008) proposed to use the Burger number Bu to classify the turbulent flow regimes in their flow past a coastal cape experiments. The Burger number is defined as

$$Bu = \left(\frac{R}{D}\right)^2, \tag{5.15}$$

where R is the internal Rossby radius, and D is the characteristic length of the cape. They found that for $Bu < 0.1$, flow is attached, for $0.1 \leq Bu < 1$, flow separation occurs and small tip eddies start to shed, and for $Bu \geq 1$, tip eddies merge to form larger eddies in the lee of the cape. However, this metric is not applicable to the test cases due to the difficulty in choosing the length scale D. We varied both the length and width of the peninsula, unlike in Magaldi et al. (2008) where the shape of the cape was fixed.

Table 5.5: Group 3: effects of the peninsula length

Case number	L_p	W_p	R_c at the tip	R_c/R	Slope at right half maximum m	Eddy initially?	Eddy after "injection"?
G03C01	25 km	4 km	0.12 km	0.04	8.66	Yes	Yes
G03C02	20 km	4 km	0.14 km	0.05	6.93	Yes	Yes
G03C03	15 km	4 km	0.19 km	0.06	5.20	Yes	Yes
G03C04	10 km	4 km	0.29 km	0.09	3.47	Yes	Yes
G03C05	5 km	4 km	0.58 km	0.18	1.73	Yes	Yes
G03C06	3 km	4 km	0.96 km	0.31	1.04	In transition	Yes

Table 5.6: Group 4: effects of the peninsula width with fixed $L_p = 15$ km

Case number	L_p	W_p	R_c at the tip	R_c/R	Slope at right half maximum m	Eddy initially?	Eddy after "injection"?
G04C01	15 km	1 km	0.01 km	0.004	20.79	Yes	Yes
G04C02	15 km	2 km	0.05 km	0.02	10.40	Yes	Yes
G04C03	15 km	4 km	0.19 km	0.06	5.20	Yes	Yes
G04C04	15 km	8 km	0.77 km	0.25	2.60	Yes	Yes
G04C05	15 km	12 km	1.73 km	0.55	1.73	In transition	Yes
G04C06	15 km	16 km	3.08 km	0.98	1.30	No	No

Table 5.7: Group 5: effects of the peninsula width with fixed $L_p = 5$ km

Case number	L_p	W_p	R_c at the tip	R_c/R	Slope at right half maximum m	Eddy initially?	Eddy after "injection"?
G05C01	5 km	1 km	0.04 km	0.01	6.93	Yes	Yes
G05C02	5 km	2 km	0.14 km	0.05	3.47	Yes	Yes
G05C03	5 km	5 km	0.90 km	0.29	1.39	In transition	Yes
G05C04	5 km	6 km	1.30 km	0.41	1.16	In transition	Yes
G05C05	5 km	7 km	1.77 km	0.56	0.99	In transition	Yes
G05C06	5 km	8 km	2.31 km	0.74	0.87	No	Yes
G05C07	5 km	10 km	3.61 km	1.15	0.69	No	No
G05C08	5 km	12 km	5.19 km	1.66	0.58	No	No

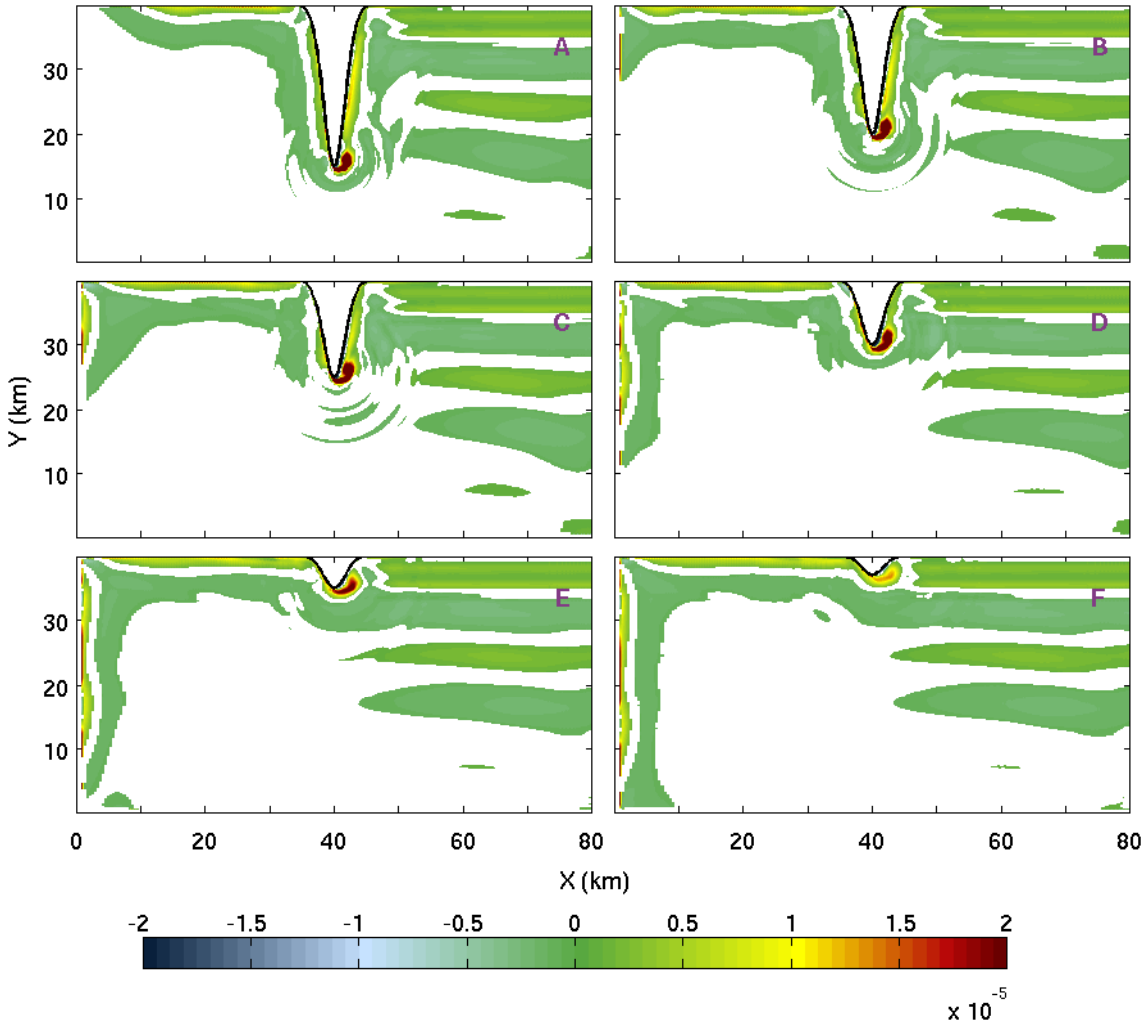

Figure 5.21: Vorticity at $z = -4.7$ m on day 3 with varying L_p's: (A) 25, (B) 20, (C) 15, (D) 10, (E) 5, and (F) 3 km.

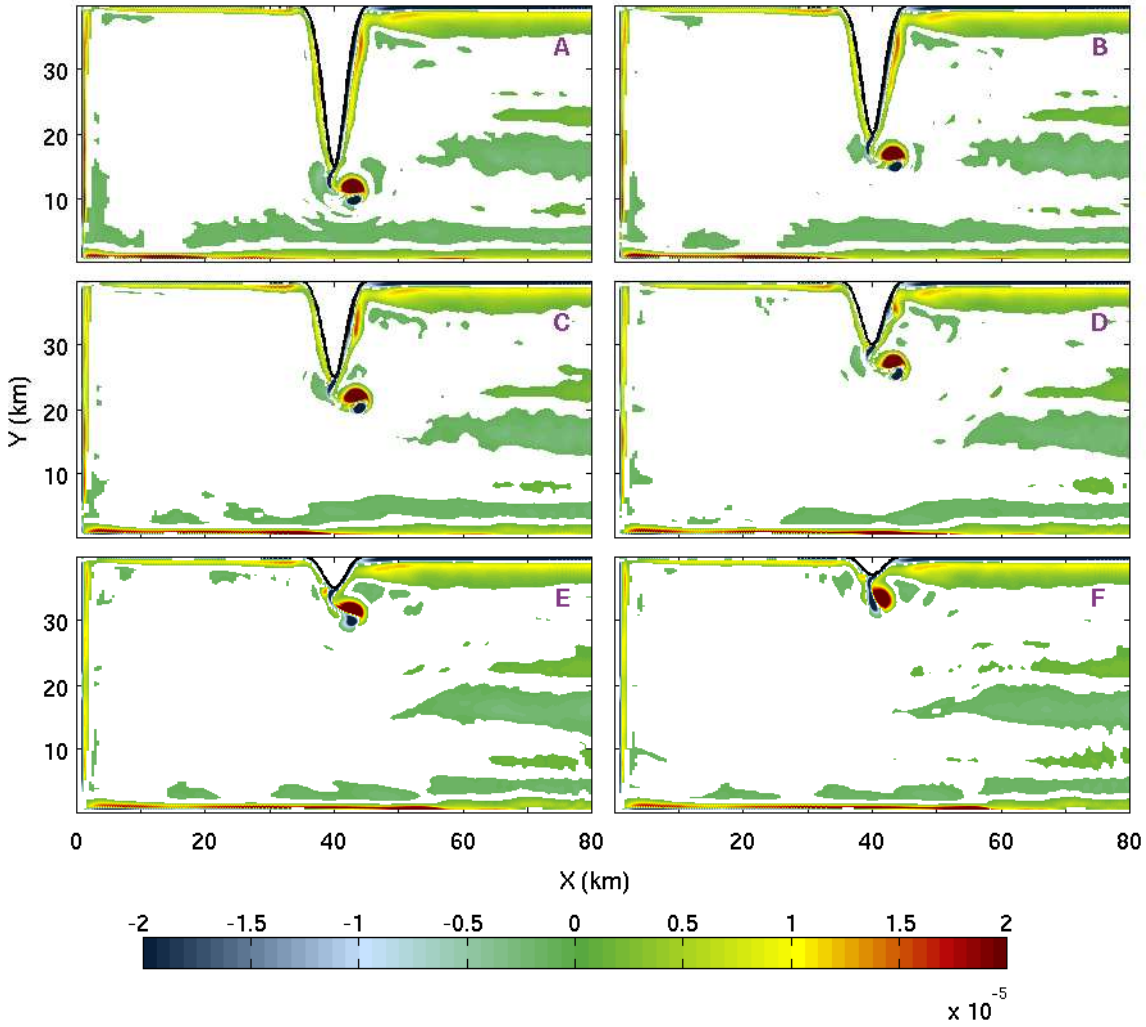

Figure 5.22: Vorticity at $z = -4.7$ m on day 10 with a fixed $W_p = 4$ km and varying L_p's: (A) 25, (B) 20, (C) 15, (D) 10, (E) 5, and (F) 3 km.

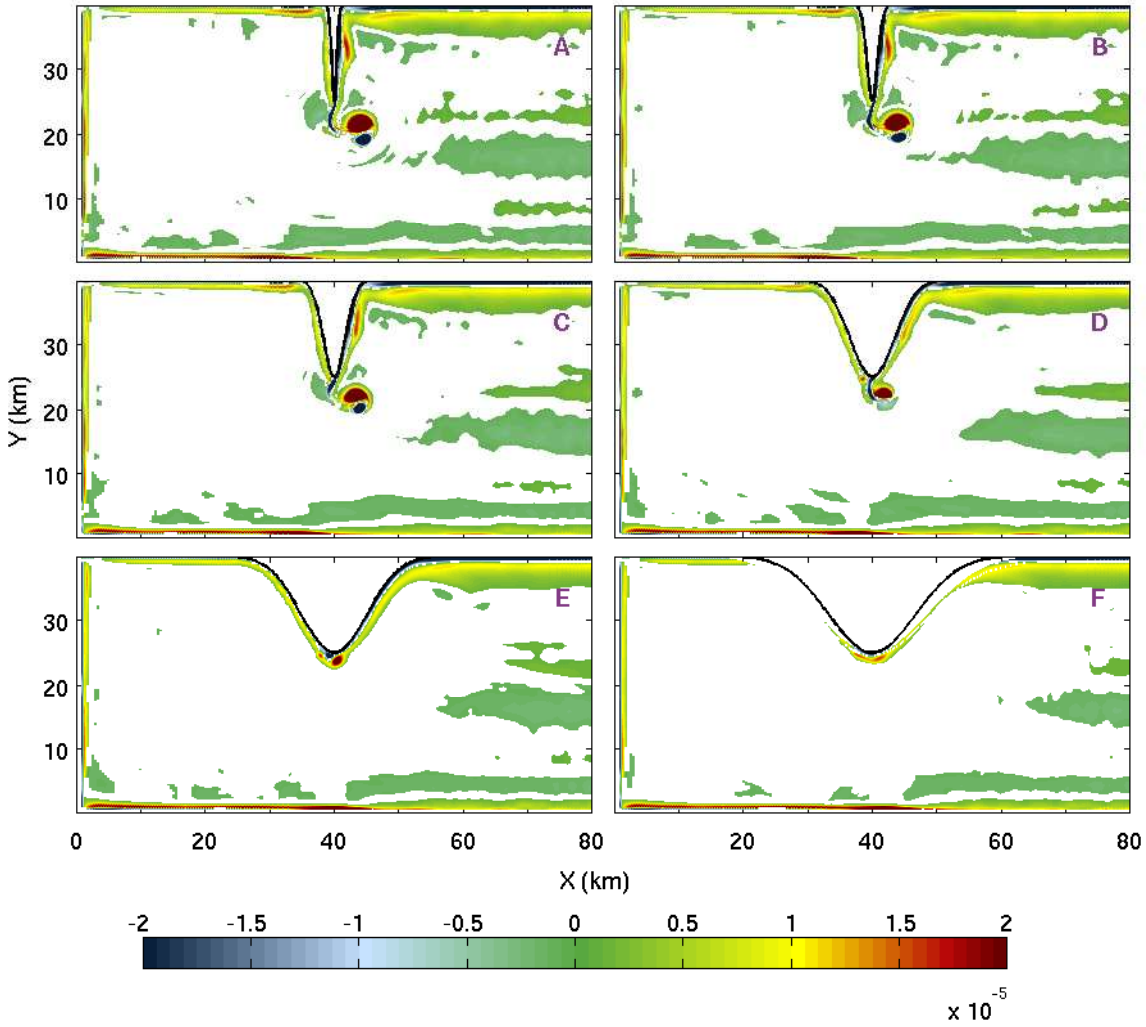

Figure 5.23: Vorticity at $z = -4.7$ m on day 10 with a fixed $L_p = 15$ km and varying W_p's: (A) 1, (B) 2, (C) 4, (D) 8, (E) 12, and (F) 16 km.

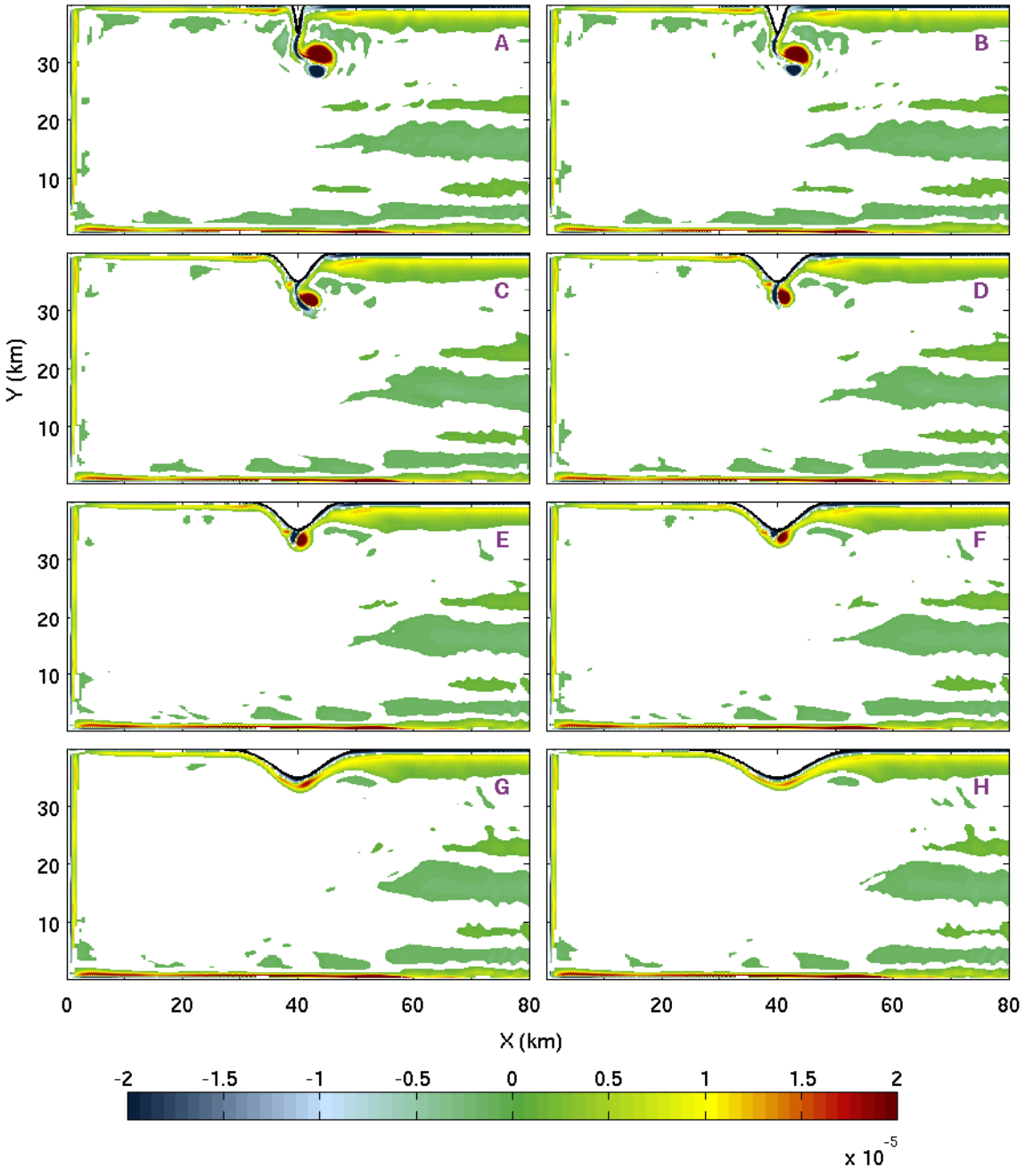

Figure 5.24: Vorticity at $z = -4.7$ m on day 10 with a fixed $L_p = 5$ km and varying W_p's: (A) 1, (B) 2, (C) 5, (D) 6, (E) 7, (F) 8, (G) 10, and (H) 12 km.

Effects of the upwelling length and position

Finally the effects of the upwelling length and position are tested by varying the initial upwelling. Six experiments are set up in details in Table 5.8 and Fig. 5.25. Again the vorticity at $z = -4.7$ m on day 10 is plotted in Fig. 5.26. Notice that due to differences in the location and size of the initial upwelling region, the eddy generation will happen at different times as well. However, after the generation the eddy remained stable for a significant time, so the comparison on day 10 is sufficient and can produce meaningful results. It is not surprising that the longer the initial upwelling is, the stronger the eddy that will be generated. The position of initial upwelling obviously can affect the eddy appearance time, but has very little affect on the eddy on day 10.

Table 5.8: Group 6: effects of the upwelling length and position

Case number	Start position	End position	Total length
G06C01	40 km	160 km	120 km
G06C02	60 km	140 km	80 km
G06C03	80 km	160 km	80 km
G06C04	40 km	120 km	80 km
G06C05	120 km	160 km	40 km
G06C06	40 km	80 km	40 km

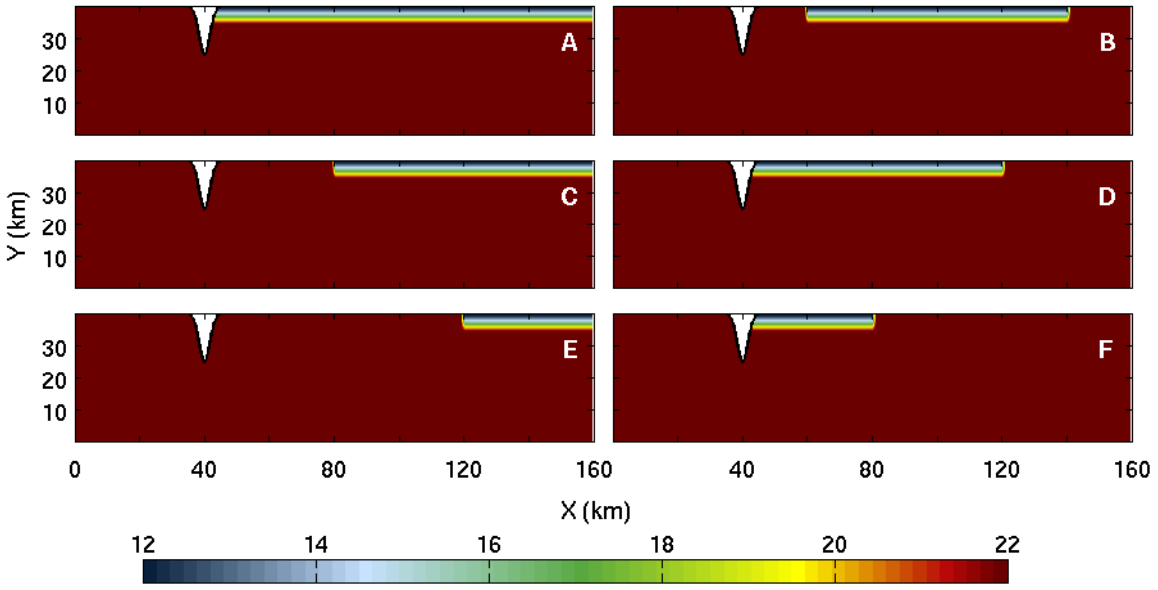

Figure 5.25: Initial temperature profiles at $z = -4.7$ m: (A) from 40 to 160, (B) from 60 to 140, (C) from 80 to 160, (D) from 40 to 120, (E) from 120 to 160, and (F) from 40 to 80 km.

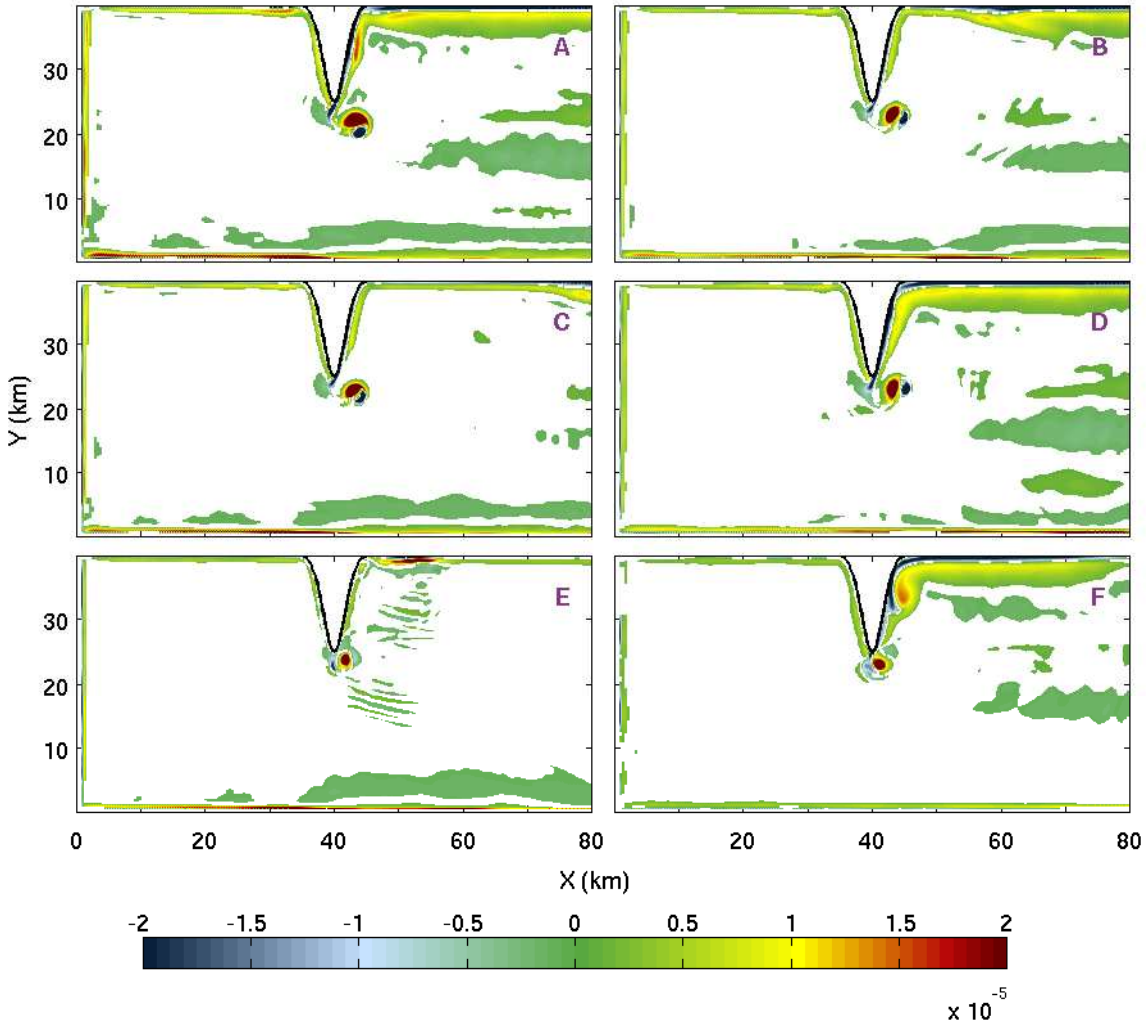

Figure 5.26: Vorticity at $z = -4.7$ m on day 10 with varying initial upwelling: (A) from 40 to 160, (B) from 60 to 140, (C) from 80 to 160, (D) from 40 to 120, (E) from 120 to 160, and (F) from 40 to 80 km.

Summary

In the idealized experiments of internal Kelvin wave propagation, it is found that the appearance of the eddies depends on the horizontal viscosity, which is obvious, and an optimal value was determined based on minimizing the horizontal viscosity while not introducing too much noise into the solution. The lateral boundary conditions have little effect on the eddy generation, except for a difference in currents near the boundary. Moreover the "free-slip" boundary condition does not seem to perform as it is supposed to. Next the effect of the peninsula size was investigated. Two metrics were proposed to determine the eddy dynamics, the ratio R_c/R and the slope at the right half width m. Both measurements have their limitations due to their definitions and the choices of the functional form of the peninsulas. Finally the initial upwelling length and position were varied, and it is found that in the idealized lake the length of the upwelling, which measures the upwelling strength, significantly affects the eddy size and strength. However, the initial position has very little affect on the eddy size.

5.3 Internal Kelvin wave propagation around Point Pelee in Lake Erie

Section 5.2 studied internal Kelvin wave propagation around a peninsula in a highly idealized lake. The shape of the peninsula was generated by an ideal mathematical function, and the bottom boundary effects were ignored by choosing a flat bottom. After the Kelvin wave propagating past the peninsula, eddies are generated on the right side boundary. Can eddies be formed the same way in real lakes? This section will explore eddy generation by Kelvin waves in Lake Erie.

5.3.1 Numerical experiment design

Similarly to the idealized case, the metalimnion near the northern shore in the central basin is partially tilted (Fig. 5.27 and 5.28). The temperature field is initialized as

$$T = T_b + \frac{T_s - T_b}{2}\Big(1 + \tanh\big(\frac{z - z_0 - \alpha y}{d}\big)\Big), \tag{5.16}$$

where $T_b = 10°\text{C}$, $T_s = 25°\text{C}$, $d = 1$ m, $z_0 = -16$ m, and $\alpha = 9.2 \times 10^{-5}$. This type of upwelling is commonly observed in Lake Erie or many other lakes (Beletsky et al. 1997). More model setup details can be found in Table 5.9. The simulation takes about 12 hours to finish a 20-day run using 128 Intel Xeon 2.5 GHz processors on SciNet.

Table 5.9: Internal Kelvin wave simulations in Lake Erie setup

Variables and parameters	Values
Grid resolution	$nx \times ny \times nz = 2000 \times 1000 \times 45$
Horizontal grid size	200 m
Vertical grid size	[0.50, 0.50, 0.75, 0.75, 0.75, 0.75, 1.00, 1.00, 1.00, 1.00, 1.00, 1.00, 1.00, 1.00, 1.00, 1.00, 1.00, 1.00, 0.75, 0.75, 0.75, 0.50, 0.50, 0.50, 0.50, 0.50, 0.50, 0.50, 0.75, 0.75, 0.75, 1.00, 1.00, 2.00, 2.00, 3.00, 3.00, 4.00, 4.00, 5.00, 5.00, 5.00, 5.00] m
Time step	dt=60 s
Horizontal viscosity	$A_h = 1.0$ m^2 s^{-1}
Vertical viscosity	$A_z = 1 \times 10^{-4}$ m^2 s^{-1}
Coriolis parameter	$f_0 = 10^{-4}$ s^{-1}
Linear EOS thermal expansion coefficient	$T_\alpha = 2 \times 10^{-4}$ °C^{-1}
Advection scheme	33 (3$^{\text{rd}}$ order direct space time with flux limiting)
Bottom boundary condition	no-slip
Lateral boundary condition	no-slip
staggerTimeStep	Yes
ridgidLid	Yes
nonHydrostatic	No

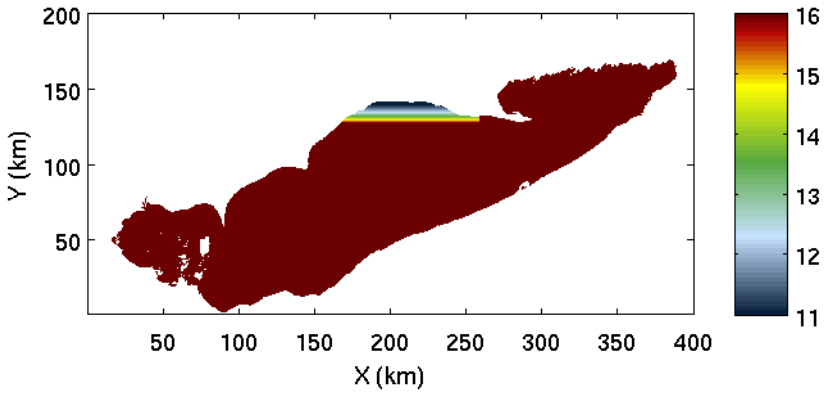

Figure 5.27: The horizontal initial temperature profile at $z = -4.5$ m

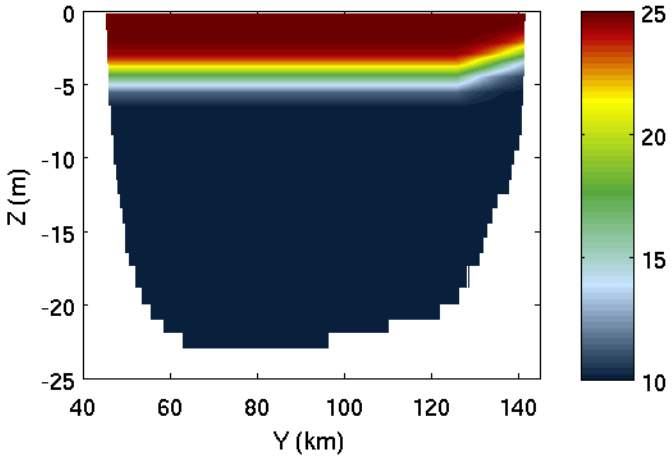

Figure 5.28: The vertical initial temperature profile on the tilted side.

5.3.2 Results and discussion

Figures 5.29 and 5.30 show the vorticity evolution near Point Pelee and Rondeau. Point Pelee is quite sharp and from the analysis in the idealized experiments, it is expected that eddies will be generated at the tip of the point. On day 6 the cold wave front arrives, and an eddy of size 3–4 km starts forming (Fig. 5.29). On the other hand, the coast near Rondeau is relatively wide. As a result, while eddies are still generated they have smaller sizes (Fig. 5.30).

McCabe et al. (2006) investigated flow separation at a headland due to tides located in a channel of Puget Sound, Washington. The headland is slightly smaller but wider than Point Pelee. The drift tracks from McCabe et al. (2006) are presented in Fig. 5.31, and we clearly see an eddy roughly 2–3 km in size being generated on the right side of the headland. Magaldi et al. (2008) studied the roles of both stratification and topographic slope in the generation of turbulent structures in the lee of capes. They determined flow regime diagrams in the Bu–α space, where Bu is the Burger number and α is the cape slope. In addition to oceans, the eddies have been observed in lakes as well. In Lake Superior McKinney et al. (2012) observed 45 eddies during the spring and summer using fine resolution Synthetic Aperture Radar (SAR) imagery, from satellite. Many eddies occurred along the southern and eastern shores as well as areas where the boundary current interacts with topographic features including islands and promontories (McKinney et al. 2012). We speculate similar eddies may be spotted in Lake Erie as well, therefore exploration of high resolution satellite images will be done in future work. The current work presents a first attempt at simulating small scale hydrodynamic processes in large lakes and contributes to our understanding of how energy is moved from large scale (the scale of the basins in Lake Erie) to smaller scales (the scale of the peninsula or Point Pelee).

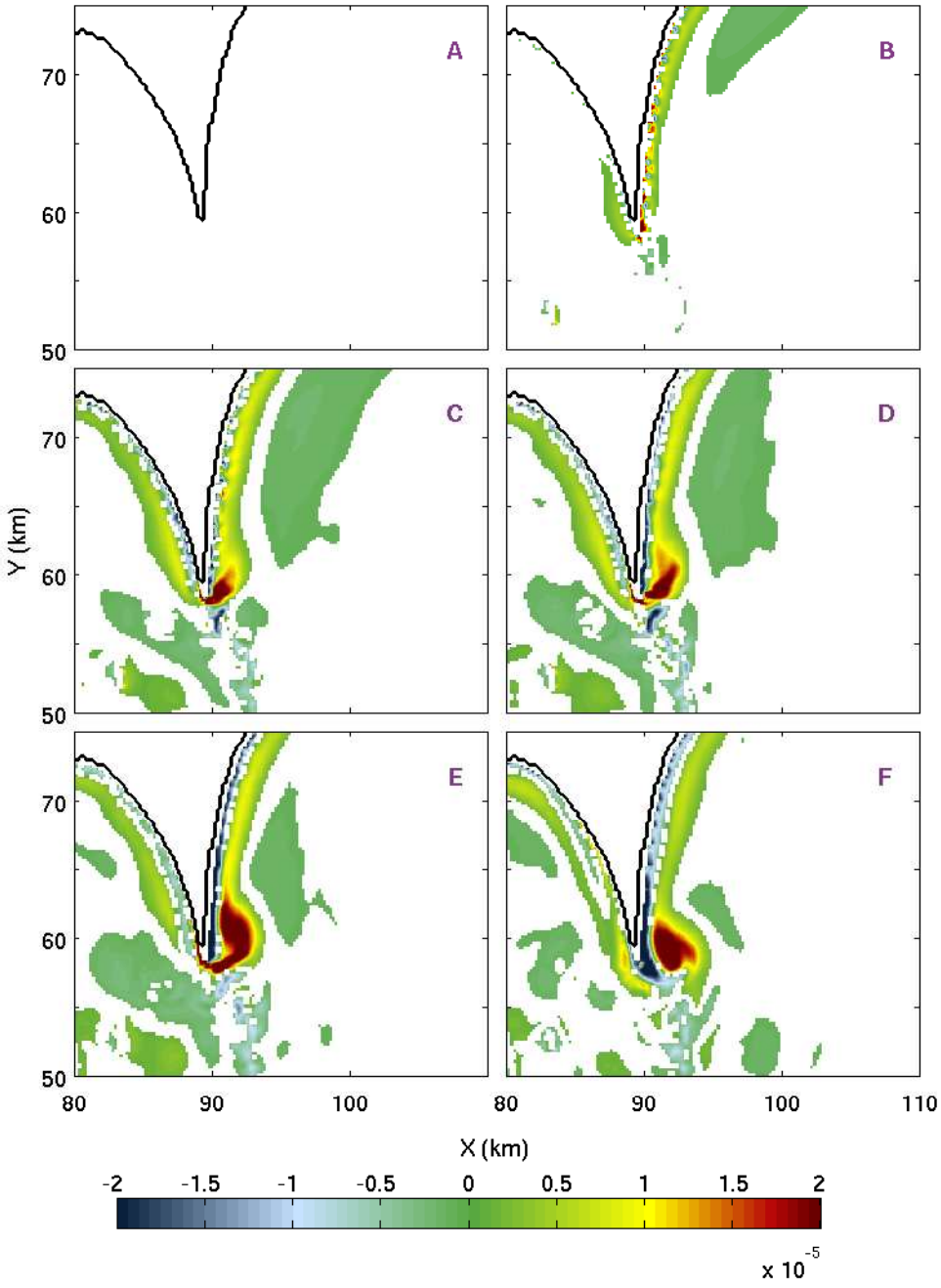

Figure 5.29: Vorticity evolution near Point Pelee at $z = -4.5$ m with on (A) 3 days, (B) 6 days, (C) 8 days, (D) 9 days, (E) 10 days, and (F) 12 days.

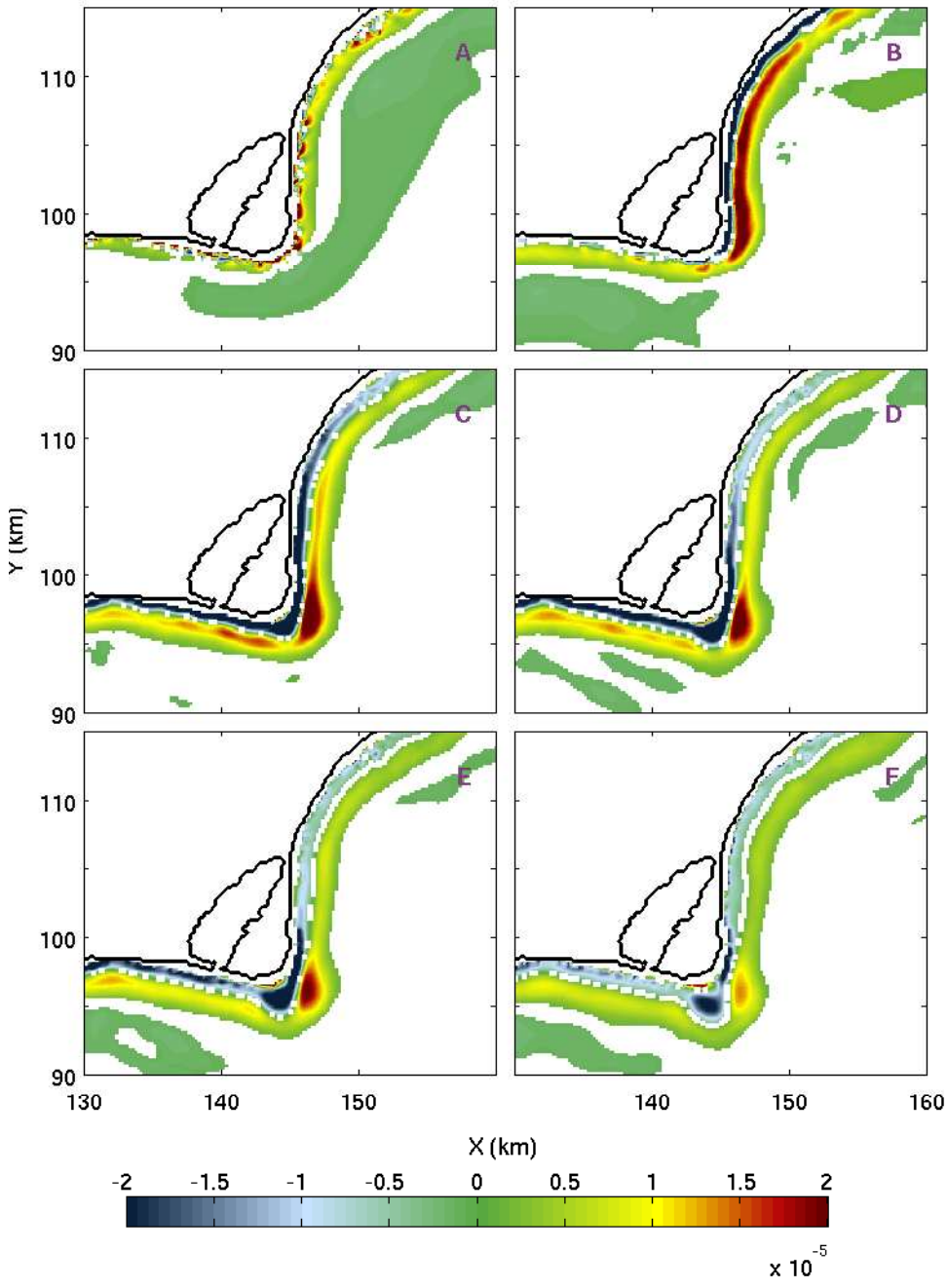

Figure 5.30: Vorticity evolution near Rondeau at $z = -4.5$ m with on (A) 3 days, (B) 6 days, (C) 8 days, (D) 9 days, (E) 10 days, and (F) 12 days.

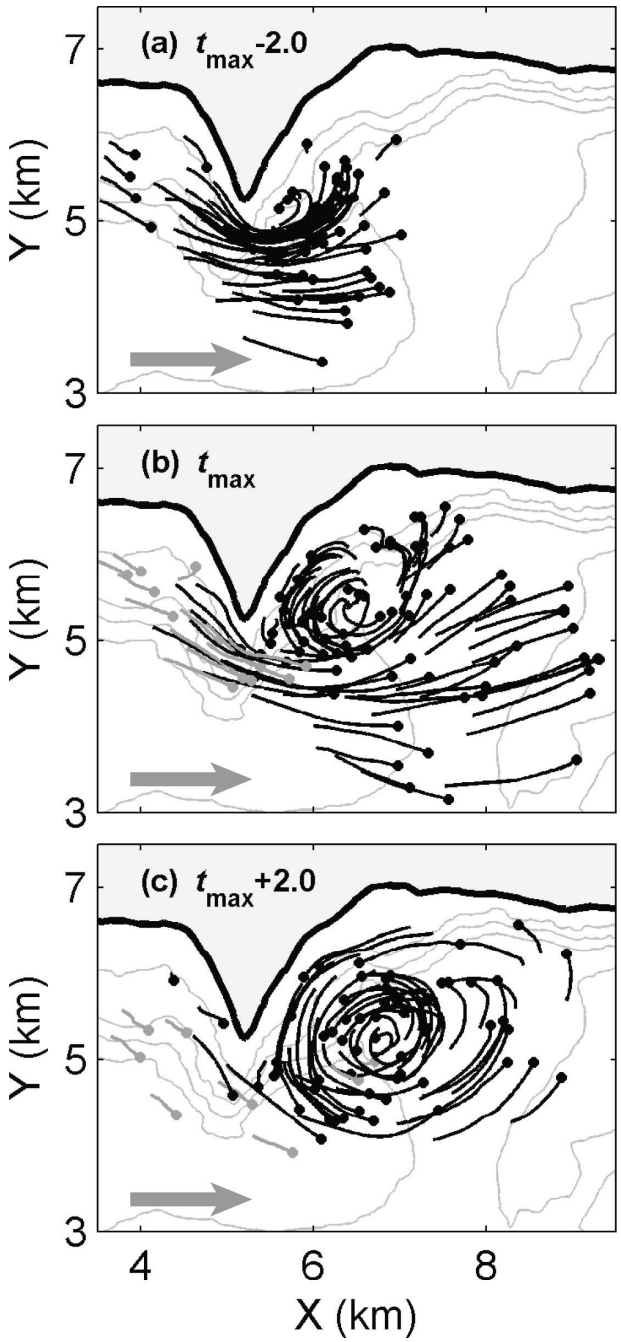

Figure 5.31: Panels of drifter tracks from McCabe et al. (2006).

Chapter 6

Conclusions and Future Work

This thesis investigated physical processes in Lake Erie, a large, shallow mid-latitude lake, from two different perspectives: climate change impacts on the thermal structure and dissolved oxygen concentration and small-scale eddy dynamics generated by internal Kelvin wave propagation past a point.

6.1 Climate impacts

Global warming and the resulting changes in meteorological forcing are anticipated to significantly affect the Laurentian Great Lakes ecosystem in many different ways. With the complexities inherent in modelling and the ecological impacts, it is important to start with an accurate account of the most direct responses of climate variations, the thermal structure. A three-dimensional hydrodynamic model ELCOM, validated by the field data collected in 2008, was used to investigate the responses of the thermal structure in Lake Erie to possible changes in air temperature and wind speed. A new method was presented to define spatially and temporally varying regions for the epilimnion, thermocline, and hypolimnion. The 2008 simulation was taken as the base case, and the observed air temperature was varied by ± 1, ± 2, and ± 4°C and the observed wind speed was varied by

±5%, ±10%, and ±20%. Increasing the air temperature warms up the epilimnion but has little effect on the hypolimnion. The stratification forms earlier and breaks down later. As a result the total duration of the stratified period is extended. The thermocline is raised modestly in the warmer air temperature scenario. Stronger winds cool down the epilimnion slightly, but warm up the hypolimnion with much larger temperature changes. The stratification duration is also affected, and the thermocline depth is noticeably deepened. Due to the large differences in basin depth and layer thickness among the three basins, the responses to the meteorological forcing changes vary with basin as well. In this thesis two methods were proposed to determine the onset and breakdown of the stratification, one based on the number of stratified grid-columns and one using the 18°C contour at a location near the centre of the basin. It was shown that patterns inferred from simple isotherm dynamics, as is typically done with one dimensional models, are not always accurate.

To study the response of dissolved oxygen concentration to the potential changes in the air temperature and wind speed, the same set of experiments were conducted by coupling ELCOM with the aquatic ecological module CAEDYM. Higher/lower air temperature decreases/increases DO in both the epilimnion and hypolimnion, but with a larger response in the former. When the air temperature increases, the stratification period is extended as previously found in the thermal structure studies. As a consequence of the continuous oxygen consumption, DO in the hypolimnion drops even lower. Wind speeds have little effect on epilimnetic DO, which is near saturation because of contact with the atmosphere, but change hypolimnion DO noticeably. Through the bottom hypoxia analysis along with the previous thermal structure studies, it was found that three factors related to lake hydrodynamics have strong influences on the hypolimnetic hypoxia: water temperature, stratification duration, and hypolimnion thickness. To be specific, warmer water temperature increases the DO consumption rate and reduces the DO equilibrium solubility, longer stratification extends the consumption duration, and a thin hypolimnion leads to an earlier onset of hypoxia by increasing the sediment oxygen demand to hypolimnion volume ratio. Therefore in a warm and quiescent year hypolimnetic hypoxia will likely become more severe if we consider the effects of meteorological forcing changes only. The present results show the potential for complicated and interactive effects of climate forcing on important

biogeochemical processes in Lake Erie as well as other large mid-latitude lakes.

To extend the current studies, we can add more scenarios and analyze additional metrics related to the thermal structure to have a more comprehensive overview on the lake physical dynamics, for instance, the initial lake temperature (a proxy for winter ice cover) and the total heat content, as suggested in Austin and Allen (2011). Besides the dissolved oxygen, other biochemical components like the total phosphorus are certainly worth studying, since they are directly related to the water quality. In addition we can validate the findings by conducting similar experiments using a different base year. Lake Erie is the shallowest in the Great Lakes, so how will the responses differ in other Great Lakes or other large mid-latitude lakes? These, and similar scenarios, are definitely worth investigating and can contribute to our understanding of the complex physical, biochemical, and ecological processes in large lakes.

6.2 Small-scale dynamics

Taking advantage of high performance computing, the generation of eddies when a baroclinic Kelvin wave propagates past a point was studied using the MITgcm. The grid resolution was refined from 2 km to 200 m. With the finer resolution it is possible to explore small-scale processes that cannot be resolved in the coarse resolution simulations examined previously. First the classical problem of incompressible viscous flow past a circular cylinder was revisited by conducting a set of numerical simulations using the MITgcm. A comparison with results in the literature showed that the MITgcm has the capability of simulating flow separation. We subsequently investigated eddies generated by internal Kelvin wave propagation around a peninsula in both an idealized lake and Lake Erie. A series of sensitivity tests was conducted on the peninsula size in the idealized case and presented some preliminary results. In the future, more metrics are needed to better characterize the Kelvin wave passing a peninsula problem. Adding more scenarios can extend the current studies, for example, varying the initial upwelling depth, slope, direction, etc. Exploring high definition satellite images will certainly help validate our current

findings. Additional simulations using the observed forcing are planned to investigate eddy generation in a realistic environment. This work presents a first attempt at simulating small scale hydrodynamic processes in large lakes and contributes to our understanding of how energy is moved from large scales (the scale of the basins in Lake Erie) to smaller scales (the scale of the peninsula or Point Pelee).

APPENDICES

Appendix A

MATLAB M-Files

A.1 Quantitative definitions of thermal structure

StoreData_thermocline_thres4.m reads in 3D temperature data and generates the thermocline, epilimnion, metalimnion, and hypolimnion regions in lakes. Please see Section 4.1 more details.

```
load('SaveData/T_default_ALL.mat');
T_ALL = T_default_ALL;
clear T_default_ALL
load('SaveData/Z.mat');

threshold_strat = 4;
c_epi = 0.25;
c_hyp = 0.25;

nTimeTotal = numel(T_ALL(:,1,1,1));
ny = numel(T_ALL(1,1,:,1));
nx = numel(T_ALL(1,1,1,:));
nz = numel(T_ALL(1,:,1,1));
thermocline = NaN(nTimeTotal,21,ny,nx);
% 01-thermocline depth   02-thermocline grid    03-thermocline T
% 04-surface depth       05-surface grid        06-surface T
% 07-bottom depth        08-bottom grid         09-bottom T
% 10-Epi boundary depth  11-Epi boundary grid   12-Epi boundary T
% 13-Hyp boundary depth  14-Hyp boundary grid   15-Hyp boundary T
```

```
% 16—Carignan Epi depth  17—Carignan Epi grid   18—Carignan Epi T
% 19—Carignan Hyp depth  20—Carignan Hyp grid   21—Carignan Hyp T
tol = 1E—6;
for iter = 1:nTimeTotal
  for i = 1:ny
    for j = 1:nx
      dTdz = diff(squeeze(T_ALL(iter,:,i,j)))./diff(Z');
      % Calculate dT/dz.
      search_iterB=1;
      search_flagB=0;
      % First find the bottom layer from Z(1) = —61.5 m.
      while(search_flagB==0)
        if (isnan(T_ALL(iter,search_iterB,i,j)))
          % If it is NaN, then move to one grid higher.
          search_iterB=search_iterB+1;
          search_flagB=0;
          if search_iterB == numel(Z)
            search_flagB=1;
            break
            % When reach the top layer and there is still no water,
            % then break. Now search_iterB = numel(Z).
          end
        else
          search_flagB=1;
          % If it is not NaN for the first time, then set search_flagB=1,
          % stop, and we find the bottom layer.
        end
      end
      if search_iterB ~= numel(Z)
        % If search_iterB==numel(Z) (Z(numel(Z)) = +1.25),
        % it means all are NaN and it is a land grid.
        thermocline(iter,7,i,j) = Z(search_iterB);
        % Store bottom water depth.
        thermocline(iter,8,i,j) = search_iterB;
        % Store ottom water grid number.
        thermocline(iter,9,i,j) = T_ALL(iter,search_iterB,i,j);
        % Store bottom water temperature (T).
      end

      search_iterS=numel(Z);
      search_flagS=0;
      % Use the same method we find the surface water grid, searcing
      % from numel(Z) to 1.
      while(search_flagS==0)
        if (isnan(T_ALL(iter,search_iterS,i,j)))
```

```
65            % If it is NaN, then move to one grid lower.
66            search_iterS=search_iterS-1;
67            search_flagS=0;
68            if search_iterS==1
69              search_flagS=1;
70              break
71              % When reach the bottom layer and there is still no water,
72              % then break. Now search_iterB = 1.
73            end
74          else
75            search_flagS=1;
76          end
77        end
78        if search_iterS~=1
79          % If search_iterS==1,
80          % it means all are NaN and it is a land grid.
81          thermocline(iter,4,i,j) = Z(search_iterS);
82          % Store surface water depth.
83          thermocline(iter,5,i,j) = search_iterS;
84          % Store surface water grid number.
85          thermocline(iter,6,i,j) = T_ALL(iter,search_iterS,i,j);
86          % Store surface water T.
87        end
88        if (T_ALL(iter,search_iterS,i,j)-T_ALL(iter,search_iterB,i,j)...
89              > threshold_strat)
90          % Impose the stratification requirement: Ts-Tb>Tthres.
91          for k=1:numel(dTdz)
92            if abs(dTdz(k) - max(dTdz))<tol
93              % Locate the max gradient. tol is very tiny, s0 we can locate
94              % the unique max value.
95              thermocline(iter,1,i,j) = Z(k);
96              % Store thermocline depth (max gradient).
97              thermocline(iter,2,i,j) = k;
98              % Store thermocline grid number.
99              thermocline(iter,3,i,j) = T_ALL(iter,k,i,j);
100             % Store thermocline T.
101           end
102         end
103         Ts = T_ALL(iter,thermocline(iter,5,i,j),i,j);
104         Tb = T_ALL(iter,thermocline(iter,8,i,j),i,j);
105         Ttherm = T_ALL(iter,thermocline(iter,2,i,j),i,j);
106         % Rename to shorter names (Ts, Tb, Ttherm) for later use.
107         if (~isnan(Ttherm))
108           % If Ttherm exists (not NaN), then we start looking for epi
109           % and hyp boundaries.
```

```
110             search_iterEpi=numel(Z);
111             % Search for the epilimnion boundary starting from top grid
112             % numel(Z) = 45, Z(45) = +1.25 m.
113             search_flagEpi=0;
114             while(search_flagEpi==0)
115               if (T_ALL(iter,search_iterEpi,i,j)<=(Ts-(Ts-Ttherm)*c_epi))
116                 % Impose relative T difference to find epi.
117                 thermocline(iter,11,i,j) = search_iterEpi;
118                 % Store epi boundary grid number.
119                 thermocline(iter,10,i,j) = Z(thermocline(iter,11,i,j));
120                 % Store epi boundary depth.
121                 thermocline(iter,12,i,j)=T_ALL(iter,thermocline(iter,11,i,j),i,j);
122                 % Store epi boundary T.
123                 search_flagEpi=1;
124               else
125                 search_iterEpi=search_iterEpi-1;
126                 % Else, move to one grid lower.
127               end
128             end
129
130             search_iterCarignanEpi=numel(dTdz);
131             % Search for the Carignan epilimnion boundary,
132             % from numel(dTdz) = 44, Z(45) = +0.75 m.
133             search_flagCarignanEpi=0;
134             while(search_flagCarignanEpi==0)
135               if dTdz(search_iterCarignanEpi)>1.0
136                 thermocline(iter,17,i,j)=...
137                     max(search_iterCarignanEpi+1,thermocline(iter,2,i,j));
138                 % Store Carignan epi boundary grid number.
139                 % search_iterCarignanEpi+1 higher than the one with dT/dz>1,
140                 % but never lower than the thermocline.
141                 thermocline(iter,16,i,j) = Z(thermocline(iter,17,i,j));
142                 % Store Carignan epi boundary depth.
143                 thermocline(iter,18,i,j)=T_ALL(iter,thermocline(iter,17,i,j),i,j);
144                 % Store Carignan epi boundary T.
145
146                 search_flagCarignanEpi=1;
147               else
148                 search_iterCarignanEpi=search_iterCarignanEpi-1;
149                 % Else, move to one grid lower.
150                 if search_iterCarignanEpi==0
151                   % If search_iterCarignanEpi==0, then no grid satisfies
152                   % dT/dz>1, hence set search_flagCarignanEpi=1 and break.
153                   search_flagCarignanEpi=1;
154                 end
```

```
155             end
156           end
157
158           search_iterHyp=1;
159           % Find the hypolimnion boundary, from Z(1) = -61.5 m.
160           search_flagHyp=0;
161           while(search_flagHyp==0)
162             if (T_ALL(iter,search_iterHyp,i,j)>=(Tb+(Ttherm-Tb)*c_hyp))
163               % Impose relative T difference to find hyp.
164               thermocline(iter,14,i,j) = search_iterHyp;
165               % Store hyp boundary grid number.
166               thermocline(iter,13,i,j) = Z(thermocline(iter,14,i,j));
167               % Store hyp boundary depth.
168               thermocline(iter,15,i,j)=T_ALL(iter,thermocline(iter,14,i,j),i,j);
169               % Store hyp boundary T.
170               search_flagHyp=1;
171             else
172               search_iterHyp=search_iterHyp+1;
173               % Else, move to one grid higher
174             end
175           end
176
177           search_iterCarignanHyp=1;
178           % Find the Carignan hypolimnion boundary from Z(1) = -61.5 m.
179           search_flagCarignanHyp=0;
180           while(search_flagCarignanHyp==0)
181             if dTdz(search_iterCarignanHyp)>1.0
182               % Here we just used the similar method as the epi, however,
183               % there is no such definition in Carignan et al. (2000).
184               if search_iterCarignanHyp>1
185                 % To ensure that it is not the first grid,
186                 % because later we need search_iterCarignanHyp-1.
187                 thermocline(iter,20,i,j) =...
188                     min(search_iterCarignanHyp-1,thermocline(iter,2,i,j));
189                 % Store Carignan hyp boundary grid,
190                 % never higher than the thermocline.
191                 thermocline(iter,19,i,j) = Z(thermocline(iter,20,i,j));
192                 % Store Carignan hyp boundary depth.
193                 thermocline(iter,21,i,j)=T_ALL(iter,thermocline(iter,20,i,j),i,j);
194                 % Store Carignan hyp boundary T.
195                 search_flagCarignanHyp=1;
196               end
197             else
198               search_iterCarignanHyp=search_iterCarignanHyp+1;
199               % Else, move to one grid higher.
```

```
                if search_iterCarignanHyp==nz
                  % If reaches the top, then use NaN the default values,
                  % set search_flagCarignanHyp=1, and break.
                  search_flagCarignanHyp=1;
                end
              end
            end
          end
        end
      end
    end
end
thermocline_default_thres4 = thermocline;
save('SaveData/thermocline_default_thres4.mat',...
    'thermocline_default_thres4','-v7.3');
% Store final data to files.
```

A.2 Averaging region temperature

StoreData_region_average.m reads in 3D temperature data and thermocline related data generated from Section A.1, and calculate the average temperature for each layer in every basin. Please see Section 4.1 for more details.

```
% Calculate and store mean layer T and thermocline depth
% with threshold percentage for the stratified grids
% output: RegionAVE(nTimeTotal,9)
% 1-West basin averaged
% 2-Central epilimnion  3-Central metalimnion  4-Central hypolimnion
% 5-Eastern epilimnion  6-Eastern metalimnion  7-Eastern hypolimnion
% 8-Central thermocline depth     9-Eastern thermocline depth
% Western basin (1:42); Central basin (43:131); Eastern basin (132:end)
% Y(42) =  93 km and Y(131) = 271 km

load('SaveData/T_default_ALL.mat');
T_ALL = T_default_ALL;
clear T_default_ALL
load('SaveData/thermocline_default_thres4.mat');
thermocline = thermocline_default_thres4;
clear thermocline_default_thres4
load('SaveData/DZ.mat');
load('SaveData/Bathy.mat');
```

```
BathyReal = Bathy;
Bathy = Bathy<0;

nTimeTotal = numel(thermocline(:,1,1,1));
regionAVE = NaN(nTimeTotal,9);
ny = numel(thermocline(1,1,:,1));
nx = numel(thermocline(1,1,1,:));
TotalWaterGrid_Central = numel(find(~isnan(BathyReal(43:131,:))));
TotalWaterGrid_East = numel(find(~isnan(BathyReal(132:end,:))));
filter_totalGrid = 1/10;

% First in Western basin, we calculate the basin averaged.
for iter = 1:nTimeTotal
  sumTZ = 0;
  sumZ = 0;
  % Sum of dT*dZ and sum of dZ for all (i,j) at one timestep.
  for i = 1:42
    % Western basin boundary
    for j = 1:nx
      surGrid = thermocline(iter,5,i,j);
      botGrid = thermocline(iter,8,i,j);
      % Read in surface and bottom grid.
      if (~isnan(surGrid))
        % If surface water grid is not NaN, then it is a water grid.
        sumTZ = sumTZ+...
        sum(squeeze(T_ALL(iter,botGrid:surGrid,i,j)).*DZ(botGrid:surGrid)');
        sumZ = sumZ+sum(DZ(botGrid:surGrid));
      end
    end
  end
  regionAVE(iter,1) = sumTZ/sumZ;
  % Store the basin-averaged temperature in Western basin.
end

% Next in Central basin we calculate the average for epi, met, and hyp.
for iter = 1:nTimeTotal
  sumTZ_epi = 0;
  sumTZ_met = 0;
  sumTZ_hyp = 0;
  sumZ_epi = 0;
  sumZ_met = 0;
  sumZ_hyp = 0;
  sumTmcln = 0;
  stra_gri_count = 0;
  for i = 43:131
```

```
64      % Central basin boundary
65      for j = 1:nx
66        thermGrid = thermocline(iter,2,i,j);
67        surGrid = thermocline(iter,5,i,j);
68        botGrid = thermocline(iter,8,i,j);
69        epiGrid = thermocline(iter,11,i,j);
70        hypGrid = thermocline(iter,14,i,j);
71        % Read in surf, bot, thermocline, epi boundary, and hyp boundary.
72        if (~isnan(surGrid) && ~isnan(thermGrid))
73          % If it is water grid and there is stratification, start averaging.
74          stra_gri_count = stra_gri_count + 1;
75          % Count the total stratified grid number.
76          sumTZ_epi = sumTZ_epi+...
77          sum(squeeze(T_ALL(iter,epiGrid:surGrid,i,j)).*DZ(epiGrid:surGrid)');
78          sumZ_epi = sumZ_epi+sum(DZ(epiGrid:surGrid));
79          sumTZ_met = sumTZ_met+...
80          sum(squeeze(T_ALL(iter,hypGrid:epiGrid,i,j)).*DZ(hypGrid:epiGrid)');
81          sumZ_met = sumZ_met+sum(DZ(hypGrid:epiGrid));
82          sumTZ_hyp = sumTZ_hyp+...
83          sum(squeeze(T_ALL(iter,botGrid:hypGrid,i,j)).*DZ(botGrid:hypGrid)');
84          sumZ_hyp = sumZ_hyp+sum(DZ(botGrid:hypGrid));
85          sumTmcln = sumTmcln + thermocline(iter,1,i,j);
86        end
87      end
88    end
89    if stra_gri_count>TotalWaterGrid_Central*filter_totalGrid
90      % Only if total stratified grid number>total grid*threshold percentage,
91      % then the averaged value can be stored.
92      regionAVE(iter,2) = sumTZ_epi/sumZ_epi;
93      regionAVE(iter,3) = sumTZ_met/sumZ_met;
94      regionAVE(iter,4) = sumTZ_hyp/sumZ_hyp;
95      regionAVE(iter,8) = sumTmcln/stra_gri_count;
96    end
97  end
98
99  % Finally in Eastern basin
100 for iter = 1:nTimeTotal
101   sumTZ_epi = 0;
102   sumTZ_met = 0;
103   sumTZ_hyp = 0;
104   sumZ_epi = 0;
105   sumZ_met = 0;
106   sumZ_hyp = 0;
107   sumTmcln = 0;
108   stra_gri_count = 0;
```

```
  for i = 132:ny
    % Eastern basin boundary
    for j = 1:nx
      thermGrid = thermocline(iter,2,i,j);
      surGrid = thermocline(iter,5,i,j);
      botGrid = thermocline(iter,8,i,j);
      epiGrid = thermocline(iter,11,i,j);
      hypGrid = thermocline(iter,14,i,j);
      % Read in surf, bot, thermocline, epi boundary, and hyp boundary.
      if (~isnan(surGrid) && ~isnan(thermGrid))
        % If it is water grid and there is stratification, start averaging.
        stra_gri_count = stra_gri_count + 1;
        % Count the total stratified grid number.
        sumTZ_epi = sumTZ_epi+...
        sum(squeeze(T_ALL(iter,epiGrid:surGrid,i,j)).*DZ(epiGrid:surGrid)');
        sumZ_epi = sumZ_epi+sum(DZ(epiGrid:surGrid));
        sumTZ_met = sumTZ_met+...
        sum(squeeze(T_ALL(iter,hypGrid:epiGrid,i,j)).*DZ(hypGrid:epiGrid)');
        sumZ_met = sumZ_met+sum(DZ(hypGrid:epiGrid));
        sumTZ_hyp = sumTZ_hyp+...
        sum(squeeze(T_ALL(iter,botGrid:hypGrid,i,j)).*DZ(botGrid:hypGrid)');
        sumZ_hyp = sumZ_hyp+sum(DZ(botGrid:hypGrid));
        sumTmcln = sumTmcln + thermocline(iter,1,i,j);
      end
    end
  end
  if stra_gri_count>TotalWaterGrid_East*filter_totalGrid
    % Only if total stratified grid number>total grid*threshold percentage,
    % then the averaged value can be stored.
    regionAVE(iter,5) = sumTZ_epi/sumZ_epi;
    regionAVE(iter,6) = sumTZ_met/sumZ_met;
    regionAVE(iter,7) = sumTZ_hyp/sumZ_hyp;
    regionAVE(iter,9) = sumTmcln/stra_gri_count;
  end
end
% Store final data to file.
regionAVE_default_thres4_filter = regionAVE;
save('SaveData/regionAVE_default_thres4_filter.mat',...
    'regionAVE_default_thres4_filter','-v7.3');
```

A.3 MITgcm Movie Maker

MITgcmMovieMaker.m is a MATLAB code I wrote to generate various animations for the MITgcm output. Below is the header information.

```
%%%%%%%%%%%%%%%%%%%%%%%%%%%%%%%%%%%%%%%%%%%%%%%%%%%%%%%%%%%%%%%%%%%%%%%%%%%%%%%%
% This script reads MDSIO type output in MITgcm and generates movies.     %
% It can make the following evolution movies:                             %
% --free surface                                                          %
% --temperature (T), salinity (S), Vorticity omega in the z direction,    %
%   and velocities (U, V, W)  on a horizontal sheet z=z0, vertical        %
%   curtains x=x0, y=y0, and arbitrary vertical curtains provided         %
%   the coordinate dat files.                                             %
% --velocity field                                                        %
% --all plots can be generated on the whole or partial domain (zoom in)   %
%                                                                         %
% Note: x0, y0, and z0 are on the grid coordinate. If the input value is  %
% not on the grid, then the code will find the nearest grid point and     %
% use it to generate movies. When the input value is exactly in the middle%
% of two grids, the grid with smaller index will be chosen. If the grid   %
% with larger index is needed, please modify the code.                    %
%                                                                         %
% Note: Large .ps files in PS_IMAGES directory are deleted at the end. If %
% they are needed, please remove the corresponding lines in the code.     %
%                                                                         %
% NEED data meta file:                                                    %
% XC.*.data (meta)  XG.*.data (meta)     --to read x-coordinate           %
% YC.*.data (meta)  YG.*.data (meta)     --to read y-coordinate           %
% RC.data (meta)    RF.data (meta)       --to read z-coordinate           %
% Depth.data (meta)                      --to generate topography outline %
% toBePlottedVariable.*.data (meta)      --to plot variable data          %
%                                                                         %
% NEED matlab functions:                                                  %
% rdmds.m: reads .data results                                            %
% converSeconds.m: converts time (in seconds) into time strings           %
% quiver_CD.m: no dots are plotted where velocities are NaN               %
%              written by Chris Dallimore                                 %
% NEED software:                                                          %
% --ImageMagick to use the command 'convert'                              %
% --Ghostscript to convert ps file to gif file                            %
%                                                                         %
% v 0.96, written by Wentao Liu, University of Waterloo                   %
%                                                                         %
%%%%%%%%%%%%%%%%%%%%%%%%%%%%%%%%%%%%%%%%%%%%%%%%%%%%%%%%%%%%%%%%%%%%%%%%%%%%%%%%
```

Here we give an example of plotting the temperature on a horizontal sheet in the Kelvin wave propagation around a Gaussian peninsula studied in Section 5.2.

Step One: choose the variable to plot "Temperature T" by entering "1".

```
>>MITgcmMovieMakerV096
-------------------------------------------------------------
----------------------Step One-------------------------------
------------Please choose which variable to plot-------------
-------------------------------------------------------------
1: Temperature T
2: Zonal velocity U
3: Meridian velocity V
4: Vertical velocity W
5: Free surface Eta
6: Salinity S
7: Velocity field
8: Vorticity omega in the z direction
-------------------------------------------------------------
Which variable would you like plot [1, 2, 3, 4, 5, 6, 7, 8]:
```

Step Two: choose "a horizontal sheet z=z0" by entering "1".

```
Temperature T is chosen to plot.
-------------------------------------------------------------
----------------------Step Two-------------------------------
----------Please choose which cross-section to plot----------
-------------------------------------------------------------
1: a horizontal sheet z=z0
2: a vertical curtain along a line x=x0
3: a vertical curtain along a line y=y0
4: an arbitrary vertical curtain, given the coordinate .dat file
-------------------------------------------------------------
Which cross-section would you like plot [1, 2, 3, 4]:
```

Step Three: input the depth of the horizontal sheet, and we type in "-4.7" here.

```
A horizontal sheet z=z0 is chosen.
-------------------------------------------------------------
----------------------Step Three-----------------------------
---------------Please specify the cross-section--------------
-------------------------------------------------------------
You choose to plot on a horizontal sheet.
The code will find the grid point nearest to the input value and use
this point to make movies. If the input is exactly in the middle of two
grid points, the grid with smaller index is chosen. Below are the
z coordinates at CENTER of cells.
  Columns 1 through 9
 -0.6362 -1.8284 -2.6654 -3.0964 -3.3516 -3.5414 -3.6992 -3.8386 -3.9665
  Columns 10 through 18
 -4.0866 -4.2015 -4.3126 -4.4210 -4.5275 -4.6327 -4.7368 -4.8404 -4.9435
  Columns 19 through 27
 -5.0465 -5.1497 -5.2531 -5.3572 -5.4622 -5.5686 -5.6768 -5.7876 -5.9021
  Columns 28 through 36
 -6.0217 -6.1486 -6.2867 -6.4422 -6.6280 -6.8742 -7.2781 -8.0735 -9.2434
  Columns 37 through 40
  -10.5182  -11.7985  -13.0791  -14.3597
Please input the value of z0 (meters):
```

Step Four: we would like to zoom in the peninsula, so choose "2".

```
Your input is z = -4.7 m.
The nearest grid is at z = -4.7368 m.
The index of the nearest grid is 16.
-------------------------------------------------------------
----------------------Step Four------------------------------
----------------------Zoom or not?---------------------------
-------------------------------------------------------------
Would you like to zoom in? [1:No   2:Yes]:
```

Next we need to enter the boundary for the zoomed in plot. The code lists the x coordinate for the first and last a few grids.

```
You choose to zoom in.
The code will find the grid point nearest to the input value and use this
point to make movies. If the input is exactly in the middle of two grid
points, the grid with smaller index is chosen.
------------------------------------------------------------
x coordinate at CENTER of cells may be too long to display.
Below are the first and last a few elements (m):
   1.0e+03 *
    0.2045    0.6135    1.0224    1.4314    1.8403
   1.0e+05 *
    1.5775    1.5816    1.5857    1.5898    1.5939    1.5980
Please input the start value of zoomed xmin (meters):
```

We choose xmin = 210.

```
Your input is xmin = 210 m.
The nearest grid is at x = 204.4921 m.
The index of the nearest grid is 1.
------------------------------------------------------------
Please input the end value of zoomed xmax (meters):
```

Similar xmax = 80E3.

```
Your input is xmax = 80000 m.
The nearest grid is at x = 79882.8906 m.
The index of the nearest grid is 603.
The code will find the grid point nearest to the input value and use this
point to make movies. If the input is exactly in the middle of two grid
points, the grid with smaller index is chosen.
------------------------------------------------------------
y coordinate at CENTER of cells may be too long to display.
Below are the first and last a few elements (m):
  100   300   500   700   900
  38900  39100  39300  39500  39700  39900
Please input the start value of zoomed ymin (meters):
```

ymin = 100.

```
Your input is ymin = 100 m.
The nearest grid is at y = 100 m.
The index of the nearest grid is 1.
------------------------------------------------------------
Please input the end value of zoomed ymax (meters):
```

ymax = 39900. Step Five: choose the figure size. Currently the size is in terms of pixels, and I will change it to actual size in cm or inch in future. MATLAB will pop up two empty plots in different sizes. We can choose "1" or "2", or "3: Customize the size by inputting the horizontal and vertical pixel numbers". We choose "3" and type in the size "1000" and "600".

```
Your input is ymax = 39900 m.
The nearest grid is at y = 39900 m.
The index of the nearest grid is 200.
------------------------------------------------------------
----------------------Step Five-----------------------------
--------------Please choose the size of the plot------------
------------------------------------------------------------
figure 1 and figure 2 are two recommendations.
1: figure 1 with 600 horizontal pixels and 450 vertical pixels.
2: figure 2 with 900 horizontal pixels and 300 vertical pixels.
3: Customize the size by inputing the horizontal and vertical pixel numbers.
------------------------------------------------------------
Which size would you like [1, 2, 3]:3
------------------------------------------------------------
You choose customize the size.
Please input the horizontal pixel number,
recommended size(50<input<1000):1000
------------------------------------------------------------
Please input the vertical pixel number,
recommended size(50<input<1000):600
------------------------------------------------------------
Is this size OK? [1: Yes  2: No]:1
```

Step Six: choose contour or pcolor.

```
Your customized plot is 1000*600.
------------------------------------------------------------
----------------------Step Six------------------------------
--------------Please choose the type of the plot-------------
------------------------------------------------------------
1: contourf
2: pcolor
------------------------------------------------------------
Which type would you like plot [1, 2]:
```

Step Seven: input time step, data dumped frequency, start time, and end time.

```
contourf is chosen.
------------------------------------------------------------
---------------------Step Seven-----------------------------
-Please specify the time parameters by checking the data file-
------------------------------------------------------------
What is your time step dt (seconds):120
------------------------------------------------------------
What is your dump_Freq (multiples of dt) from the file data (seconds):7200
------------------------------------------------------------
The iteration number is the 10 digits number in the data/meta file name.
What is your iteration number for the START time (no unit):0
------------------------------------------------------------
What is your iteration number for the END time (no unit):7200
Your timestep is 120 s.
Your dump frequency is 7200.
Your start time is 0.
Your end time is 7200.
```

Step Eight: enter the minimum and maximum values for the colorbar

```
------------------------------------------------------------
---------------------Step Eight-----------------------------
---------Please specify min and max of the colorbar----------
------------------------------------------------------------
What is MIN value of your colorbar:15
------------------------------------------------------------
What is MAX value of your colorbar:25
Your minCaxis is 15.
Your maxCaxis is 25.
```

Finally type in a name for the movie.

```
Finally, what is your name of the movie (no space allowed):
```

In addition to entering the data one by one, we can also run the code in a script where the required variables values are assigned.

```
%-------------------------------------------------------------------------------
%STEP 1
% 1=T, 2=U, 3=V, 4=W, 5=Eta, 6=S, 7=velocity field, 8=omega_z
plot_var = 1;
%-------------------------------------------------------------------------------
%STEP 2
% 1=horizontal sheet, 2=vertical along x=x0, 3=verocal along y=y0,
% 4=arbitrary curtain. NO COMBINATION of plot=7 and plot_sec=4!
plot_sec = 1;
%-------------------------------------------------------------------------------
%STEP 3
% plot_input is the input value for the specified cross section.
plot_input = -4.7;
% plot_vert_dat_name = abc.dat % if an arbitrary curtain is chosen.
%-------------------------------------------------------------------------------
%STEP 4: 1= no zoom, 2=zoom. If plot_zoom=2 then specify below
flag_whole_zoom = 1; % 0=whole; 1=zoom in
if flag_whole_zoom == 0
    plot_zoom = 1;
else
```

```
    plot_zoom = 2;
    plot_zoom_xmin_input = 210;
    plot_zoom_xmax_input = 80e3;
    plot_zoom_ymin_input = 100;
    plot_zoom_ymax_input = 39900;
    % plot_zoom_zmin_input = -0.25; %top
    % plot_zoom_zmax_input = -19; % bottom
end
%-------------------------------------------------------------------------------
% STEP 5: 1=600*450, 2=900*300, 3=customize. If 3 is chosen, specify.
plot_size = 3;
screen_pos_a3 = 1000; % length of the plot (pixes).
screen_pos_a4 = 600; % width of the plot (pixes).
%-------------------------------------------------------------------------------
% STEP 6: 1=contourf, 2=pcolor.
plot_type = 1;
%-------------------------------------------------------------------------------
% STEP7
plot_dt = 120; % time step
plot_dump = 7200; % dump frequency
plot_starttime = 0; % start time
plot_endtime = 7200; % end time
%-------------------------------------------------------------------------------
% STEP 8, specify the colorbar or the gap number in velocity field
minCaxis = 15;
maxCaxis = 25;
% vel_field_gapnumber = 10; % this is for velocity field only
%-------------------------------------------------------------------------------
% STEP 9, input the name of user_add part.
if flag_whole_zoom == 0
    user_add ='13MAR_200m_base_whole';
else
    user_add ='13MAR_200m_base_zoom';
end
%-------------------------------------------------------------------------------
MITgcmMovieMakerV096
```

Appendix B

ELCOM and the MITgcm Input Files

B.1 2008 Lake Erie ELCOM setup

```
! ------------------------------------------------------------------- !
 FILE                       run_elcom.dat
! ------------------------------------------------------------------- !
 'Lake Erie'                TITLE
 'Wentao Liu'               ANALYST
 'UWaterloo'                ORGANIZATION
 'ELCOM Version2.2.2'       COMMENT
! ------------------------------------------------------------------- !
! input file names (include exact file extension)
 sparsedata.unf         3D_data_file            ! produced by pre_elcom
 usedata.unf            preprocessor_file       ! produced by pre_elcom
 2008ic_temp_357.dat    initial_profile_file    ! water temp initial STN357
 2008ic_temp_341.dat    initial_profile_file    ! water temp initial STN341
 2008ic_temp_84.dat     initial_profile_file    ! water temp initial STN84
 2008ic_temp_452.dat    initial_profile_file    ! water temp initial STN452
 2008met_01_Extend.dat  boundary_condition_file ! sec01 met, eastern
 2008met_02_Extend.dat  boundary_condition_file ! sec02 met, central-east
 2008met_03_Extend.dat  boundary_condition_file ! sec03 met, central-west
 2008met_04_Extend.dat  boundary_condition_file ! sec04 met, western
 2008_flwi_Det.dat      boundary_condition_file ! inflow data 1-Detroit
```

```
 2008_flwo_Nia.dat      boundary_condition_file ! outflw data 2-Niagara
 2008_flwi_Mau.dat      boundary_condition_file ! inflow data 3-Maumee
 2008_flwi_Snd.dat      boundary_condition_file ! inflow data 4-Sandusky
 2008_flwi_Cuy.dat      boundary_condition_file ! inflow data 5-Cuyahoga
 2008_flwi_Gra_ON.dat   boundary_condition_file ! inflow data 6-Grand_ON
 2008_flwi_Rzn.dat      boundary_condition_file ! inflow data 7-Raisin
 2008_flwi_Ver.dat      boundary_condition_file ! outflw data 8-Vermilion
 2008_flwi_Rky.dat      boundary_condition_file ! inflow data 9-Rocky
 2008_flwi_Gra_OH.dat   boundary_condition_file ! inflow data 10-Grand_OH
 2008_flwi_Cat.dat      boundary_condition_file ! inflow data 11-Cattaraugus
 2008_flwi_Buf.dat      boundary_condition_file ! inflow data 12-Buffalo
 datablock_wt_2km.db    datablock_file          ! output definition file
! ------------------------------------------------------------------------ !
! file directories (require quote marks around)
! (note that incomplete quotes can cause code to hang)
 'infiles'      infile_dir          ! input file directory
 'unffiles'     outfile_unf_dir     ! output unf directory
 'txtfiles'     outfile_txt_dir     ! output txt directory
! ------------------------------------------------------------------------ !
! output file names (do not include file extension)
 save               restart_save_file
 restart_final      restart_out_file
! ------------------------------------------------------------------------ !
! simulation modules (on = 1, off = 0)
 1  iheat_input        !  surface thermodynamics
 1  iflow              !  inflow/outflow
 1  itemperature       !  temperature
 0  isalinity          !  salinity
 1  idensity           !  density (baroclinic forcing)
 0  ntracer            !  number of tracers
 0  ICAEDYM            !  water quality module
 1  icoriolis          !  turn off/on coriolis forcing
 2  idatablock         !  datablock version control
 2  ic_dist_weighting  !  exponent horiz interp for profile init conditions
! ------------------------------------------------------------------------ !
! time controls
 2008112.000  start_date_cwr      ! CWR Julian day
 300          del_t               ! Time step in seconds, 5 min
```

```
 55584        iter_max            ! Number of time steps
! ------------------------------------------------------------------- !
! frequency of outputs
 60       iter_out_monitor      ! Diagnostic output to screen interval
 5760     iter_out_save         ! Separate restart file write interval
 5760     iter_out_restart      ! Overwriting restart file write interval
 0        start_output_monitor  ! Start diagnostic output to screen
 0        start_output_save     ! Start restart file write
! ------------------------------------------------------------------- !
! initialization options
 0  irestart            !  start from restart file  (yes=1/no=0)
 0  user_init_u_vel     ! 1 = use stub routine in elcom_user.f90
 0  user_init_v_vel
 0  user_init_w_vel
 0  user_init_temperature
 0  user_init_salinity
 0  user_init_tracer
 0  user_init_height
 0  user_init_extinction
 0  user_update
! ------------------------------------------------------------------- !
! turbulence modeling
! (0=no mixing, 1=static stability mixing, 2=shear mixing)
 6  iclosure        ! turbulence model
                    ! (0=no mixing, 1=static stability mixing, 6=mixed layer)
 1.0e-4 drag_btm_cd ! drag coefficient on bottom cells
! ------------------------------------------------------------------- !
! model settings and controls
 1.0    model_grav_damp_x   ! damping of gravity for x baroclinic term
 1.0    model_grav_damp_y   ! damping of gravity for y baroclinic term
! ------------------------------------------------------------------- !
! scalar max and min for debugging
 0      MIN_WTR_TEMP
 40     MAX_WTR_TEMP
 0      MIN_SALINITY
 35     MAX_SALINITY
 0      MIN_DO
 15     MAX_DO
```

```
 0      IHARDLIMIT           ! 1 = Hard limit scalar values by min/max
! -------------------------------------------------------------------- !
! debug output controls
 0  debug_check              ! level of error checking
 0  debug_print              ! level of debug printing
 0  debug_point              ! sparse data index point for debug output
 1  debug_baroclinic_x       ! error trapping on = 1, off = 0
 1  debug_baroclinic_y       ! error trapping on = 1, off = 0
! -------------------------------------------------------------------- !
! conjugate gradient iteration controls
 1.e-16   CGM_TOL              ! CGM tolerance
 30       CGM_MIN              ! minimum iterations of CGM
 1000     CGM_MAX              ! maximum iterations of CGM
! -------------------------------------------------------------------- !
! default values (superseded by other inputs)
0        DEFAULT_HEIGHT
0.0      DEFAULT_TRACER_1
0.0      DEFAULT_TRACER_2
0.0      DEFAULT_TRACER_3
0.0      DEFAULT_TRACER_4
0.0001   DEFAULT_SALINITY
11.5     DEFAULT_WTR_TEMP
0.0      DEFAULT_WIND_SPEED
0.0      DEFAULT_WIND_DIR
0.3      DEFAULT_PAR_EXTINCTION
3        DEFAULT_BC        ! 1=no-slip,2=free-slip,3=drag all, 9=turbulent BBL
10       WIND_SPEED_HEIGHT ! Wind sensor height
3.5      SCALAR_HEIGHT     ! Met sensor height
```

B.2 Idealized internal Kelvin wave propagation

"data" file in /input which specifies the main parameters for the experiment.

```
# Model parameters
# Continuous equation parameters
&PARM01
tRef=25.,25.,25.,25.,25.,25.,25.,25.,25.,25.,25.,24.,24.,24.,
23.,23.,22.,21.,20.,18.,17.,16.,15.,14.,13.,12.,11.,11.,11.,
10.,10.,10.,10.,10.,10.,10.,10.,10.,10.,10.,
sRef=40*0.,
viscAh=0.25,
viscAz=1.E-4,
no_slip_sides=.TRUE.,
no_slip_bottom=.TRUE.,
diffkhT=1.E-4,
diffKzT=1.E-6,
f0=1.E-4,
beta=0.,
tAlpha=2.E-4,
sBeta=0.,
gravity=9.81,
tempAdvScheme=33,
staggerTimeStep=.TRUE.,
rigidLid=.TRUE.,
implicitFreeSurface=.FALSE.,
useSingleCpuIO=.TRUE.,
globalFiles=.TRUE.,
nonHydrostatic=.FALSE.,
eosType='LINEAR',
readBinaryPrec=64,
&
# Elliptic solver parameters
&PARM02
cg2dMaxIters=1000,
cg2dTargetResidual=1.E-7,
&
# Time stepping parameters
```

```
&PARM03
startTime=0,
endTime=871200.0,
deltaTmom=120.0,
deltaTtracer=120.0,
abEps=0.1,
pChkptFreq=0.0,
chkptFreq=0.0,
dumpFreq=0.0,
monitorFreq=7200.0,
&
# Gridding parameters
&PARM04
usingCartesianGrid=.TRUE.,
usingSphericalPolarGrid=.FALSE.,
delXFile='Pelee.dx',
delY=200*200.0,
delRFile='Pelee.dz',
&
&PARM05
bathyFile='topog.box',
hydrogThetaFile='tRefFile.bin',
zonalWindFile=,
meridWindFile=,
&
```

References

Arend, K., D. Beletsky, J. DePINTO, S. Ludsin, J. Roberts, D. Rucinski, D. Scavia, D. Schwab, and T. Höök. 2011. Seasonal and interannual effects of hypoxia on fish habitat quality in central Lake Erie. Freshwater Biology **56**: 366–383, doi:10.1111/j.1365-2427.2010.02504.x.

Austin, J. A., and J. Allen. 2011. Sensitivity of summer Lake Superior thermal structure to meteorological forcing. Limnology and Oceanography **56**: 1141–1154, doi:10.4319/lo.2011.56.3.1141.

Beletsky, D., and D. J. Schwab. 2001. Modeling circulation and thermal structure in Lake Michigan: Annual cycle and interannual variability. Journal of Geophysical Research **106**: 19745–19771, doi:10.1029/2000JC000691.

Beletsky, D., W. P. Oconnor, D. J. Schwab, and D. E. Dietrich. 1997. Numerical simulation of internal Kelvin waves and coastal upwelling fronts. Journal of Physical Oceanography **27**: 1197–1215, doi:10.1175/1520-0485(1997)027<1197:NSOIKW>2.0.CO;2.

Beletsky, D., D. J. Schwab, and M. McCormick. 2006. Modeling the 1998-2003 summer circulation and thermal structure in Lake Michigan. Journal of Geophysical Research **111**: C10010, doi:10.1029/2005JC003222.

Bennington, V., G. A. McKinley, N. Kimura, and C. H. Wu. 2010. General circulation of Lake Superior: Mean, variability, and trends from 1979 to 2006. Journal of Geophysical Research-Oceans **115**: C12015, doi:10.1029/2010JC006261.

Blumberg, A. F., and D. M. Ditoro. 1990. Effects of climate warming on dissolved oxygen concentrations in Lake Erie. Transactions of the American Fisheries Society **119**: 210–223, doi:10.1577/1548-8659(1990)119<0210:EOCWOD>2.3.CO;2.

Blumberg, A. F., and G. L. Mellor. 1987. A description of a three dimensional coastal ocean circulation model, pp. 1–16. *In* Three Dimensional Ocean Models, Estuarine, Coastal and Shelf Science vol.5. American Geophysical Union, doi:10.1029/CO004p0001.

Bocaniov, S., and R. Smith. 2009. Plankton metabolic balance at the margins of very large lakes: Temporal variability and evidence for dominance of autochthonous processes. Freshwater Biology **54**: 345–362, doi:10.1111/j.1365-2427.2008.02120.x.

Bocaniov, S., S. Schiff, and R. Smith. 2012. Plankton metabolism and physical forcing in a productive embayment of a large oligotrophic lake: Insights from stable oxygen isotopes. Freshwater Biology **57**: 481–496, doi:10.1111/j.1365-2427.2011.02715.x.

Bolsenga, S., and C. Herdendorf [eds.]. 1993. Lake Erie and Lake St. Clair Handbook. Wayne State University Press.

Bouard, R., and M. Coutanceau. 1980. The early stage of development of the wake behind an impulsively started cylinder for 40 <Re< 10^4. Journal of Fluid Mechanics **101**: 583–607, doi:10.1017/S0022112080001814.

Bouffard, D., L. Boegman, and Y. R. Rao. 2012. Poincaré wave-induced mixing in a large lake. Limnology and Oceanography **57**: 1201–1216, doi:10.4319/lo.2012.57.4.1201.

CAEDYM Science Manual. 2006. Computational Aquatic Ecosystem DYnamics Model, v2.3 Science Manual. Centre for Water Research, University of Western Australia.

CAEDYM User Manual. 2006. Computational Aquatic Ecosystem DYnamics Model, v2.3 User Manual. Centre for Water Research, University of Western Australia.

Carignan, R., D. Planas, and C. Vis. 2000. Planktonic production and respiration in oligotrophic Shield lakes. Limnology and Oceanography **45**: 189–199, doi:10.4319/lo.2000.45.1.0189.

Casulli, V., and R. Cheng. 1992. Semi-implicit finite difference methods for three-dimensional shallow water flow. International Journal for Numerical Methods in Fluids **15**: 629–648, doi:10.1002/fld.1650150602.

Charlton, M., and J. Milne. 2004. Review of thirty years of change in Lake Erie water quality. NWRI Contribution No. 04-167.

Collins, W., and S. Dennis. 1973. Flow past an impulsively started circular cylinder. Journal of Fluid Mechanics **60**: 105–127, doi:10.1017/S0022112073000078.

Coutanceau, M., and J. Defaye. 1991. Circular cylinder wake configurations: A flow visualization survey. Applied Mechanics Reviews **44**: 255, doi:10.1115/1.3119504.

Deremble, B., A. Hogg, P. Berloff, and W. Dewar. 2011. On the application of no-slip lateral boundary conditions to 'coarsely' resolved ocean models. Ocean Modelling **39**: 411–415, doi:10.1016/j.ocemod.2011.05.002.

Desai, A., J. Austin, V. Bennington, and G. McKinley. 2009. Stronger winds over a large lake in response to weakening air-to-lake temperature gradient. Nature Geoscience **2**: 855–858, doi:10.1038/ngeo693.

Diehl, S., S. Berger, R. Ptacnik, and A. Wild. 2002. Phytoplankton, light, and nutrients in a gradient of mixing depths: Field experiments. Ecology **83**: 399–411, doi:10.1890/0012-9658(2002)083[0399:PLANIA]2.0.CO;2.

Donaldson, M., S. Cooke, D. Patterson, and J. Macdonald. 2008. Cold shock and fish. Journal of Fish Biology **73**: 1491–1530, doi:10.1111/j.1095-8649.2008.02061.x.

ELCOM Science Manual. 2006. Estuary, Lake and Coastal Ocean Model ELCOM, v2.2 Science Manual. Centre for Water Research, University of Western Australia.

ELCOM User Manual. 2006. Estuary, Lake and Coastal Ocean Model ELCOM, v2.2 User Manual. Centre for Water Research, University of Western Australia.

Falkowski, P., and J. Raven. 2007. Aquatic photosynthesis, 2nd ed. Princeton University Press.

Fang, X., H. Stefan, J. Eaton, J. McCormick, and S. Alam. 2004. Simulation of thermal/dissolved oxygen habitat for fishes in lakes under different climate scenarios: Part 1. Cool-water fish in the contiguous US. Ecological Modelling **172**: 13–37, doi:10.1016/S0304-3800(03)00282-5.

Gill, A. 1982. Atmosphere-Ocean Dynamics. Academic Press.

Goldstein, S., and L. Rosenhead. 1936. Boundary layer growth, pp. 392–401. *In* Mathematical Proceedings of the Cambridge Philosophical Society, vol. 32. Cambridge Univ Press, doi:10.1017/S0305004100019101.

Hodges, B. 1998. Heat budget and thermodynamics at a free surface: Some theory and numerical implementation. Centre for Water Research, University of Western Australia.

Hodges, B., J. Imberger, A. Saggio, and K. Winters. 2000. Modeling basin-scale internal waves in a stratified lake. Limnology and Oceanography **45**: 1603–1620, doi:10.4319/lo.2000.45.7.1603.

Huang, A. N., Y. R. Rao, and Y. Y. Lu. 2010a. Evaluation of a 3-D hydrodynamic model and atmospheric forecast forcing using observations in Lake Ontario. Journal of Geophysical Research **115**: C02004, doi:10.1029/2009JC005601.

Huang, A. N., Y. R. Rao, Y. Y. Lu, and J. Zhao. 2010b. Hydrodynamic modeling of Lake Ontario: An intercomparison of three models. Journal of Geophysical Research **115**: C12076, doi:10.1029/2010JC006269.

Intergovernmental Panel on Climate Change. 2007. Climate Change 2007: Synthesis Report. Contribution of Working Groups I, II and III to the Fourth Assessment Report of the Intergovernmental Panel on Climate Change. Cambridge University Press.

Kalita, J. C., and R. K. Ray. 2009. A transformation-free HOC scheme for incompressible viscous flows past an impulsively started circular cylinder. Journal of Computational Physics **228**: 5207–5236, doi:10.1016/j.jcp.2009.04.016.

Kramer, D. 1987. Dissolved oxygen and fish behavior. Environmental Biology of Fishes **18**: 81–92, doi:10.1007/BF00002597.

Kundu, P., and I. Cohen. 2004. Fluid Mechanics, 3rd ed. Elsevier Academic Press.

Kunz, T., and S. Diehl. 2003. Phytoplankton, light and nutrients along a gradient of mixing depth: A field test of producer-resource theory. Freshwater Biology **48**: 1050–1063, doi:10.1046/j.1365-2427.2003.01065.x.

Lam, D., and W. Schertzer. 1987. Lake Erie thermocline model results: Comparison with 1967–1982 data and relation to anoxic occurrences. Journal of Great Lakes Research **13**: 757–769, doi:10.1016/S0380-1330(87)71689-X.

Lam, D. C. L., and W. M. Schertzer. 1999. Potential climate change effects on Great Lakes hydrodynamics and water quality. American Society of Civil Engineers.

Lamb, K. G. 2004. On boundary-layer separation and internal wave generation at the Knight Inlet sill. Proceedings of the Royal Society of London Series A, Mathematical Physical and Engineering Sciences **460**: 2305–2337, doi:10.1098/rspa.2003.1276.

Laval, B., J. Imberger, B. R. Hodges, and R. Stocker. 2003. Modeling circulation in lakes: Spatial and temporal variations. Limnology and Oceanography **48**: 983–994, doi:10.4319/lo.2003.48.3.0983.

Lehman, J. T. 2002. Mixing patterns and plankton biomass of the St. Lawrence Great Lakes under climate change scenarios. Journal of Great Lakes Research **28**: 583–596, doi:10.1016/S0380-1330(02)70607-2.

Leon, L., R. Smith, S. Malkin, D. Depew, M. Hipsey, J. Antenucci, S. Higgins, R. Hecky, and R. Rao. 2012. Nested 3D modeling of the spatial dynamics of nutrients and phytoplankton in a Lake Ontario nearshore zone. Journal of Great Lakes Research **38**: 171–183, doi:10.1016/j.jglr.2012.02.006.

Leon, L. F., R. E. H. Smith, M. R. Hipsey, S. A. Bocaniov, S. N. Higgins, R. E. Hecky, J. P. Antenucci, J. A. Imberger, and S. J. Guildford. 2011. Application of a 3D hydrodynamic-biological model for seasonal and spatial dynamics of water quality and phytoplankton in Lake Erie. Journal of Great Lakes Research **37**: 41–53, doi:10.1016/j.jglr.2010.12.007.

Leon, L. K., J. Imberger, R. E. H. Smith, R. E. Hecky, D. C. L. Lam, and W. M. Schertzer. 2005. Modeling as a tool for nutrient management in Lake Erie: A hydrodynamics study. Journal of Great Lakes Research **31**: 309–318, doi:10.1016/S0380-1330(05)70323-3.

Lynch, A. J., W. W. Taylor, and K. D. Smith. 2010. The influence of changing climate on the ecology and management of selected Laurentian Great Lakes fisheries. Journal of Fish Biology **77**: 1764–1782, doi:10.1111/j.1095-8649.2010.02759.x.

Magaldi, M., T. Özgökmen, A. Griffa, E. Chassignet, M. Iskandarani, and H. Peters. 2008. Turbulent flow regimes behind a coastal cape in a stratified and rotating environment. Ocean Modelling **25**: 65–82, doi:10.1016/j.ocemod.2008.06.006.

Marshall, J., A. Adcroft, C. Hill, L. Perelman, and C. Heisey. 1997a. A finite-volume, incompressible Navier Stokes model for studies of the ocean on parallel computers. Journal of Geophysical Research **102**: 5753–5766, doi:10.1029/96JC02775.

Marshall, J., C. Hill, L. Perelman, and A. Adcroft. 1997b. Hydrostatic, quasi-hydrostatic, and nonhydrostatic ocean modeling. Journal of Geophysical Research **102**: 5733–5752, doi:10.1029/96JC02776.

McCabe, R., P. MacCready, and G. Pawlak. 2006. Form drag due to flow separation at a headland. Journal of physical oceanography **36**: 2136–2152, doi:10.1175/JPO2966.1.

McCormick, M. J. 1990. Potential changes in thermal structure and cycle of Lake Michigan due to global warming. Transactions of the American Fisheries Society **119**: 183–194, doi:10.1577/1548-8659(1990)119<0183:PCITSA>2.3.CO;2.

McKinney, P., B. Holt, and K. Matsumoto. 2012. Small eddies observed in Lake Superior using SAR and sea surface temperature imagery. Journal of Great Lakes Research doi:10.1016/j.jglr.2012.09.023.

Mesinger, F., G. DiMego, E. Kalnay, K. Mitchell, P. C. Shafran, W. Ebisuzaki, D. Jovic, J. Woollen, E. Rogers, E. H. Berbery, M. B. Ek, Y. Fan, R. Grumbine, W. Higgins, H. Li, Y. Lin, G. Manikin, D. Parrish, and W. Shi. 2006. North American regional reanalysis. Bulletin of the American Meteorological Society **87**: 343–360, doi:10.1175/BAMS-87-3-343.

Michalak, A., E. Anderson, D. Beletsky, S. Boland, N. Bosch, T. Bridgeman, J. Chaffin, K. Cho, R. Confesor, I. Daloğlu, et al. 2013. Record-setting algal bloom in Lake Erie caused by agricultural and meteorological trends consistent with expected future conditions. Proceedings of the National Academy of Sciences **110**: 6448–6452, doi:10.1073/pnas.1216006110.

MITgcm Manual. 2013. MITgcm Manual. MIT Department of EAPS.

Monismith, S. G. 1986. An experimental study of the upwelling response of stratified reservoirs to surface shear stress. Journal of Fluid Mechanics **171**: 407–439, doi:10.1017/S0022112086001507.

Mortimer, C. H. 1974. Lake hydrodynamics. verhandlungen internationale vereinigung limnologie **20**: 124–197.

Mortsch, L., and F. H. Quinn. 1996. Climate change scenarios for Great Lakes Basin ecosystem studies. Limnology and Oceanography **41**: 903–911, doi:10.4319/lo.1996.41.5.0903.

Mortsch, L., H. Hengeveld, M. Lister, L. Wenger, B. Lofgren, F. Quinn, and M. Slivitzky. 2000. Climate change impacts on the hydrology of the Great Lakes-St. Lawrence system. Canadian Water Resources Journal **25**: 153–179, doi:10.4296/cwrj2502153.

Obolkin, V., and V. Potemkin. 2006. The impact of large lakes on climate in the past: A possible scenario for Lake Baikal. Hydrobiologia **568**: 249–252, doi:10.1007/s10750-006-0307-9.

O'Sullivan, P., and C. Reynolds [eds.]. 2004. The Lakes Handbook: Limnology and Limnetic Ecology. Wiley-Blackwell.

Patterson, J. C., B. R. Allanson, and G. N. Ivey. 1985. A dissolved oxygen budget model for Lake Erie in summer. Freshwater Biology **15**: 683–694, doi:10.1111/j.1365-2427.1985.tb00242.x.

Pattiaratchi, C., A. James, and M. Collins. 1987. Island wakes and headland eddies: A comparison between remotely sensed data and laboratory experiments. Journal of Geophysical Research **92**: 783–794, doi:10.1029/JC092iC01p00783.

Rao, D. B. 1966. Free gravitational oscillations in rotating rectangular basins. Journal of Fluid Mechanics **25**: 523–555, doi:10.1017/S0022112066000235.

Rao, Y. R., and D. J. Schwab. 2007. Transport and mixing between the coastal and offshore waters in the Great Lakes: A review. Journal of Great Lakes Research **33**: 202–218, doi:10.3394/0380-1330(2007)33[202:TAMBTC]2.0.CO;2.

Rao, Y. R., N. Hawley, M. N. Charlton, and W. M. Schertzer. 2008. Physical processes and hypoxia in the central basin of Lake Erie. Limnology and Oceanography **53**: 2007–2020, doi:10.4319/lo.2008.53.5.2007.

Robertson, D. M., and R. A. Ragotzkie. 1990. Changes in the thermal structure of moderate to large sized lakes in response to changes in air temperature. Aquatic Sciences **52**: 360–380, doi:10.1007/BF00879763.

Rodgers, G. K. 1987. Time of onset of full thermal stratification in Lake Ontario in relation to lake temperatures in winter. Canadian Journal of Fisheries and Aquatic Sciences **44**: 2225–2229, doi:10.1139/f87-273.

Rucinski, D. K., D. Beletsky, J. V. DePinto, D. J. Schwab, and D. Scavia. 2010. A simple 1-dimensional, climate based dissolved oxygen model for the central basin of Lake Erie. Journal of Great Lakes Research **36**: 465–476, doi:10.1016/j.jglr.2010.06.002.

Saggio, A., and J. Imberger. 1998. Internal wave weather in a stratified lake. Limnology and Oceanography **43**: 1780–1795, doi:10.4319/lo.1998.43.8.1780.

Schlichting, H., and K. Gersten. 2004. Boundary-layer theory. Springer.

Schwab, D. J., and K. Bedford. 1994. Initial implementation of the Great Lakes forecasting system: A real-time system for predicting lake circulation and thermal structure. Water Quality Research Journal of Canada **29**: 203–220.

Schwab, D. J., and J. A. Morton. 1984. Estimation of overlake wind speed from overland wind speed: A comparison of three methods. Journal of Great Lakes Research **10**: 68–72, doi:10.1016/S0380-1330(84)71808-9.

Sheng, J. Y., and Y. R. Rao. 2006. Circulation and thermal structure in Lake Huron and Georgian Bay: Application of a nested-grid hydrodynamic model. Continental Shelf Research **26**: 1496–1518, doi:10.1016/j.csr.2006.01.019.

Shore, J. A. 2009. Modelling the circulation and exchange of Kingston Basin and Lake Ontario with FVCOM. Ocean Modelling **30**: 106–114, doi:10.1016/j.ocemod.2009.06.007.

Simons, T. J. 1974. Verification of numerical models of Lake Ontario: Part I. Circulation in spring and early summer. Journal of Physical Oceanography **4**: 507–523, doi:10.1175/1520-0485(1974)004<0507:VONMOL>2.0.CO;2.

Trenberth, K., J. Fasullo, and J. Kiehl. 2009. Earth's global energy budget. Bulletin of the American Meteorological Society **90**: 311–323, doi:10.1175/2008BAMS2634.1.

Tritton, D. 1959. Experiments on the flow past a circular cylinder at low Reynolds numbers. Journal of Fluid Mechanics **6**: 547–567, doi:10.1017/S0022112059000829.

Trolle, D., D. P. Hamilton, C. A. Pilditch, I. C. Duggan, and E. Jeppesen. 2011. Predicting the effects of climate change on trophic status of three morphologically varying lakes: Implications for lake restoration and management. Environmental Modelling & Software **26**: 354–370, doi:10.1016/j.envsoft.2010.08.009.

Tuann, S., and M. Olson. 1978. Numerical studies of the flow around a circular cylinder by a finite element method. Computers & Fluids **6**: 219–240, doi:10.1016/0045-7930(78)90015-4.

Verburg, P., and J. P. Antenucci. 2010. Persistent unstable atmospheric boundary layer enhances sensible and latent heat loss in a tropical great lake: Lake Tanganyika. Journal of Geophysical Research **115**: D11109, doi:10.1029/2009JD012839.

Wetzel, R. 2001. Limnology: Lake and River Ecosystems, 3rd ed. Academic Press.

Wuest, A., and A. Lorke. 2003. Small-scale hydrodynamics in lakes. Annual Review of Fluid Mechanics **35**: 373–412, doi:10.1146/annurev.fluid.35.101101.161220.